Title

Investigating density fluctuations and rotation in tokamak plasmas with Doppler back-scattering

Author

Pratt, Quinn Thomas

Publication Date

2024

Peer reviewed|Thesis/dissertation

UNIVERSITY OF CALIFORNIA

Los Angeles

Investigating density fluctuations and rotation in tokamak plasmas with Doppler back-scattering

A dissertation submitted in partial satisfaction
of the requirements for the degree
Doctor of Philosophy in Physics

by

Quinn Thomas Pratt

2024

ABSTRACT OF THE DISSERTATION

Investigating density fluctuations and rotation in tokamak plasmas with Doppler back-scattering

by

Quinn Thomas Pratt
Doctor of Philosophy in Physics
University of California, Los Angeles, 2024
Professor Troy A. Carter, Chair

This dissertation reports advancements in measuring density fluctuations and flow velocity in tokamak plasmas using the Doppler back-scattering (DBS) diagnostic. Two separate investigations are presented: measurements of the back-scattered power perpendicular wavenumber spectrum, and a thorough cross-diagnostic comparison of $E \times B$ rotation measurements. To measure the perpendicular wavenumber spectrum using DBS, the launch-angle(s) of the probing beam were scanned to probe different values of $k_\perp$ at the cutoff layer. Measurements were made in RF-heated H-mode plasmas with low collisionality and dominant electron-heating – a regime expected to be relevant for future burning plasmas. The back-scattered power spectrum, $P_s(k_\perp)$, is found to exhibit exponential decay. In normalized wavenumbers, the exponential decay factor ($P_s(k_\perp) \propto e^{-\zeta(k_\perp \rho_s)}$) was found to be $\zeta \approx 1.7$ over the majority of the spectrum and $\zeta \approx 3.9$ at high-$k_\perp \rho_s$. Novel synthetic diagnostic modeling was performed to test models of plasma turbulence against the measured $P_s(k_\perp)$. DBS instrumental effects and the plasma density fluctuations, δn, were each modeled with varying levels of physics-fidelity. Reduced model beam-tracing and quasi-linear gyro-fluid results are compared with higher-fidelity full-wave and nonlinear gyrokinetics simulations. Ultimately, mixed-agreement between measurements and simulations across the wavenumber spectrum is found. At the lowest measured wavenumbers $k_\perp \rho_s \leq 0.4$ and for $k_\perp \rho_s \geq 1.2$

simulations and measurements agree as to the shape of the wavenumber spectrum. Over the range $0.4 < k_\perp \rho_s < 1.2$, simulations and measurements disagree as to the rate of spectral decay. Transport modeling found that while the reduced quasi-linear model can match the experimental fluxes, it does not reproduce the higher-fidelity nonlinear gyrokinetic behavior in the electron energy channel. In a separate investigation, rigorous cross-diagnostic comparisons were made between DBS and the charge-exchange recombination spectroscopy (CER) diagnostics. Measurements were made in an L-mode plasma where neutral beam injection (NBI) applied a variable external torque. In analyzing the DBS measurements, novel spectral fitting methods and uncertainty propagation were used to construct the DBS-CER comparison dataset. Statistical analysis suggests a tendency for DBS and CER to agree within their respective uncertainties. Across the comparison dataset, the average difference in $\omega_{E\times B}$ was found to be $|\bar{d}| = 0.1$ kRad/s. The 95% confidence interval for their agreement was found to be approximately 5 kRad/s in terms of $\omega_{E\times B}$. The phase velocity of δn fluctuations was estimated using linear gyro-fluid analysis and found to be negligible relative to $v_{E\times B}$. The results of the rotation investigation provide a certain level of mutual-validation for DBS and CER in measuring $E \times B$ rotation.

The dissertation of Quinn Thomas Pratt is approved.

Terry Rhodes

George J. Morales

Christoph Niemann

Eduardo Paulo Jorge da Costa Alves

Troy A. Carter, Committee Chair

University of California, Los Angeles

2024

Dedicated to Riley, my parents, and my sisters.

TABLE OF CONTENTS

LIST OF FIGURES

LIST OF TABLES

ACKNOWLEDGMENTS

I would like to thank my advisors: Professor Troy Carter and Dr. Terry Rhodes. Both Terry and Troy showed me unwavering support over the years; always finding time to discuss the latest developments in my research and providing insightful feedback. I would like to thank Troy for allowing me to complete my doctoral research remotely at the DIII-D National Fusion Facility, and I thank Terry for guiding me on-site at DIII-D and encouraging me to pursue a broad range of research projects. I also thank the entire UCLA-PDG group: Drs. Tony Peebles, Neal Crocker, Kshitish Barada, Rongjie Hong, Guiding Wang, Lei Zeng, and Julius Damba for helping collect and analyze data, and contributing to my education over the years. I also thank Larry Bradley and Roman Lantsov for their support with laboratory hardware and electronics.

I am grateful to the entire DIII-D team for their contributions to my research and their support in conducting the experiments featured in this dissertation. Specifically, I would like to thank Drs. Brian Grierson, and Colin Chrystal for charge exchange measurements, analysis, and discussions regarding tokamak rotation theory. Special thanks to those who directly supported my Ph.D. experiment on DIII-D, specifically: Drs. Kathreen Thome and James Yang for assisting with ECH and NBI, Dr. Al Hayatt for serving as the physics operator, and Dr. Ruifeng Xi for coordinating other diagnostics. Furthermore, I am grateful to those who assisted with additional analysis of data from my experiment including Drs. Shaun Haskey and Tyler Cote.

I would like to thank Drs. Sterling Smith, Orso Meneghini, and other OMFIT developers for guiding me in software development and reviewing my code contributions. I also thank Dr. Chris Holland for his support with the CGYRO code and enlightening discussions regarding synthetic diagnostics. I am indebted to Dr. Tom Neiser for numerous discussions concerning the TGLF code. Special thanks are due to Dr. Valerian Hall-Chen for many discussions of beam-DBS theory and for his assistance with the SCOTTY code. I also thank Dr. Juan Ruiz Ruiz for discussions regarding gyrokinetics, beam-DBS theory, and synthetic

diagnostics.

I would also like to acknowledge my undergraduate physics and engineering advisors at the University of San Diego including Professors Greg Severn and Imane Khalil along with numerous other professors in the physics, mathematics and engineering departments. I am appreciative of Kyle Callahan for his assistance over the years with a broad range of DIII-D experimental analysis topics. I thank Josh Larson for his help getting me started with COMSOL modeling. My heartfelt appreciation goes to my fellow UCLA Ph.D. students: Dr. Marcos Flores, Briley Lewis, Joey Marcinik, and Thomas Dellaert for their support, friendship, and tireless enthusiasm for physics. Finally, I am deeply thankful for my wife Riley, for tolerating years of physics discussions and for her love and support throughout my Ph.D. studies. The work set forth in this dissertation would not be possible without support from numerous other friends, and colleagues to whom I owe a debt of gratitude.

VITA

2018	B.A. Physics, B.S. & B.A. Mechanical Engineering University of San Diego, San Diego, CA, USA
2019	M.S. Physics University of California Los Angeles, Los Angeles, CA, USA
2019–present	Ph.D. Candidate, Department of Physics & Astronomy University of California Los Angeles, Los Angeles, CA, USA

PUBLICATIONS AND PRESENTATIONS

Density wavenumber spectrum measurements, synthetic diagnostic development, and tests of quasilinear turbulence modeling in the core of electron-heated DIII-D H-mode plasmas.
Q. Pratt *et al.* 2024 Nucl. Fusion 64 016001

New measurements of H-mode core density fluctuation wavenumber spectra and tests of quasilinear turbulence modeling.
Q. Pratt *et al.*, Invited Oral Presentation, 65$^{\text{th}}$ Annual Meeting of the APS Division of Plasma Physics, Denver, CO, Oct. 31, 2023

Turbulent density wavenumber spectrum measurements and linear simulations of ECH H-mode plasmas in DIII-D.
Q. Pratt *et al.*, Poster Presentation, 64$^{\text{th}}$ Annual Meeting of the APS Division of Plasma Physics, Spokane, WA, Oct. 18, 2022

Comparison of Doppler back-scattering and charge exchange measurements of $E \times B$ plasma rotation in the DIII-D tokamak under varying torque conditions.
Q Pratt *et al.* 2022 Plasma Phys. Control. Fusion 64 095017

New cross-channel calibration for mm-wave scattering diagnostics at the DIII-D tokamak.
Q. Pratt *et al.*, Poster Presentation, 63$^{\text{rd}}$ Annual Meeting of the APS Division of Plasma Physics, Pittsburg, PA, Nov. 8, 2021

Comparison of DBS and CER measurements of $E \times B$ rotation in the DIII-D Tokamak.
Q. Pratt *et al.*, Poster Presentation, 62$^{\text{nd}}$ Annual Meeting of the APS Division of Plasma Physics, Remote, Nov. 10, 2020

CHAPTER 1

Introduction

1.1 Nuclear fusion energy

Nuclear fusion is the synthesis of heavier nuclei from lighter subatomic components. Energy is released when the fusion product is in a more energetically favorable configuration. Harnessing the energy released during fusion reactions is the ultimate goal of fusion energy research. Since the 1950s, when research began, the field has made enormous progress toward achieving net energy production. However, no fusion experiment to date has achieved this goal. Although the challenges of fusion are daunting, the promise of near limitless energy continues to push the field forward.

For fusion to take place, nuclei must overcome (or tunnel through) the repulsive Coulomb barrier to allow strong nuclear interactions to occur. This necessitates that a significant population of the nuclei have substantial kinetic energy. The energy required is well beyond the ionization threshold of lighter elements. Thus, an environment supporting nuclear fusion will be a fully-ionized plasma. The task of achieving fusion on earth is directly linked with the confinement and heating of a plasma.

There are two leading strategies for plasma confinement: Inertial Confinement Fusion (ICF) and Magnetic Confinement Fusion (MCF). In each case, lighter nuclei are driven to extreme temperatures/densities such that the probability of fusion reactions is appreciable. Then, importantly, the plasma must be confined for a long enough time to release significant energy to the environment (e.g. to heat steam and spin a turbine). Ideally, a fraction of the fusion energy remains in the plasma to provide self-heating, alleviating some external heating requirements. In this thesis we focus on MCF confinement, specifically the tokamak

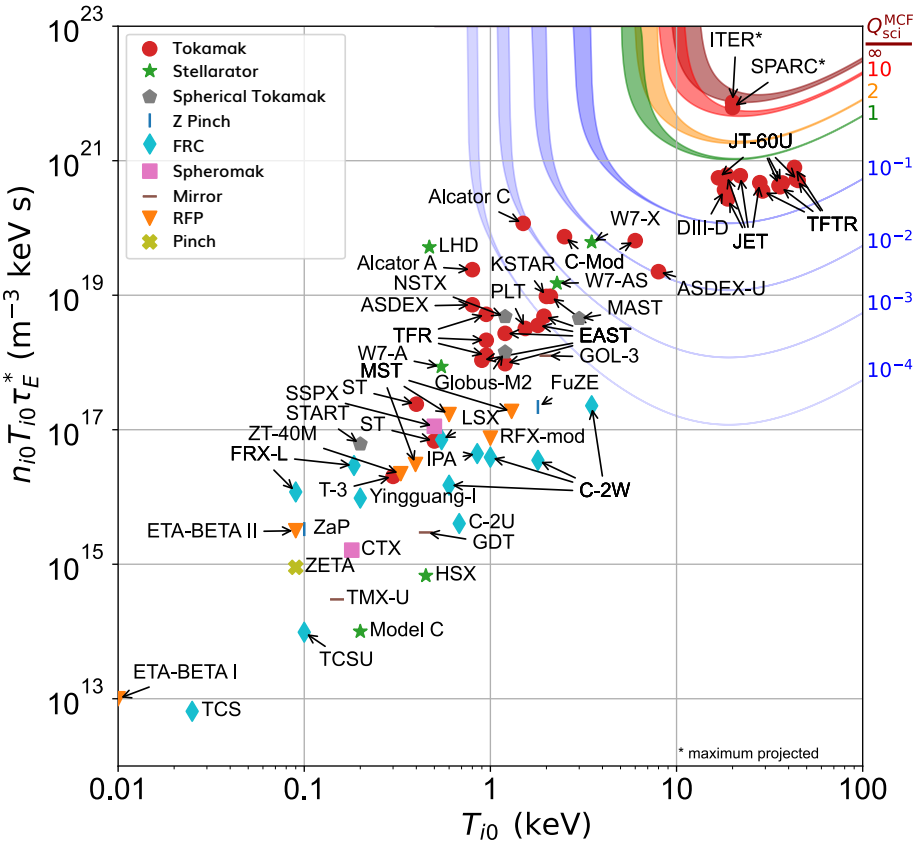

Figure 1.1: Record Lawson triple-product values for various MFE configurations. Contours of $Q_{sci.}$ are also shown in the upper right of the axis. The maximum projected $nT\tau_E$ for planned tokamaks (ITER, SPARC) is also shown. This figure was adapted from [1].

configuration (see Section 2.1).

Balancing the power from external heating and plasma self-heating against losses due to bremsstrahlung radiation and loss of thermal energy over τ_E (the energy confinement time) results in a criterion for 'scientific breakeven' [1]. The scientific breakeven milestone is defined as $Q_{\text{sci.}} = 1$, where $Q_{\text{sci.}} = P_{\text{fus.}}/P_{\text{ext.}}$ is the ratio of the fusion power and the external heating power. In theory, if plasma self-heating is sufficient to exceed all losses, the external power can be removed leading to $Q_{\text{sci.}} \to \infty$. The $Q_{\text{sci.}} \to \infty$ limit is refereed to as 'ignition'. The preceding power balance analysis can be re-cast in terms a required plasma density (n), ion temperature (T) and τ_E to achieve a certain value of $Q_{\text{sci.}}$. The Lawson 'triple-product', $L = nT\tau_E$, combines all three parameters into a single figure of merit for nuclear fusion.

In terms of L, specifying a target value for $Q_{\text{sci.}}$ implies a critical $nT\tau_E \geq L_{\text{crit.}}$. Generally speaking, for a given fusion reaction, there exists a minimum $L_{\text{crit.}}$ as a function of ion temperature. Therefore, we seek the confinement scheme, auxiliary heating methods, and fuel with the minimum required $L_{\text{crit.}}$ to produce fusion energy at a fixed (scientific) gain of $Q_{\text{sci.}}$.

One favorable fusion reaction is between deuterium and tritium (D-T),

$$^{2}_{1}\text{H} + ^{3}_{1}\text{H} \rightarrow ^{4}_{2}\text{He}(3.5 \text{ MeV}) + ^{1}_{0}\text{n}(14.1 \text{ MeV}),$$

which has minimum $L_{\text{crit.}} \approx 3 \times 10^{21}$ [keV·s/m^3] at $T = 14$ [keV] (for ignition). Figure 1.1 illustrates a database of record $nT\tau_E$ values from [1] for a variety of MCF configurations. Also displayed in Figure 1.1 are contours of $Q_{\text{sci.}}$ for the D-T reaction. For all the MCF configurations shown in Figure 1.1, tokamaks are closest to achieving $Q_{\text{sci.}} = 1$ by a significant margin[1]. For example, with significant external heating, $T_i > 14$ [keV] was achieved (transiently) thirty years ago on the TFTR tokamak with densities approaching 1×10^{20} [m^{-3}] [2]. These 'super shot' plasmas obtained record tokamak performance while using D-T fuel. However, achieving breakeven ($L \geq L_{\text{crit.}}$ for $Q_{\text{sci.}} \geq 1$) was not possible. For the demonstrative case of TFTR, the required $\tau_E \approx 2$ [s] for breakeven was 10× larger than what was possible at the time. To this day, τ_E on the order of 1-10 seconds remains 10-100× larger than what is currently achieved on tokamak devices. Extending the energy confinement time of hot, dense plasmas without compromising other important aspects (stability, impurity content, first-wall integrity, etc.) is at the heart of modern tokamak research.

The low energy confinement time observed in tokamak devices is related to the physics of plasma transport. Experimental observations of tokamak transport (i.e. the flux of particles, heat, and momentum across magnetic field lines) exceeded initial theoretical predictions by an order of magnitude or more. These initial, baseline transport predictions are part of what is now called the 'neoclassical theory' of tokamak transport. Historically, the amount of

[1]It is worth noting that because tokamaks achieved early success in the form of record ion temperatures, other MCF schemes have historically received less attention.

transport exceeding the neoclassical prediction was dubbed 'anomalous transport'. Today, this anomalous transport is largely attributed to 'micro-turbulence' arising from unstable ion gyro-radius scale plasma modes. The last two decades of tokamak research has featured significant developments in experimental methods of measuring micro-turbulence and advances in theoretical and numerical modeling to quantitatively predict micro-turbulence driven transport.

Experimental measurements generally capture individual fluctuating fields, e.g. the fluctuating plasma density, δn, or fluctuating temperature, δT. These fluctuating fields – often measured with limited wavenumber/spatial resolution – are not sufficient for directly calculating turbulent fluxes from experimental data. Instead, simulations are used to calculate turbulent fluxes and the simulated δn and δT are compared with fluctuation measurements. The turbulent fluxes predicted by these simulations are large enough to account for the experimentally-observed transport. However, validating these turbulent-transport models against experimental measurements and developing robust reduced models remains an active area of research.

1.2 Summary of the dissertation

This dissertation presents a variety of results based on measurements using the Doppler back-scattering (DBS) diagnostic. Perhaps the most significant results are those pertaining to the density fluctuation wavenumber spectrum, $\delta\hat{n}(k_\perp)$. In addition to measurements of the wavenumber spectrum, a synthetic DBS diagnostic model was developed to test theories of plasma turbulence. The synthetic diagnostic model is used to interpret measurements and test both a quasi-linear gyro-fluid model and higher-fidelity nonlinear gyrokinetics simulations. The $\delta\hat{n}(k_\perp)$ measurements were made in H-mode plasmas sustained only with electron-cyclotron resonance RF heating (ECH). The ECH H-mode plasma regime is expected to be relevant for future burning plasmas where fusion-born alpha particles primarily heat electrons and high temperature core plasmas possess low collisionality. The ECH H-mode discharges studied as part of this doctoral research are part of a less-frequently studied

tokamak plasma regime. While the overall MHD stability, energy confinement, and micro-turbulence character appears similar to more traditional discharges heated by neutral beam injection (NBI); the precise role of unstable electron modes remains unclear.

DBS $\delta\hat{n}(k_\perp)$ measurements, when interpreted in terms of spectral power laws ($|\delta\hat{n}|^2 \propto k_\perp^{-\nu}$), suggest a wavenumber spectrum with variable spectral decay, $0.6 \leq \nu \leq 9.4$, over a broad range of spatial scales, $0.2 \leq k_\perp \rho_s \leq 6$. In fact, the measured spectrum is almost purely exponential in normalized wavenumber space, suggesting the possibility of long-range δn correlations tangent to magnetic flux surfaces (binormal direction). For $k_\perp \rho_s \geq 1.2$ and $k_\perp \rho_s \leq 0.3$, the spectral decay (ν) predicted by turbulence simulations agrees remarkably well with the DBS measurements. However, for $0.4 < k_\perp \rho_s < 1.2$, the turbulence models predict steeper spectral decay than what was observed experimentally. This result is complicated by the fact that the model of DBS instrumental effects, namely beam-tracing, may become less accurate at low-$k_\perp$. The investigation of the $\delta\hat{n}(k_\perp)$ wavenumber spectrum in ECH H-mode plasmas along with advances in DBS modeling to interpret results and test simulations constitutes a large fraction of this dissertation.

In addition to the wavenumber spectrum investigation, a separate investigation is presented which focuses on the frequency spectrum of fluctuations measured by DBS. Specifically, the $E \times B$ rotation inferred from the Doppler shift of back-scattered waves. In the rotation investigation, we compare radial profiles of plasma $E \times B$ rotation based on DBS measurements with values from the charge-exchange recombination spectroscopy (CER) diagnostic. Profiles of $E \times B$ rotation are compared under varying externally-applied torque conditions (due to neutral beam injection). Generally, the $E \times B$ values derived from the two independent diagnostics are found to agree within their respective uncertainties. Statistical analysis of the DBS-CER cross-diagnostic comparison dataset is used to quantify discrepancies and bound when differences may be statistically significant. In some cases, the high time-resolution DBS measurements were found capture the beam-induced prompt torque on the plasma. Additional analysis is presented to estimate the prompt-torque density, the $E \times B$ shearing rate, and the turbulence phase velocity using DBS measurements.

1.2.1 Summary of publications related to this dissertation

In the past decade there have been several developments in DBS theory and hardware which have directly impacted this thesis. The 3D scattering effect of 'mismatch attenuation' – a reduction in the scattering signal when the probing DBS beam is not perpendicular to the background magnetic field at cutoff – has been given particular attention. New quasi-optical DBS hardware was installed in the DIII-D tokamak; including multi-axis mirrors allowing for the toroidal steering of DBS beams (see T. Rhodes *et al.* [3]). Simultaneously, the beam-DBS theoretical framework was developed by V. Hall-Chen *et al.* [4]; providing a means to quantitatively predict the level of mismatch attenuation. In subsequent work by J. Damba and V. Hall-Chen *et al.* [5,6], predictions from the beam-DBS theory were validated against scans of the *toroidal* DBS launch-angle in DIII-D discharges.

The beam-DBS theoretical framework also provides a model of the DBS instrument function (sometimes called a transfer function or weighting function). The work in Chapter 4 of this thesis directly uses the beam-DBS theory to develop and apply a synthetic DBS diagnostic. The application of this synthetic diagnostic to DBS $\delta\hat{n}(k_\perp)$ measurements in ECH H-mode plasmas was published by the author in [7]. The work presented in Chapter 4 also makes use of results from Ruiz-Ruiz *et al.* [8] in modeling DBS and relating the wavenumbers used in simulations to experiment (see Appendix C).

Separately, the rotation investigation in Chapter 5 corresponds to work published by the author in [9]. Aside from these published works, this doctoral research also included the development of an open-source collection of DBS analysis software in the form of an OMFIT module. The OMFIT-DBS module is discussed in more detail in Appendix A and in the OMFIT-DBS tutorial document available on the OMFIT website (`omfit.io`). The OMFIT-DBS module has aided in the analysis of DBS data from both the DIII-D and MAST-U tokamaks and is currently being prepared to analyze data from an upcoming NSTX-U DBS diagnostic. The OMFIT-DBS module has aided DBS analysis in published works including [5, 7, 9–11].

1.3 Outline of the dissertation

This dissertation is divided into six chapters and three appendices:

1. Chapter 1 (this chapter) is the introductory chapter.

2. Chapter 2 includes background information on turbulent transport in tokamak plasmas. In Chapter 2 we also discuss the quasilinear code TGLF used in later analysis. Prior work comparing DBS measurements with simulations is also reviewed.

3. Chapter 3 contains a comprehensive description of the DBS diagnostic. In Chapter 3 we present theory of the DBS scattering process as well as relevant cold-plasma wave theory in the electron-cyclotron range of frequencies. We present the DIII-D DBS electronics and quasi-optical hardware as well as DBS analysis methods. Beyond data analysis, we also present the ray-tracing, beam-tracing, and full-wave methods of simulating the probing DBS wave in the background plasma. Chapter 3 also contains a discussion of the synthetic DBS diagnostic developed as part of this thesis and some discussion of non-ideal/complicating effects in DBS including nonlinear scattering.

4. Chapter 4 presents the density fluctuation wavenumber spectrum investigation in ECH H-mode plasmas. We present the experiment, detailed DBS measurements and results from extensive turbulence/transport modeling. Some of the work presented in Chapter 4 was also published by the author in [7].

5. Chapter 5 presents the $E \times B$ rotation investigation including cross-diagnostic comparisons with the CER diagnostic. We provide some additional background on tokamak rotation and the principles of CER. We present the measured rotation profiles, statistical analysis of the DBS-CER cross-diagnostic comparisons, and some additional analysis of prompt-torque, $E \times B$ shear ($\gamma_{E\times B}$), and estimations of the turbulence phase velocity. Some of the work presented in Chapter 5 was also published by the author in [9].

6. Chapter 6 is the concluding chapter, summarizing the dissertation and discussing avenues for future work.

7. Appendix A discusses the OMFIT-DBS module in detail.

8. Appendix B presents models for the DBS frequency spectrum including the theory-based Taylor model and some *ad hoc* 3-parameter and 4-parameter lineshape models.

9. Appendix C provides details of the nonlinear CGYRO simulations featured in Chapter 4 as well as a discussion of converting wavenumbers between simulation and experiment.

CHAPTER 2

Background: turbulent transport in tokamaks

In this chapter we provide an overview of turbulent transport in tokamak devices. Section 2.1 describes the tokamak configuration with an emphasis on the geometry of the magnetic field and common tokamak coordinate systems. Subsection 2.1.1 briefly describes the parameters of the DIII-D tokamak. Section 2.2 discusses tokamak transport scaling laws and the gyro-Bohm transport paradigm. Section 2.3 presents an overview of the kinetic theory of tokamak transport. Neoclassical and turbulent transport are discussed in Subsections 2.3.1 and 2.3.2 respectively. An overview of quasi-linear transport and the TGLF model is presented in Section 2.4. Section 2.5 provides a phenomenological overview of common tokamak micro-instabilities. Finally, Section 2.6 provides a summary of recent turbulent-transport research along with a description of previous comparisons between DBS measurements and turbulence simulations.

2.1 The tokamak configuration

Tokamaks are magnetic confinement fusion devices designed to confine a hot plasma using an externally-applied toroidal magnetic field. Figure 2.1 provides a 3D rendering of a tokamak. In an inductive tokamak scenario, a central solenoid is used to create a time-changing magnetic flux; inducing a toroidal electric field (transformer circuit in Figure 2.1). The toroidal electric field induces a current in the plasma which in turn produces a poloidal magnetic field necessary for tokamak stability. Importantly, the total magnetic field in a tokamak is helical rather than purely toroidal.

The magnitude and direction of the plasma-generated poloidal magnetic field depends on

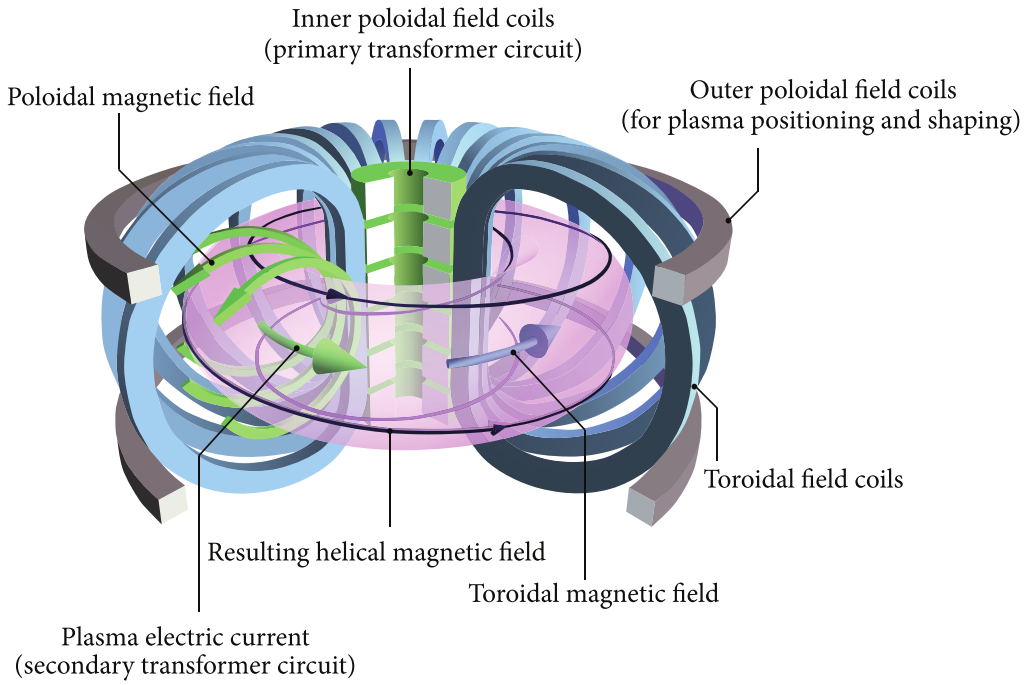

Figure 2.1: Schematic of the tokamak MCF configuration from [12].

the total current density, $\mathbf{j}$, inside the plasma. In general, the helicity of the total magnetic field varies over the plasma minor radius. This shear in the magnetic field is captured by the rotational transform, ι, or its reciprocal q (the safety factor). MHD theory describes the macroscopic distribution of currents in the plasma and the relationship between magnetic forces and the total plasma pressure. The equilibrium equation,

$$\mathbf{j} \times \mathbf{B} = \nabla p, \tag{2.1}$$

can be used to derive the Grad-Shafranov partial differential equation describing the axisymmetric distribution of poloidal magnetic flux ψ. Equation 2.1 also implies that the macroscopic $\mathbf{j}$ and $\mathbf{B}$ are embedded in nested 'flux surfaces'. These flux surfaces play a central role in tokamak theory both as (theoretical) isosurfaces of density, temperature, and bulk rotation, and as the basis for the field-aligned coordinate system.

Figure 2.2 illustrates common tokamak coordinate systems. In Figure 2.2(a) a flux surface is depicted in 3D with an embedded helical magnetic field line. Figure 2.2(a) depicts the

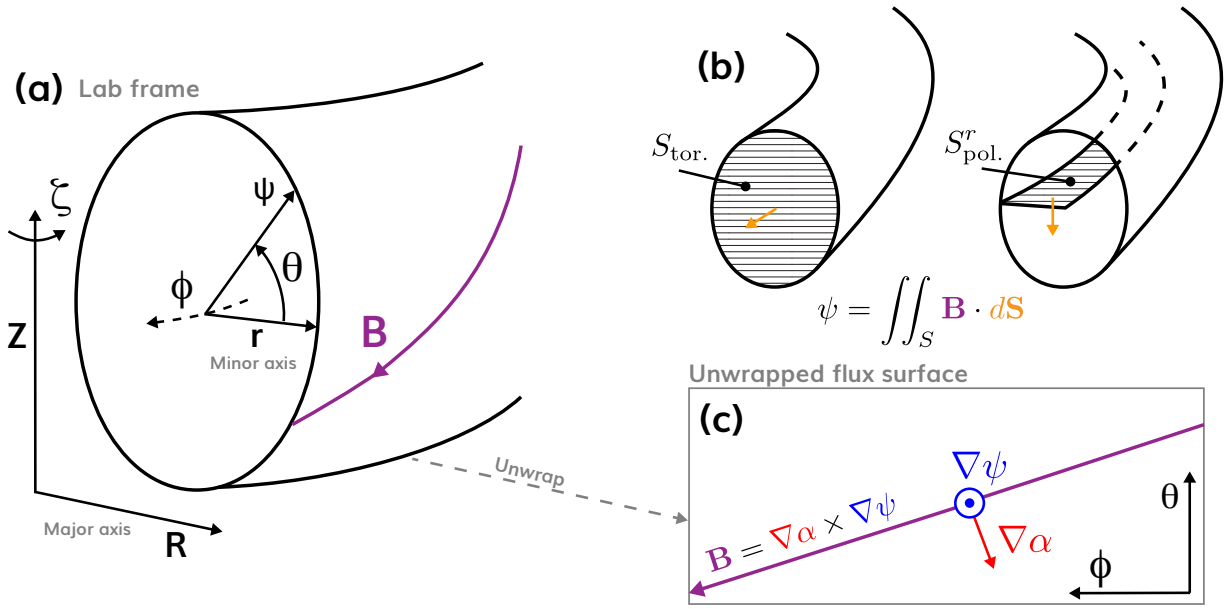

Figure 2.2: Schematic of the tokamak coordinate systems.

lab-cylindrical, (R, ζ, Z), and the simple-toroidal, (r, θ, ϕ), right handed coordinate systems. Note that for non-circular flux surfaces the minor radius, r, varies with the poloidal angle, θ, around the flux surface. For this reason we also show the flux surface label ψ. In principle, any monotonic quantity can be used to label flux surfaces (including r). However, it is natural to use labels which are constant on flux surfaces (e.g. the poloidal magnetic flux, ψ).

Figure 2.2(b) illustrates two magnetic flux conventions: on the left side of 2.2(b) we provide a surface $S_{\text{tor.}}$ at constant toroidal angle ϕ, and on the right side of Figure 2.2(b) we provide a ribbon-type surface[1] $S^r_{\text{pol.}}$ at constant θ. Both the poloidal flux, ψ_p, and toroidal flux, ψ_t, are common flux surface labels (depending on which surface in Figure 2.2(b) is selected for integration). Flux surface labels are typically normalized by their value at the separatrix (the last closed flux surface or LCFS). For example,

$$\rho_t(r) = \sqrt{\frac{\psi_t(r)}{\pi B_{\phi 0}}} \tag{2.2}$$

[1]One can define a disk-type poloidal flux complimentary to the ribbon-type poloidal flux shown in Figure 2.2(b) – see [13]

is the square root of the toroidal magnetic flux normalized by the on-axis toroidal magnetic field. The flux surface label $\rho = \rho_t/\rho_t(a)$ is $\rho_t(r)$ normalized with respect to its separatrix ($r = a$) value. The flux surface label ρ is used throughout this dissertation.

Theoretical descriptions of tokamaks often make use of analytic parameterizations of flux surfaces, i.e. formulas for a flux surface's $R(r, \theta)$ and $Z(r, \theta)$. For example, the Miller [14] and MXH [15] models allow for flux surfaces with non-trivial shapes. More complex flux surface shapes can be parameterized by the elongation κ, triangularity δ, and other scalars. Theoretical tokamak descriptions generally use field-aligned coordinates (i.e. coordinates where the magnetic field becomes a straight line). Figure 2.2(c) illustrates a field-aligned coordinate system using the Clebsch-type magnetic field, $\mathbf{B} = \nabla\alpha \times \nabla\psi$ where $\psi = \psi_p/2\pi$ and $\alpha = \phi + \nu(\psi, \theta)$ with the coordinate $\nu(\psi, \theta)$ encoding the helicity of the magnetic field [16]. The (ψ, θ, α) coordinate system is discussed in more detail in Appendix C. For a mathematically rigorous treatment of flux coordinates see [13].

2.1.1 The DIII-D tokamak

DIII-D is a conventional, midsize tokamak located in San Diego, CA, USA [17]. DIII-D has major radius $R_0 = 1.66$ m with typical plasma LCFS minor radius $a = 0.67$ m for an aspect ratio $R_0/a = A \approx 2.5$ and inverse aspect ratio $\epsilon = A^{-1} \approx 0.4$. The maximum on-axis toroidal magnetic field is $B_{\phi 0} \approx 2.2$ T and the maximum plasma current is $I_p = 2$ MA. For the work considered in this thesis, DIII-D has the following auxiliary heating and current-drive capabilities: eight neutral beam injection (NBI) sources along four beam-lines, and four (gyrotron) electron cyclotron heating (ECH) sources. The first wall of DIII-D is graphite – making Carbon the typical impurity species in DIII-D plasmas.

Figure 2.3 provides a plan view of the DIII-D tokamak along with an example magnetic equilibrium reconstruction from the EFIT code [18]. The four NBI beam-lines with two sources each (R/L) are labeled in Figure 2.3(a) according to their toroidal locations on the machine. The four ECH inputs are also shown in Figure 2.3(a) near the 270° toroidal location. Two DBS systems (discussed in more detail in Chapter 3) are also shown in Figure

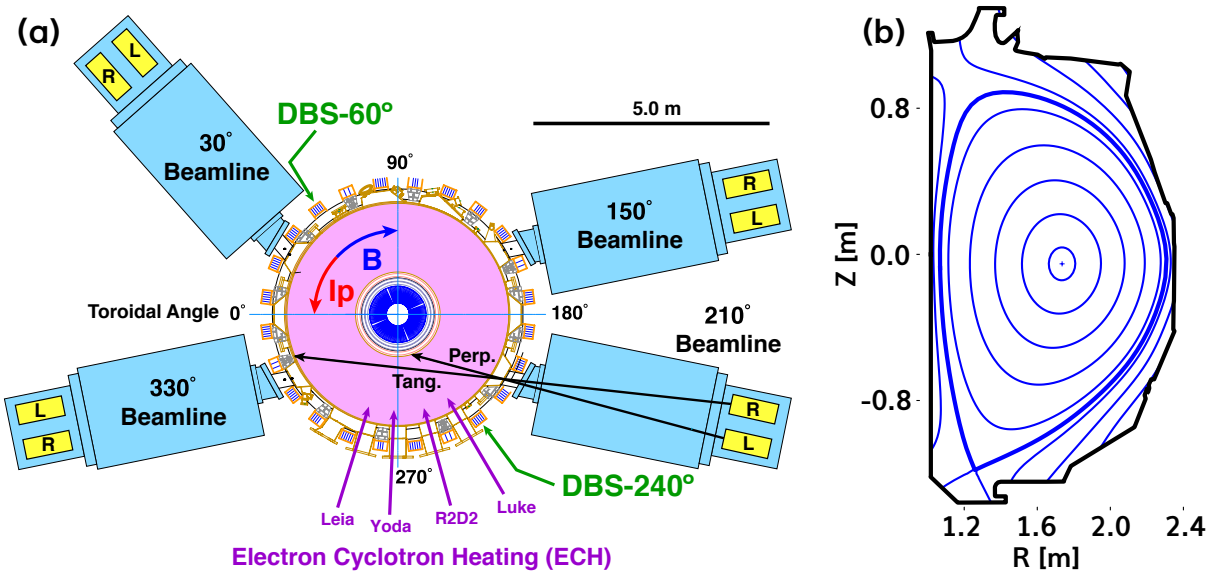

Figure 2.3: Plan view of the DIII-D tokamak with an example magnetic equilibrium. In (a) the 'normal' orientation of the magnetic field and plasma current, I_p are shown. The 210° neutral beam is shown in the counter-I_p direction. The location of the four ECH launchers used at the time of the study in Chapter 4 is shown. The labels for the ECH lines correspond to the gyrotrons. The location of the DBS60 and DBS240 systems are also shown. In (b) an example magnetic equilibrium is shown with flux surfaces (contours of ψ).

2.3(a) and are labeled by their toroidal locations. The magnetic equilibrium shown in Figure 2.3(b) is an example of an elongated (LCFS $\kappa \approx 1.7$), lower single null (diverted) plasma. The term 'lower single null' refers to the formation of a single X-point in the lower half of the separatrix.

2.2 Tokamak transport scaling paradigms

One of the most important questions in magnetic fusion energy research is how plasma transport scales as a function of physics parameters. To answer this question, transport scaling laws have been devised to reduce the complexities of transport down to a handful of variables. Scaling laws can be cast in terms of engineering variables with absolute units (e.g. R [m], I_p [MA], etc.), or in terms of dimensionless plasma parameters (defined below). Ideally, an empirical scaling law would cover a broad range of input parameters such that

overall trends can be deduced. To this end, tokamak researchers from around the world have combined experimental data from multiple tokamaks to establish benchmark empirical scaling laws. These scaling laws been used to guide research and extrapolate toward future devices. In this section we provide a heuristic description of Bohm and gyro-Bohm tokamak scaling paradigms [19]. We also define several dimensionless plasma parameters which appear in later chapters.

Fundamental work regarding plasma transport across magnetic field lines is due to Bohm, where a diffusion coefficient was found to be, $\chi_B \propto T/eB$. From this expression, we can define the Bohm-time, $\tau_B = a^2/\chi_B$ – a characteristic time for Bohm-like diffusion across a system of size a (e.g. the minor radius of the LCFS in a tokamak). The Bohm-time is a natural quantity to normalize other transport timescales such as the energy confinement time, τ_E, introduced in Section 1.1. We may posit that the normalized energy confinement time, τ_E/τ_B has some (unknown) functional dependence on other dimensionless plasma parameters,

$$\tau_E/\tau_B = F(\rho_*, \beta, \nu_*, \ldots). \tag{2.3}$$

In Equation 2.3 the normalized ion-sound gyro radius is,

$$\rho_* \equiv \rho_s/a = \frac{c_s}{a\Omega_i} \tag{2.4}$$

with sound speed, $c_s \equiv \sqrt{T_e/m_i}$, and ion cyclotron frequency, $\Omega_i \equiv Z_i eB/m_i$. Also in Equation 2.3,

$$\beta \equiv \frac{\sum_s n_s T_s}{B^2/(2\mu_0)} \tag{2.5}$$

is the ratio of the total (summed over species s) kinetic pressure to the magnetic pressure. Finally, in Equation 2.3,

$$\nu_{*s} \equiv \frac{\nu_{is}}{\overline{v}_s \epsilon^{3/2}/(qR)} \tag{2.6}$$

is the ratio of the collision frequency to the trapped particle bounce frequency for species s where ν_{is} is the ion-s collision frequency, q is the safety factor, R is the major radius, $\overline{v}_s$ is the

thermal velocity for species s, and $\epsilon = r/R$ is the inverse aspect ratio. For the presentation here we will restrict the function F to depend on ρ_*, β, and ν_* although in general other dimensionless parameters may be relevant. Note that the logic behind Equation 2.3 can be applied to an arbitrary, local, species-dependant transport timescale τ (not only the macroscopic τ_E). For macroscopic timescales such as τ_E, the parameters ρ_*, β, and ν_* are often evaluated for the main ion species and may be volume-averaged.

Two special cases of Equation 2.3 are defined with respect to the ρ_* dependence within the function F,

$$\tau_E/\tau_B = \begin{cases} \rho_*^{-1} F(\beta, \nu_*) & \text{for gyro-Bohm transport,} \\ F(\beta, \nu_*) & \text{for Bohm transport.} \end{cases} \tag{2.7}$$

For the case of gyro-Bohm transport, the function F is taken to scale inversely with the normalized gyro-radius ρ_*. For Bohm transport F is independent of ρ_*. The scaling with ρ_* has a significant impact on projections to future tokamak devices. In contrast with other dimensionless parameters, it is believed ρ_* will change the most as we construct next-generation devices operating at higher B-field and larger size a (both imply smaller ρ_*). Thus, MFE research would benefit from a scaling of the form $\tau_E/\tau_B \propto \rho_*^{-|x|}$, as is the case in gyro-Bohm scaling ($x = 1$). Observations of tokamak transport in the H-mode scenario have largely demonstrated approximate gyro-Bohm scaling[2] [20]. However, L-mode confinement often exhibits Bohm-like scaling. For reference, the IPB98(y,2) multi-machine empirical scaling law is,

$$\tau_{E,\mathrm{IPB98}(y,2)}/\tau_B \propto \rho_*^{-0.7} \beta^{-0.9} \nu_*^{-0.01} M^{0.96} q^{-3.0} \epsilon^{0.73} \kappa_a^{2.3}, \tag{2.8}$$

for ELMy H-mode plasmas with M being the average ion mass and $\kappa_a \equiv \mathrm{area}/\pi a^2$ (related to the flux surface elongation) [21]. The $\rho_*^{-0.7}$ term in Equation 2.8 is indicative of approximately gyro-Bohm scaling.

Focusing on the ρ_* dependence of Equation 2.7, we can define the gyro-Bohm timescale, $\tau_{gB} = \rho_*^{-1}\tau_B$, for an arbitrary transport process. This relationship is also sometimes written

[2]Notable exceptions include transport scaling with the main ion mass, which is the subject of ongoing research.

in terms of diffusivities using the fact that $\tau_{gB}/\tau_B \propto \chi_B/\chi_{gB}$. The gyro-Bohm diffusivity is then related to the Bohm diffusivity with $\chi_{gB} = \rho_* \chi_B$. Inserting the Bohm diffusion coefficient, $\chi_B \propto T/eB \propto c_s \rho_s$, the unit gyro-Bohm diffusivity can be defined as, $\chi_{gB} = (c_s/a)\rho_s^2$. Along with this gyro-Bohm unit diffusivity, we can define a series of gyro-Bohm transport fluxes which are often used to normalize results from simulations. Using electrons as the reference species, the gyro-Bohm particle flux is,

$$\Gamma_{gB,e} = n_e c_s (\rho_s/a)^2, \tag{2.9}$$

and the gyro-Bohm energy flux is,

$$Q_{gB,e} = n_e T_e c_s (\rho_s/a)^2. \tag{2.10}$$

These definitions come from considering diffusive transport processes e.g. $\Gamma_{gB} = \chi_{gB} \nabla n$ and taking $\nabla n \sim n/a$. It is important to note that plasma transport does not generally follow a simple Fick-ian constitutive relationship (proportionality between fluxes and gradients in kinetic quantities). However, effective diffusivities are often used in transport analysis and the gyro-Bohm fluxes are defined by considering diffusive behavior.

Working backwards from the unit gyro-Bohm diffusivity, $\chi_{gB} = (c_s/a)\rho_s^2$, one can interpret the implied diffusive transport process as a random-walk with perpendicular length scale on the order of ρ_s and characteristic time on the order of a/c_s. These are the fundamental length and timescales associated with 'microscopic' turbulent transport discussed later in this chapter. Given the implicit importance of $\mathcal{O}(\rho_s)$ phenomena – it is reasonable to approach transport from a kinetic/gyrokinetic framework where finite ρ_s effects are included. In the following section we delve into a more rigorous treatment of the theory plasma transport in tokamaks.

2.3 Kinetic theory of tokamak transport

In principle, the transport of particles, heat, and momentum across magnetic field lines in a tokamak can be evaluated in the kinetic theoretical framework by solving the plasma kinetic equation for the 6+1 dimensional distribution function $f_a(\mathbf{x}, \mathbf{v}, t)$,

$$\frac{\partial f_a}{\partial t} + \mathbf{v} \cdot \nabla f_a + \frac{q_a}{m_a}\left(\mathbf{E} + \frac{1}{c}(\mathbf{v} \times \mathbf{B})\right) \cdot \frac{\partial f_a}{\partial \mathbf{v}} = \mathcal{C}[f_a] + \mathcal{S}_a \tag{2.11}$$

where the subscript a labels the plasma species (not to be confused with the tokamak minor radius), $\mathcal{C}$ is a plasma collision operator, and $\mathcal{S}$ is a source term. Along with Maxwell's equations, we obtain a closed system which theoretically contains the relevant physics. However, for realistic tokamak parameters, phase-space dynamics occur over many orders of magnitude; making it nearly impossible to solve Equation 2.11 directly. Allowing the distribution function and electromagnetic fields to contain fluctuating components, an initial step is taken to separate the problem by expanding quantities, $X = X + \delta X$ where a plain X now represents $\langle X \rangle_{\text{ens.}}$. The ensemble-averaged kinetic equation becomes,

$$\frac{\partial f_a}{\partial t} + \mathbf{v} \cdot \nabla f_a + \frac{q_a}{m_a}\left(\mathbf{E} + \frac{1}{c}(\mathbf{v} \times \mathbf{B})\right) \cdot \frac{\partial f_a}{\partial \mathbf{v}} = \langle \mathcal{C}[f_a] \rangle_{\text{ens.}} + \mathcal{D}_a + \mathcal{S}_a, \tag{2.12}$$

where the additional $\mathcal{D}_a$ term on the RHS contains the interaction between fluctuating components of the fields and the distribution function,

$$\mathcal{D}_a \equiv -\frac{q_a}{m_a}\left\langle \left(\delta\mathbf{E} + \frac{1}{c}(\mathbf{v} \times \delta\mathbf{B})\right) \cdot \frac{\partial(\delta f_a)}{\partial \mathbf{v}} \right\rangle_{\text{ens.}}. \tag{2.13}$$

Provided $\mathcal{C}$ and $\mathcal{D}$ conserve particle number, Sugama and Horton [22] derive a set of flux surface averaged transport equations from the ensemble-averaged kinetic equation (Eq. 2.12 above). In the following discussion we focus on the particle transport channel – similar expressions exist for energy and momentum transport [22]. The flux surface averaged particle

transport equation is,

$$\frac{\partial \langle n_a \rangle_{\text{fs.}}}{\partial t} + \frac{1}{V'} \frac{\partial}{\partial r}(V' \Gamma_a) = \left\langle \int d^3 v \mathcal{S}_a \right\rangle_{\text{fs.}} , \tag{2.14}$$

where V' captures the differential plasma volume within flux surfaces, and $\langle \dots \rangle_{\text{fs.}}$ represents the flux surface average. The plasma density is,

$$n_a = \int d^3 v f_a \tag{2.15}$$

and the particle flux is,

$$\Gamma_a = \left\langle \int d^3 v f_a \mathbf{v} \cdot \nabla r \right\rangle_{\text{fs.}} . \tag{2.16}$$

It is important to note that the structure of Equation 2.14 is akin to a typical conservation law i.e. $\partial_t(\text{density}) + \nabla \cdot (\text{flux}) = (\text{source})$. However, as noted in the previous section, the particle flux is not simply proportional to the density gradient, i.e. $\Gamma \neq -D\nabla n$, with D being a diffusion coefficient. Instead, the particle flux is fundamentally the radial velocity moment of the distribution function using Equation 2.16.

Continuing with the demonstrative case of particle transport: in steady-state ($\partial_t = 0$), Equation 2.14 becomes a balance between the flux (Eq. 2.16) and the source term. The distribution function appearing in the these equations is taken to be a solution of the ensemble-averaged kinetic equation (Eq. 2.12) which remains intractable to solve directly. The standard analytical procedure is to produce approximate solutions of the kinetic equation by exploiting separation of spatio-temporal scales depending on the dynamics of interest. In modern tokamak transport theory there are two specific reductions of Equation 2.12 which are commonly solved in place of the full kinetic equation: the drift-kinetic equation (DKE) and the gyrokinetic equation (GKE). Each reduction and its impact on transport is discussed in the following subsections.

2.3.1 Neoclassical transport

Example derivations of the DKE can be found in [23, 24]. The derivation by Hazeltine in [23] uses the order-parameter, $\delta \equiv \omega/\Omega \ll 1$, where ω represents the characteristic frequency of the dynamics under consideration and Ω is the cyclotron frequency for a given species[3]. The ordering $\delta \ll 1$ implies we are interested in phenomena occurring much slower than cyclotron motion (an appropriate limit for tokamak transport). Traditionally, one transforms to coordinates $(\mathbf{x}, \mu, \varepsilon, \vartheta, t)$, where velocity-space is replaced by the magnetic moment $\mu = m_a v_\perp^2/2B$, the total energy $\varepsilon = m_a v^2/2 + q_a\phi$, and the gyro-phase angle ϑ. In these coordinates, the DKE results from expanding the total distribution function into a gyro-phase averaged component and an oscillating component with respect to the gyro-phase, $f_a = \overline{f_a} + \tilde{f}_a$. The component of ensemble-averaged distribution function that varies over the gyro-phase is ordered $\tilde{f}_a \sim \mathcal{O}(\delta)$. The resulting DKE (see Equation 19 of [23]) describes the (slow, $\delta \ll 1$) evolution of the gyro-phase averaged distribution function.

To solve the DKE one typically exploits another scale-separation; namely an expansion in the normalized ion gyro-radius $\rho_{*i} \equiv \rho_i/L$ (where L is the system size, for a tokamak $L = a$ the minor radius – not to be confused with the species subscript label). The resulting expansion of the DKE is solved to $\mathcal{O}(\rho_{*i})$ (with appropriate treatment of the collision operator) such that the $\mathcal{O}(\rho_{*i}^2)$ fluxes can be evaluated[4]. The second-order fluxes resulting from this procedure are responsible for *neoclassical* transport, i.e. the transport of particles, heat, and momentum arising from collisions between guiding-centers executing drift motion in toroidal geometry. In practice, the code `NEO` [25] can be used to evaluate neoclassical fluxes for realistic profiles and magnetic equilibria from tokamak experiments.

---

[3]Hazeltine does not perform the ensemble-averaging step, thus there is no factor $\mathcal{D}_a$ in their work.

[4]Using the particle flux in Equation 2.16 as an example: at first order in ρ_{*i} the velocity $\mathbf{v}$ is replaced by the magnetic and $E \times B$ drift velocities $\mathbf{v} \to \mathbf{v}_D + \mathbf{v}_E$. At $\mathcal{O}(\rho_{*i})$ the magnetic drift velocity is also $\mathcal{O}(\rho_{*i})$ but the $E \times B$ drift is $\mathcal{O}(\rho_{*i}^2)$. Thus, when the gyro-phase averaged distribution function is expanded in powers of ρ_{*i} in Equation 2.16, we obtain a *second*-order flux from $\overline{f_a}^{(0)}\mathbf{v}_E + \overline{f_a}^{(1)}\mathbf{v}_D$. There is no $\mathcal{O}(\rho_{*i})$ flux from $\overline{f_a}^{(0)}\mathbf{v}_D$ because the flux surface average nullifies $\mathbf{v}_D$ motion.

2.3.2 Turbulent transport

To evaluate transport driven by plasma fluctuations – often called 'turbulent' transport – we return to the kinetic equation (Eq. 2.11) and focus on the the fluctuating component of the distribution function (δf_a) rather than its ensemble-averaged counterpart (plain f_a). Derivations of the GKE by Sugama can be found in [22] (for electrostatic fluctuations) and [26] (for electromagnetic fluctuations). Similar to the DKE method, an expansion in ρ_{*i} is performed. The GKE ordering asserts,

$$\frac{\delta f_a}{f_a} \sim \frac{q_a \delta\phi}{T_a} \sim \frac{\varepsilon v_{Ta} |\delta \mathbf{A}|}{c T_a} \sim \frac{k_\parallel}{k_\perp} \sim \frac{(\omega - \mathbf{k}\cdot\mathbf{V_0})}{\Omega_a} \sim \delta \equiv \frac{\rho_s}{L}, \tag{2.17}$$

where background rotation, $\mathbf{V_0}$, and the fluctuating vector potential, $\delta\mathbf{A}$, are included in the rotating/electromagnetic case treated in [26]. The ordering of $k_\parallel \ll k_\perp$ implies that spatial variations perpendicular to the background magnetic field can be scale-separated from variations along the field. It is common for an additional WKB expansion to be performed fluctuating quantities. For an arbitrary fluctuating quantity δX the expansion is,

$$\delta X(\mathbf{x}, \varepsilon, \mu, \vartheta, t) = \sum_{\mathbf{k}_\perp} \delta X_{\mathbf{k}_\perp}(\mathbf{x}, \varepsilon, \mu, \vartheta, t) \exp[iS(\mathbf{x}, t)], \tag{2.18}$$

where the perpendicular wavenumber is defined with respect to the eikonal phase, $\mathbf{k}_\perp \equiv \nabla_{\mathbf{x}} S$. Substituting the WKB expansion for fluctuating quantities in the kinetic equation re-casts the problem in terms of fluctuating amplitudes, $\delta X_{\mathbf{k}_\perp} = \delta X(\mathbf{k}_\perp)$. Then, taking a gyro-average of the $\mathcal{O}(\rho_{*i})$ evolution equation for the fluctuating distribution function reveals adiabatic and non-adiabatic components,

$$\delta f_{a1}(\mathbf{k}_\perp) = -\frac{q_a \delta\phi(\mathbf{k}_\perp)}{T_a} f_{a0} + \delta h_a(\mathbf{k}_\perp) e^{-i\mathbf{k}_\perp \cdot \boldsymbol{\rho}_a}. \tag{2.19}$$

The non-adiabatic part of the fluctuating distribution function, δh_a, can be calculating at the next order in ρ_{*i}. The nonlinear GKE for δh_a is obtained by gyro-averaging the kinetic equation for $\delta f_{a2}(\mathbf{k}_\perp)$, i.e. the $\mathcal{O}(\delta^2)$ component of the fluctuating distribution function

(see Eq. 18 in [26]). Once the GKE for δh_a is solved, the turbulent transport fluxes can be evaluated. For example, the ensemble/flux-surface averaged particle flux (Equation 2.16 above) is of the form,

$$\Gamma_a = \left\langle \left\langle \int d^3v \sum_{\mathbf{k}_\perp} \delta h^*_{a,\mathbf{k}_\perp} \delta \mathbf{v}_{\mathbf{k}_\perp} \cdot \nabla r \right\rangle_{\text{ens.}} \right\rangle_{\text{fs.}} . \tag{2.20}$$

For example, in the electrostatic, cold-plasma limit[5], the fluctuating velocity, $\delta\mathbf{v}$, is simply due to $E \times B$ motion,

$$\delta \mathbf{v}_{\mathbf{k}_\perp} = \frac{c}{B} \left[-i\mathbf{k}_\perp \delta\phi_{\mathbf{k}_\perp} \times \hat{\mathbf{b}} \right] . \tag{2.21}$$

In this limit, the particle flux (Eq. 2.22) is evidently the result of non-adiabatic density fluctuations undergoing turbulent $E \times B$ motion – an expected result from the typical drift-wave picture of turbulent transport [27]. Thus, for electrostatic fluctuations, the flux-surface averaged particle flux is of the form,

$$\Gamma_a = \sum_{\mathbf{k}_\perp} \left\langle \left\langle \frac{-ick_b}{B} \delta n^*_{a,\mathbf{k}_\perp} \delta\phi_{\mathbf{k}_\perp} \right\rangle_{\text{ens.}} \right\rangle_{\text{fs.}} , \tag{2.22}$$

where k_b is the binormal component of $\mathbf{k}_\perp$ (mutually perpendicular to ∇r and $\hat{\mathbf{b}}$).

In practice, the code `CGYRO` [16] can be used to solve the nonlinear gyrokinetic equation and evaluate turbulent transport fluxes for realistic tokamak parameters. The code is discussed in more detail in Appendix C. In addition to the nonlinear GKE, CGYRO can be used to solve its linear counterpart for eigenmode analysis, i.e. calculating mode growth rates and real frequencies. CGYRO also internally computes fluctuating moments of the distribution function, e.g. δn (including the adiabatic contribution). In this dissertation we make use of *local* gyrokinetic simulations where formally $\rho_* \to 0$ and the input parameters come from a single radial location. The simulation domain takes the form of a periodic 'flux tube' described in more detail in Appendix C. Numerical discretization alters the form of the flux calculations into sums over the numerical grids. For example, the electrostatic particle

[5]This limit allows us to expand $J_0(x) = 1 + \frac{1}{4}x^2 + \mathcal{O}$ with $x = k_\perp v_\perp / \Omega$ appearing in $\delta\mathbf{v}_{\mathbf{k}_\perp}$.

flux calculation is of the form,

$$\Gamma_a \propto \sum_{k_y} \sum_{k_x} \left\langle \mathrm{Re}\left[ik_y \delta n_{a,k_x,k_y}(\theta,t) \delta\phi^*_{k_x,k_y}(\theta,t) \right] \right\rangle_{t,\mathrm{fs.}}, \tag{2.23}$$

where the flux-surface average involves a sum over the poloidal angle (θ) and the ensemble average is replaced by a suitable time-average. This expression is used to motivate the underlying form of the fluxes used in quasilinear transport models discussed in the next section.

2.4 Quasilinear transport

Although the nonlinear gyrokinetic model presented in Section 2.3.2 can be used to calculate turbulent transport fluxes in realistic tokamak geometry; even local simulations come at a considerable computational cost (potentially thousands of CPU-hours). Instead, reduced models based on quasilinear theory of have been developed to approximate turbulent fluxes at a significant speedup ($<$ 1 CPU-minute). The quasilinear approach involves solving a linearized system of equations for unstable plasma modes (i.e. obtaining growth rates and frequencies). On their own, linear solutions describe exponentially growing perturbations which, in reality, grow until saturated by a nonlinear mechanism. Thus, these linear solutions must be supplemented with a model for saturation (called a saturation rule).

In general, one has the freedom to mix-and-match linear results with different saturation rules. For example, one may compute an eigenvalue spectrum using linear gyrokinetics or one may approximate the gyrokinetic physics with a gyro-fluid system of equations. In this dissertation we use the quasilinear Trapped Gyro-Landau Fluid code `TGLF` [28]. The TGLF system of equations is based on velocity moments of the linearized gyrokinetic equation. Trapped and passing particles are treated by integrating different portions of velocity-space. The system of equations is closed by approximating kinetic effects such as Landau damping – see [29]. TGLF calculates quasi-linear transport fluxes using a saturation rule based on nonlinear gyrokinetic simulations. To date, there are three TGLF saturation rules with

increasingly advanced physics: SAT0 [28, 30], SAT1 [31, 32], and SAT2 [33, 34]. The first saturation rule (SAT0) is local in k_y (no coupling between modes) and independent of k_x. In SAT0, mode saturation was approximated by reducing the magnitude of linear growth rates using a term proportional to the $E \times B$ shearing rate, $\gamma_{k_y} \rightarrow \gamma_{k_y} - \alpha_{E\times B}|\gamma_{E\times B}|$. The quantity $\alpha_{E\times B}$ is an example of a parameter which would be fit to a database of nonlinear gyrokinetic simulations. In cases of high $\gamma_{E\times B}$, modes could be completely 'quenched' under the SAT0 model. The complete quenching of modes and predictions of the momentum flux were later found to be inaccurate. Ultimately, SAT0 was replaced by SAT1 including a more sophisticated 'spectral-shift' model for the 2D (k_x, k_y) saturated potential spectrum, $\delta\phi_{\mathbf{k}_\perp}$ [31]. The SAT1 spectral shift model related $E\times B$ shear with a k_x-shift in the potential spectrum along with a reduction in $\delta\phi_{\mathbf{k}_\perp}$ amplitude. The SAT1 model also included non-local mixing of different k_y modes as a means of modeling the effects of multi-scale zonal flow saturation [32]. The SAT1 model was later updated to SAT2 with the addition of a model related to the magnetic geometry (and other enhancements) [33]. Magnetic geometry effects were included by allowing the $\delta\phi_{\mathbf{k}_\perp}$ model to vary with the poloidal angle, θ.

Each TGLF saturation rule includes parameters which are fit to a growing database of nonlinear gyrokinetic simulations spanning a range of tokamak conditions. Extensive verification work has been carried out to test TGLF and its underlying saturation rules [34]. In general, the latest saturation rule is best equipped to mimic the higher-fidelity gyrokinetics. It should be noted that the development of new saturation rules and reduced systems of gyro-fluid equations continues to be an active area of research [35, 36].

To introduce the concept of quasilinear weights and the saturated intensity spectrum, we return to the discrete expression for the particle flux given above in Equation 2.23. The quasilinear (QL) form of the particle flux can be written,

$$\Gamma_s^{\mathrm{QL}} = \sum_{k_y} \Delta k_y I_{k_y}^{\mathrm{model}} \mathrm{W}\Gamma_{s,k_y}^{\mathrm{QL}}, \tag{2.24}$$

where $I_{k_y}^{\mathrm{model}}$ is the QL intensity spectrum, and $\mathrm{W}\Gamma_{s,k_y}^{\mathrm{QL}}$ is the QL weight for the particle flux

(cf. Eq. 25 in [34]). The factor of Δk_y is needed because the QL intensity model is designed to be grid-independent[6]. The weight and intensity spectra in Equation 2.24 are the two pillars of quasilinear transport theory. The weights are directly related to the phase shift between fluctuating fields. For example, the QL weight for the particle flux is,

$$\mathrm{W}\Gamma^{\mathrm{QL}}_{s,k_y} = \frac{\left\langle \mathrm{Re}[ik_y \delta n_{s,k_y} \delta\phi^*_{k_y}] \right\rangle_{t,\theta}}{\left\langle |\delta\phi_{k_y}|^2 \right\rangle_{t,\theta}}. \tag{2.25}$$

In this expression, the fluctuating density and potential (δn and $\delta\phi$) are amplitudes of eigenmodes (single k_y) resulting from a linear calculation[7]. Part of the quasilinear assumption is that the QL weights (phase-shifts) are preserved when the fields are nonlinearly saturated. Given this approximation, nonlinear effects are completely determined by the model intensity, $I^{\mathrm{model}}_{k_y}$. For the SAT2 model, the QL-intensity is a formula for the saturated potential spectrum evaluated at the peak $k_x = k_{x0}$, squared, and flux-surface averaged i.e.,

$$I^{\mathrm{model}}_{k_y} = \left\langle \left(\delta\phi(\theta)^{\mathrm{model}}_{k_y} \Big|_{k_x = k_{x0}} \right)^2 \right\rangle_\theta . \tag{2.26}$$

At the heart of the SAT2 saturation rule there is a 3D (k_x, k_y, θ) model for the saturated potential spectrum,

$$\delta\phi(\theta)^{\mathrm{model}}_{k_y,k_x} = \frac{G(\theta)}{\sqrt{\Delta k_y}} \frac{\gamma^{\mathrm{model}}_{k_y} / (k^{\mathrm{model}}_x k_y)}{\left[1 + \left(\frac{k_{x0}}{k^{\mathrm{model}}_x}\right)^2 + \left(\frac{k_x - k_{x0}}{k^{\mathrm{model}}_x}\right)^2\right] \left[1 + \left(\alpha_x \frac{k_{x0}}{k^{\mathrm{model}}_x}\right)^{\sigma_x}\right]}. \tag{2.27}$$

The numerator of Equation 2.27 has the same form as the traditional mixing-length diffusion estimate $\sim \gamma/k^2_\perp$. The factor $G(\theta)$ is designed to capture the flux surface geometry dependence and the Δk_y measure is related to the grid-independence of the model. The first term in the square brackets in the denominator creates a Lorentzian k_x-dependence with spectral

[6]In these expressions I will ignore normalizing factors to keep the expressions simple. The reader is referred to [33, 34] for more comprehensive definitions and normalizations.

[7]The linear mode amplitudes can be calculating using the TGLF system of equations or with linear gyrokinetics.

shift k_{x0} and width k_x^{model}. The second bracketed term in the denominator is designed to attenuate the peak of the spectrum as the shift increases. The two parameters $\alpha_x = 1.21$ and $\sigma_x = 2$ are examples of parameters which are fit to a database of nonlinear gyrokinetics simulations. The precise definitions and normalizations of each term (γ^{model}, $G(\theta)$, etc.) in Equation 2.27 can be found in [33,34]. To summarize, quasilinear estimates of the transport fluxes can be calculated given the QL weights (cross-phase between the relevant fluctuating fields) and the QL intensity spectrum (model for the nonlinearly-saturated $\delta\phi$ amplitude).

2.4.1 TGLF model for the fluctuating density

In this subsection we describe a quasilinear δn model based on TGLF. Generally speaking, it is of interest to develop models for the fluctuating density $\delta n_s(k_x, k_y, \theta, t)$ to compare model predictions with experimental fluctuation measurements. While δn can be readily obtained from nonlinear gyrokinetic simulations (by taking a moment of the fluctuating distribution function); as part of this doctoral research we sought to calculate a model δn spectrum with reduced computational overhead.

The starting point for the δn model is the TGLF 3D saturated potential spectrum in Equation 2.27. To relate the density spectrum to the 3D potential spectrum we use the QL-weight for the density field. Similar to the QL-weight for the particle flux (Equation 2.25), the density weight is defined as,

$$\mathrm{W}n^{\mathrm{QL}}_{s,k_y} = \frac{\left\langle |\delta n_{s,k_y}|^2 \right\rangle_{t,\theta}}{\left\langle |\delta \phi_{k_y}|^2 \right\rangle_{t,\theta}}, \tag{2.28}$$

where the δn and $\delta\phi$ moments are obtained from the (linear) TGLF solution eigenvector for the most unstable mode (and $k_x = 0$). In using linear quantities to compute this weight, we assume that the ratio in Equation 2.28 is preserved in the saturated state – just as we assume the cross-phase between fields in preserved when calculating QL-weights associated with transport. Finally, we calculate an approximation of the saturated density spectrum

with,

$$\delta n_s^2(\theta)^{\text{model}}(k_x, k_y) = \text{W} n_{s,k_y}^{\text{QL}} \cdot \delta\phi^2(\theta)_{k_y,k_x}^{\text{model}}. \tag{2.29}$$

This model for the saturated density spectrum will be tested and applied in Chapter 4 to create a reduced-model synthetic DBS diagnostic.

2.5 Plasma micro-instabilities

Gradients in kinetic quantities (density, temperature) across the minor radius of tokamak plasmas provide free energy to seed micro-instabilities. These plasma instabilities are generally drift-wave type oscillations which – if unstable – grow exponentially until saturating. In this section we provide an overview of three common tokamak micro-instabilities (ITG, TEM, and ETG). We take a primarily phenomenological approach in describing these plasma modes. Detailed descriptions of tokamak micro-instabilities can be found in a number of reviews and textbooks [19, 27].

2.5.1 The ITG mode

The Ion Temperature Gradient (ITG) mode is an ion-scale ($k_\perp \rho_s \approx 0.1 - 1$) plasma micro-instability. The ITG mode is particularly deleterious for plasma confinement because of its relatively large perpendicular wavelength and resonance with the main ion population. The instability is generally driven by the parameter $\eta_i = L_{n_i}/L_{T_i}$, where $L_X \equiv -(d \ln X/dr)^{-1}$ is the gradient scale length. Thus, for a fixed value of the density gradient, the ITG mode can be destabilized beyond a critical ion temperature gradient, $(a/L_{T_i})^{\text{crit.}}$. Estimates of the critical temperature gradient fall in the range of $1 \leq (a/L_{T_i})^{\text{crit.}} \leq 5$, similar to values obtained experimentally in tokamak plasmas.

Various treatments of the ITG mode exist in the literature: collisionless/dissipative, slab/toroidal magnetic field, low/high β. The electrostatic ($\beta = 0$), dissipative (fluid), slab ITG is perhaps the most basic scenario. In this simplified limit, some essential features of the ITG mode can be found: the mode propagates in the ion diamagnetic direction, there

exists a critical η_i value for instability[8], the growth rate increases with η_i and with the ratio T_i/T_e [37]. When more realistic physics are included, one finds a mixture of stabilizing and destabilizing effects e.g. magnetic shear can be stabilizing while curved field lines can be destabilizing (both are present in tokamaks) [38]. Furthermore, with increasing β, the ITG mode can be electromagnetically stabilized and another instability – the kinetic ballooning mode (KBM) – can be destabilized [39]. Finally, in the presence of a large trapped particle fraction (low-collision frequency) the ITG and trapped electron mode (discussed next) can become coupled – further complicating the ion-scale micro-instability picture [40].

2.5.2 The TEM

The Trapped Electron Mode (TEM) is an ion/intermediate-scale ($k_\perp \rho_s \approx 1$) plasma instability. The TEM instability arises due to a resonance between mode frequencies and the bounce-frequency of mirror-trapped electrons executing 'banana orbits' on the low-field side of the tokamak. Similar to the ITG instability, several limiting cases have been documented in the literature: collisionless/dissipative, low/high-β. Simple slab models of this instability are generally not available because a trapped population is required; implying a non-trivial magnetic field. The TEM is often identified as a $k_\perp \rho_s \approx 1$ mode having the following properties: propagation in the electron diamagnetic direction, growth rate increasing with decreasing collisions (the resonant population of trapped particles increases), and growth rate increasing with ∇n and/or ∇T [41]. Similar to the ITG mode, the TEM may be stabilized by magnetic shear and destabilized by magnetic curvature [42]. TEMs also have a have complicated dependence on the ratio T_e/T_i, depending on the value of a/L_n [43].

2.5.3 The ETG mode

The Electron Temperature Gradient (ETG) mode is the electron equivalent to the ITG mode. This instability occurs at much smaller perpendicular scale $k_\perp \rho_s \gg 1$ ($k_\perp \rho_e \approx 1$) and

[8]The precise critical η_i values derived from the fluid models are not entirely accurate – the fluid description itself assumes $\eta_i \gg 1$.

is driven unstable by η_e. Due to their small length scale, ETG modes are not expected to drive significant transport in the core of conventional tokamaks. However, they are theoretically impervious to suppression by $E \times B$-shear when compared with the ITG/TEM instabilities [44]. For this reason, ETGs has been theorized to be responsible for electron energy transport in the tokamak edge as a result of the formation of elongated radial 'streamers' [44, 45]. Similar to the ITG mode, this mode can be treated with slab or curved magnetic field models. Critical values of η_e have been theorized to depend on similar parameters as the ITG mode i.e. magnetic shear, T_e/T_i [46].

2.6 Recent turbulent-transport research and open-questions

After decades of validation work (outlined in Subsection 2.6.1), gyrokinetics is widely regarded as a sufficient model for turbulent transport in tokamaks [47]. However, open questions and issues remain concerning: (1) the applicability of gyrokinetics to key tokamak operational scenarios, (2) the validity of gyrokinetics in certain regions within the plasma, (3) sensitivity to background conditions, and (4) the fidelity of reduced-models based on gyrokinetics [48]. Firstly, in deriving the gyrokinetic model from kinetic plasma theory, we assumed the ordering in Equation 2.17. In certain tokamak scenarios, e.g. with large populations of energetic particles, the GKE ordering may become invalid; resulting in inaccurate predictions of transport and micro-turbulence. Similarly, the GKE ordering is clearly violated in the plasma edge/H-mode pedestal region where ρ_{*i} can be on the same order as the perpendicular length scale. This issue is more pronounced when simulating present day machines (ρ_{*i} is expected to be much smaller in future devices). Complications also arise in extending models beyond the last-closed flux surface (i.e. into the scrape-off-layer, SOL); where magnetic field lines are open and significant neutral populations may be present [49]. Validating SOL models is also difficult due to unknown neutral particles densities, complex plasma-wall interactions, and poloidal asymmetries of neutral sources. The inner core may also pose issues for gyrokinetic modeling both because of energetic particles and possible large MHD activity (e.g. sawteeth oscillations).

Gyrokinetic turbulent transport can also exhibit a sensitive relationship between the predicted fluxes and the input parameters (e.g. between Q_i and a/L_{T_i}) [50]. This relationship manifests as transport 'stiffness' which has also been observed experimentally [51]. This phenomenon complicates the prediction of kinetic profiles. Small deviations from critical gradient values can result in large variations in the predicted turbulent flux. This places additional emphasis on accurate prediction of the critical gradient itself, given that plasmas profiles are often stuck near the critical value. Finally, despite significant advances in computing, nonlinear gyrokinetics simulations remain very computationally expensive. The modeling community will continue to rely on reduced models (e.g. the gyro-fluid model TGLF) for profile prediction, experiment interpretation, and eventually real-time control applications. It is increasingly important to verify that reduced descriptions are reproducing the higher-fidelity physics models. This is particularly true when threshold/critical gradient behavior is present in the system.

The speed and fidelity of reduced transport models directly impacts the tokamak 'integrated modeling' area of research. Over the past decade, reduced models of turbulent transport have been used to develop integrated modeling workflows where multiple aspects of a tokamak discharge including the magnetic equilibrium, auxiliary heating/current-drive, core transport, and pedestal properties are modeled self-consistently [52,53]. At the heart of integrated modeling workflows is a transport solver (e.g. TGYRO [54]) which generally uses a reduced model (e.g. TGLF) to calculate turbulent fluxes at multiple plasma radii. Integrated tokamak modeling is used to predict the performance of next-generation devices [55]. There is a new effort to develop transport solvers that leverage higher-fidelity gyrokinetics with more reasonable computational cost. The highest-fidelity multi-channel transport simulation of core tokamak transport using nonlinear gyrokinetics was recently reported [56].

2.6.1 Gyrokinetic validation efforts

There have been significant efforts over the past decade to validate the gyrokinetic model using fluctuation diagnostics [57]. Being unable to directly measure the internal fluctuating

transport fluxes, these validation efforts typically measure fluctuating fields, δT, δn, and their cross-phase α_{nT} [58]. Measurements of $\delta T_e/T_e$ fluctuations can be made using the correlation electron cyclotron emission (CECE) diagnostic. Cross-phase measurements can also be made by combining CECE and fluctuation reflectometry or DBS measurements [59,60]. Comparisons of $\delta n/n$ are often made using either beam emission spectroscopy (BES), DBS, or other scattering diagnostics [61, 62]. In many cases, nonlinear gyrokinetics can reproduce the observed fluxes and trends within experimental uncertainty [63–65]. In some cases gyrokinetics can match both the fluxes and fluctuation diagnostics [66]. However, some comparisons with fluctuation diagnostics have uncovered discrepancies between simulations and experiments [58, 67].

As part of this thesis we present DBS measurements of the binormal density fluctuation wavenumber spectrum. In Chapter 4 we present comparisons with nonlinear gyrokinetics, quasi-linear gyro-fluid simulations, and DBS measurements. In what follows we describe some previous efforts to compare DBS measurements with nonlinear gyrokinetics: Work by Casati *et al.* [68, 69] compared ion-scale DBS measurements with nonlinear GYRO and found good agreement both in the perpendicular wavenumber spectrum and the frequency spectrum. In work by Holland *et al.* [70] a synthetic DBS diagnostic was presented to compare intermediate-$k_\perp \rho_s$ δn fluctuations with nonlinear GYRO simulations. Little correspondence was found between simulation and experiment (neither wavenumber nor frequency spectra comparisons were presented). Hillesheim *et al.* [71] also presented a synthetic DBS diagnostic based on nonlinear GYRO and 2D full-wave simulations. In their work, Hillesheim presented a synthetic frequency spectrum with a shape and Doppler shift that appear to agree with measurements (Neither $\delta n/n$ magnitude nor wavenumber spectra were presented). Similar agreement between nonlinear GYRO and the DBS frequency spectrum was found in [72].

Later work by Happel *et al.* [73] compared DBS measurements with nonlinear GENE simulations and found agreement as to the radial variation in δn (neither the k-spectrum nor frequency spectrum comparisons were reported). However, discrepancies between measurements and simulation were found in the trend of δn with increased ECH heating. Re-

lated work by Stroth *et al.* [74] and Lechte *et al.* [75] compared DBS measurements with a 2D full-wave synthetic DBS diagnostic and nonlinear GENE to simulate the turbulence. In their work, Lechte finds that nonlinear saturation of the scattering may have impacted measurements – stressing the importance of the full-wave synthetic diagnostic approach to DBS. In later work by Lechte *et al.* [76, 77] and Happel *et al.* [78], they report discrepancies between DBS measurements and simulated full-wave/GENE synthetic DBS. These discrepancies are attributed to nonlinear scattering and diagnostic polarization-dependant complications. When these effects are accounted for, there is reasonable agreement between measurements and nonlinear GENE. Finally, work by Höfler [61] reported DBS wavenumber spectrum measurements compared with nonlinear full-wave synthetic DBS/GENE simulations. Their work found some discrepancies between the simulations and measurements, particularly at high-k where the simulations predicted steeper spectral decay.

2.7 Summary

In this chapter we presented relevant background on turbulent transport in tokamaks for the work presented in this dissertation. We introduced the tokamak geometry and typical coordinate systems in Section 2.1. Scaling laws for tokamak transport were discussed in Section 2.2. The kinetic theory of tokamak transport was presented in Section 2.3 including: neoclassical transport driven by collisions and toroidal drift action on the gyro-averaged distribution function, as well as turbulent transport driven by the non-adiabatic component of the gyro-averaged fluctuating distribution function. The quasi-linear approach to turbulent transport was introduced in Section 2.4 with special discussion of the TGLF model which will be used in Chapter 4 to model DBS measurements. An overview of plasma microinstabilities was provided in Section 2.5 where we highlighted the three primary instabilities with $k_\perp \rho_s \geq 0.1$. The phenomenological traits of these instabilities will be used again to interpret linear and nonlinear results from simulations in Chapter 4. Finally, Section 2.6 summarized recent research in turbulent-transport with an emphasis on validation of the gyrokinetic model and previous comparisons with DBS measurements.

CHAPTER 3

The Doppler back-scattering diagnostic

In this chapter we provide a comprehensive description of the Doppler back-scattering (DBS) diagnostic. DBS is a fusion plasma diagnostic installed in tokamaks and stellarators around the world [79–83]. DBS is a versatile technique capable of measuring multiple physical quantities including: the amplitude of density fluctuations [73], turbulent flow velocity [9, 80], velocity oscillations (e.g. GAMs) [84], turbulent correlation lengths [85], and the tilt-angle of turbulent eddies [86]. In this thesis we focus on the former two measurements: the wavenumber-resolved amplitude of density fluctuations (Chapter 4) and the velocity of turbulent structures (Chapter 5).

In Section 3.1 we present the theory of DBS measurements starting with a local description of the scattering process. Subsections of 3.1 summarize relevant cold-plasma wave physics, the beam-DBS model for the back-scattered power, a summary of the measured frequency, and finally some theory pertaining to the shape of the frequency spectrum. In Section 3.2 we describe the DBS hardware on the DIII-D tokamak. In sections 3.3 through 3.6 we discuss the analysis and interpretation of DBS data including ray tracing, beam-tracing, and full-wave simulations. Section 3.7 presents synthetic DBS diagnostic developments – a key part of this doctoral research. Finally, more advanced topics in wave physics and non-ideal effects pertaining to DBS are addressed in Section 3.8.

3.1 Theory of DBS

DBS uses a beam of electromagnetic radiation to probe density fluctuations inside a magnetized plasma. Unlike some scattering diagnostics, such as Thomson scattering, the probing

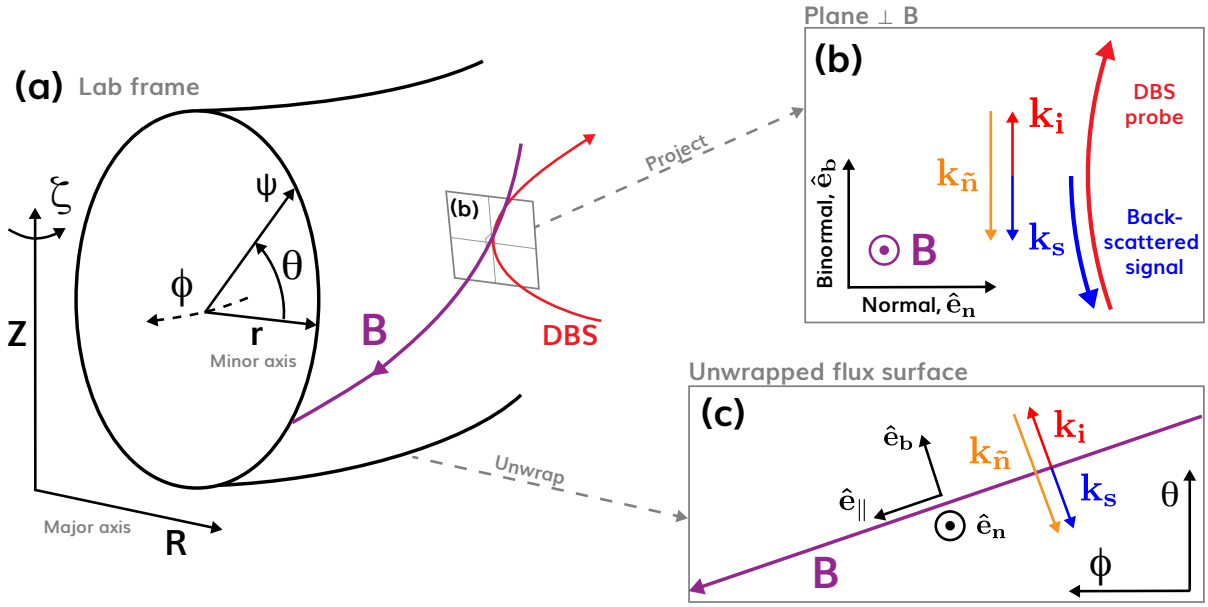

Figure 3.1: Diagram of DBS scattering. In (a) we show a 3D illustration of a plasma cutoff along with the lab-cylindrical and simple-toroidal coordinate systems. The probing DBS ray is shown in red, an example magnetic field line is shown in purple. In (b) we show a projection of the 2D plane perpendicular to the magnetic field line. In (c) we show an unwrapped projection of the flux surface shown in (a).

radiation does not penetrate directly through the plasma. Instead, DBS uses radiation in the electron-cyclotron range of frequencies where critical layers (cutoffs and resonances) are present. In this range of frequencies the plasma index of refraction varies across the minor radius, leading to significant refraction of the probing wave. While resonance layers are deleterious to DBS (the probing radiation may be absorbed), access to wave cutoffs is essential for performing well-localized measurements. Another key aspect of DBS is the use of steerable optics for directing radiation into the plasma. Unlike profile reflectometry, the probing DBS beam is intentionally aimed such that it strikes plasma cutoff surfaces at a finite angle with respect to the surface normal. The ability to steer the probing DBS beam and control its trajectory near the cutoff surface is a core tenet of DBS metrology.

3.1.1 Scattering geometry

Figure 3.1 provides a representative scattering diagram for DBS. The lab frame is shown in 3D in Figure 3.1(a) with common tokamak coordinate systems: the lab-cylindrical (R, ζ, Z) and the simple-toroidal (r, θ, ϕ). In Figure 3.1(a) the DBS wave is represented by a ray entering the plasma from the low-field side (LFS, large R), refracting vertically, and ultimately striking a flux surface at the ray turning point. The tokamak magnetic field, $\mathbf{B}$, is embedded in the flux surface shown in Figure 3.1(a). The $\mathbf{B}$ field line is drawn to pierce a plane labeled (b) while intersecting the DBS ray. Figure 3.1(b) provides a projection of the plane perpendicular to $\mathbf{B}$. Finally, Figure 3.1(c) illustrates the unwrapped flux surface where $\mathbf{B}$ becomes a straight line and the DBS ray, at its turning point, becomes a tangent vector.

The planes shown in Figures 3.1(b,c) also depict the $(\hat{\mathbf{e}}_\mathbf{n}, \hat{\mathbf{e}}_\mathbf{b}, \hat{\mathbf{e}}_\parallel)$ coordinate system. The unit vector $\hat{\mathbf{e}}_\mathbf{n}$ points in the normal direction (aligned with $|\nabla\psi| \sim \hat{\mathbf{e}}_\mathbf{r}$, where ψ is the poloidal magnetic flux) and the unit vector $\hat{\mathbf{e}}_\mathbf{b}$ points in the binormal direction - mutually perpendicular to $\mathbf{B}$ and $\hat{\mathbf{e}}_\mathbf{n}$. The unit vector $\hat{\mathbf{e}}_\parallel = \hat{\mathbf{b}}$ points along the magnetic field. It is important not to confuse the binormal direction, $\hat{\mathbf{e}}_\mathbf{b}$, with the direction of the magnetic field, $\hat{\mathbf{b}}$. Inside the plasma, an arbitrary vector field $\mathbf{a}$ can be decomposed into its parallel and perpendicular components using the $(\hat{\mathbf{e}}_\mathbf{n}, \hat{\mathbf{e}}_\mathbf{b}, \hat{\mathbf{e}}_\parallel)$ basis, i.e. $\mathbf{a} = \mathbf{a}_\perp + a_\parallel \hat{\mathbf{b}}$, with $\mathbf{a}_\perp = a_n \hat{\mathbf{e}}_\mathbf{n} + a_b \hat{\mathbf{e}}_\mathbf{b}$. In the limit of vanishing magnetic pitch, the binormal direction reduces to the poloidal direction $\hat{\mathbf{e}}_\mathbf{b} \rightarrow \hat{\mathbf{e}}_\theta$. It should be noted that the pitch of the magnetic field in Figure 3.1(c) has been exaggerated to distinguish the binormal $(\hat{\mathbf{e}}_\mathbf{b})$ and poloidal $(\hat{\mathbf{e}}_\theta)$ directions[1].

In DBS we focus on perpendicular wavenumbers, $k_\perp$, motivated by the fact that tokamak instabilities are anisotropic with respect to the background magnetic field such that turbulent structures have very large parallel wavelengths, $k_\parallel \ll k_\perp$. In the theory presented here we will largely ignore the parallel structure of instabilities and focus on scattering in the plane perpendicular to $\mathbf{B}$ (Figure 3.1(b)). Importantly, the 2D plane perpendicular to $\mathbf{B}$ is

[1]Exaggerated relative to what is common in standard tokamak configurations where the pitch-angle of the field is typically less than $\pm 20°$. Note that in spherical tokamaks the pitch-angle can be much larger, in which case the cartoon in Figure 3.1 is not an exaggeration.

embedded in the 3D lab frame, it is not simply a slice at constant toroidal angle. Thus, we cannot generally ignore the 3D structure of the tokamak magnetic field nor the 3D trajectory of the DBS wave. However, in special cases with low magnetic pitch or low incidence angle of the DBS beam, the problem can become roughly 2D. This approximation can be useful for reducing model complexity (and computational cost when performing full-wave simulations).

When scattering from fluctuations in the plasma density, δn, the wave momentum and energy are conserved such that the scattered wave has,

$$\mathbf{k}_s = \mathbf{k}_i + \mathbf{k}_{\delta n} \tag{3.1a}$$

$$\omega_s = \omega_i + \omega_{\delta n}, \tag{3.1b}$$

wherein the subscript s refers to the scattered wave, the subscript i refers to the incident wave and the δn subscript refers to the density fluctuation. For the scattered wave to exactly reverse along the incident trajectory (180° back-scattering) we require $\mathbf{k}_s = -\mathbf{k}_i$. The wavenumber matching condition in Equation 3.1(a) implies that the density fluctuation resulting in 180° back-scattering has,

$$\mathbf{k}_{\delta n} = -2\mathbf{k}_i. \tag{3.2}$$

Similarly, the difference between the frequencies of the incident and back-scattered wave is,

$$\omega_{\delta n} = \omega_s - \omega_i = \omega_{\text{Dopp.}}. \tag{3.3}$$

Equation 3.2 is referred to as the Bragg matching condition. The Bragg condition is applicable along the entire DBS trajectory. However, we will focus on the cutoff location for now and return to scattering along the trajectory in Subsection 3.1.4. Equation 3.3 states that the Doppler shift between the incident and back-scattered wave can be directly related to the frequency of the δn fluctuation. The frequency of the scattered wave will be discussed in more detail in Subsection 3.1.5.

When interpreting DBS measurements, it is common practice to reduce the 3D wave scattering problem to a single probed-location (or 'measured location' or 'scattering location'). The nominal measured location is taken to be the cutoff (turning point), $\rho_{\text{meas.}} = \rho_c$ and the nominal measured wavenumber is taken to be, $\mathbf{k}_{\text{meas.}} = -2\mathbf{k_i}|_{\rho=\rho_c}$. By definition, the incident DBS wave will have a vanishing normal component at the turning point, $k_{i,n}|_{\rho=\rho_c} \to 0$, with respect to the cutoff surface[2]. Ideally, the incident DBS wave will also have vanishing parallel component at the turning point such that $k_{i,\parallel}|_{\rho=\rho_c} \to 0$. This can be achieved by steering the DBS wave in the toroidal direction to offset the pitch in magnetic field and refractive effects. The case illustrated in Figures 3.1(b,c) is an example of 'perfect matching', i.e. the DBS wave becomes purely binormal at cutoff. In this ideal case, the Bragg condition states that any back-scattered wave originating from the cutoff can be identified with a purely binormal δn fluctuation, $\mathbf{k}_{\text{meas.}} = k_{\delta n}\hat{\mathbf{e}}_\mathbf{b}$, and its magnitude is $k_{\text{meas.}} = k_{\delta n} = -2k_i|_{\rho=\rho_c}$ by the Bragg condition.

If instead we do not have perfect matching at the turning point, i.e. the incident DBS wave has a finite $k_{i,\parallel}$ at cutoff, interpretation of the back-scattered wave can become more complicated. Based on the geometric ray picture, 180° back-scattering requires fluctuations have $\mathbf{k}_{\delta\mathbf{n}} = -2\mathbf{k_i} = -2(k_{i,b}\hat{\mathbf{e}}_\mathbf{b} + k_{i,\parallel}\hat{\mathbf{e}}_\parallel)$. However, fluctuations with $k_\parallel \sim k_\perp$ are not expected to exist appreciably in the plasma. In theses cases, the geometric ray picture can break down and we must consider the structure of the DBS wave transverse to the direction of propagation. Back-scattering in cases with $k_{i,\parallel} \neq 0$ at cutoff and the associated signal attenuation will be discussed in more detail in Subsection 3.1.4.

In summary, the ray description of DBS scattering is illustrated in Figure 3.1. Conservation of wave momentum relates the incident wavevector to the wavevector of fluctuations within the plasma (Equation 3.2). Wave conservation of energy relates the Doppler shift in the frequency of the back-scattered wave to the frequency of fluctuations (Equation 3.3). Each DBS trajectory is assigned a nominal measured location and a nominal measured

[2]It should be noted that the cutoff surface is not necessarily a flux surface. In cases of very high incidence angle there may be a finite $k_{i,n}$ at the turning point. However, this normal component generally small relative to the binormal component and is ignored for this discussion.

wavenumber based on the turning point (cutoff). The nominal measured wavenumber is taken to be the binormal wavenumber of fluctuations at the cutoff satisfying $k_{\delta n} = -2k_i|_{\rho=\rho_c}$.

3.1.2 Wave physics in the background plasma

The 3D evolution of the incident DBS wave inside the background plasma is captured by the homogeneous wave equation,

$$\boldsymbol{\nabla} \times (\boldsymbol{\nabla} \times \mathbf{E}) - \frac{\omega^2}{c^2}(\boldsymbol{\epsilon} \cdot \mathbf{E}) = 0. \tag{3.4}$$

Fourier analysis of Equation 3.4 yields the eigenvalue problem,

$$\left[(\mathbf{kk} - k^2\mathbf{1}) + \frac{\omega^2}{c^2}\boldsymbol{\epsilon}\right] \cdot \mathbf{E} = 0, \tag{3.5}$$

wherein non-trivial solutions require that ω and $\mathbf{k}$ satisfy the dispersion relation,

$$\det\left((\mathbf{kk} - k^2\mathbf{1}) + \frac{\omega^2}{c^2}\boldsymbol{\epsilon}\right) = \det(\mathbf{D}) = \mathcal{D}(\mathbf{k}, \omega) = 0. \tag{3.6}$$

In Equations 3.4-3.6 the background plasma is adequately described[3] in the electron cyclotron range of frequencies by the cold (lossless) permittivity tensor,

$$\boldsymbol{\epsilon} = \mathbf{1} - \frac{\omega_{pe}^2}{\omega^2 - \Omega_e^2}(\mathbf{1} - \hat{\mathbf{b}}\hat{\mathbf{b}}) + \frac{i\omega_{pe}^2\Omega_e}{\omega(\omega^2 - \Omega_e^2)}(\hat{\mathbf{b}} \times \mathbf{1}) - \frac{\omega_{pe}^2}{\omega^2}\hat{\mathbf{b}}\hat{\mathbf{b}}, \tag{3.7}$$

where $\hat{\mathbf{b}}$ is a unit vector in the direction of $\mathbf{B}$ and $(\hat{\mathbf{b}} \times \mathbf{1})$ indicates the skew-symmetric matrix $[\mathbf{b}]_\times$. In a Cartesian coordinate system (x, y, z) with $\hat{\mathbf{b}} = \hat{\mathbf{z}} = (0, 0, 1)$ Equation 3.7

[3]Kinetic effects not captured by the cold plasma treatment will be discussed later in this section and in Section 3.8.

takes the familiar form found in Stix [87],

$$\boldsymbol{\epsilon} = \begin{pmatrix} S & iD & 0 \\ -iD & S & 0 \\ 0 & 0 & P \end{pmatrix}. \tag{3.8}$$

For modes in the electron cyclotron/electron plasma range of frequencies where $\omega \gg \Omega_i, \omega_{pi}$ the scalar components (S, D, P) take the Altar-Appleton-Hartree form,

$$S = \frac{1}{2}(R + L) \tag{3.9a}$$

$$D = \frac{1}{2}(R - L) \tag{3.9b}$$

$$P = 1 - \frac{\omega_{pe}^2}{\omega^2} \tag{3.9c}$$

$$R = 1 - \frac{\omega_{pe}^2}{\omega(\omega + \Omega_e)} \tag{3.9d}$$

$$L = 1 - \frac{\omega_{pe}^2}{\omega(\omega - \Omega_e)}. \tag{3.9e}$$

In Equation 3.9, $\omega_{pe} \equiv \sqrt{n_e e^2/\epsilon_0 m_e}$ is the electron plasma frequency and $|\Omega_e| \equiv eB/m_e$ is the electron cyclotron frequency[4]. For perpendicular propagation, $\mathbf{k} \perp \mathbf{B}$, the dispersion relationship in Equation 3.6 factors into two cases with orthogonal polarizations,

$$n_\perp^2 = \frac{c^2 k_\perp^2}{\omega^2} = \begin{cases} P & \text{for O-mode,} \quad \mathbf{E} \parallel \mathbf{B} \\ RL/S & \text{for X-mode,} \quad \mathbf{E} \perp \mathbf{B} \end{cases} \tag{3.10}$$

In practice, the probing DBS wave is polarized before entering the plasma to couple efficiently to either the ordinary (O) or extraordinary (X) modes. The propagation of the DBS wave in the plasma strongly depends on which polarization is used. Each polarization has a separate set of cutoffs (where $k \to 0$) and resonances (where $k \to \infty$). Solving Equation 3.10 for ω

[4]In Equation 3.9 the electron cyclotron frequency is algebraic, i.e. $\Omega_e = -eB/m_e$.

when $k_\perp = 0$ reveals the cutoffs for each polarization,

$$\omega_{O/X} = \begin{cases} \omega_{pe} & \text{for O-mode,} \quad \mathbf{E} \parallel \mathbf{B} \\ \frac{1}{2}\left(\pm \Omega_e + \sqrt{\Omega_e^2 + 4\omega_{pe}^2} \right) & \text{for X-mode,} \quad \mathbf{E} \perp \mathbf{B} \end{cases} \tag{3.11}$$

where the positive branch in ω_X corresponds to the right-hand cutoff and the negative branch is the left-hand cutoff. The O-mode cutoff is simply the electron plasma frequency. Thus, ω_O surfaces coincide with the flux surfaces (i.e. $\omega_O \propto \sqrt{n_e} \rightarrow \omega_O$ is a flux-function[5]) whereas the X-mode cutoff surfaces are functions of both the density and the B-field; and are therefore not flux-functions.

Resonant frequencies for each polarization are values of ω for which $k \rightarrow \infty$. Based on Equation 3.10 one would find only the X-mode upper hybrid resonance, $\omega_{UHR}^2 \equiv \Omega_e^2 + \omega_{pe}^2$. However, kinetic/thermal effects not accounted for in the cold plasma treatment give rise to infinite resonances for each polarization at integer harmonics of the electron cyclotron frequency, i.e. $\omega = p\Omega_e$ (with $p = 1, 2, ...$). The more complete 'warm plasma' dielectric tensor is needed to describe perpendicular propagation near resonances, i.e. at $\omega \approx p\Omega_e$ or $\omega \approx \omega_{UHR}$. More advanced effects related to propagation near resonances will be discussed in Section 3.8. The key result from a more advanced treatment is that the efficacy of a given resonance to absorb incident radiation depends strongly on the polarization and harmonic number (p) [88]. For the DBS frequencies considered here, O1, X1, and X2 are the most relevant electron cyclotron resonances.

Figure 3.2 provides representative radial profiles of fundamental frequencies across the midplane. For the situation shown in Figure 3.2, the eight DBS frequencies encounter the right-hand X-mode cutoff on the LFS of the tokamak. The 2nd harmonic of the cyclotron frequency ($2 \times f_{ce}$) technically extends to larger R, intersecting the highest DBS frequencies. However, the absorption in this region is negligible due to vanishing plasma density.

[5]To be a flux-function is to be constant on surfaces of constant magnetic flux, ψ. We often plots quantities as functions of normalized radial coordinates (e.g. ρ) which label the nested flux-surfaces. When quantities are not flux-functions it is formally improper to plot versus ρ.

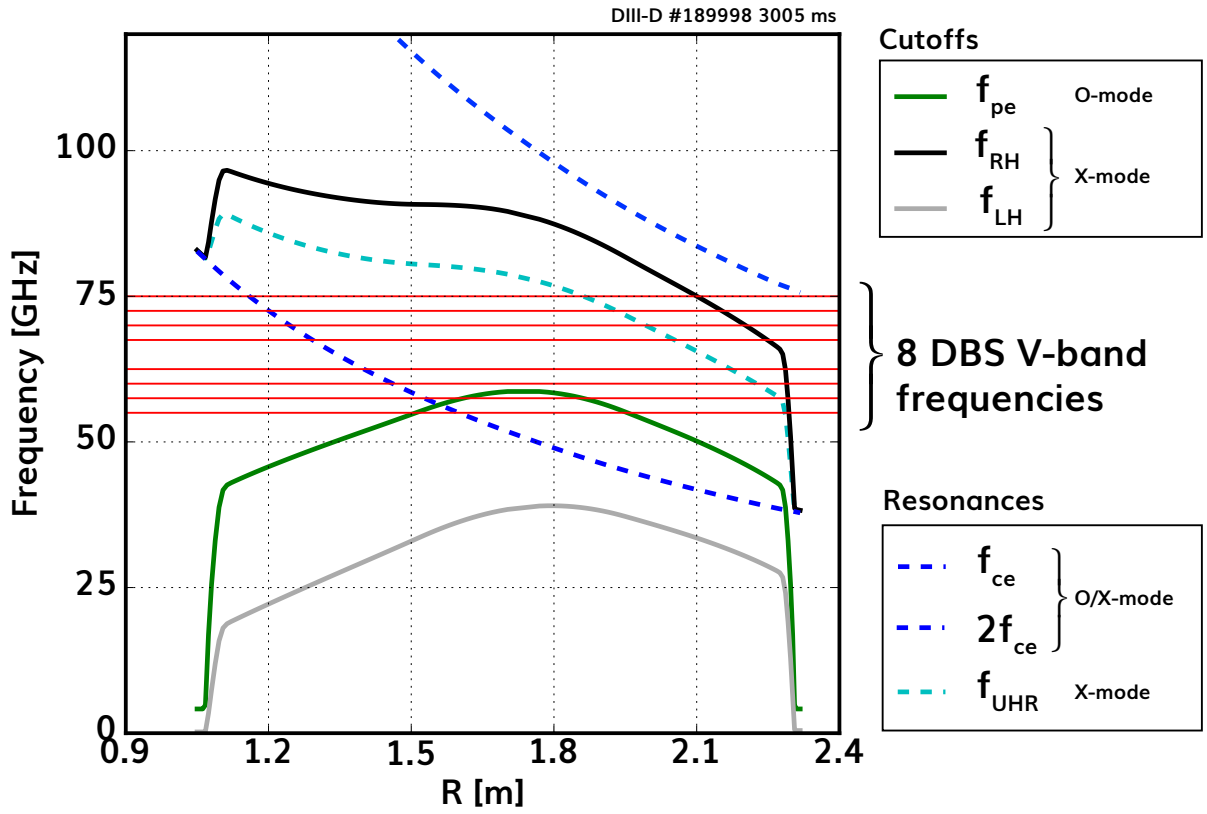

Figure 3.2: Fundamental plasma frequencies for DIII-D discharge 189998 at 3005 ms. All quantities are evaluated at the plasma midplane. Resonances are shown with dashed lines, cutoffs are shown with solid lines. The eight DBS frequencies are shown with horizontal red lines. Note that $2f_{ce}$ is technically both an O/X-mode resonance, but O2 absorption is generally not efficient.

In summary, propagation of the probing DBS wave in the background plasma is described by the theory outlined in this subsection. Depending on the polarization of the probing wave, multiple cutoffs and resonances may exist across the plasma for a given frequency. The physics underlying the scattering process and quantifying the back-scattered power is covered in the next subsection.

3.1.3 Plasma scattering of electromagnetic waves

To describe electromagnetic wave scattering by a plasma, we begin by comparing the spatial and temporal (k_i and ω) properties of the incident radiation with fundamental scales within

the plasma. As discussed previously, the frequency of the incident DBS wave is on the same order as ω_{pe}, Ω_e. Thus, the radiation is expected to experience significant refraction and ultimately be reflected. Theories developed in the limit of $\omega \gg \omega_{pe}, \Omega_e$ are not generally applicable to DBS. Similarly, we can compare the wavenumber of the probing radiation relative to the Debye length in the plasma. The parameter $\alpha \equiv (k_i \lambda_{De})^{-1}$ encodes the extent to which electrons in the plasma appear free in their response to the wave. For values of $\alpha \ll 1$ scattering is said to be non-collective such that the plasma can be treated as a volume of free electrons. The opposing limit of $\alpha \geq 1$ corresponds to collective scattering where cooperative plasma motion dominates the response to the probing wave [89].

The electron Debye length is given by,

$$\lambda_{De}\ [\text{cm}] \approx 743 \sqrt{\frac{T_e}{1\ [\text{eV}]} \left(\frac{n_e}{1\ [\text{cm}^{-3}]} \right)^{-1}}. \tag{3.12}$$

The vacuum wavelength of a 60 GHz electromagnetic wave is 5 mm ($k_i \approx 1.3$ rad/mm). Thus, for $T_e = 1$ keV and $n_e = 2 \times 10^{13}$ cm^{-3}, $\lambda_{De} \approx 0.05$ mm, making $\alpha \approx 15$. Thus, for DBS we are clearly in the collective scattering regime as opposed to other diagnostics such as Thomson scattering which generally operates with $\alpha \ll 1$ and $\omega \gg \omega_{pe}$. The fact that collective plasma phenomena and refraction cannot be ignored significantly complicates the theoretical description of DBS plasma scattering.

Although the limits used in Thomson scattering theory are not applicable to DBS, other approximation schemes can be used to simplify the scattering problem. Generally speaking, the total electric field in the plasma will be the superposition of the incident wave and the scattered wave, $\mathbf{E} = \mathbf{E_i} + \mathbf{E_s}$. The scattered field, $\mathbf{E}_s$, can be thought of as being generated by a current density in the plasma induced by $\mathbf{E_i}$. In general, the total $\mathbf{E}$ and plasma $\mathbf{j}$ are difficult to calculate as they must satisfy both Maxwell's equations and the plasma kinetic equation. The wave equation (in Gaussian units) is,

$$\boldsymbol{\nabla} \times (\boldsymbol{\nabla} \times \mathbf{E}) - \frac{\omega^2}{c^2} \mathbf{E} = \frac{4\pi i \omega}{c^2} \mathbf{j}. \tag{3.13}$$

Assuming a linear constitutive relation, the current density and the electric field are related via a convolution integral[6],

$$\mathbf{j}(\omega, \mathbf{r}) = \int d\mathbf{r}' \boldsymbol{\sigma}(\omega; \mathbf{r}, \mathbf{r}') \mathbf{E}(\omega, \mathbf{r}'), \tag{3.14}$$

where $\boldsymbol{\sigma}$ is the conductivity tensor. Next, allowing for fluctuations in the plasma, we separate the conductivity tensor into a background and fluctuating component, $\boldsymbol{\sigma} = \boldsymbol{\sigma}_0 + \boldsymbol{\delta\sigma}$. Then, the wave equation can be rewritten as,

$$\boldsymbol{\nabla} \times (\boldsymbol{\nabla} \times \mathbf{E}) - \frac{\omega^2}{c^2} \left[\mathbf{1} + \frac{4\pi i}{\omega} \boldsymbol{\sigma}_0 \right] \mathbf{E} = \frac{4\pi i \omega}{c^2} \boldsymbol{\delta\sigma} \cdot \mathbf{E}, \tag{3.15}$$

where the conductivity tensors are taken to be linear convolution operators acting upon $\mathbf{E}$. In the limit where $\boldsymbol{\delta\sigma} = 0$, Equation 3.15 reduces to the homogeneous wave equation (Eq. 3.4).

Next, we introduce the order parameter $\varepsilon \equiv ||\boldsymbol{\delta\sigma}/\boldsymbol{\sigma}_0|| \ll 1$ encoding the magnitude of the perturbation relative to the background. The total electric field is expanded in a perturbation series, $\mathbf{E} = \mathbf{E}_0 + \mathbf{E}_1$. The leading two wave equations from this expansion are,

$$\mathcal{O}(\varepsilon^0): \quad \boldsymbol{\nabla} \times (\boldsymbol{\nabla} \times \mathbf{E}_0) - \frac{\omega^2}{c^2} \left[\mathbf{1} + \frac{4\pi i}{\omega} \boldsymbol{\sigma}_0 \right] \mathbf{E}_0 = 0 \tag{3.16a}$$

$$\mathcal{O}(\varepsilon^1): \quad \boldsymbol{\nabla} \times (\boldsymbol{\nabla} \times \mathbf{E}_1) - \frac{\omega^2}{c^2} \left[\mathbf{1} + \frac{4\pi i}{\omega} \boldsymbol{\sigma}_0 \right] \mathbf{E}_1 = \frac{4\pi i \omega}{c^2} \boldsymbol{\delta\sigma} \cdot \mathbf{E}_0. \tag{3.16b}$$

We now identify $\mathbf{E}_0 = \mathbf{E}_i$ as the incident wave satisfying the homogeneous wave equation in the background plasma (Equation 3.16(a)). Meanwhile, the RHS of Equation 3.16(b) states that the source current density for the $\mathbf{E}_1$ field is due to the interaction between the incident field $\mathbf{E}_0$ and plasma fluctuations (in $\boldsymbol{\delta\sigma}$). Thus, $\mathbf{E}_1 = \mathbf{E}_s$ is the electric field of the scattered wave. Terminating the perturbation series at this order is equivalent to the (first) Born approximation. Limitations of this approximation are addressed more in Section 3.8.

[6] In this expression we have performed a Fourier-Laplace transformation in time assuming the conductivity tensor is stationary (i.e. only a function of $t - t'$). The stationary approximation is appropriate for ω much greater than collective plasma motion (e.g. drift-wave dynamics).

The preceding approximation reduces the general wave equation (Eq. 3.13) to the following equation where $\mathbf{E}_i$ and $\mathbf{E}_s$ are separated,

$$\boldsymbol{\nabla} \times (\boldsymbol{\nabla} \times \mathbf{E}_s) - \frac{\omega^2}{c^2} \boldsymbol{\epsilon} \cdot \mathbf{E}_s = \frac{\omega^2}{c^2} \boldsymbol{\delta\epsilon} \cdot \mathbf{E}_i. \tag{3.17}$$

Wherein the permittivity tensor, $\boldsymbol{\epsilon} = (\mathbf{1} + 4\pi i \boldsymbol{\sigma}/\omega)$, has been substituted for the conductivity tensor. In the cold-plasma limit, density fluctuations give rise to a simple expression for the fluctuating permittivity tensor,

$$\boldsymbol{\delta\epsilon} = \frac{\delta n_e}{n_e} (\boldsymbol{\epsilon} - \mathbf{1}). \tag{3.18}$$

This can be seen by observing that $(\boldsymbol{\epsilon} - \mathbf{1}) \propto \omega_{pe}^2 \propto n_e$ in Equation 3.7. The scattered wave field (and the scattered power) can now be approximated by solving Equation 3.17 given the wave field in the background plasma, $\mathbf{E}_i$, and a model for the density fluctuations in $\boldsymbol{\delta\epsilon}$. However, solving Equation 3.17 remains a very challenging task. The following subsection describes further analytical methods for calculating the amplitude (and power) of a back-scattered wave.

3.1.4 Back-scattered power

While multiple theories treating DBS exist [90, 91], we will focus on the beam-DBS theory developed in detail by V. Hall-Chen *et al.* in [4]. The beam-DBS theoretical framework assumes the probing and scattered waves take the form of Gaussian beams. Expressions for the back-scattered power and weighting function can be derived using another theoretical framework related to the electromagnetic reciprocity theorem [92]. The core principle behind the reciprocity framework is to relate the electric field at the receiving antenna to a remote, fluctuating current density inside the plasma while avoiding a calculation of the scattered wave field throughout the plasma. Unlike textbook versions of electromagnetic reciprocity, we must account for anisotropy in magnetized plasma permittivity. Plasma anisotropy requires us to calculate both $\mathbf{E}_i$ in the background plasma and its reciprocal counterpart $\mathbf{E}^{(+)}$ in a 'transposed plasma' (i.e. a fictitious plasma with $\boldsymbol{\epsilon} = \boldsymbol{\epsilon}^\top$). Transposing the permittiv-

ity tensor preserves time-reversal symmetry, and is equivalent to reversing the background magnetic field, $\mathbf{B} \rightarrow -\mathbf{B}$.

The essential steps for calculating the received signal amplitude using reciprocity are as follows: perform a dot-product of $\mathbf{E}^{(+)}$ with Equation 3.17. Then, use the 'reciprocal' wave equation involving $\mathbf{E}^{(+)}$ and $\boldsymbol{\epsilon}^{\top}$ to write,

$$\nabla \cdot \left[(\nabla \times \mathbf{E}_s) \times \mathbf{E}^{(+)} - (\nabla \times \mathbf{E}^{(+)}) \times \mathbf{E}_s \right] = \frac{\omega^2}{c^2} \mathbf{E}^{(+)} \cdot \boldsymbol{\delta\epsilon} \cdot \mathbf{E}_i. \tag{3.19}$$

Performing a volume integral of the above equation allows one to use the divergence theorem on the LHS to exchange the volume integral with a surface integral. With careful choice of the volume/surface over which to perform the integral and appropriate boundary conditions for the reciprocal beam, cancellation occurs and the amplitude of the received scattered wave field, A_r, can be calculated. For the Gaussian beam case, the resulting expression for the received amplitude is,

$$A_r = \frac{i\omega}{2c} \int_V d^3r \mathbf{E}^{(+)} \cdot \boldsymbol{\delta\epsilon} \cdot \mathbf{E_i}, \tag{3.20}$$

cf. Eq. 98 of [4]. The domain of the volume integral in Equation 3.20 encloses the plasma. Notably, the scattered wave field, $\mathbf{E}_s$, does not appear in the integrand. This is the power of the reciprocity approach: with knowledge of $\mathbf{E}_i$ in the background plasma (and its reciprocal counterpart $\mathbf{E}^{(+)}$) and a model for the fluctuating $\boldsymbol{\delta\epsilon}$, the amplitude of the received, back-scattered radiation can be evaluated.

From Equation 3.20, the received back-scattered power, P_r, can be calculated by substituting Gaussian beam expressions for the electric fields and taking $P_r = |A_r|^2$. The complete derivation is lengthy and complicated (see [4]). The final beam-P_r expression is discussed in more detail later in this subsection. First, we will use a simplified model to motivate measurements of the $\delta n(\mathbf{k})$ wavenumber spectrum using DBS (the subject of Chapter 4). For this simplified exercise we treat the measured wavenumber of the DBS wave, $\mathbf{k}_{\text{meas.}}$, as a constant with respect to space. It should be emphasized that this is not a general result. In reality, the measured wavenumber varies along the probing trajectory. Nevertheless, with

this simplification the final expression for the back-scattered wave amplitude takes the form,

$$A_r = \int_V d^3r \delta n(\mathbf{r}) U(\mathbf{r}) e^{i\mathbf{k}_{\mathbf{meas.}}\cdot\mathbf{r}}, \tag{3.21}$$

where the weighting function, $U(\mathbf{r}) \propto (\boldsymbol{\sigma}\mathbf{E}_i)\mathbf{E}^{(+)}$. In general, the weighting function encodes instrumental effects relating to how well the probing electric field illuminates a given location in the plasma. For this exercise it suffices to imagine $U(\mathbf{r}) \propto |E_i|$ in the vicinity of the cutoff.

Within this simplified model, we treat $\mathbf{k}_{\text{meas.}}$ as a constant with respect to space. The domain of the integral in Equation 3.21 is essentially set by $U(\mathbf{r})$ which follows the trajectory of the probing DBS beam. The scattered power is calculated via $P_r = |A_r|^2$,

$$P_r(\mathbf{k}_{\text{meas.}}) = \iint d^3\mathbf{r} d^3\mathbf{r}' \delta n(\mathbf{r}) \delta n^*(\mathbf{r}') U(\mathbf{r}) U^*(\mathbf{r}') e^{i\mathbf{k}_{\text{meas.}}\cdot(\mathbf{r}-\mathbf{r}')}. \tag{3.22}$$

We then perform an ensemble average, exploiting many realizations of the fluctuating density. We assume δn is a stationary random process[7] such that the autocorrelation function, $R(\mathbf{r}, \mathbf{r}') \equiv \langle \delta n(\mathbf{r}) \delta n^*(\mathbf{r}') \rangle$, depends only on the difference in position, i.e. $R(\mathbf{r}, \mathbf{r}') \to R(\mathbf{r}' - \mathbf{r})$. The autocorrelation function is then related to the spectral density function, $S(\mathbf{k})$, by Fourier transform,

$$R(\mathbf{r}' - \mathbf{r}) = \int \frac{d^3\mathbf{k}}{(2\pi)^3} S(\mathbf{k}) e^{i\mathbf{k}\cdot(\mathbf{r}'-\mathbf{r})}. \tag{3.23}$$

To write the average back-scattered power in k-space we substitute Equation 3.23 for $\langle \delta n(\mathbf{r}) \delta n^*(\mathbf{r}') \rangle$ in Equation 3.22 to find,

$$\langle P_r(\mathbf{k}_{\text{meas.}}) \rangle = \iiint d^3\mathbf{r} d^3\mathbf{r}' \frac{d^3\mathbf{k}}{(2\pi)^3} S(\mathbf{k}) \cdot U(\mathbf{r}) U^*(\mathbf{r}') e^{i(\mathbf{k}-\mathbf{k}_{\text{meas.}})\cdot(\mathbf{r}'-\mathbf{r})}. \tag{3.24}$$

[7] We do not necessarily need to assume density fluctuations are a stationary random process. Instead one may assume that the weighting function is sufficiently narrow in real-space to achieve scale separation between U and δn. For example see arguments in [4, 92].

Exchanging the order of integration we can group real-space terms (involving $\mathbf{r}$, $\mathbf{r}'$) to write,

$$\langle P_r(\mathbf{k}_{\text{meas.}})\rangle = \int \frac{d^3\mathbf{k}}{(2\pi)^3}\, S(\mathbf{k}) \left| \int d^3\mathbf{r}\, U(\mathbf{r}) e^{-i(\mathbf{k}-\mathbf{k}_{\text{meas.}})\cdot\mathbf{r}} \right|^2 . \tag{3.25}$$

We recognize the term inside the modulus-square ($|\ldots|^2$) to be the Fourier transform of the weighting function $\mathcal{F}[U] = \hat{U}$ (we use the 'hat' symbol, $\hat{}$, to denote a Fourier amplitude). Importantly, the Fourier transform of the weighting function is evaluated at $\mathbf{k} - \mathbf{k}_{\text{meas.}}$,

$$\langle P_r(\mathbf{k}_{\text{meas.}})\rangle = \int \frac{d^3\mathbf{k}}{(2\pi)^3}\, S(\mathbf{k}) |\hat{U}(\mathbf{k} - \mathbf{k}_{\text{meas.}})|^2. \tag{3.26}$$

Finally, one can show that the stationary random process assumption implies that the spectral density function is equivalent to the averaged, modulus-square of the (Fourier-space) fluctuating density, $S(\mathbf{k}) = \langle|\delta\hat{n}(\mathbf{k})|^2\rangle$. The $\delta\hat{n}(\mathbf{k})$ spectrum is written as a function of the vector $\mathbf{k}$ to allow for anisotropy in the perpendicular (k_n, k_b) plane[8].

Equation 3.26 states that the back-scattered power as a function of the measured wavenumber, $\langle P_r(\mathbf{k}_{\text{meas.}})\rangle$, is essentially a convolution of the fluctuating wavenumber spectrum, $\langle|\delta\hat{n}(\mathbf{k})|^2\rangle$ with the DBS k-space weighting function, $\hat{U}(\mathbf{k})$. When we vary the launch-angle of the DBS beam, we change the measured wavenumber $\mathbf{k}_{\text{meas.}}$. Thus, a launch-angle scan systematically translates the DBS weighting function in k-space to probe different regions of $\langle|\delta\hat{n}(\mathbf{k})|^2\rangle$. In the (non-physical) limit where $\hat{U}(\mathbf{k} - \mathbf{k}_{\text{meas.}}) \to \delta(\mathbf{k} - \mathbf{k}_{\text{meas.}})$ we would obtain a 'perfect' measurement of $\langle|\delta\hat{n}(\mathbf{k}_{\text{meas.}})|^2\rangle$.

Returning to the Gaussian beam model from [4], Equation 3.20 is evaluated with Gaussian beam expressions for $\mathbf{E}_i$ and $\mathbf{E}^{(+)}$ and the average back-scattered power is $\langle P_r\rangle = \langle|A_r|^2\rangle$. As opposed to the simplified model discussed previously, wavenumbers are allowed to evolve along the beam trajectory. The final expression for the average back-scattered power (Eq.

[8]Recall that we ignore scattering from structures in the parallel direction.

196 of [4]) is a real-space integral along the trajectory of the beam,

$$\langle P_s \rangle = \frac{P_{ant}\sqrt{\pi^3}e^4}{2c^2\omega_i^2\epsilon_0^2 m_e^2} \int dl \langle |\delta\hat{n}|^2 \rangle U_p U_b \frac{g_{ant}^2}{g^2} e^{-2\theta_m^2/\Delta\theta_m^2}, \tag{3.27}$$

where the coordinate l is the path length of the trajectory. The integrand of Equation 3.27 contains the spectral density of δn fluctuations as well as four terms constituting the DBS weighting function, $U(l)$. We will give a description of our implementation of Equation 3.27 with a summary of the effects it captures while the full definition and derivation of each term can be found in [4].

The integral in Equation 3.27 is taken along the trajectory of the beam through the plasma with all terms evaluated at the wavevector $\mathbf{k}_{\text{meas.}}(l)$ satisfying the Bragg scattering condition (Equation 3.2) at each point along the beam path. The measured wavevector points in a direction (denoted $\hat{\mathbf{e}}_1$) perpendicular to the background magnetic field and coplanar with the beam group velocity, $\mathbf{g}$. To properly evaluate the density fluctuation spectrum along the beam path, we project the vector $\mathbf{k}_{\text{meas.}}(l)$ into its (local) normal and binormal components,

$$k_{\text{meas.}}\hat{\mathbf{e}}_1 = k_{n,\text{meas.}}\hat{\mathbf{e}}_n + k_{b,\text{meas.}}\hat{\mathbf{e}}_b. \tag{3.28}$$

Wherein $k_{n,\text{meas.}}$ and $k_{b,\text{meas.}}$ are the measured normal and binormal wavenumbers, respectively. Note that every term in Eq. 3.28, including the unit vectors, varies along the path of the beam trajectory and can be parameterized by the path-length l. Thus, in the integrand of Equation 3.27, $\langle |\delta\hat{n}|^2 \rangle$ is evaluated at $\mathbf{k} = k_{n,\text{meas.}}\hat{\mathbf{e}}_n + k_{b,\text{meas.}}\hat{\mathbf{e}}_b$ at each point l.

In addition to the $\langle |\delta\hat{n}|^2 \rangle$ spectrum, the integrand of Equation 3.27 contains four terms constituting the DBS weighting function. The following summary describes the physical implications of each term in the weighting function:

(1) The polarization term,

$$U_p = \frac{\omega^4\epsilon_0^2 m_e^2}{e^4 n_e^2} |n^2[1 - (\hat{n}\cdot\hat{\mathbf{e}})^2] - 1|^2, \tag{3.29}$$

depends on whether the probing radiation is O or X-mode. In the O-mode case it can be shown that $U_p \approx 1$ but in the X-mode case U_p is more complicated and depends on the relative magnitude of ω_{pe} and Ω_e along the beam trajectory.

(2) The beam term,

$$U_b = \frac{1}{\sqrt{2}} \frac{\det[\mathrm{Im}\{\mathbf{\Psi}\}]}{|\det[\mathbf{M}]| \sqrt{-\mathrm{Im}\{M_{yy}^{-1}\}}}, \tag{3.30}$$

involves the complex-valued beam matrix $\mathbf{\Psi}$ and its modified version $\mathbf{M}$. The matrix $\mathbf{\Psi}$ encodes the Gaussian beam width and phase front radius of curvature. The modified beam matrix, $\mathbf{M}$, includes terms related to the curvature and shear of the magnetic field. The magnetic field terms only modify the real part of $\mathbf{\Psi}$, i.e. the part associated with phase front curvature. The $\mathbf{\Psi}$ matrix will be discussed in more detail in Section 3.5.

(3) The mismatch term, $e^{-2\theta_m^2/\Delta\theta_m^2}$, also varies along the beam trajectory, but is primarily set by the initial launch angle(s) relative to the plasma magnetic equilibrium. The mismatch angle is given by $\theta_m \equiv \sin^{-1}(\hat{\mathbf{k}} \cdot \hat{\mathbf{e}}_{\parallel})$. Improper aiming of the probing DBS beam results in a Gaussian attenuation of the back-scattered signal. When mismatch is not accounted for, measurements of the scattered power can be compromised (i.e. much lower than the real value). The parameter $\Delta\theta_m$ sets the width of the Gaussian mismatch attenuation. Generally speaking, $\Delta\theta_m$ is smaller for larger $k_{\mathrm{meas.}}$, i.e. when making higher-$k_{\mathrm{meas.}}$ measurements it becomes increasingly important to have $\theta_m < \Delta\theta_m$ at cutoff. For the cases presented here, $\Delta\theta_m \sim \mathcal{O}(10^\circ)$ near cutoff. Thus, the beam should be aimed toroidally such that it strikes the cutoff surface within 10° of orthogonal to the local $\mathbf{B}$. This appears to be a significant margin, but depending on how far the beam travels through the plasma, differences on the order of 0.5° in the toroidal launch angle can have a significant impact on θ_m at cutoff. This mismatch effect was studied in detail on DIII-D and validated against the beam-DBS theory [5, 6].

(4) Finally, the ray term g_{ant}^2/g^2 is best understood in cases where $\theta_m \approx 0$. The ray term, $\propto g^{-2}$, varies along the beam trajectory as k^{-2}. Thus, when the beam reaches cutoff and the normal component of $\mathbf{k}$ vanishes, k^{-2} is maximized. This effect creates an Airy-type

enhancement of the probing field at cutoff, contributing to the localization of the measurement. This k^{-2} component of the weighting function is a central part of established DBS measurement theory [91].

3.1.5 The frequency of back-scattered waves

The previous subsection outlined the theory underlying the back-scattered power. In this subsection we focus on the frequency of the back-scattered radiation. Equation 3.3 states that the back-scattered radiation is Doppler shifted by an amount equal to the frequency of the density fluctuations, $\omega_{\text{Dopp.}} = \omega_{\delta n}$. To build our understanding we approximate that the signal is entirely localized to the cutoff with no parallel wavenumber, $k_{i,\parallel}|_{\rho=\rho_c} = 0$. The frequency of the density fluctuations can be written in terms of the velocity of said fluctuations, $\mathbf{v}$, and the measured wavenumber, $\mathbf{k}_{\text{meas.}} = \mathbf{k}_{\delta\mathbf{n}}|_{\rho=\rho_c}$,

$$\begin{aligned} \omega_{\delta n} &= \mathbf{k}_{\delta n} \cdot \mathbf{v} && \text{(3.31a)} \\ &= k_{\delta n}(\hat{\mathbf{e}}_b \cdot \mathbf{v}). \\ &= k_{\delta n}(v_{E\times B} + v_{\text{ph.}}). && \text{(3.31b)} \end{aligned}$$

Where we have used the fact that with no parallel wavenumber at cutoff, the measured wavenumber is purely binormal. The binormal velocity of the fluctuating density includes $E\times B$ advection and the phase velocity of the fluctuations. We can re-write Equation 3.31(b) in terms of a measured velocity,

$$v_{\text{meas.}} = \frac{\omega_{\text{Dopp.}}}{k_{\text{meas.}}} = \frac{\omega_{\delta n}}{k_{\delta n}} = v_{E\times B} + v_{\text{ph.}}. \tag{3.32}$$

Equation 3.32 is commonly used in DBS analysis to interpret the Doppler shift of the scattered signal. The $E \times B$ velocity in Equation 3.32 is $v_{E\times B} = E_r/B$, with the radial/normal direction pointing $\propto |\nabla\psi|$. Note that while the background magnetic field varies $B \sim 1/R$ in a tokamak, the radial electric field, E_r, can vary significantly over the plasma (and is not

a flux-function) leading to a wide range of $v_{E\times B}$ values[9].

The phase velocity, $v_{\text{ph.}}$, in Equation 3.32 is a wavenumber-dependant quantity arising from the saturated nonlinear state of plasma fluctuations. It is common to estimate its magnitude using the real frequency of (linearly) unstable plasma modes. In the wavenumber range relevant to DBS, modes are expected to have real frequency, $\omega \approx \omega_{D,s}$ or $\omega_{*,s}$. Where,

$$\omega_{*,s} = k_\perp \frac{\mathbf{B} \times \nabla P_s}{q_s n_s B^2} \tag{3.33}$$

is the diamagnetic drift frequency for species s and,

$$\omega_{D,s} = k_\perp \overline{v}_s^2 / \Omega_s \frac{\mathbf{B} \times \nabla \mathbf{B}}{B^2} \tag{3.34}$$

is the magnetic drift frequency[10]. We can re-write Equations 3.33 and 3.34 in terms of dimensionless parameters given the ion sound speed defined as $c_s \equiv \sqrt{T_e/m_i}$ and the ion sound gyro-radius defined as $\rho_s \equiv c_s/\Omega_i$,

$$\omega_{*,e} = -k_\perp \rho_s \left[a/L_{T_e} + a/L_{n_e}\right](c_s/a) \tag{3.35a}$$

$$\omega_{*,i} = k_\perp \rho_s \frac{T_i}{ZT_e} \left[a/L_{T_i} + a/L_{n_i}\right](c_s/a) \tag{3.35b}$$

$$\omega_{D,e} = -k_\perp \rho_s (a/R)(c_s/a) \tag{3.35c}$$

$$\omega_{D,i} = -\frac{T_i}{ZT_e}\omega_{D,e}. \tag{3.35d}$$

In Equation 3.35 $a/L_X \equiv -(a/X)\nabla X$ is the normalized inverse gradient scale-length. For common tokamak parameters, the drift frequencies in Equation 3.35 imply phase velocities, $|v_{\text{ph.}}| \approx 1$ [km/s]. Whether or not this approximation translates to reality depends on whether the effective nonlinear turbulent frequency remains on the order of the linear mode

[9]Typical E_r values on the DIII-D tokamak range from 0 to > 50 [kV/m]. Note that 1 [kV/m/T] = 1 [km/s]. Thus, with $E_r = 30$ [kV/m] and B = 1.5 [T] we have $v_{E\times B} = 20$ [km/s].

[10]This expression can be viewed as the combined curvature and ∇B drift velocities with the approximation that the velocities $v_\parallel^2 + \frac{1}{2}v_\perp^2 \sim \overline{v}_s^2$.

frequency. Furthermore, in situations with large inverse gradient scale lengths, such as the H-mode pedestal, the value of $\omega_{*,s}$ may become large.

Importantly, there is no general *a priori* reason to neglect the magnitude of $v_{E\times B}$ nor $v_{\text{ph.}}$ when interpreting the Doppler shift of the back-scattered radiation. However, when independent measurements of $v_{E\times B}$ are available (e.g. from charge-exchange spectroscopy (CER)) and/or the value of $v_{\text{ph.}}$ can be estimated from simulations, this added information can assist the interpretation of DBS. Specifically, in plasmas with significant rotation, one often has $v_{E\times B} \gg v_{\text{ph.}}$. In this limit, the measured velocity is approximately the local $E \times B$ velocity, and DBS measurements can be used to infer the local value of E_r. This application of DBS, and comparisons with CER under varying NBI-torque conditions will be discussed in detail in Chapter 5.

For cross-diagnostic comparisons it is important to make use of quantities which are theoretically flux functions. This (theoretically) eliminates discrepancies when diagnostics measure at different locations in the R, Z plane. The radial electric is manifestly not a flux function as its value depends on a spatial gradient, $E_r = -\hat{\mathbf{e}}_r \cdot \nabla\phi$. The gradient over space can be normalized with the gradient of the poloidal magnetic flux, $|\nabla\psi| = RB_p$, to produce a flux function,

$$\omega_{E\times B} = \frac{E_r}{RB_p}. \tag{3.36}$$

This quantity is dubbed the toroidal $E \times B$ angular velocity. For the application in Chapter 5, $\omega_{E\times B}$ is calculated from DBS quantities as,

$$\omega_{E\times B} = \frac{\omega_{\text{Dopp.}} B}{k_{\text{meas.}} RB_p}, \tag{3.37}$$

where all quantities are evaluated at the DBS cutoff location. The importance of this quantity in the theory of rotation in axisymmetric plasmas will be discussed in Subsection 5.1.1.

3.1.6 The DBS frequency spectrum

In the previous subsection we assumed that back-scattered radiation could be identified with a single binormal wavenumber at the cutoff location and the motion of density fluctuations could be captured by a single binormal velocity ($v_{E\times B}+v_{\text{ph.}}$). Upon relaxing this assumption we predict a broadening of the frequency spectrum about the nominal Doppler shift, $\omega_{\text{Dopp.}} = k_{\text{meas.}}(v_{E\times B} + v_{\text{ph.}})$. We present a simplified model for the width of the frequency spectrum by considering two effects:

- Variation in velocities over the scattering volume for a fixed k, i.e. $\Delta\omega_v = k\Delta v$, due to either (1) spatial variation in the background $v_{E\times B}$ and/or (2) turbulent variation in $v_{\text{ph.}}$.
- Variation in the measured wavenumber due to the finite probed volume for a fixed background velocity v, i.e. $\Delta\omega_k = v\Delta k$.

In reality, these broadening mechanisms are connected given that Δk is inherently related to the size of the probed volume which may impact the magnitude of Δv. If we approximate these frequency broadening mechanisms as independent effects, the total broadening would add in quadrature such that,

$$\Delta\omega = \sqrt{(k\Delta v)^2 + (v\Delta k)^2} \tag{3.38a}$$

$$\Delta f = \frac{1}{2\pi}\sqrt{(k\Delta v)^2 + \left(\frac{2\pi f_{\text{Dopp.}}}{k}\Delta k\right)^2}, \tag{3.38b}$$

where 3.38(b) is written using the corresponding DBS quantities ($k = k_{\text{meas.}}$). Large mean v is expected to broaden the frequency spectrum through $v\Delta k$ but the spread in Δv is assumed to be independent of the mean v. This simplified model predicts that when $v = 0$, the spectral width is minimized ($\Delta\omega = |k\Delta v|$) and the value of Δv can be deduced. Figure 3.3 exemplifies the relationship between the spectral width and the Doppler shift using DBS data from the experiment discussed in Chapter 5.

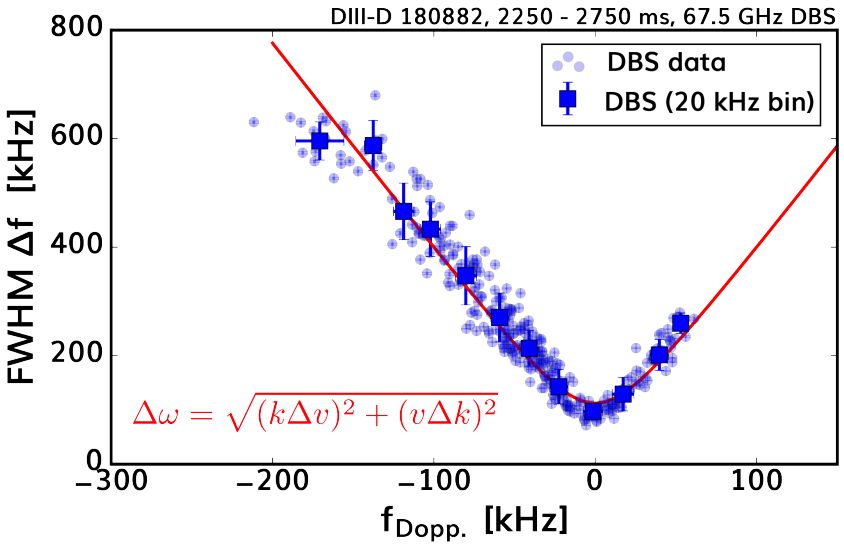

Figure 3.3: An example relationship between the spectral width (FWHM) and the Doppler shift. The DBS data shown is from the 67.5 GHz channel of the DBS60 system. The background plasma is discussed in detail in Chapter 5. To improve the performance of the fit, DBS data is collated into 20 kHz bins with respect to $f_{\text{Dopp.}}$ to evaluate statistics.

Figure 3.3 suggests that the width of the frequency spectrum indeed follows the trend predicted in Equation 3.38. The solid curve in Figure 3.3 is the result of a fit using Equation 3.38(b) with the value of k set to the value from ray tracing ($k = 0.7$ cm^{-1}). The fit finds $\Delta k = 2.7$ cm^{-1}, and $\Delta v = 10.1$ [km/s]. The fit-implied value of Δk is on the same order of magnitude as estimates using other methods [93]; albeit large relative to k due to the low incidence angle in this case. The fit-implied value of Δv is significantly larger than any spatial variation in the $v_{E\times B}$ value over the volume probed by DBS (see rotation profiles shown in Chapter 5 – Figure 5.5). Thus, through the lens of this simplified $\Delta\omega$ model, we conclude that a significant fraction of the spectral width comes from the turbulent $\Delta v_{\text{ph.}}$. Furthermore, the fit-derived value of $\Delta v_{\text{ph.}}$ (≈ 10 km/s) implies $\Delta v_{\text{ph.}} > v_{\text{ph.}}$, or equivalently $\Delta\omega_{\delta n} > \omega_{\delta n}$ (assuming the $\omega_{\delta n}$ is on the order of the linear estimates, Eq. 3.35). These results suggest that the width of the DBS frequency spectrum is directly related to the dynamics of turbulent density fluctuations. Furthermore, based on the case shown in Figure 3.3, models for the DBS frequency spectrum should account for turbulent variation in the

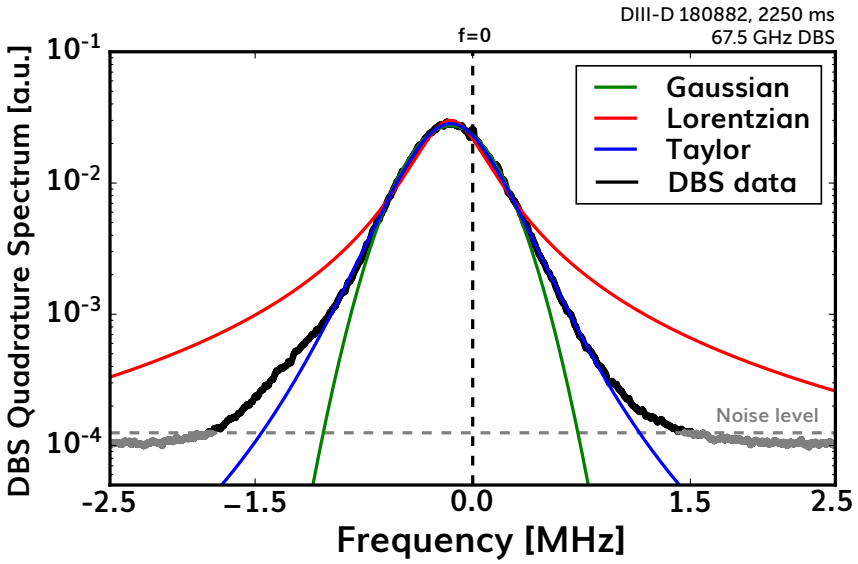

Figure 3.4: An example DBS amplitude spectrum from the study presented in Chapter 5. The DBS data used for the fit is limited to values above the noise level (horizontal dashed line). The DC ($f = 0$) frequency is shown with a vertical dashed line.

frequency of unstable modes $\Delta\omega_{\delta n}$.

The so-called 'Taylor model' is an example of a theory-based model which has successfully been applied to DBS frequency spectra [69,94,95]. An example derivation of the Taylor model is provided in Appendix B. The final expression for the spectral density function, $S(\omega)$ is the Fourier transform of the following auto-correlation function,

$$R(\tau) = F(k)e^{ik\overline{v}\tau} \exp\left(- k^2u^2\tau_{ac}^2(\tau/\tau_{ac} - 1 + e^{-\tau/\tau_{ac}})\right). \tag{3.39}$$

wherein the turbulence-modulated velocity fluctuations, δv, are characterized by mean-square amplitude $u^2 = \langle|\delta v|^2\rangle$, auto-correlation time τ_{ac}, and mean velocity $\overline{v}$. The dimensionless Kubo number, $K = ku\tau_{ac}$, describes the strength of the δv modulation relative to its auto-correlation time. In the slow/diffusive limit, $K \gg 1$, the frequency spectrum echos the statistics of δv, i.e. $S(\omega)$ is Gaussian for the assumptions leading to Equation 3.39. In the fast/convective limit, $K \ll 1$, $S(\omega)$ becomes a Lorentzian. Thus, for intermediate $K \approx 1$, we expect frequency spectra with intermediate shapes.

Figure 3.4 illustrates an example DBS (quadrature amplitude) frequency spectrum from the investigation in Chapter 5. Figure 3.4 shows the Gaussian, Lorentzian and Taylor models fit to the DBS data. In this case, the Lorentzian model fails to accurately fit the peak and the tails of the spectrum. The Gaussian model more accurately fits the shape in the vicinity of the peak, but fails to capture the shape of the spectral tails. Finally, the Taylor model appears to more accurately capture the shape of the measured spectrum over a span of $\approx$ 2 MHz covering more than a factor of $\approx$ 100 in amplitude. For the case shown in Figure 3.4 the Kubo number is intermediate ($K \approx 1.26$), hence the failure of the limiting Gaussian/Lorentzian cases. However, it should be noted that although the Gaussian and Lorentzian fits fail to capture the overall shape of the spectrum, both models appear to adequately identify the Doppler shift. Furthermore, the Gaussian fit in particular will result in only a small under-prediction of the spectral power (integral of the square of the curves in Figure 3.4) relative to integrating the data directly.

The physics underlying the shape of the DBS frequency spectrum was also considered in work by Maggs *et al.* in [96]. In their work, DBS data from an L-mode DIII-D discharge was analyzed to distinguish between chaotic and stochastic behavior using multiple metrics. The DBS data was found to exhibit chaotic behavior overall. One indicator of chaotic dynamical behavior is exponential decay in the power (frequency) spectrum [97]. In related work, Maggs *et al.* related the exponential nature of the frequency spectrum to the interaction between unstable modes and the production of Lorentizian pulses in the time domain [98,99]. Exponential decay can be observed in the DBS frequency spectrum by fitting with a Laplace line shape (exponential 'tent' function – see Appendix B, eq. B.17). In some cases, see Figure 4 in [96], the Laplace line shape can provide an excellent fit to the entire observed power spectrum. However, as discussed in [96], the spectrum may not form a pronounced 'tent' at the peak; instead the peak can be rounded. In the work by Maggs, a rounded peak in the frequency spectrum is attributed to the finite wavenumber resolution of DBS. Additional distortion of the exponential 'tent' feature was found to occur for large mean flows and at reduced signal amplitude (see Figure 8 of [96]).

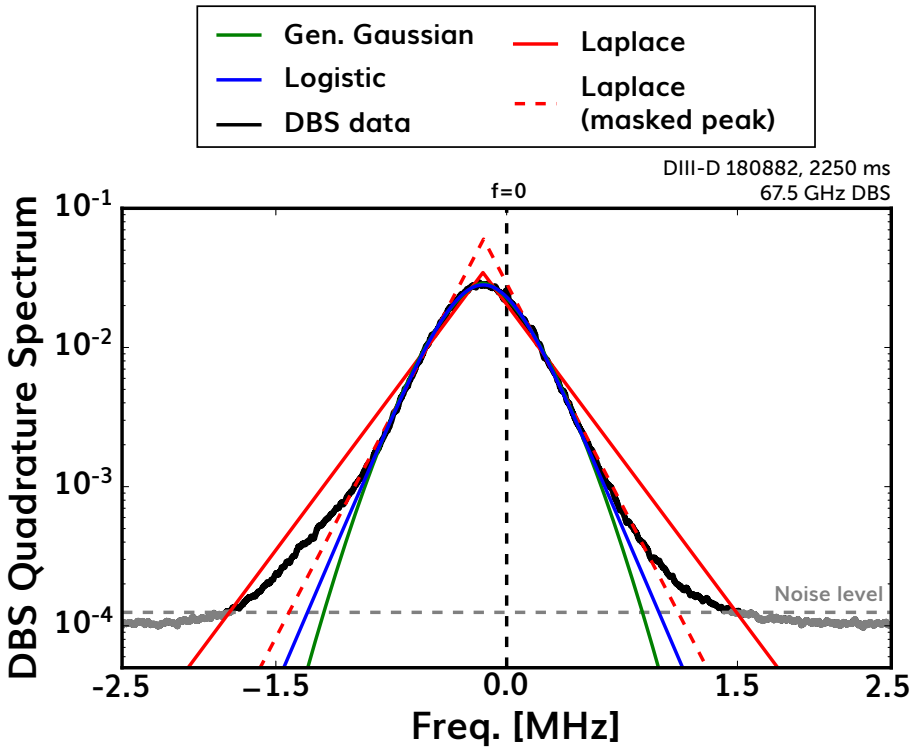

Figure 3.5: An example DBS amplitude spectrum from the study presented in Chapter 5. The DBS data used for the fit is limited to values above the noise level (horizontal dashed line). The DC ($f = 0$) frequency is shown with a vertical dashed line.

Figure 3.5 provides a comparison of lineshape models with exponential tail behavior. The DBS data in Figure 3.5 is identical to the data shown in Figure 3.4. When all DBS data above the noise-level is considered, the Laplace (exponential 'tent') lineshape fails to capture the overall shape of the spectrum (solid red line in Figure 3.5) – this is due to the rounded peak in the spectrum. To fit the exponential decay while avoiding the rounded peak one can mask the peak of the spectrum[11]. The masked-peak fit provides a much better fit to the tails of the frequency spectrum but overestimates the spectral power significantly due to extrapolation near the peak.

Alternative lineshape models with exponential tail behavior are also shown in Figure 3.5. The Generalized Gaussian model (Equation B.21) uses the additional shape parameter β to

[11]To determine the width of the mask, we iterate over various mask-widths and pick the width resulting in the best fit statistics.

continuously fill the function-space between Gaussian ($\beta = 2$) and Laplace ($\beta = 1$). For the case shown in Figure 3.5, $\beta = 1.6$ and therefore the tails are not strictly exponential. Finally, the logistic model (Equation B.18) is capable of fitting the rounded peak of the DBS spectrum with purely exponential tail behavior. For the case shown in Figure 3.5 the exponential decay time-constant, τ in the asymptotic behavior $S(\omega) \sim e^{-\omega\tau}$, is $\tau \approx 780$ ns for the Laplace model (masked peak) and $\tau \approx 950$ ns for the logistic model. These two values of τ are close to those reported in [96] (mean value of τ from their measurements was 715 ns).

In reality, the shape of the DBS frequency spectrum varies from experiment to experiment depending on a multitude of variables. There does not yet exist a simple, robust theory-based model for the frequency spectrum. However, it should be noted that the full-wave/nonlinear-gyrokinetics synthetic DBS diagnostic to be presented in Section 3.7 can partially reproduce the observed frequency spectrum (see Figure 4.25(a)). Empirically, observed frequency spectra tend to exist between Gaussian, Lorentzian and exponential-type lineshapes. This fact motivates fitting spectra with ad-hoc lineshape models dependant on the observed spectral shape. In addition to an outline of a derivation of the Taylor model, Appendix B details other models commonly used for the DBS frequency spectrum.

3.2 Doppler back-scattering hardware

The hardware components of DIII-D Doppler back-scattering systems can be divided into three groups: signal generation electronics, quasi-optics, and receive electronics. There are two DBS systems installed on the DIII-D tokamak. Both DBS systems have essentially identical electronics, but their quasi-optics differ significantly. These differences will be addressed in the following subsections.

The signal-generation and receive electronics used by both systems is presented by W. Peebles *et al.* in [79]. Figure 3.6 provides an RF component diagram of the DBS electronics. Both systems consist of eight simultaneous, fixed-frequency channels spanning the V-band

(55-75 GHz). The signal consisting of eight simultaneous frequencies is generated using a nonlinear transmission line (NLTL). The signal is then transferred from rectangular WR-15 waveguide to free space waves using corrugated, conical horn antennae. The signal received from the plasma is isolated using a using a directional coupler. Both the launched signal and the signal returning from the plasma are down-converted from the V-band to intermediate frequencies (2 - 10.5 GHz) using a local Gunn oscillator.

The intermediate frequency signals (launch and receive) are eight-way power divided and filtered around their nominal frequencies. Finally, the filtered plasma signals are mixed with their respective launch signals using quadrature mixers. The quadrature mixers preserve the phase between the received signal relative to the launched signal. The preservation of the phase information is vital for reconstructing the phasor representing the scattering signal from the plasma. The in-phase (I) and quadrature (Q) outputs of each of the eight mixers are amplified and passed to the DIII-D data acquisition system.

3.2.1 The DBS60 system

The DBS60 system is located at the 60° toroidal location of the DIII-D tokamak (see Figure 2.3). The toroidal location of the system is only relevant as a label to distinguish this system from the DBS240 system. The DBS60 quasi-optical layout is illustrated in Figure 3.7. The probing radiation generated inside of the electronics box is converted to a free-space beam by a corrugated conical horn antenna. The expanding beam emanating from the horn antenna is roughly collimated by a plano-convex lens. Finally, the beam is focused into the plasma by a parabolic mirror. The poloidal angle of the parabolic mirror is controlled remotely. The toroidal angle of the DBS60 system is fixed to 0°.

3.2.2 The DBS240 system

The DBS240 system is located at the 240° toroidal location of the DIII-D tokamak (see Figure 2.3). The DBS240 system is illustrated in Figure 3.8. Similar to the DBS60 system, corrugated conical horn antennas and lenses are used to produce a roughly collimated beam.

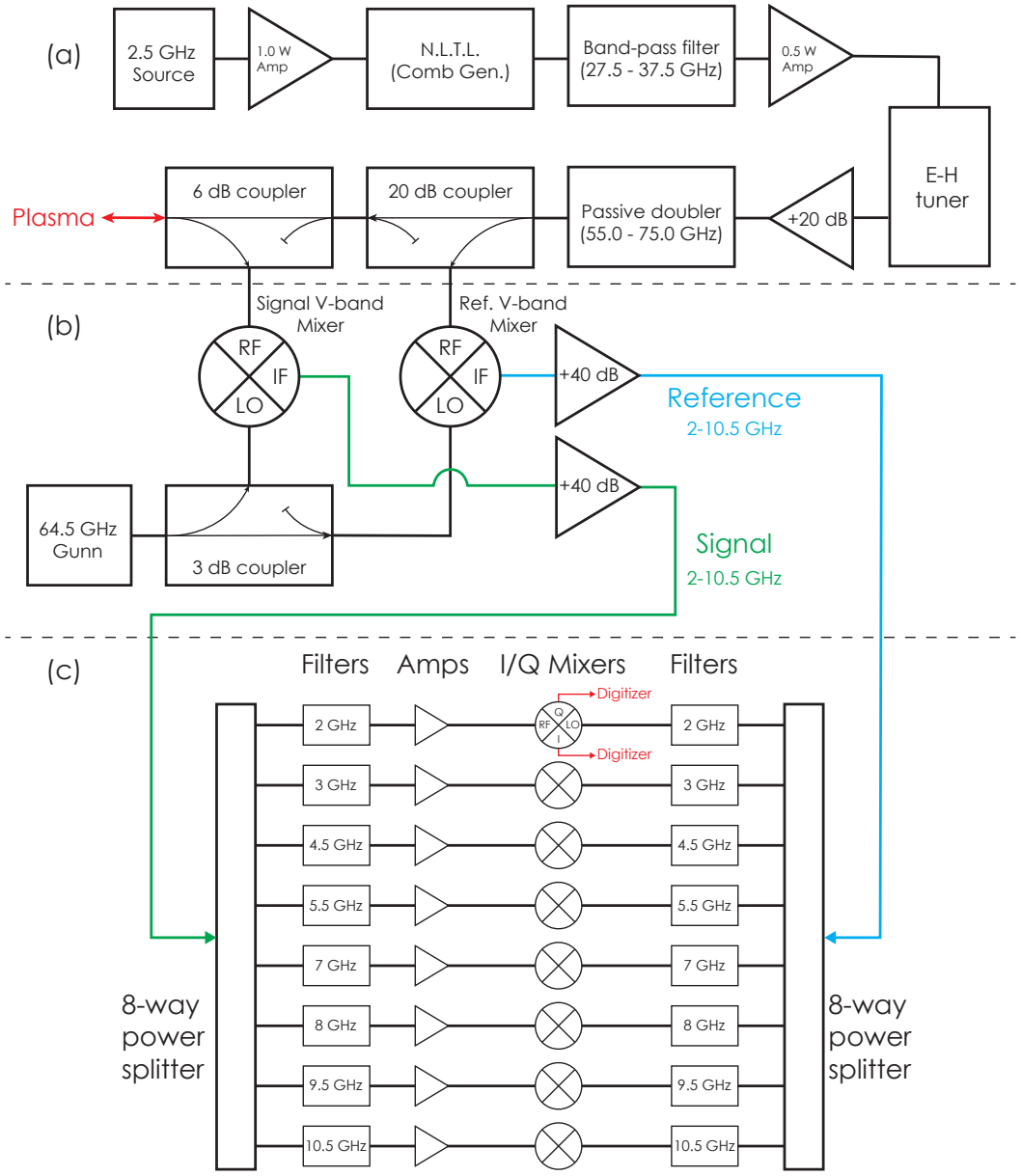

Figure 3.6: Component diagram illustrating the electronics of the DBS60 and DBS240 systems. The diagram is divided into three portions (a,b,c) with dashed lines. 3.6(a) illustrates the signal-generation portion of the electronics whereby a 2.5 GHz source is converted into eight simultaneous V-band frequencies. 3.6(b) illustrates the first frequency down-conversion process where V-band mixers and a V-band Gunn LO convert from the V-band to the 2-10.5 GHz range. 3.6(c) shows the final frequency down-conversion where the eight channels are separated and mixed together in quadrature. The I, Q outputs of each mixer are digitized (only one mixer is annotated for clarity).

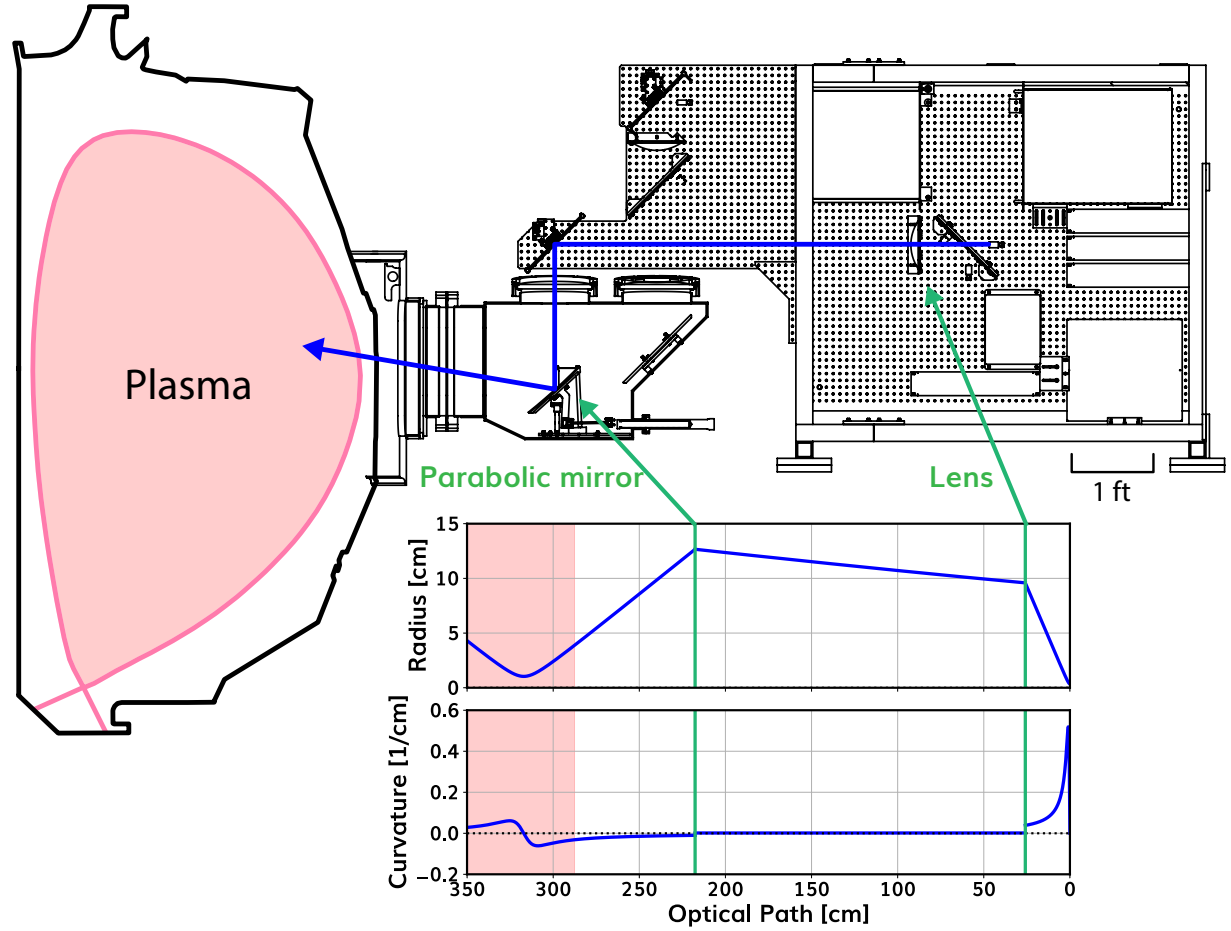

Figure 3.7: Quasi-optical schematic of the DBS60 system.

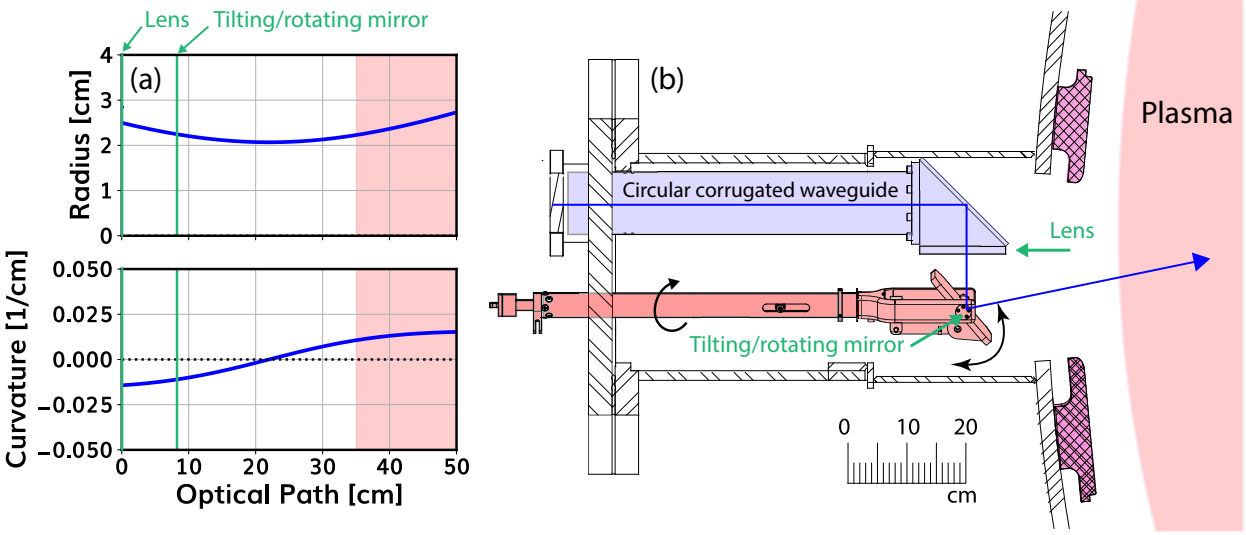

Figure 3.8: Quasi-optical schematic of the DBS240 system.

Unlike the DBS60 system, the DBS240 system couples the free-space beam into an oversized waveguide. At the outlet of the waveguide closest to the tokamak, a metallic dichroic lens is used to focus the wave emanating from the waveguide onto a multi-axis mirror. The DBS240 mirror has the ability to steer the beam in the poloidal and toroidal directions [3].

3.3 Analysis of Doppler back-scattering data

The data analysis procedure for any one DBS channel is described in the following: the I, Q mixer outputs are digitized at a high sampling rate (typically ≥ 5 MHz). The scattering signal is reconstructed as a time-series of complex numbers: $S(t) = I(t) + iQ(t)$. We use a short-time Fourier transform (STFT) method to calculate a spectrogram of $S(t)$. Hanning windows are used to suppress spectral leakage. Optionally, adjacent records of data are overlapped (typically 50%) to recover time resolution lost to windowing. The output of this procedure is called the quadrature spectral density (or simply the 'quadrature spectrum'), $\hat{S}(f) = \mathrm{STFT}[S(t)]$.

DBS observables can be calculated directly from the quadrature linear spectral density. For example, the Doppler shift ($f_{\mathrm{Dopp.}}$), and the signal power (P_s). The Doppler shift can be numerically approximated by a simple weighted spectral average,

$$f_{\mathrm{Dopp.}} \approx \frac{\sum_f f \cdot \hat{S}(f)}{\sum_f \hat{S}(f)} \tag{3.40}$$

and the signal power can be approximated by numerically integrating the modulus-square of the linear spectral density,

$$P_s \approx \int_{-f_{\mathrm{Nyq.}}}^{f_{\mathrm{Nyq.}}} |\hat{S}(f)|^2 df, \tag{3.41}$$

where $f_{\mathrm{Nyq.}}$ is the Nyquist frequency[12]. However, attributing the calculated Doppler shift and the signal power to a particular location/mode within the plasma assumes that the demodulated scattering signal, $S(t)$, contains only one Doppler-shifted component originating

[12] $f_{\mathrm{Nyq.}} = 2.5$ MHz for 5 MHz sampling rate used in the experiments in this thesis.

from a well-localized region in the plasma. In reality, the spectrum of the back-scattered signal may contain multiple peaks or transient effects which should be filtered out for more accurate determination of $f_{\text{Dopp.}}$ and P_s.

Notch filters can be used to isolate the Doppler shifted component in $\hat{S}(f)$ before further processing. The filter is applied by removing portions of $\hat{S}(f)$ for $f_{LP} \leq f \leq f_{HP}$ where f_{LP} and f_{HP} are adjustable low-pass and high-pass frequencies. Noise can also be removed by specifying a noise level $\hat{S}_N$ and discarding $\hat{S}(f) \leq \hat{S}_N$. These optional pre-processing steps can improve the accuracy in calculating $f_{\text{Dopp.}}$ and P_s from spectra where $\hat{S}(f)$ is non-trivial. Transient events, namely edge-localized modes (ELMs), are often visible in $\hat{S}(f)$ and can impact spectral analysis. ELMs are dynamic MHD modes driven by steep gradients in the edge pressure or current density. These events can be removed through an ELM-phase synchronized analysis. The time basis of the $\hat{S}(f)$ spectrogram is mapped to the phase of the ELM. Then, time slices of $\hat{S}(f)$ are removed based on an acceptance interval of ELM-phase (e.g. [50, 95%]).

Our ability to isolate Doppler-shifted components of the observed $\hat{S}(f)$ spectrum is often improved by fitting peak-like lineshape models to all, or a portion of the measured $\hat{S}(f)$. Example fit outputs were shown previously in Figures 3.4 and 3.5. Beyond the models discussed in Subsection 3.1.6, other ad-hoc lineshape models are discussed in Appendix B. Generally, peak-like linehsape models with 3-4 parameters (amplitude, center, width, and shape) can reproduce the observed spectra. When multiple peaks are present in the spectrum it can be advantageous to fit composite models with multiple lineshape components to the data. However, for more than two peaks this process can be computationally slow using nonlinear least-squares fitting. In these situations, multiple components can be isolated quickly with Mixture Model (MM) clustering algorithms such as the Gaussian Mixture Model (GMM [100]) and the Students-T Mixture Model (TMM [101]). An example of the MM analysis method is shown in Appendix B.

As part of this doctoral research, an open-source collection of DBS data analysis routines were developed by the author and made available in the form of an OMFIT module. OMFIT

[102] is an open-source framework used throughout the tokamak research community to facilitate simulations and analysis of experimental data. The DBS module contains routines for fetching DBS data from multiple tokamaks, and spectral analysis including prepossessing, fitting and MMs. The module also organizes kinetic profiles, calculates cutoffs/resonances, and orchestrates beam/ray tracing simulations (discussed in the following sections). The OMFIT DBS module is described in more detail in Appendix A.

3.4 Ray tracing

The analysis techniques in the previous section are used to calculate the Doppler shift, $f_{\text{Dopp.}}$, and the signal power, P_s, from DBS data. To interpret measurements further, we must determine the trajectory (and wavevector) of the probing radiation through the plasma. For each DBS frequency, we must (theoretically) solve the wave equation (Equation 3.4) in our non-uniform plasma with the incident field provided as a boundary condition. Instead, it is standard practice to find approximate solutions to Equation 3.4 in the geometric optics limit by solving the ray tracing equations.

Formally, we define an order parameter $\delta \equiv (Lk)^{-1} \ll 1$ where k is the wavenumber of the probing radiation and L is the length-scale of variations in the background plasma, $L^{-1} \sim \nabla n/n \sim \nabla B/B$. Furthermore, we assume that variations in the background plasma with respect to time are negligible compared to frequency of the probing radiation, $\omega \gg \tau_{eq}^{-1} \sim \partial_t n/n \sim \partial_t B/B$. Then, we use the following ansatz for the wave electric field,

$$\mathbf{E}(\mathbf{r}, t) = \tilde{\mathbf{E}}(\mathbf{r}) e^{iS(\mathbf{r}) - i\omega t}, \tag{3.42}$$

where spatial variation in the eikonal $S(\mathbf{r})$ are taken to be, $S^{-1}|\nabla S| \sim L^{-1}$. The amplitude of the electric field is also expanded in powers of the order parameter δ,

$$\tilde{\mathbf{E}}(\mathbf{r}) = \tilde{\mathbf{E}}^{(0)}(\mathbf{r}) + \tilde{\mathbf{E}}^{(1)}(\mathbf{r}) + \mathcal{O}. \tag{3.43}$$

Then, the electric field in Equation 3.42 and the expansion of its amplitude in Equation 3.43 are substituted into the wave equation (Equation 3.4). The resulting equation, to order δ^0, is simply Equation 3.5 with $\mathbf{E} \to \tilde{\mathbf{E}}^{(0)}$ and $\mathbf{k} = \nabla S$ defining the local wavevector.

The ray tracing equations can be derived by taking partial derivatives of $\mathcal{D}(\mathbf{k}, \omega, \mathbf{r}) = 0$ with roots taken to be values of $\omega = H(\mathbf{k}, \mathbf{r})$. The resulting set of equations is,

$$\frac{d\mathbf{r}}{d\tau} = \nabla_{\mathbf{k}} H = -\frac{\partial \mathcal{D}/\partial \mathbf{k}}{\partial \mathcal{D}/\partial \omega} \tag{3.44a}$$

$$\frac{d\mathbf{k}}{d\tau} = -\nabla H = \frac{\partial \mathcal{D}/\partial \mathbf{r}}{\partial \mathcal{D}/\partial \omega}, \tag{3.44b}$$

where τ parameterizes the trajectory and the symbol H is used in place of ω to allude to Hamilton's equations of motion. The system of ODEs given in Equation 3.44 can be integrated numerically to provide the trajectory (and wavevector) of an electromagnetic wave in a nonuniform plasma. The initial conditions are the starting position and wavevector. In solving Equation 3.44 one must also solve the local dispersion relation, $\mathcal{D}(\mathbf{k}, \mathbf{r}, \omega) = 0$ along the trajectory.

Several software packages exist to solve the ray tracing equations in a tokamak geometry. In this thesis we use the code `GENRAY` [103] with the cold-plasma dispersion relation (`id=3`). The `GENRAY` code takes the magnetic equilibrium (a `gEQDSK` file) and the electron density profile, $n_e(\rho)$ as inputs. We also provide the wave frequency, polarization, launch position and angle(s). The code calculates the trajectory of the ray and the evolution of the index of refraction $\mathbf{n} \equiv c\mathbf{k}/\omega$. Specifically, the code provides components of the index of refraction, $n_\parallel = |\mathbf{n} \cdot \hat{\mathbf{b}}|$ and $n_\perp = \sqrt{n^2 - n_\parallel^2}$.

When interpreting DBS measurements, the nominal measured location, $\rho_{\text{meas.}}$, is the turning-point of the trajectory, i.e. ρ where $n_\perp$ is minimized. The measured wavenumber

determined by the Bragg condition (Equation 3.2) at $\rho_{\text{meas.}}$,

$$\rho_{\text{meas.}} = \text{argmin}_{\rho}(|n_{\perp}|) \tag{3.45a}$$

$$k_{\text{meas.}} = -2\frac{\omega}{c}\left(n_{\perp}|_{\rho=\rho_{\text{meas.}}}\right), \tag{3.45b}$$

where $\text{argmin}_{\rho}(\dots)$ determines the ρ value that minimizes $n_{\perp}(\rho)$. Equation 3.45 is used to post-process `GENRAY` simulations.

3.5 Beam tracing

Similar to ray tracing, beam tracing is a method of approximating electromagnetic wave solutions to Maxwell's equations in a non-uniform medium. In beam tracing, the length-scale of the wave transverse to the propagation direction is taken to be W satisfying $\lambda \ll W \ll L$, i.e. the width of the beam is large relative to the wavelength of the radiation but small compared to characteristic background variation in the medium. This introduces a secondary order parameter, $\zeta = (kW)^{-1} \sim (LW)^{-1} \ll 1$, and complicates the expansion of the wave equation and the electric field amplitude. Following [4], the eikonal function $S(\mathbf{r})$ in Equation 3.42 is taken to be,

$$S(\mathbf{r}) = s(\tau) + \mathbf{k}_w(\tau)\cdot\mathbf{w} + \frac{1}{2}\mathbf{w}\cdot\boldsymbol{\Psi}_w\cdot\mathbf{w} + \mathcal{O}. \tag{3.46}$$

In this equation, τ parameterizes the path of the central ray $\mathbf{q}(\tau)$ and $\mathbf{w} = \mathbf{r} - \mathbf{q}(\tau)$ defines a position vector transverse to the central ray. The function,

$$s(\tau) = \int_0^{\tau} \mathbf{k}(\tau')\cdot\hat{\mathbf{g}}(\tau')d\tau' \tag{3.47}$$

encodes the evolution of the wavenumber along the central ray (to zeroth order, $\nabla S(\mathbf{r}) = \mathbf{k}$). Terms with subscript w in Equation 3.46 are perpendicular to the effective group velocity, $\mathbf{g} \equiv d\mathbf{q}/d\tau$. The quantity $\boldsymbol{\Psi}_w$ in Equation 3.46 is a complex-valued, symmetric matrix

encoding the width of the beam and the radius of curvature of phase-fronts. In an orthogonal, beam-following basis $(\hat{\mathbf{x}}, \hat{\mathbf{y}}, \hat{\mathbf{g}})$ the real and imaginary parts of $\mathbf{\Psi}_w$ can be diagonalized to reveal,

$$\mathrm{Re}\{\mathbf{\Psi}_w\}_{ii} = \frac{k^3}{k_g^2}\frac{1}{R_i} \tag{3.48a}$$

$$\mathrm{Im}\{\mathbf{\Psi}_w\}_{ii} = \frac{2}{W_i^2}, \tag{3.48b}$$

where i indexes the principal axes of the beam, R_i is the radius of curvature of the phase fronts and W_i is the beam half-width along said axis.

To derive the beam tracing equations, the electric field amplitude (Equation 3.43) and the wave equation (Equation 3.4) are expanded through $\mathcal{O}(\delta^2)$ and $\mathcal{O}(\zeta^2)$. This is a lengthy process (see Appendix A of [4]) resulting in a hierarchy of equations representing an approximate solution to the wave equation. The derivation of the beam tracing equations reproduces the ray tracing equations in its first order and yields evolution equations for higher order terms such as the components of the matrix $\mathbf{\Psi}$.

The system of beam tracing equations is summarized as,

$$\frac{d\mathbf{q}}{d\tau} = \nabla_{\mathbf{k}} H \tag{3.49a}$$

$$\frac{d\mathbf{k}}{d\tau} = -\nabla H \tag{3.49b}$$

$$\frac{d\Psi_{ij}}{d\tau} = -\frac{\partial^2 H}{\partial r_i \partial r_j} - \Psi_{il}\frac{\partial^2 H}{\partial k_l \partial r_j} - \Psi_{mj}\frac{\partial^2 H}{\partial r_i \partial k_m} - \Psi_{in}\Psi_{pj}\frac{\partial^2 H}{\partial k_n \partial k_p}. \tag{3.49c}$$

The first two equations are identical to the ray tracing equations in Equation 3.44. This system of ODEs can be solved numerically in tokamak geometry by codes such as `TORBEAM` [104] or `SCOTTY` [4]. In this thesis we use the code `SCOTTY` for 3D beam tracing and DBS-relevant postprocessing. When numerically integrating equations 3.49(a)-(c), initial conditions for the starting beam position, wavevector, and the $\mathbf{\Psi}$ components are required. The initial $\mathbf{\Psi}$ components can be estimated by analyzing the quasioptical configuration for each system

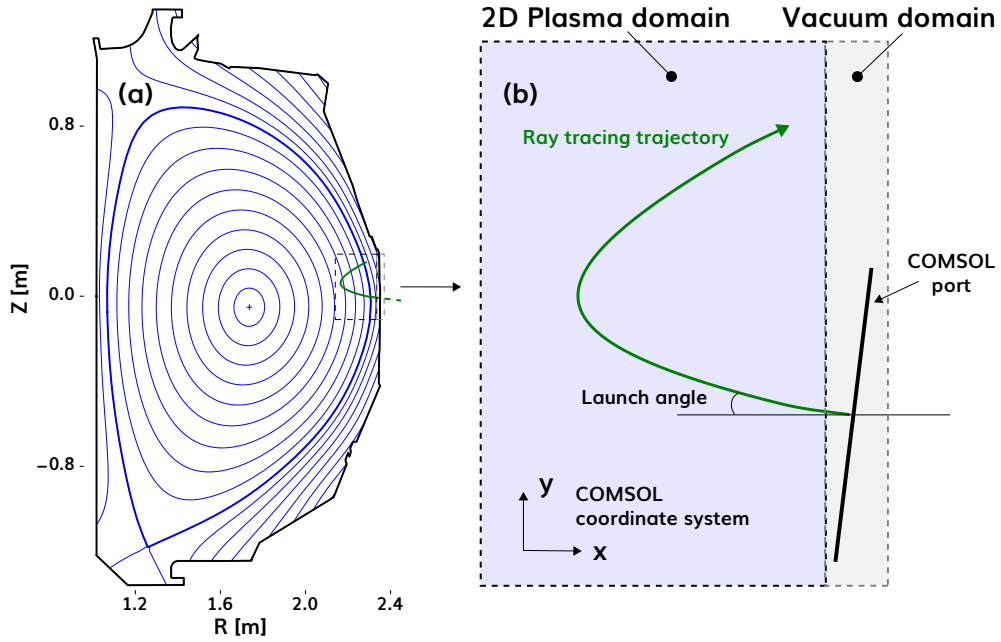

Figure 3.9: Diagram illustrating a representative 2D COMSOL model for DBS.

(Figures 3.7 and 3.8) using Guassian beam ABCD-matrix methods found in Goldsmith [105].

3.6 Full-wave simulations

In Sections 3.4 and 3.5 we presented methods for approximating solutions to the electromagnetic wave equation for the interpretation of DBS measurements. Numerical solutions of the wave equation can also be calculated without an ansatz for the electric field nor expansion methods. These 'full-wave' calculations are performed by directly solving the wave equation in the plasma with appropriate boundary conditions to represent the incident DBS wave. Although this approach represents the highest physics fidelity, it is a departure from the previous ray/beam tracing methods in terms of computational cost and model complexity. In this dissertation we employ the commercial software COMSOL to solve the electromagnetic wave equation in the plasma. Specifically, we solve the frequency-domain wave equation (Equation 3.4) in a two dimensional rectangle encompassing the plasma-vacuum boundary.

Figure 3.9 illustrates a representative COMSOL model used for DBS modeling. COMSOL uses a Cartesian (x, y, z) coordinate system when solving the wave equation. The incident

DBS wave is introduced into the simulation by specifying the **E**-field along a line segment. This line segment acts as the model 'port' and the **E**-field is taken to be a tilted, linearly polarized Gaussian beam,

$$\mathbf{E}_{\text{port}} = \begin{bmatrix} -\sin\theta\cos(\phi) \\ \cos\theta\cos(\phi) \\ \sin(\phi) \end{bmatrix} E_0 \sqrt{\frac{w_0}{w(x'-d)}} \exp\left(\frac{-y'^2}{w^2(x'-d)} - ik_0 \frac{y'^2}{2R(x'-d)} - ik_0(x'-d) + i\eta(x'-d) \right) \tag{3.50}$$

wherein,

$$w(z) = w_0\sqrt{1+(z/z_R)^2} \tag{3.51a}$$

$$R(z) = z(1+(z_R/z)^2) \tag{3.51b}$$

$$\eta(z) = \frac{1}{2}\arctan(z/z_R) \tag{3.51c}$$

$$z_R = \frac{\pi w_0^2}{\lambda_0} = \frac{1}{2}k_0 w_0^2 \tag{3.51d}$$

$$x' = x\cos(\theta) - y\sin(\theta) \tag{3.51e}$$

$$y' = x\sin(\theta) + y\cos(\theta) \tag{3.51f}$$

$$E_0 = \sqrt{\frac{Z_0 2\langle P_i\rangle/\Delta z}{w_0\sqrt{\pi/2}}}. \tag{3.51g}$$

In these equations, θ is the poloidal launch-angle of the incident beam, ϕ is the edge magnetic pitch-angle (used to polarize the **E**-field), d is the distance of the port relative to the beam's (vacuum) waist location, k_0 is the vacuum incident wavenumber, w_0 is the (vacuum) beam waist, $Z_0 \approx 377$ [Ω] is the vacuum impedance, and $\langle P_i\rangle/\Delta z$ is the 2D time-averaged input power. The entire COMSOL domain shown in Figure 3.9(b) is surrounded by a 'perfectly matched layer' (PML) to absorb incident radiation. The COMSOL port shown in Figure 3.9(b) uses the 'domain-backed' option such that any back-scattered/reflected radiation passes through the port to be absorbed by the PML on the right of the domain.

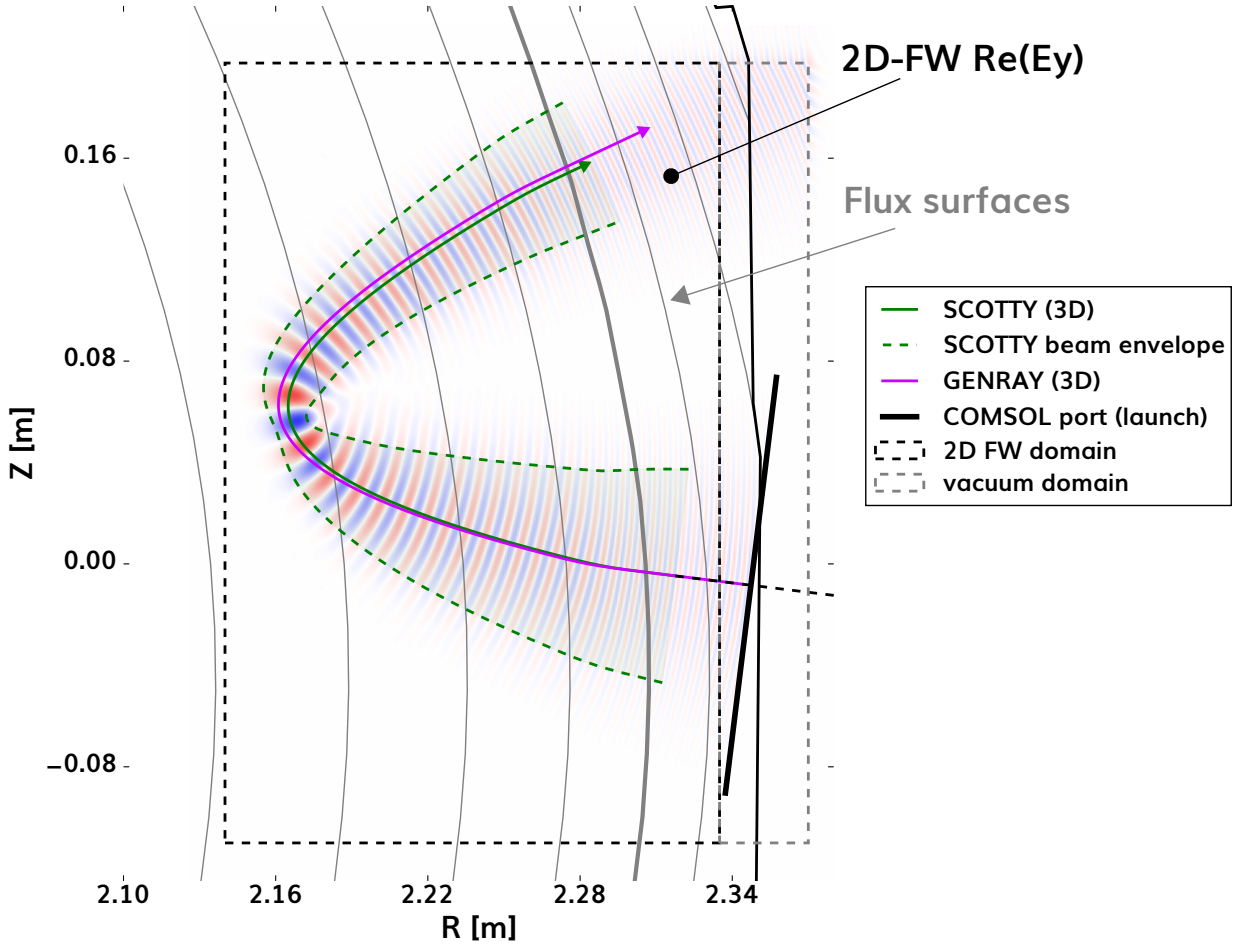

Figure 3.10: Results of a 2D COMSOL full-wave simulation of the DBS probing beam. Two dimensional projections of the 3D trajectories from GENRAY (ray tracing) and SCOTTY (beam tracing) are overlaid for comparison. The DBS configuration shown corresponds to X-mode polarization, 72.5 GHz RF frequency, and 7° poloidal launch angle. Flux surfaces are shown in grey with the separatrix ($\rho = 1$) in bold.

Figure 3.10 shows the result of a 2D full-wave COMSOL simulation along with 2D projections of 3D beam tracing (using SCOTTY) and 3D ray tracing (using GENRAY) simulations. Both SCOTTY and GENRAY predict that the central ray of the DBS beam travels ≈ 2 cm in the toroidal direction (into the page). The comparison in Figure 3.10 suggests that both SCOTTY and GENRAY are accurately approximating the trajectory of the wave. Beyond the trajectory of the central ray, SCOTTY is accurately capturing the evolution of the beam envelope through the plasma (dashed green lines). Figure 3.10 also shows a slight (mm scale) discrepancy between SCOTTY and GENRAY with respect to the trajectory of the central ray. In Figure 3.10 we can also observe the characteristic enhancement of the E-field amplitude near the cutoff discussed in Subsection 3.1.4.

3.7 Synthetic diagnostic development

In general, a synthetic diagnostic is a model designed to predict one or more observable quantities from simulated (or analytic) inputs. Synthetic diagnostics enable more direct comparisons between simulation/theory and experiment by accounting for instrumental effects e.g. spatial/wavenumber resolution. One of the primary results of this thesis is the development of a synthetic DBS diagnostic based on the beam-DBS theoretical framework outlined in Subsection 3.1.4. The beam-DBS model for the back-scattered power accounts for all of the instrumental effects captured by the weighting function, $U(l)$, in Equation 3.27. We use the beam-DBS framework to predict the back-scattered power as a function of the measured wavenumber, i.e. the back-scattered power wavenumber spectrum, $P_s(k_{\text{meas.}})$. The predicted $P_s(k_{\text{meas.}})$ can then be directly compared with measurements from a scan of the DBS launch-angle(s).

Creating a synthetic diagnostic for DBS is particularly challenging due to the integrated nature of the fluctuating density, δn, in DBS theory. In the beam-DBS framework Equation 3.27 (repeated here),

$$\langle P_s \rangle \propto \int dl \langle |\delta \hat{n}|^2 \rangle U_p U_b \frac{g_{ant}^2}{g^2} e^{-2\theta_m^2/\Delta\theta_m^2}. \tag{3.52}$$

provides the average back-scattered power as an integral along the DBS trajectory parameterized by the path-length l. The weighting function, $U(l) = U_p U_b \frac{g_{ant}^2}{g^2} e^{-2\theta_m^2/\Delta\theta_m^2}$, plays only a partial role in localizing measurements to the vicinity of the cutoff. The fluctuating density spectrum, $\langle|\delta\hat{n}|^2\rangle$, and its intrinsic anisotropy in the $\mathbf{k}_\perp$ plane, are essential for localizing measurements and identifying the nominal $k_{\text{meas.}}$. Therefore, the underlying $\langle|\delta\hat{n}|^2\rangle$ cannot be easily decoupled from measured values of P_s.

The weighting function in the integrand of Equation 3.52 depends on the background plasma and the DBS configuration (launch position, steering angles). We use the code `SCOTTY` outlined in Section 3.5 to evaluate the weighting function for a given trajectory. The density spectrum, $\langle|\delta\hat{n}|^2\rangle$, is separately modeled by either an analytic function or by numerical simulation of plasma fluctuations. Given the weighting function from `SCOTTY` and a model $\langle|\delta\hat{n}|^2\rangle$, the synthetic diagnostic is complete, i.e. theory-based predictions of the measured P_s can be calculated.

We apply our synthetic DBS diagnostic to solve both forward and inverse modeling problems:

- Forward problem: Given a model $\delta\hat{n}$, what $P_s(k_{\text{meas.}})$ would we theoretically observe from DBS?
- Inverse problem: Given experimental measurements of $P_s(k_{\text{meas.}})$, what is a plausible $\delta\hat{n}$?

On the one hand, the forward modeling problem is a straightforward evaluation of Eq. 3.52 provided one has access to $\delta\hat{n}$. Unfortunately, modeling $\delta\hat{n}$ via simulations can be computationally expensive for two reasons: (1) the saturated fluctuation spectrum is an inherently nonlinear quantity, and (2) Depending on the range of probed wavenumbers, multi-scale simulations may be necessary for a complete comparison with measurements. As part of this research we have performed some large nonlinear CGYRO simulations (described in Appendix C), but in general this can be a prohibitive requirement for DBS modeling. Therefore, one of the primary outputs of this thesis is the development of a novel method to

obtain an approximate $\delta\hat{n}$ spectrum using the reduced quasi-linear code TGLF. The TGLF-based method for approximating δn (see Subsection 2.4.1) dramatically lowers the barrier for predictive/interpretive DBS modeling.

On the other hand, the inverse modeling problem is solved by first assuming a particular, analytic model for $\langle|\delta\hat{n}(k_n, k_b; \vec{\mu})|^2\rangle$ where $\vec{\mu}$ represents a set of model parameters. Then, we iterate $\vec{\mu}$ until the model $\langle|\delta\hat{n}|^2\rangle$ reproduces measured values of P_s via Equation 3.52. This approach introduces bias through the functional form of the model $\langle|\delta\hat{n}|^2\rangle$ and may converge for several different models. Convergence indicates that the $\delta\hat{n}$ spectrum, with optimized parameters $\vec{\mu}_*$, can reproduce the observations. For example,

$$\langle|\delta\hat{n}|^2\rangle \propto \frac{1}{1 + \left(\frac{|k_n|}{w_n}\right)^{\gamma} + \left(\frac{|k_b - k_b^*|}{w_b}\right)^{\beta}}. \tag{3.53}$$

is an analytic model proposed in [8]. This power-law model has five parameters: $\vec{\mu} = [w_n, \gamma, k_b^*, w_b, \beta]$. Where w_n and w_b are inverse lengths in the normal and binormal directions respectively. The exponents γ and β are spectral indices in the normal and binormal directions and the wavenumber k_b^* allows the spectrum to be shifted to a finite k_b to representing the dominant instability driving scale. An alternative model is,

$$\langle|\delta\hat{n}|^2\rangle \propto \exp\left(-\left(\frac{|k_n|}{w_n}\right)^{\gamma} - \left(\frac{|k_b - k_b^*|}{w_b}\right)^{\beta}\right). \tag{3.54}$$

where the same set of parameters, $\vec{\mu} = [w_n, \gamma, k_b^*, w_b, \beta]$, is used with similar physical meanings.

Separate from the beam-DBS model for P_s, we have also implemented a synthetic DBS model combining nonlinear gyrokinetics and full-wave COMSOL simulations of the probing DBS electric field. While this approach represents the highest physics fidelity of the models considered in this dissertation, it has several drawbacks: (1) the COMSOL simulations considered here are 2D to limit model complexity and computational cost, and (2) the COMSOL results do not allow us to isolate distinct physical effects in the manner provided

by beam tracing simulations, i.e. COMSOL simply provides the E-field over a spatial grid, and (3) the nonlinear CGYRO simulations are performed in the local limit – perturbations away from the cutoff are not simulated. Despite these limitations, the full-wave synthetic diagnostic allows us to perform high-fidelity predictions of the received signal amplitude due to scattering near the cutoff layer.

Returning to Equation 3.20, we substitute Equation 3.18 for the fluctuating component of the permittivity tensor and use $\boldsymbol{\sigma} = \frac{\omega}{4\pi i}(\boldsymbol{\epsilon} - \mathbf{1})$ to write,

$$A_r = -\frac{2\pi}{c}\int_V d^3r \frac{\delta n}{n}(\boldsymbol{\sigma}\mathbf{E_i}) \cdot \mathbf{E}^{(+)} \tag{3.55a}$$

$$A_r = -\frac{2\pi}{c}\int_V d^3r \delta n(\mathbf{r}) U(\mathbf{r}). \tag{3.55b}$$

Where the weighting function, $U(\mathbf{r})$, is implicitly defined as containing every term in the integrand other than $\delta n(\mathbf{r})$. By replacing $\delta n(\mathbf{r})$ and $U(\mathbf{r})$ with their spatial Fourier transforms, we obtain the wavenumber-space equivalent of Equation 3.55(b),

$$A_r(t) = -\frac{2\pi}{c}\int \frac{d^3k}{(2\pi)^3}\delta\hat{n}(\mathbf{k}, t)\hat{U}(-\mathbf{k}). \tag{3.56}$$

To apply Equation 3.56, we use the COMSOL model presented in Section 3.6 to simulate the 2D full-wave DBS $\mathbf{E}_i$ in the background plasma and $\mathbf{E}^{(+)}$ in the transposed plasma (background plasma with $\mathbf{B} \to -\mathbf{B}$). The real-space weighting function, $U(\mathbf{r})$, is evaluated using $\mathbf{E}^{(+)}$, $\mathbf{E}_i$, and the cold-plasma conductivity tensor, $\boldsymbol{\sigma}$. Finally, the Fourier transform of the weighting function, $\hat{U}(\mathbf{k})$, is calculated numerically.

The $\hat{U}(\mathbf{k})$ weighting function is originally defined over wavenumbers corresponding to the COMSOL lab-frame Cartesian coordinate system (Figure 3.9). An additional coordinate transformation is required to map the weighting function onto a radial/normal and binormal grid (relative to the background magnetic field). Then, the weighting function can be evaluated over the CGYRO numerical grid using methods outlined in Appendix C. The result of this procedure is a wavenumber-space weighting function, $\hat{U}(k_x, k_y)$, which can be applied at each timestep of a nonlinear CGYRO simulation. The resulting vector of $A_r(t)$

can be Fourier transformed in time to obtain a synthetic DBS frequency spectrum, $\hat{A}_r(\omega)$. Synthetic DBS frequency spectra using this COMSOL-CGYRO method are presented in Chapter 4.

3.8 Complicating effects in DBS

3.8.1 Effects related to DBS hardware

The description of the DIII-D Doppler back-scattering systems provided in Section 3.2 referenced the generation and propagation of a beam of electromagnetic radiation in the V-band (55-75 GHz). The quasi-optical elements featured in Figures 3.7 and 3.8 are intended to transport and focus the probing radiation into the plasma. In reality, quasi-optical elements may not perform perfectly, and may produce a beam that deviates from the ideal Gaussian expectation. However, laboratory measurements of the beam profiles do suggest the beams are Gaussian in nature [3]. Nevertheless, there will be uncertainty as to the initial conditions provided to ray/beam-tracing simulations which could impact the interpretation of measurements.

3.8.2 Other wave phenomena impacting DBS

The preceding description of wave physics related to DBS treated the background plasma in the 'cold' limit. The cold limit is applicable when velocities of interest (i.e. the phase velocity of the DBS wave) exceeds the plasma thermal velocity by a significant margin ($\omega/k \gg \overline{v}_s \equiv \sqrt{T_s/m_s}$). For perpendicular propagation in the electron cyclotron range of frequencies this condition is usually satisfied with two exceptions: (1) propagation near resonant layers ($k \to \infty$), and (2) very high temperature plasmas. We will discuss each below and its potential impact on DBS.

Proper description of wave propagation near resonance layers requires the use of the 'hot plasma' dispersion relation. In the limit of perpendicular propagation ($k_\parallel \to 0$) the

hot dispersion relationship factors into two orthogonal modes (O/X-mode) akin to the cold plasma limit (Equation 3.10). As discussed previously, kinetic treatment of both the X and O mode waves uncovers infinite resonances at integer harmonics of the electron cyclotron frequency. The X-mode also gains an additional longitudinal ($\mathbf{E} \parallel \mathbf{k}$), electrostatic ($\mathbf{E} = -\nabla\phi$) branch called Bernstein waves. In the frequency range relevant to DBS, these are electron Bernstein waves (EBWs). Critical layers for EBW modes exist at the upper hybrid frequency and $\omega = p\Omega_e$ ($p \in \mathbb{N}$) depending on ω and the magnitude of ω_{UHR}. For the situation in Figure 3.2 ($\omega_{LH} < \Omega_e < \omega_{UHR} < \omega_{RH} < \omega$) EBWs are completely cutoff from the low-field side of the tokamak. However, EBWs can propagate in certain regions between cyclotron harmonics, ω_{UHR}, and the cold-plasma X-mode cutoffs (ω_{LH} and ω_{RH}).

With respect to DBS measurements, the preceding discussion of EBWs serves to illustrate the potential for complicating effects near critical layers in the plasma. In the vicinity of critical layers it is possible for waves to tunnel and/or undergo mode conversion processes whereby the probing radiation may be ultimately absorbed by resonances. Absorption by the electron cyclotron resonance (or its 2nd harmonic) was discussed previously in Subsection 3.1.2. During experiments, one must verify that the DBS channels of interest are safe from absorption by cyclotron harmonics. However, one has less control over unintentional mode conversion and tunneling. Mode conversion and tunneling may occur where steep plasma gradients bring multiple critical layers in close spatial proximity. For example, in Figure 3.2 the right-hand X-mode cutoff appears in close spatial proximity to the upper hybrid resonance in the plasma edge. It is possible for wave energy to tunnel through the right-hand cutoff and spawn waves which are ultimately absorbed by resonances.

The other limit challenging the cold plasma approximation is for high temperature plasmas[13] where the electron kinetic energy can approach a non-negligible fraction of the electron rest mass energy. In this situation relativistic effects (and thermal effects) in the plasma may become important. Relativistic/thermal corrections to cold plasma waves in reflectometry

[13]Given $m_e \approx 511$ [keV/c^2], a plasma with $T_e = 10$ [keV] has electron thermal kinetic energy $\approx 1\%$ of the rest mass energy.

applications was treated by Mazzucato in [106] where a simple modification to the electron mass was found to be a good approximation at temperatures expected in burning plasmas,

$$m_e \to m_e \sqrt{1 + \frac{5T_e}{m_e c^2}}. \tag{3.57}$$

This correction can be applied to the cold plasma dielectric, Equation 3.8, allowing us to avoid numerically solving the full kinetic/relativistic dispersion relation. For the plasmas considered in this thesis, the correction in Equation 3.57 results in a $\lesssim 1\%$ modification of the frequency profiles shown in Figure 3.2. This supports using the cold plasma dielectric to model DBS in these plasmas.

3.8.3 Nonlinear scattering effects

The physics of electromagnetic wave scattering in plasmas was discussed previously in Subsection 3.1.3 where the problem was cast in terms of an expansion in the smallness of plasma fluctuations relative to the background (cf. Eq. 3.16). Normally one truncates the expansion at first order to form the (first) Born approximation. However, the approximation breaks down when the fluctuation amplitude becomes large enough to modify the background. This produces entrained fields and multiple scattering events. When we enter this regime, the outgoing electric field amplitude is no longer linearly related to the fluctuation amplitude, δn (and therefore the scattered power P_s is not proportional to δn^2).

The problem of linear vs. nonlinear diagnostic response has been treated extensively in the literature [107]. For DBS measurements authors typically use the nonlinearity parameter γ,

$$\gamma \equiv \left(\frac{\delta n}{n_0}\right)^2 \frac{G^2 \omega^2 x_c \ell_c}{c^2} \ln \frac{x_c}{\ell_c}, \tag{3.58}$$

derived using a WKB expansion of the electric field near the cutoff in a slab model [107]. In Equation 3.58, $\delta n/n_0$ is the normalized fluctuation amplitude, ω is the angular frequency of the probing wave, x_c is the radial distance between cutoff and the plasma boundary, ℓ_c is

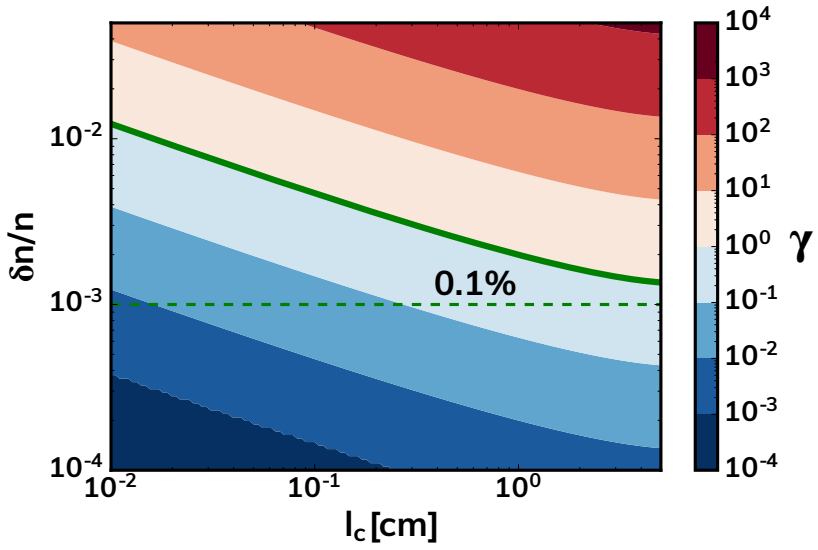

Figure 3.11: Contours of the nonlinearity parameter γ defined in eq. 3.58. We consider $\delta n/n_0 \in [0.5, 10^{-4}]$ and $\ell_c \in [10^{-2}, 5]$ cm. All other quantities in γ are evaluated for X-mode 72.5 GHz DBS using profiles at the midplane of discharge 189998, 3000 ms. The $\gamma = 1$ contour (green) separates the nonlinear and linear regimes. The $\delta n/n_0 = 0.1\%$ level is shown with a horizontal dashed line.

the radial correlation length of fluctuations, and G is a polarization-dependent term,

$$G = \begin{cases} 1 & \text{for O-mode} \\ \dfrac{(\omega^2 - 2\omega_p^2)(\omega^2 - \omega_c^2) + \omega_p^4}{(\omega^2 - \omega_p^2 - \omega_c^2)^2} & \text{for X-mode,} \end{cases} \tag{3.59}$$

related to the radial wavenumber dependence on the radial coordinate. The nonlinear regime theoretically exists for $\gamma \gtrsim 1$. Unfortunately, the γ parameter depends on difficult to measure, or simply inaccessible, quantities such as $\delta n/n_0$ and ℓ_c. To estimate γ for the experiment considered in Chapter 4, we create a large grid of reasonable ℓ_c and $\delta n/n_0$ values while evaluating all other terms at the plasma midplane.

Figure 3.11 illustrates contours of γ with log-scale colors. We denote the $\gamma = 1$ contour as the dividing line between linear and nonlinear. We draw a horizontal line for $\delta n/n_0 = 0.1\%$ which we take to be a reasonable estimate for *core* H-mode fluctuation amplitudes. With fixed $\delta n/n_0 = 0.1\%$, regardless of the radial correlation length we find $\gamma < 1$. At radial

correlation lengths, ℓ_c less than 1 mm we see that $\delta n/n_0$ can approach 1% and we remain in the linear regime. This result supports the conclusion that, for results presented in Chapter 4, we are operating in the linear response regime of the diagnostic.

Going beyond the γ parameter estimate, the linear/nonlinear diagnostic response can be addressed using 2D full-wave COMSOL simulations. In these COMSOL simulations we include a 'coherent' density fluctuation localized to the cutoff layer using the toy-model,

$$\frac{\delta n}{n}(\rho,\theta) = \left(\frac{\delta n}{n}\right)_0 \cos(m\theta) e^{-(\rho-\rho_c)^2/2(\Delta\rho)^2}, \tag{3.60}$$

wherein m is the poloidal mode number, $(\delta n/n)_0$ is the amplitude of the density perturbation relative to the background, ρ_c is the cutoff location, and $\Delta\rho$ sets the radial extent of the perturbation. The poloidal wavenumber is related to m through, $k_\theta = m(dl/d\theta)^{-1}$ where l is the arc-length of the flux surface in cm. To investigate the linear/nonlinear response we set k_θ to the 'matching' wavenumber to produce a 180° back-scattered wave. For the 7° launch-angle case shown in Figure 3.10, the matching wavenumber is $k_\theta = 6.4$ [rad/cm]. Centering the density perturbation around ρ_c and fixing $k_\theta = 6.4$ allows us to clearly identify the back-scattered component of the total **E** field as an outgoing wave to the right of the port (leaving the simulation domain, to be absorbed by the PML). If we were to select k_θ different from the matching value, the scattered field would not return along the incident trajectory; rather it would be scattered in another direction, complicating this analysis.

Figure 3.12 illustrates results of COMSOL simulations of linear/nonlinear scattering. In Figure 3.12(a) we overlay the full-wave E_y-field along with contours of the cutoff-localized, coherent $\delta n/n$ perturbation (Equation 3.60). In Figure 3.12(a) we also overlay the SCOTTY beam-tracing result in the background (unperturbed) plasma. This is the same beam-tracing result as Figure 3.10. Annotations in Figure 3.12(a) highlight the entrained E-field – a signature of nonlinear scattering – and the outgoing back-scattered wave leaving the domain to the right of the port.

Figure 3.12(b) shows the results of a scan of the perturbation amplitude, $(\delta n/n)_0$, in

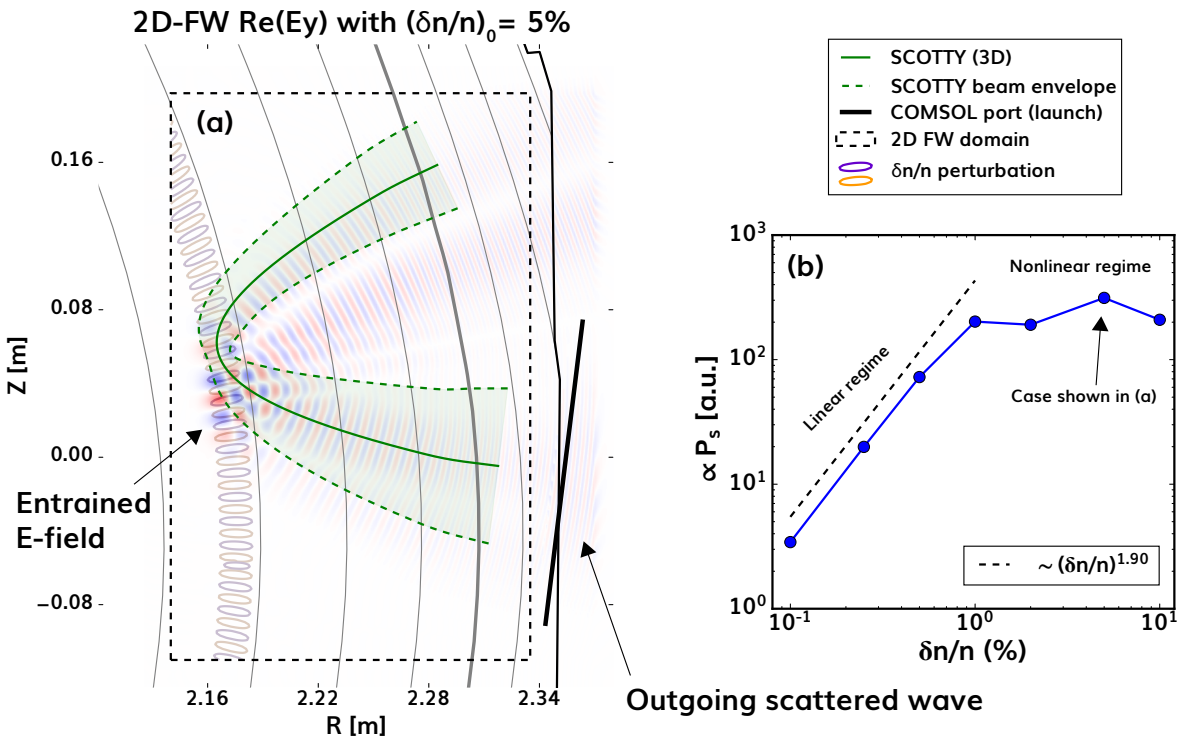

Figure 3.12: Nonlinear scattering simulation using full-wave 2D COMSOL.

Equation 3.60. Each point in Figure 3.12(b) corresponds to a different COMSOL 2D-FW simulation. For $(\delta n/n)_0 < 1\%$ the diagnostic response is linear with the power of the scattered wave following $P_s \propto (\delta n)^2$. However, for $(\delta n/n)_0 > 1\%$ the scattered power saturates and the diagnostic response is said to be nonlinear. The transition from linear to nonlinear scattering with increasing $(\delta n/n)_0$ is an expected result, and is fairly general. However, it is important to note that the particular point of saturation in Figure 3.12(b) depends on the background plasma, and on our toy-model for the density perturbation. We can compare the 1% saturation threshold with the γ calculation in shown in Figure 3.11. The 1% value derived from COMSOL simulations appears to be roughly consistent with a $\gamma \approx 10$ (for $\ell_c \approx 1$ [cm]; roughly the $\Delta\rho$ width of the perturbation). However, the radial correlation length of our toy-model δn perturbation is not strictly well-defined.

3.8.4 Potential issues with ray/beam tracing

The ray and beam-tracing methods, presented in Sections 3.4 and 3.5 respectively, are only formally applicable when the underlying assumptions about the separation of scales between the medium and the wave are satisfied. For example, in ray tracing we introduced the order parameter $\delta \equiv (Lk)^{-1} \ll 1$. When the wave approaches a cutoff ($k \to 0$), the $\delta \ll 1$ ordering is no longer satisfied and the ray tracing approximation for the wave field (formally) breaks down. This is a well understood problem in WKB theory.

Ray/beam tracing programs can integrate the ray equations near cutoff without issue *except* in situations where the change in k over space is extreme. For example, in low launch-angle cases, cutoffs cause a large change in the radial wavenumber, k_r, such that $\Delta k_r = 2k_r$ over a small spatial region. Numerical issues can arise wherein the program struggles to remain on the proper solution-trajectory through ray phase space (where the dispersion relationship must be locally satisfied). In these situations the ray/beam tracing solutions can become inaccurate. This effect can complicate the interpretation of DBS measurements. Despite a long history of ray tracing theory and simulation, addressing the issue of solutions near caustics remains an area of active research [108].

Beam tracing suffers from the same complications near cutoffs as ray tracing. Additionally, beam tracing relies on an additional ordering related to the transverse size of the beam, W, relative to the wavelength, λ. The $W > \lambda$ ordering can also be violated near cutoffs when 'beam pinching' drives $W < \lambda$. This particular effect has been the focus of validation efforts and remains an open area of research [109].

CHAPTER 4

Wavenumber spectrum investigation

In this chapter we present an investigation of the fluctuating density wavenumber spectrum, $\delta\hat{n}(k_\perp)$, in DIII-D ECH H-mode plasmas (H-modes with ECH as the only auxiliary heating source[1]). The ECH H-mode regime is relevant for studying plasmas with dominant electron-heating, low collisionality $\nu_{*e} < 1$ (Eq. 2.6), and zero injected torque. The former two characteristics are expected to be relevant for future burning plasmas where fusion-born alphas will predominantly heat electrons and high core temperatures provide low ν_*. Future fusion reactors are also expected to have reduced reliance on NBI, and are therefore expected to have low to zero *injected* torque (the extent to which *intrinsic* torque, especially in RF-heated plasmas, is able to produce non-negligible rotation is the subject of ongoing research [110, 111]). In larger machines with more dense plasmas, NBI systems will have less impact on rotation; applying a smaller normalized torque. The majority of the work presented in this chapter has been published in by the author in [7].

The ECH H-mode plasma scenario provides access to a regime expected to present significant TEM microturbulence activity. In plasmas with low ν_*, the trapped particle fraction is naturally larger and the electron and ion transport channels can become somewhat decoupled. With core electron heating via ECH, the plasma can theoretically obtain large ∇T_e, providing a drive for the collisionless TEM (and ETG modes at higher-$k_\perp\rho_s$). Transport phenomena such as density peaking and stiff electron thermal transport have been attributed to the prevalence of TEMs [112,113]. The extent to which these intermediate-high $k_\perp\rho_s$ modes such as TEM and ETGs contribute to transport in this scenario is studied (indirectly) with

[1]There is also Ohmic heating from the inductive current-drive which is not considered auxiliary in this context.

DBS measurements of intermediate-scale ($k_\perp \rho_s \approx 1$) density fluctuations.

The primary experimental result of this investigation is a unique dataset of Doppler back-scattering measurements from a scan of the probing launch-angle(s). The DBS data was analyzed to produce a well-resolved wavenumber spectrum of the back-scattered power, $P_s(k)$, shown in Figure 4.6. The wavenumber spectrum exhibits exponential spectral decay over the entire range of probed wavenumbers. Significant effort was directed toward leveraging the measured $P_s(k)$ to test models of plasma turbulence. Synthetic diagnostic modeling was used to relate $|\delta\hat{n}(k_\perp)|^2$ spectra from codes to the measured DBS $P_s(k)$. The resulting comparison between the synthetic $P_s^{\text{syn.}}(k)$ and the measured $P_s(k)$ shows mixed agreement (Figure 4.13). The synthetic diagnostic model is also used to interpret DBS measurements at the lowest and highest wavenumbers where diagnostic effects may impact the $P_s \propto |\delta n|^2$ proportionality.

Additional modeling using TGLF and linear/nonlinear CGYRO suggests that transport in these plasmas is dominated by ITG-scale modes ($k_\perp \rho_s < 1$). Using the transport solver TGYRO, TGLF is capable of reproducing the experimental heat flux levels across the plasma core. However, with small (+5%) increases in the temperature gradient inverse scale-length, a/L_{T_e}, TGLF predicts that TEMs begin to dominate the transport spectrum, driving a nonlinear increase in Q_e. TGLF predictions of the Q_e vs. a/L_{T_e} relationship and the electron particle flux spectrum do not agree with the higher-fidelity nonlinear gyrokinetics.

4.1 Experiment

Figure 4.1 illustrates the evolution of a typical ECH H-mode discharge from this study (DIII-D 189998). The plasma current and magnetic field are held constant at $I_p = 0.9$ MA, and $B_\phi = -1.8$ T (i.e. opposite the I_p direction). Figure 4.1(a) shows the line-averaged density, $\langle n \rangle \times 10^{19}$ m^{-3}, and the plasma current, I_p. Figure 4.1(b) shows the auxiliary heating P_{ECH}, and P_{NBI} in MW. Figure 4.1(c) shows the core electron and ion temperatures, T_e and T_i in keV. Figure 4.1(d) shows edge recombination light filtered to observe the Deuterium Balmer-

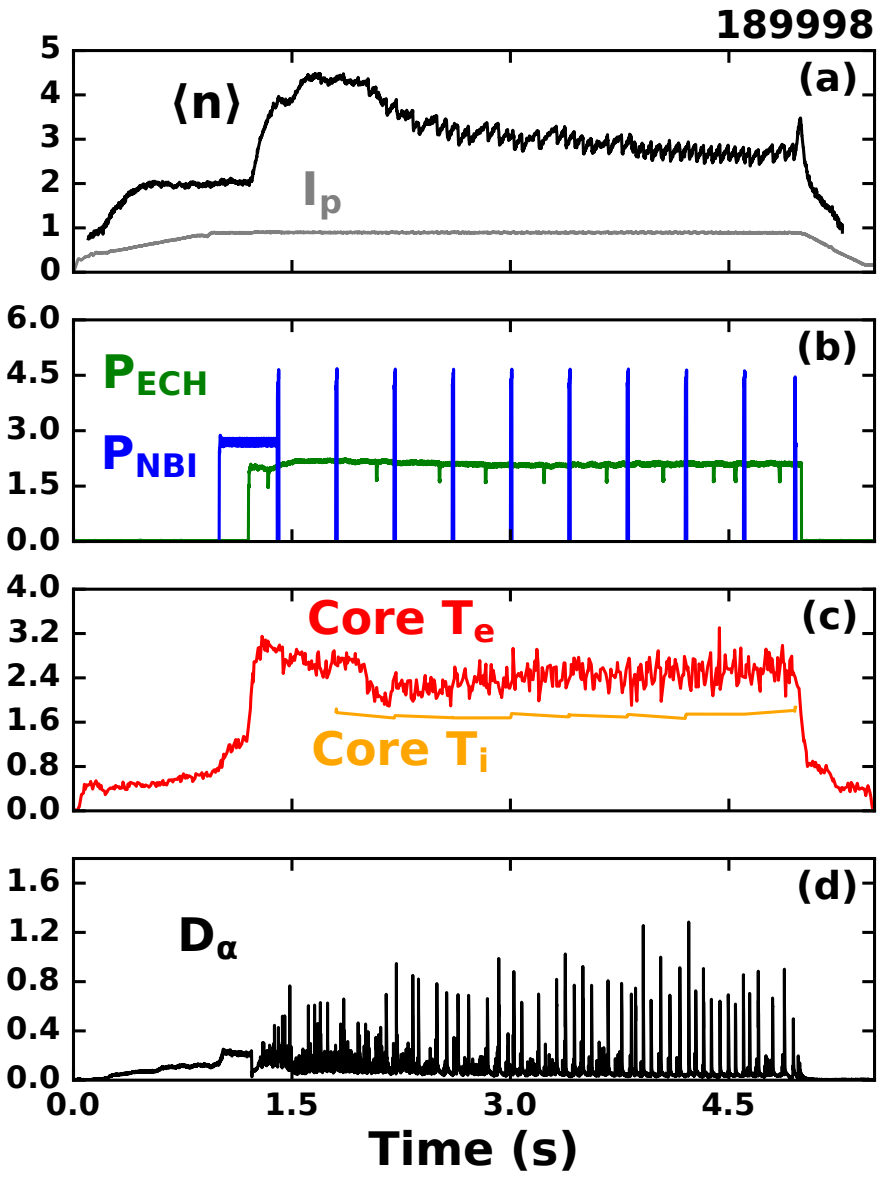

Figure 4.1: Evolution of DIII-D discharge 189998. 4.1(a) shows the line-averaged density ($\times 10^{13}$ cm^{-3}) and the plasma current in MA. 4.1(b) shows both the ECH and NBI heating in MW. 4.1(c) shows the core T_e and the core T_i in keV. 4.1(d) shows the D_α filterscope (a.u.).

α (D_α) atomic line (a.u.).

Once the I_p-flattop is established, 2.7 MW of NBI is used over 400 ms to assist the LH transition (see Figures 4.1(a,b)). This initial NBI pulse uses two sources in opposing (tangential) directions such that near zero torque is applied to the plasma. Halfway through

the NBI pulse, 2.1 MW of ECH was applied near the core of the plasma ($\rho_{\mathrm{ECH}} \sim 0.3$, see Figure 4.2(b)) and held constant for the remainder of the discharge. This sequence of external heating was used to trigger a reproducible H-mode transition while imparting near zero torque on the plasma. We were reliably able to sustain the H-mode with ECH as the only external heating source.

Neutral beam 'blips' were used to obtain data from beam-dependent diagnostics such as Motional Stark Effect (MSE) and Charge Exchange Recombination Spectroscopy (CER). MSE provides measurements of the internal magnetic pitch-angle which are used to constrain the equilibrium reconstruction [114]. CER provides measurements of the impurity (Carbon) temperature, density, and velocity [115]. The blip from a single NBI source lasts 10 ms. Each pulse visible in Figure 4.1(b) consists of two simultaneous blips (both are directed co-I_p). Blips are spaced 400 ms apart, resulting in only sparse data from both MSE and CER. The long inter-blip time minimizes the influence of heating, torque, and fast particles from NBI on the background plasma[2].

These discharges do not use gas feedback to control the line average density. The density rises to its maximum value after the LH transition. Then, over the next 400 ms, the density drops due to a combination of global ECH density pump-out, high ELM frequency, and the lack of a core particle-source from NBI. Global density pump-out is an effect where ECH increases the turbulence-drive, leading to increased transport [116]. The plasma finally enters a quasi-stationary phase with lower ELM frequency and a density of $\langle n \rangle \sim 2.8 \times 10^{19}$ m^{-3} around 2500 ms.

The ECH H-mode plasmas are diverted discharges in the lower-single-null (LSN) configuration with LCFS plasma elongation, $\kappa = 1.7$. The poloidal cross-section of the plasma and the fundamental frequencies relevant for DBS are shown in the previous chapter (Figures 3.9(a) and 3.2 respectively). The edge safety factor, $q_{95} \approx 6$, and the normalized plasma beta, $\beta_n \approx 0.9$, yield no significant MHD activity with $\beta_n \equiv \beta/(I_p/(B_{T0}a))$ where B_{T0} is

[2]Inter-blip time of 400 ms is $\approx 3 \times \tau_E$ (energy confinement time) and $\approx 3 \times \tau_s$ (beam slowing-down time, see Equation 5.9)

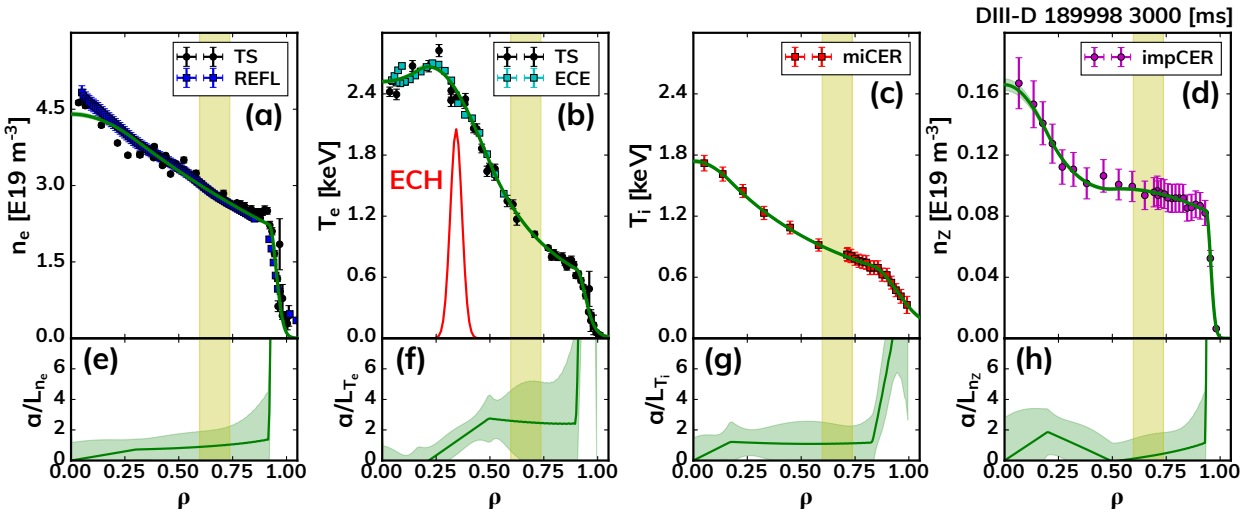

Figure 4.2: Radial profiles (a-d) of n_e, T_e, T_i, and n_Z and their normalized inverse gradient scale-lengths (e-h) for discharge 189998, 3000 ms. 4.2(a) shows the electron density with data from the Thomson scattering (TS) and profile reflectometry (REFL) diagnostics. 4.2(b) show the electron temperature profile with data from TS and electron-cyclotron emission (ECE). The deposition of ECH is also plotted in 4.2(b). 4.2(c) shows the main-ion temperature measured with main-ion charge exchange recombination spectroscopy (miCER). 4.2(d) shows the carbon density, n_Z, measured by impurity-CER (impCER). 4.2(e-h) provide profiles of the inverse gradient scale-lengths normalized with respect to the separatrix minor radius, a. In frames (a-d) the solid green lines are fits to the data. In all frames the shaded vertical band indicates the radial region of interest.

the on-axis toroidal magnetic field and a is the midplane minor radius of the LCFS. The normalized confinement factor $H_{98,y2} \approx 1$, indicating the plasma energy confinement time (τ_E) is in accordance with the ITER multi-machine H-mode confinement regression [21], with $H_{98,y2} \equiv \tau_E/\tau_{E,\mathrm{IPB98}(y,2)}$ (see Equation 2.8).

Figure 4.2 shows an array of representative kinetic profiles and their inverse gradient scale-lengths, $a/L_X \equiv -(a/X)\nabla X$. Data from the DIII-D Thomson scattering (TS) system and the Profile Reflectometry system (Refl.) [117] are used in combination as inputs to an n_e profile fit (Fig. 4.2a). Similarly, the electron-cyclotron emission (ECE) diagnostic [118] is used in combination with TS to fit T_e (Fig. 4.2b). Impurity-CER (impCER) provides measurements of the Carbon impurity density, temperature, and toroidal/poloidal velocity in the plasma (Fig. 4.2d) while main-ion CER (miCER) measures the main-ion (Deuterium) T_i

profile (Fig. 4.2c) [115]. The effective ion charge-state of the plasma, $Z_{\text{eff}} \equiv \sum_i n_i Z_i^2/n_e \approx 2$. Profile fits are performed using the OMFITprofiles module [119]. The uncertainties in the fits are calculated with linear error propagation theory, accounting for the correlation between fit-model parameters.

The n_e profile (Fig. 4.2(a)) appears roughly linear over the core region with a value of $a/L_{n_e} \approx 1$ over the radial regime of interest ($\rho \approx 0.7$). The density peaking factor, $(n_e|_{\rho=0.4})/(n_e|_{\rho=0.8}) \approx 1.4$. By contrast, core ECH produces a peaked T_e profile (Fig. 4.2(b)) with a relatively large value of $a/L_{T_e} \approx 2.5$ (at $\rho \approx 0.7$). The T_e profile also exhibits off-axis peaking with a negative gradient in the deep core ($\rho < 0.2$). This is attributed to the possible existence of a transport barrier near the $q = 1$ surface has been observed in other experiments with near-core ECH [120, 121]. The existence of hollow T_e profiles with near-axis ECH can also be interpreted as a signature of fractional transport [122]. The gradient-ratio defined as, $\eta_s \equiv L_{n_s}/L_{T_s} = (n_s \nabla T_s)/(T_s \nabla n_s)$, has a value $\eta_e \approx 2.5$ in the radial regime of interest. The maximum $T_e/T_i = 2.0$ at $\rho = 0.33$ and $T_e/T_i > 1$ everywhere inside the pedestal-top. Due to high electron-heating and relatively low line-averaged density, the plasma achieves very low electron collisionality. In the core $\nu_e^* < 0.1$, while the pedestal has $\nu_{*e} < 1$. Recall, $\nu_{*e} \equiv \nu_{i,e}(qR\bar{v}_e^{-1}\epsilon^{-3/2})$, where ν_{ie} is the electron-ion collision frequency, q is the safety factor, $\bar{v}_e$ is the electron thermal velocity, $\epsilon \equiv r/R$ is the inverse aspect ratio, and R is the flux surface major radius. In terms of kinetic quantities, $\nu_e^* \propto n_e T_e^{-2}$. The dimensionless quantities ν_{*e}, η_e, and T_e/T_i appear in tokamak/plasma theory (see Sections 2.2 and 2.5). Without NBI, the main ions are heated by collisions with electrons. The electron-ion heat source is largest in the core (where T_e and T_i differ the most) and extends to the pedestal-top.

4.2 DBS measurements

Both the DBS60 and DBS240 systems were used to perform a scan of the measured wavenumber by systematically changing the launch-angle(s) of the probing beam. Recall that the 60

and 240 suffixes refers to the toroidal locations of the DBS systems[3]. Importantly, the DBS240 system has the ability to steer the probe beam both toroidally and poloidally [3]. The toroidal steering capability of the DBS240 system allows us to match the magnetic pitch-angle and avoid mismatch attenuation at higher-k [5] (discussed previously in Subsection 3.1.4). The DBS60 system has a fixed toroidal launch-angle of 0° making it most suitable for lower-k measurements.

The launch-angles of both DBS systems remain constant during a plasma discharge. Therefore, we repeat discharges to scan the launch-angles (and therefore the measured wavenumber). For the wavenumber scan presented here, we repeated the same ECH H-mode discharge a total of six times: 189993, 189994, 189997, 189998, 190129, 190315. All repeats are in good agreement during the time period of interest ($t > 2500$ ms) with the exception of 190129 which exhibited larger excursions in line-averaged density and back-transitioned to L-mode before the I_p ramp-down. Data from each discharge and DBS system can be analyzed using spectral methods outlined in Section 3.3. Figure 4.3 provides a macroscopic view of DBS data from the wavenumber scan in the form of multiple spectrograms with log-scaled colors. Regions of higher spectral power are indicated with yellow/orange and regions of lower spectral power are shown in purple/black. The spectrograms are arranged from top-to-bottom in order of increasing probed-k. Ray tracing simulations to determine the probed-k are discussed later in this section.

Close inspection of Figure 4.3 shows that as probed-k increases, the peak in the spectrum becomes increasingly Doppler-shifted to more negative frequencies and its amplitude decreases. For this plasma, negative Doppler shift indicates lab-frame motion in the ion diamagnetic drift direction. In the bottom plot of Figure 4.3 (highest k) the Doppler-shifted signal is reduced to a faint signal with $f_{\text{Dopp.}} \approx -1$ MHz. This increase in the observed Doppler shift is expected as the Doppler shift is proportional to the measured wavenumber, i.e. in general $\omega_{\text{Dopp.}} = \mathbf{k_{meas.}} \cdot \mathbf{v}$. The decrease in spectral power is also expected assuming fluctuations decrease in amplitude at smaller scales following e.g. $|\delta n| \sim k^{-\nu}$. Transient events

[3]The toroidal locations of the DBS systems are irrelevant other than as a label.

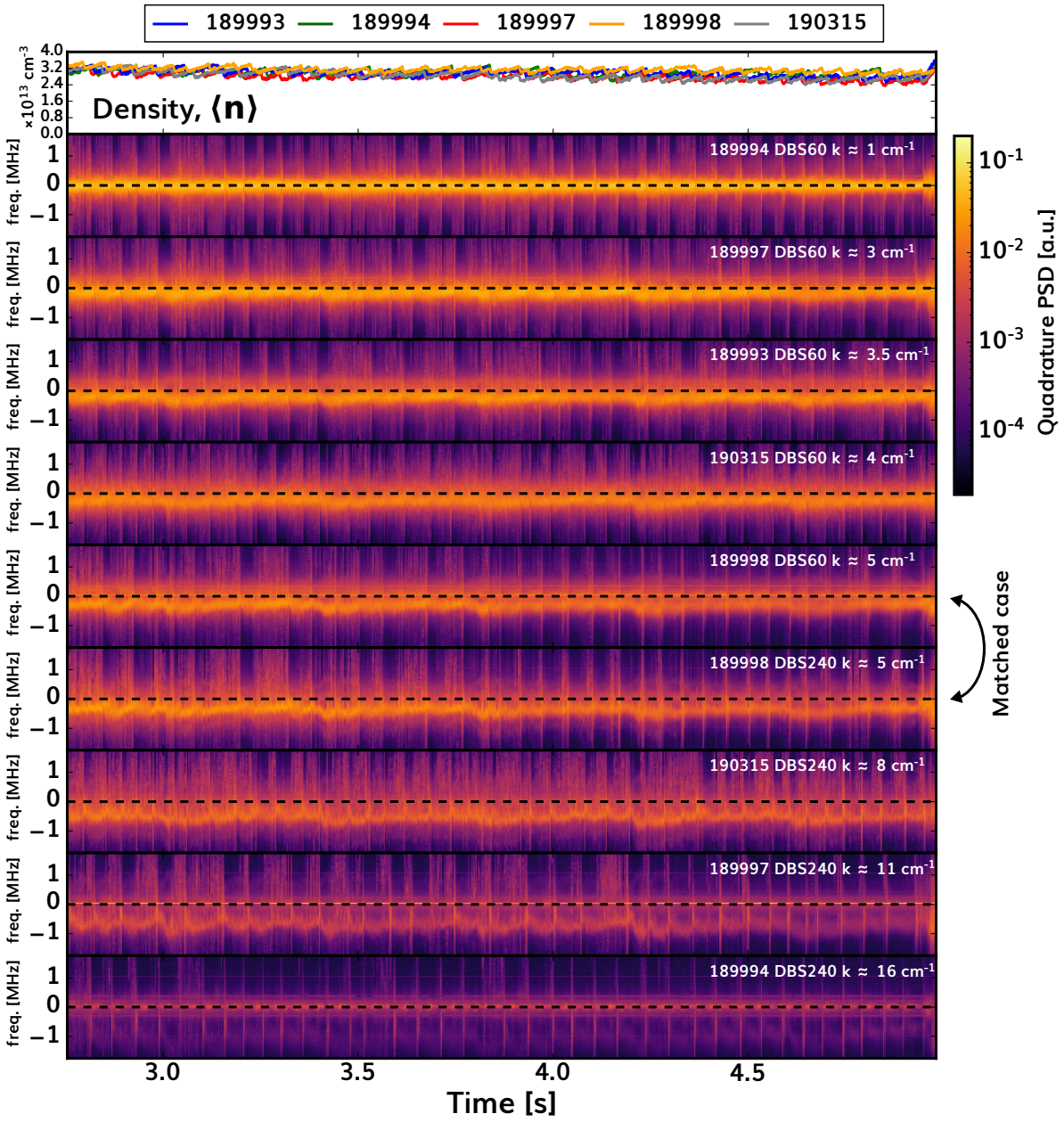

Figure 4.3: Wavenumber scan DBS spectrograms covering multiple discharges including data both DBS systems. All spectrograms correspond to the 72.5 GHz channel and cover the same time ($2800 < t < 4800$ ms) for each discharge. The top plot shows the line average density for each discharge. The lower 9 plots show spectrograms annotated with their discharge number, DBS system, and approximate probed-k. All spectrograms use the same log-scaled colors. Data from discharge 189998 is labeled 'matched case' (where both DBS systems targeted the same wavenumber). Data from discharge 190129 is not shown in this figure because it is only a satisfactory match over a shorter time interval. Data from the DBS240 system for discharge 189993 is not shown for clarity (launch angles were similar to discharge 189998).

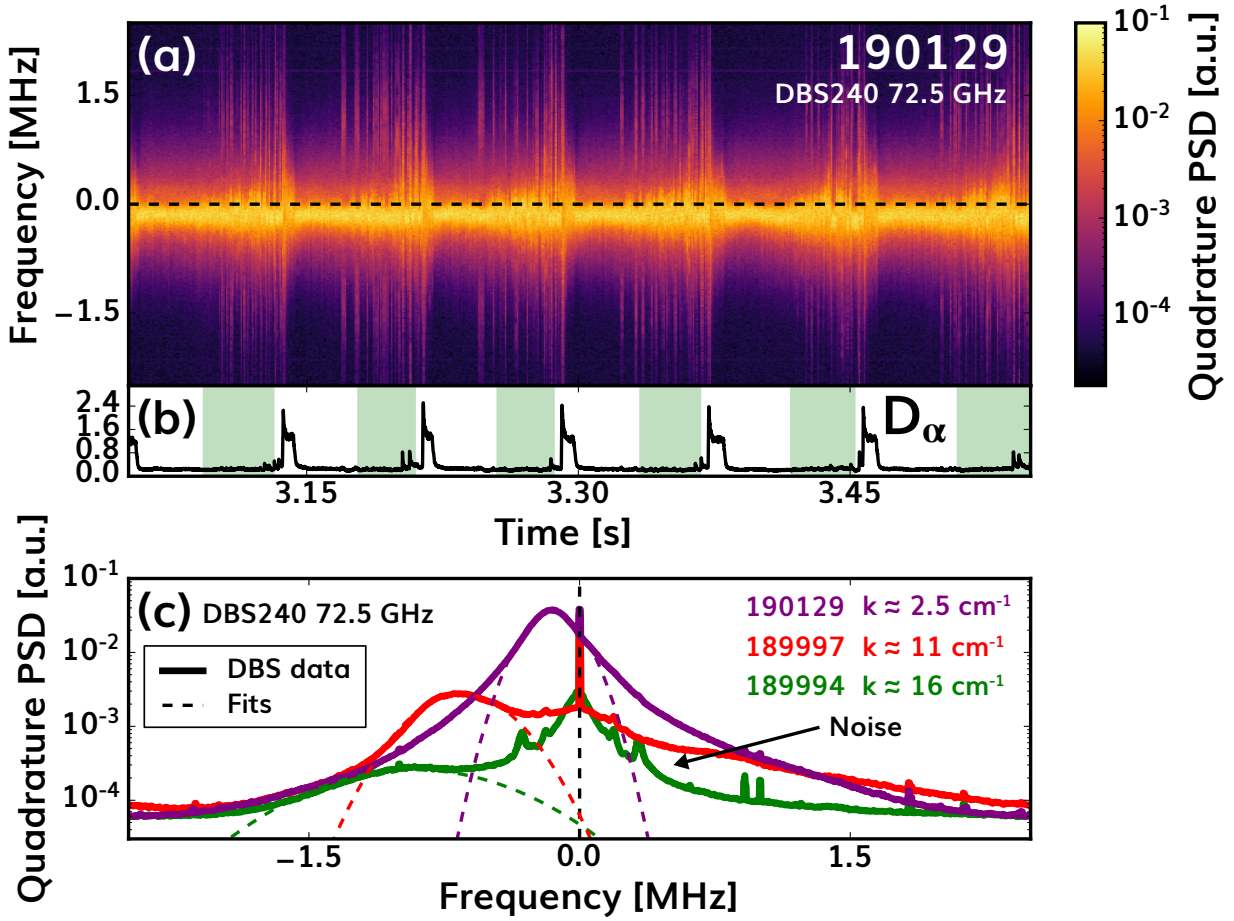

Figure 4.4: 4.4(a) DBS spectrogram for the 72.5 GHz channel of the DBS240 system for discharge 190129. 4.4(b) shows the time-synchronized D_α filterscope signal. The shaded spans in (b) represent the 50%-95% ELM-phase regions which are considered free from the influence of the preceding ELM and used for further DBS analysis. Several small signals are visible in the D_α trace which were below the threshold used for ELM detection. 4.4(c) shows time-averaged spectrograms for three discharges: 190129 ($k_{\text{meas.}} \approx 2.5$ cm^{-1}), 189997 ($k_{\text{meas.}} \approx 11$ cm^{-1}), and 189994 ($k_{\text{meas.}} \approx 16$ cm^{-1}). Negative frequency in 4.4(a,c) indicates lab-frame motion in the ion diamagnetic drift direction.

are also visible in the spectrograms shown in Figure 4.3. Semi-periodic, large-amplitude broadband events correspond to ELMs. Intermittent, low-amplitude broadband events often preceding ELMs may be ELM-related precursor modes or other intermittent phenomena.

For more detailed analysis, DBS data from each discharge and DBS system are divided into multiple (generally 3-4) 150 ms windows centered 300 ms after NBI blips. These time

windows were selected to minimize the influence of NBI. Following methods in Section 3.3, we determine the back-scattered power by integrating the Doppler-shifted component in the frequency spectrum. Figure 4.4(a) provides a spectrogram from discharge 190129 over a 500 ms time interval where a good match was obtained with the other discharges. Beyond minimizing the influence of NBI blips with our choice of time windows, we also remove the influence of ELMs on the DBS scattered-power calculation by performing an ELM phase-synchronized analysis. Every 150 ms window of DBS data is synchronized to the corresponding D_α filterscope signal (see Figure 4.4(b)). We retain time-slices of each spectrogram corresponding to 50 - 95% ELM-phase only. These time-slices are shown as shaded regions in Figure 4.4(b). The ELM-filtering process reduces the total number of spectrogram time-slices by approximately 50%. The remaining 'valid', i.e. not influenced by ELMs, time-slices are analyzed to identify the Doppler-shifted component and its spectral power.

Figure 4.4(c) over-plots three time-averaged spectrograms from discharges 190129, 189997, and 189994. Similar to Figure 4.3, Figure 4.4(c) shows increasingly negative Doppler shift and decreasing spectral power as we increase the probed-k. Figure 4.4(c) also shows Gaussian fits to the Doppler-shifted component in each spectrum (dashed lines). The Gaussian lineshape was selected because it performed consistently-well across a broad range of a spectral powers and Doppler shifts. Due to the logarithmic scale of Figure 4.4(c), the fits appear very poor in capturing the overall spectrum. However, the fits are sufficient in capturing the spectral power near the Doppler shifted peak (the primary quantity for this investigation). Additional spectral components are also visible in Figure 4.4(c): narrow and broadband features centered around $f = 0$ and low amplitude narrow 'spikes' at other frequencies. The narrow spikes at $f \neq 0$ are visible in multiple discharges appearing at the same frequency – they are attributed to electronic noise and ignored. The narrow and broadband spectral components centered at zero are also common in DBS data. These components with $f = 0$ are often attributed to scattering away from the cutoff location and are considered noise relative to the Doppler shifted component. Where necessary, the Doppler shifted component is isolated by applying a high-pass notch filter to remove spectral power near zero frequency

before fitting.

All DBS data presented in this chapter is from the same frequency (72.5 GHz) channel of each multi-channel system. Using a single channel allows us to avoid cross-*channel* calibrations and more directly compare data between discharges. To build a cohesive wavenumber spectrum by combining measurements from both DBS systems, one discharge (189998) was used to determine a suitable cross-*system* calibration factor by targeting the same wavenumber. This is done by determining launch angles for each system such that $k_{\text{meas.}}^{\text{DBS60}} = k_{\text{meas.}}^{\text{DBS240}}$. Then, because they are theoretically measuring the same fluctuations, a calibration factor, $C = P_s^{\text{DBS60}}/P_s^{\text{DBS240}}$, is determined. To validate this technique, we used another discharge (190129) to match the probed wavenumber of both systems to a different value and verified C was constant.

The polarization (X-mode) was also held fixed for all wavenumber scan discharges. Using consistent polarization also makes for a simpler comparison across discharges. The subtleties of combining O/X-mode wavenumber scan data was explored extensively by Happel *et al.* in [78] with related modeling by Lechte *et al.* in [77]. Following methods in Section 3.4, 3D ray tracing simulations are used determine the measured wavenumber, $k_{\text{meas.}}$, for each 150 ms window of DBS data (generally 3-4 windows per discharge). Figure 4.5 illustrates the ray tracing results for the wavenumber scan. Figure 4.5(a) provides an annotated poloidal cross section of the plasma with a subset of the ray trajectories from the wavenumber scan. Notably, we show the lowest probed wavenumber and the highest probed wavenumber along with the matched-wavenumber case used for cross-system calibration. The cross-system cases can also be seen in Figure 4.5(c) as overlapping square/circle symbols for discharges 189998 and 190129.

Figures 4.5(a,c) show the tendency of higher launch angles to probe larger radii. This is an expected effect due to refraction and increasingly oblique incidence relative to the X-mode cutoff. This effect broadens distribution of probed-ρ locations despite constant launch frequency (72.5 GHz). Furthermore, small variations in the density profile across discharges and over time within any one discharge, also broadens the probed-ρ. Figure 4.5(d) shows a

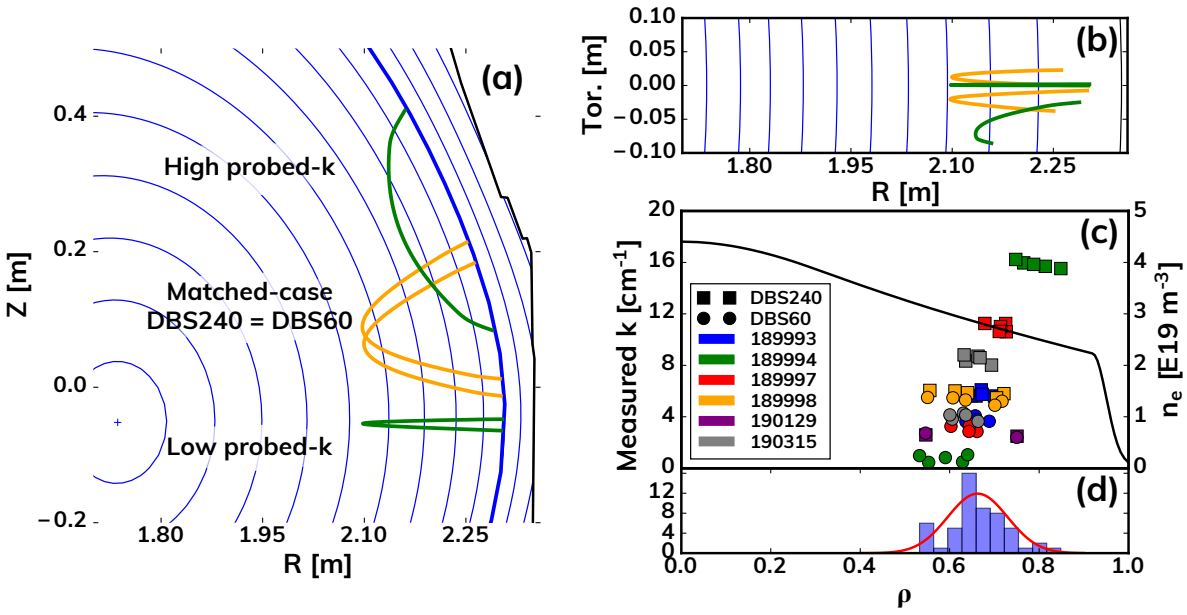

Figure 4.5: Ray tracing results illustrating the DBS launch-angle scan. 4.5(a) shows a poloidal projection of the 3D ray trajectories for a subset of the scan. The equilibrium plotted in 4.5(a) is from discharge 189998, 3000 ms. 4.5(b) shows a top-down projection of the ray trajectories in 4.5(a). The y-axis of (b) indicates propagation in the toroidal (tor.) direction. 4.5(c) plots all probed wavenumbers and radial locations for the entire dataset. The density profile from 189998, 3000 ms is provided against the right-hand axis for reference. 4.5(d) shows a histogram of the probed-locations along with a Gaussian approximation with average and standard deviation, $\rho \sim 0.67 \pm 0.07$.

histogram of the probed ρ locations for the entire wavenumber-scan dataset. The mean and standard deviation of the probed radial locations are $\rho \sim 0.67 \pm 0.07$. The mean probed location is used later for more extensive analysis. The $\rho = 0.67 \pm 0.07$ radial span corresponds to the vertical shaded region shown previously in Figure 4.2. As per Figures 4.2(e-h), the inverse gradient scale-lengths do not vary significantly over this regime ($< 5\%$ variation relative to the value at $\rho = 0.67$). Therefore, we do not expect significant changes in the microturbulence over the probed DBS locations.

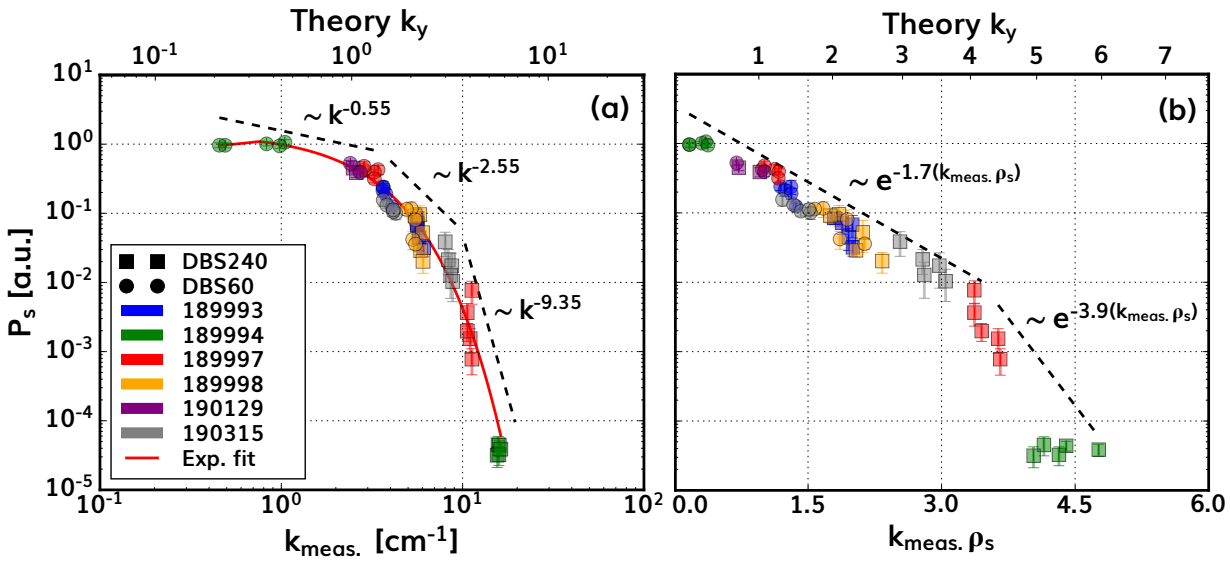

Figure 4.6: Back-scattered power wavenumber spectrum. The DBS data follows the same marker/color scheme as Figure 4.5(c). In (a), black dashed lines represent linear (in log-log) fits with each spectral index provided by annotations. The linear fits, which normally pass through the data points, have been displaced to make them visible. The red line is the result of a nonlinear fit using the exponential function in Equation 4.1. Note the secondary x-axis above the plot providing a mapping between the real-space $k_{\text{meas.}}$, and the normalized k_y. In (b) the same data is plotted against a linear $k_{\text{meas.}}\rho_s$ axis. In (b) the linear fits, in semilogx space, are shown with black dashed lines and are displaced from data to make them more visible.

4.3 DBS results

The primary experimental result is the back-scattered power wavenumber spectrum, $P_s(k_{\text{meas.}})$ shown in Figure 4.6. The reported P_s values are obtained directly from measurements and therefore include any/all instrumental effects[4]. We observe a spectrum with variable spectral decay: for lower wavenumbers ($k < 3.5$ cm^{-1}) the spectrum is nearly flat with $P_s \sim k^{-0.6}$, for intermediate wavenumbers ($3.5 < k < 8.5$ cm^{-1}) the spectrum decays with $P_s \sim k^{-2.6}$, and for high wavenumbers ($k > 8.5$ cm^{-1}) we observe steep decay with $P_s \sim k^{-9.4}$. The variable slope in our $P_s(k_{\text{meas.}})$ spectrum motivated a nonlinear fit using a generalized exponential

[4]No 'corrections' have been applied to the reported P_s values other than a single cross-system calibration factor discussed previously.

function,

$$P_s(k) = \exp\left(-\left|\frac{k-b}{c}\right|^d\right). \tag{4.1}$$

The optimal $P_s(k_{\text{meas.}})$ fit has parameters: $b = 0.8$ [cm^{-1}], $c = 1.9$ [cm^{-1}], and $d = 1.1$. Interestingly, the proximity of d to 1.0 implies an almost purely exponential scattered-power spectrum. The implications of an exponential spectrum were discussed previously in the context of the frequency spectrum in Subsection 3.1.6 and will be discussed further in Section 4.5. The DBS data in Figure 4.6(a) is also re-plotted against $k_{\text{meas.}}\rho_s$ in Figure 4.6(b) using a linear x-axis. To normalize the $k_{\text{meas.}}$ wavenumber by the experimental ion-sound gyroradius, $\rho_s \equiv c_s/\Omega_D$, we use the local ρ_s value corresponding to each cutoff location. The overall $k_{\text{meas.}}\rho_s$ vs. $k_{\text{meas.}}$ trend, including radial variation in ρ_s, is $k_{\text{meas.}}\rho_s \approx 0.45(k_{\text{meas.}}/1[\text{cm}])^{0.84}$, not thought to be a general result. In Figure 4.6(b) we also observe variable decay. For $k_{\text{meas.}}\rho_s < 3.5$ the spectrum decays exponentially with $\zeta \approx 1.7$ ($\zeta : P_s \sim e^{-\zeta(k_{\text{meas.}}\rho_s)}$). For $k_{\text{meas.}}\rho_s > 3.5$ the spectrum decays with $\zeta \approx 3.9$.

The secondary x-axis above Figure 4.6(a) (also used in later figures) shows the mapping between $k_{\text{meas.}}$ and the theoretical, dimensionless k_y value discussed in Appendix C. Equation C.16(b) is used to calculate k_y given the measured binormal wavenumber, $k_b = k_{\text{meas.}}$. The plasma parameters in Eq. C.16(b) (κ, q, etc.) are evaluated using local quantities for each data point in Figure 4.6. Thus, this mapping includes the radial variation of κ, q, etc. over the entire DBS dataset. The overall k_y vs. $k_{\text{meas.}}$ trend for this plasma and dataset was found to follow $k_y \approx 0.44(k_{\text{meas.}}/1[\text{cm}])^{0.92}$, not thought to be a general result. Purely by coincidence, when the trends for k_y and $k_{\text{meas.}}\rho_s$ are combined, we find $k_y \approx 1.1(k_{\text{meas.}}\rho_s)^{1.1}$. Given that the exponent and the scale factor relating k_y and $k_{\text{meas.}}\rho_s$ are close to unity, the upper k_y axes on Figure 4.6, and subsequent figures, can *roughly* be used as $k_{\text{meas.}}\rho_s$. It is important to note that generally $k_{\text{meas.}}\rho_s \neq k_y$.

The experimental $P_s(k_{\text{meas.}})$ values shown in Figure 4.6 are expected to be proportional to the square magnitude of the density fluctuation wavenumber spectrum, $P_s \propto |\delta n|^2$. However, DBS instrumental effects may alter the $P_s \propto |\delta n|^2$ proportionality and affect our interpretation of the measurements and our intention to use the measurements in Figure 4.6 to

test simulations of plasma turbulence. Therefore, additional forward/inverse synthetic diagnostic modeling (introduced in Section 3.7) is presented next. All detailed analysis in the following subsections uses profiles and the magnetic equilibrium from a single, representative discharge/time: DIII-D 189998, 3000 ms.

4.4 Modeling results

4.4.1 Turbulence simulations

TGLF, linear and nonlinear CGYRO simulations were performed for the representative discharge/time (DIII-D 189998, 3000 ms). The inputs to both TGLF and CGYRO were produced from a set of plasma profiles and a corresponding kinetic equilibrium. The plasma profiles are fits to the experimental data shown previously in Figure 4.2. The kinetic equilibrium contains the bootstrap contribution to the current density and self-consistent profile/flux-surface alignment. As part of the kinetic-EFIT process, the TRANSP code was run to evolve the plasma current density and perform power-balance calculations[5].

Eigenvalue spectrum

TGLF and linear CGYRO calculate the eigenvalue spectrum $(\omega, \gamma)_{k_y}$ at the nominal DBS location ($\rho = 0.67$). The SAT2 saturation rule is used for all TGLF modeling results presented here unless otherwise noted. The linear CGYRO eigenvalue spectrum is calculated by performing a series of single-k_y simulations covering the same grid of k_y wavenumbers as the default TGLF wavenumber grid for SAT2 (`KYGRID_MODEL=4`). The eigenvalue spectrum from each code are compared in Figure 4.7. We find reasonable agreement between the two codes with respect to $(\omega, \gamma)_{k_y}$. Both codes agree that for $k_y < 0.7$, modes propagate in the ion-drift direction with growth rates, $\gamma < 0.1[c_s/a]$ with the exception of one TEM-type mode at $k_y \approx 0.3$ predicted by TGLF. For $k_y > 0.7$ modes propagate in the electron-drift direction

[5]Recall that NBI is not used for heating nor current drive in these ECH H-mode plasmas. Furthermore, the ECH was aimed for perpendicular incidence (no current drive).

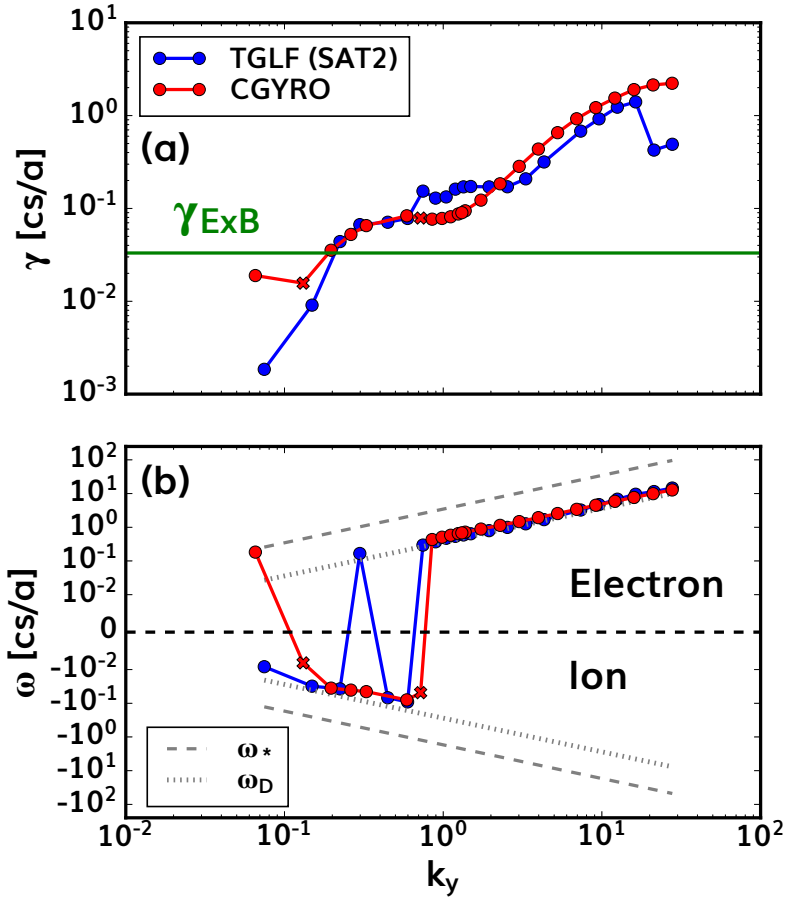

Figure 4.7: Comparison of linear eigenvalue spectra calculated by TGLF and CGYRO. Both TGLF and CGYRO are run at $\rho = 0.67$ using identical inputs from discharge 189998, 3000 ms. The 'x' markers on the CGYRO line indicate cases where long-lived ($> 300\ a/c_s$), weak oscillations prevented complete convergence. Figure 4.7(a) shows the growth rates along with the local $E \times B$ shear. Figure 4.7(b) shows the real frequency of the modes. The dashed and dotted lines in (b) correspond to the drift frequencies given in Equation 3.35.

with increasing γ. The intermediate-scale region ($0.5 \leq k_y \leq 2$), just above the transition from the ion-direction to the electron-direction, is also where the TGLF and CGYRO disagree the most in terms of γ (TGLF is $\approx 2\times$ CGYRO there). Figure 4.7(b) also shows the normalized drift frequencies defined in Equation 3.35 as dashed/dotted lines. The calculated $\omega(k_y)$ at nearly every k_y tracks the magnetic drift frequency, $\omega_{D,s}$, consistent with curvature-driven drift wave instabilities. Finally, it should be noted that the first *subdominant* mode calculated by TGLF (not shown) is a TEM-type mode for $k_y < 0.7$. The growth rates of

the first subdominant mode, for $k_y < 0.7$, are close in magnitude to the dominant ITG-type modes shown in Figure 4.7(a). This explains the single TEM mode at $k_y \approx 0.3$ predicted by TGLF.

Tests of the quasi-linear approximation

In order to perform the forward modeling of DBS measurements, we require a model for the density fluctuation spectrum, $\delta\hat{n}(k_n, k_b)$. Theoretically, the density spectrum can be approximated in a quasi-linear fashion using methods outlined in Subsection 2.4.1. The final expression for the density spectrum (Equation 2.29) combines the quasi-linear weights for the density field, $\mathrm{W}n^{\mathrm{QL}}_{e,k_y}$ (Equation 2.28), with the TGLF model for the nonlinear, saturated potential spectrum, $\delta\hat{\phi}(k_x, k_y)$ (Equation 2.27).

The following results are presented to test the TGLF quasi-linear approximation for the density field in this case. The quasi-linear weights for the density field, $\mathrm{W}n^{\mathrm{QL}}_{e,k_y}$ (Equation 2.28), are a linear quantity and can therefore also be calculated with linear CGYRO. Both the TGLF and linear CGYRO weights can also be compared with the *nonlinear* CGYRO weight for the density field, i.e. Equation 2.28 evaluated with nonlinear quantities[6]. If the quasi-linear approximation is correct, all three values would agree, indicating the linear ratio of density to potential fluctuations is preserved in the nonlinear saturated state. Recall that in calculating the TGLF $\mathrm{W}n^{\mathrm{QL}}_{e,k_y}$ weight, only the dominant unstable mode is used at each k_y.

For an additional test of the TGLF quasi-linear assumption, we can compare the cross-phase between fluctuating fields. In this case we compare the cross-phase between the fluctuating density and temperature fields calculated by TGLF, linear CGYRO, and nonlinear

[6]The quasilinear weight in Equation 2.28 includes a flux-surface average. For the large nonlinear simulation shown in this section (discussed in Appendix C) results are output only at $\theta = 0$. Thus, there is no flux-surface average for the nonlinear quantities.

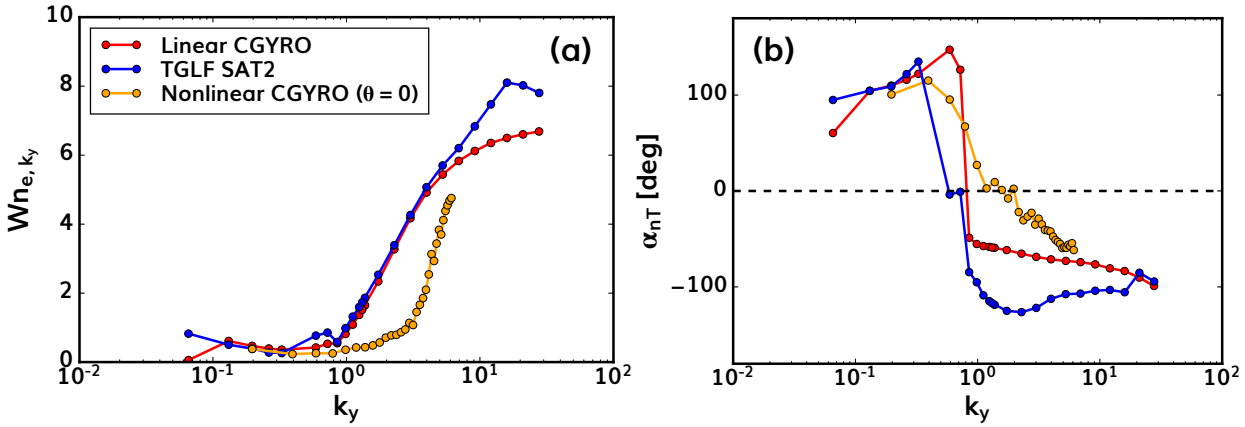

Figure 4.8: Comparison of two values relevant for quasilinear theory. In (a) we show a comparison of QL-weight for the density field, $\mathrm{W}n^{\mathrm{QL}}_{e,k_y}$ between TGLF-SAT2 and linear CGYRO. In (a) we also show the nonlinear weight calculated from a nonlinear CGYRO simulation. In (b) we show the cross-phase between the δn and δT fields.

CGYRO. The $\delta n_e, \delta T_e$ cross-phase, $\alpha_{n_e T_e}$ is defined as,

$$\alpha_{n_e T_e} = \left\langle \frac{\arg[\delta n_e^* \delta T_e]}{|\delta n_e||\delta T_e|} \right\rangle_{t,\theta}, \tag{4.2}$$

where arg denotes the argument (angle) of the complex number and the subscript θ indicates a flux-surface average. The fluctuating temperature field is calculated from CGYRO as, $\delta T_e = \frac{2}{3}\delta E_e - \delta n_e$, where δE_e is the fluctuating energy (pressure) moment of the distribution function. If the quasi-linear approximation is correct, the nonlinear/linear CGYRO and TGLF values would agree, indicating the linear cross-phase between fields is preserved in the nonlinear saturated state.

Figure 4.8 provides the results of a three-way comparison between TGLF, linear CGYRO, and nonlinear CGYRO. Figure 4.8(a) provides a comparison of the $\mathrm{W}n^{\mathrm{QL}}_{e,k_y}$ density weights. We observe very good agreement between TGLF and linear CGYRO over a broad range of k_y. This verifies the TGLF calculation of the linear ratio between δn_e and $\delta\phi$. Also in Figure 4.8(a), the nonlinear weight for the density field calculated by nonlinear CGYRO appears to agree with the linear values for $k_y \leq 1$. However, in the range of $k_y \in [2, 4]$ the nonlinear density weight is significantly lower than the linear results. Therefore, in range $2 \leq k_y \leq 4$

we might expect the quasi-linear approximation to be less accurate for this case.

Figure 4.8(b) provides the results of the $\delta n_e, \delta T_e$ cross-phase comparison. The TGLF and linear CGYRO values agree over the ion-scale ($k_y \leq 0.3$), at the ion/electron transition ($k_y \approx 0.7$), and at the highest $k_y \geq 10$. When comparing the linear and nonlinear CGYRO cross-phase calculations we observe approximate agreement at the lowest $k_y \leq 0.7$ and the highest $k_y \approx 6$. In general the nonlinear cross-phase appears 'smoothed' over the entire range of k_y, i.e. there is no sharp transition between electron and ion scales as observed in the linear calculations; this is likely due to nonlinear mode coupling. Similar to the comparison in Figure 4.8(a), the nonlinear cross-phase does not agree with the linear values over the range $1 \leq k_y \leq 4$. Therefore, in range $1 \leq k_y \leq 4$ we might expect the quasi-linear approximation to be less accurate for this case.

Density and potential spectra

Somewhat independent of the previous comparison of the cross-phase and weights, the TGLF model for the saturated potential spectrum, $\delta\hat{\phi}(k_x, k_y)$ (Equation 2.27), can be verified against the higher-fidelity *nonlinear* gyrokinetics (i.e. CGYRO) for this case. Figure 4.9 shows a comparison between the TGLF-SAT2 $\delta\hat{\phi}$ model and the $\delta\hat{\phi}$ output from a nonlinear CGYRO simulation (both evaluated at $\theta = 0$). Figures 4.9(a-d) provide 2D (k_x, k_y) comparisons of the fluctuating potential spectrum. Figure 4.9(e) over-plots the $k_x = 0$ slice of the 2D $\delta\hat{\phi}$ wavenumber spectrum from each code. We find the TGLF-SAT2 model accurately captures both the shape and magnitude of the nonlinear $\delta\hat{\phi}$ spectrum calculated by CGYRO. Figure 4.9(f) provides a slice of the spectrum near the peak at $k_y \approx 0.3$. The comparison in Figure 4.9(f) can be used to evaluate the k_x-model built into the TGLF and discussed previously in Section 2.4. The Lorentzian k_x-model built into TGLF appears to accurately reproduce the nonlinear gyrokinetics. The spectral shift due to $\gamma_{E\times B}$ does appear slightly over-predicted for this case relative to the CGYRO spectrum. For this case the nonlinear potential spectrum appears to be well-approximated by the TGLF model.

Similarly, we compare the quasi-linear TGLF $\delta\hat{n}$ wavenumber spectrum (Equation 2.29)

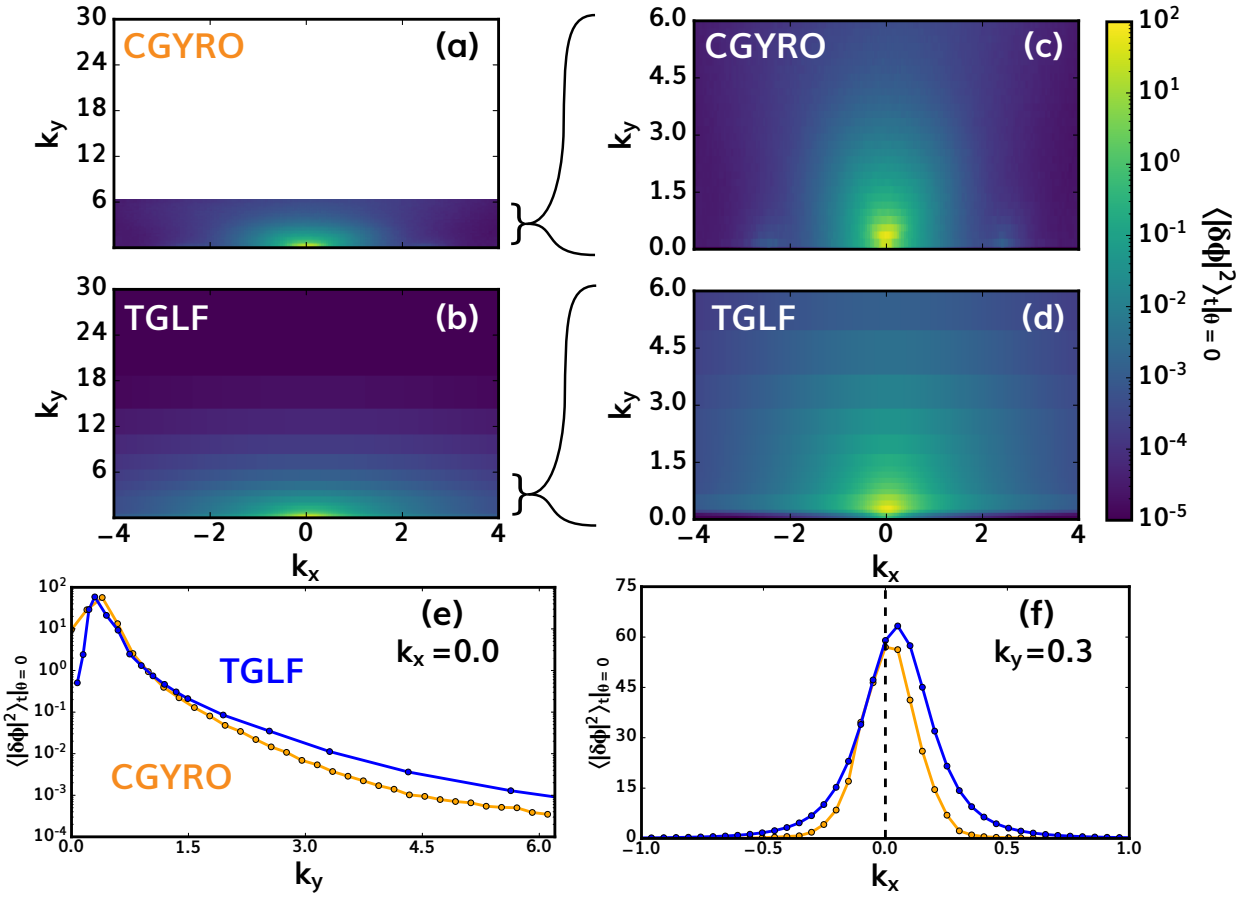

Figure 4.9: Comparison of the gyro-Bohm normalized $\delta\hat{\phi}(k_x, k_y)$ spectra simulating using nonlinear CGYRO and calculated using the TGLF-based method.

with the $\delta\hat{n}$ calculated by nonlinear CGYRO. Figure 4.10 illustrates the $\delta\hat{n}$-comparison between the codes. We focus our attention on the comparison in Figure 4.10(e). We find that over the ion-scale ($k_y < 0.7$) both codes agree in terms of the magnitude and spectral shape. However, TGLF appears to over-predict the $\delta\hat{n}$ fluctuations over the intermediate-scale relative to nonlinear CGYRO. This discrepancy cannot be independently attributed to inaccuracies in the quasi-linear weights, nor the TGLF model for the potential spectrum (as these were verified above). Instead, as observed in previous comparisons, the quasilinear approximation itself (Equation 2.29) appears less accurate over the intermediate scale for this case (at least for the $\delta\hat{n}_e$ field). However, despite the disagreement over the intermediate scale, the asymptotic behavior of the spectra, i.e. the spectral decay at high-k_y, appear to agree.

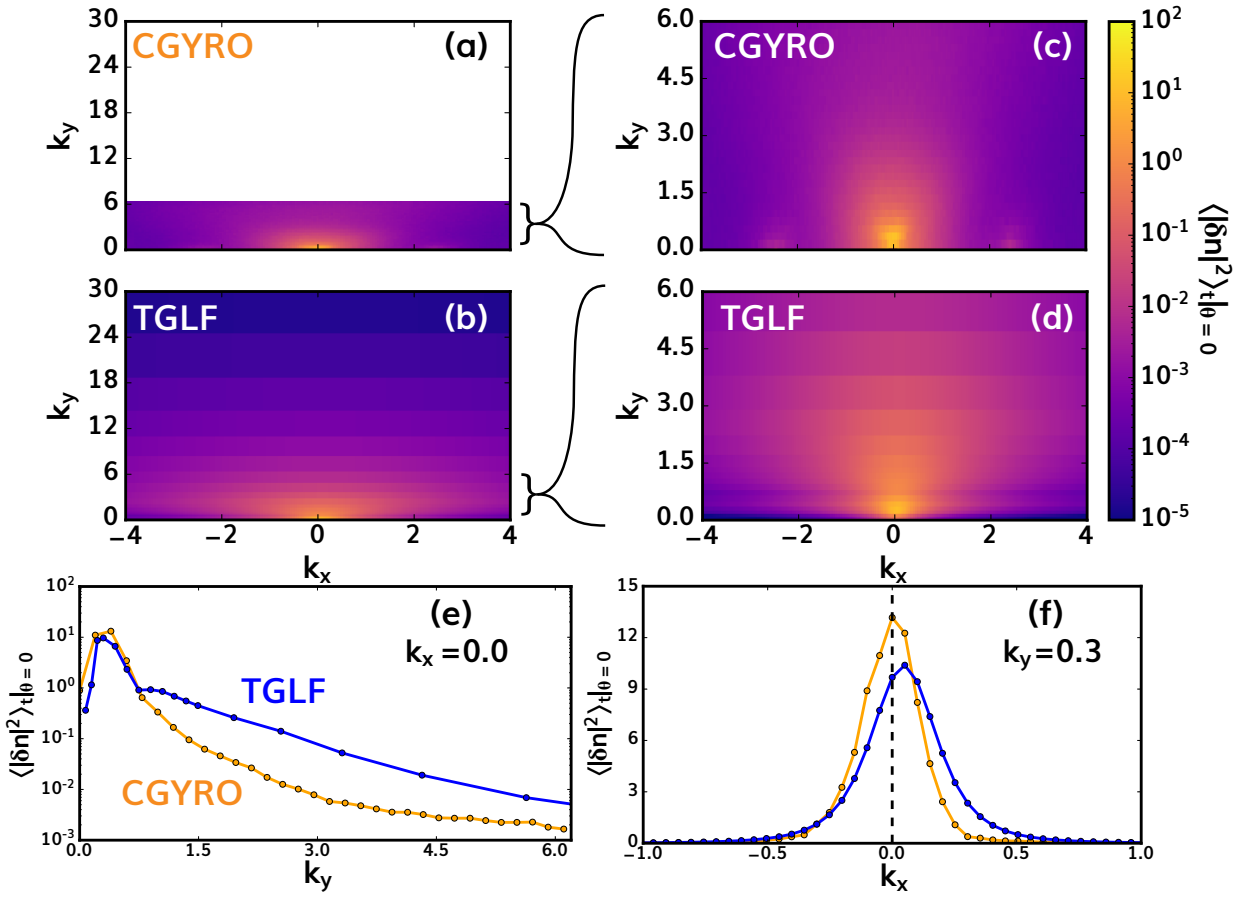

Figure 4.10: Comparison of the gyro-Bohm normalized $\delta\hat{n}(k_x, k_y)$ spectra simulated with nonlinear CGYRO and calculated using the TGLF method.

4.4.2 Forward modeling DBS results

In this subsection we show the results of forward-modeling the DBS back-scattered power wavenumber spectrum, $P_s(k)$. Recall, one has the freedom to provide any model $\delta\hat{n}(k_n, k_b)$ to predict $P_s(k)$. In this work we use the TGLF and CGYRO $\delta\hat{n}$ spectra presented in Section 4.4.1 and shown in Figure 4.10. We use the symbols $P_s^{\mathrm{TGLF}}(k_{\mathrm{meas.}})$ and $P_s^{\mathrm{CGYRO}}(k_{\mathrm{meas.}})$ to denote the synthetic DBS back-scattered power wavenumber spectrum based on TGLF and nonlinear CGYRO models for $\delta\hat{n}$ respectively.

For a detailed look at the synthetic DBS results we will focus on the averaged probed location ($\rho = 0.67$) and return to radial variation in the $\delta\hat{n}$ predicted by TGLF later. Figure 4.11 provides an image of the TGLF-$\delta\hat{n}^2(k_n, k_b)$ with log-scaled color at $\rho = 0.67$.

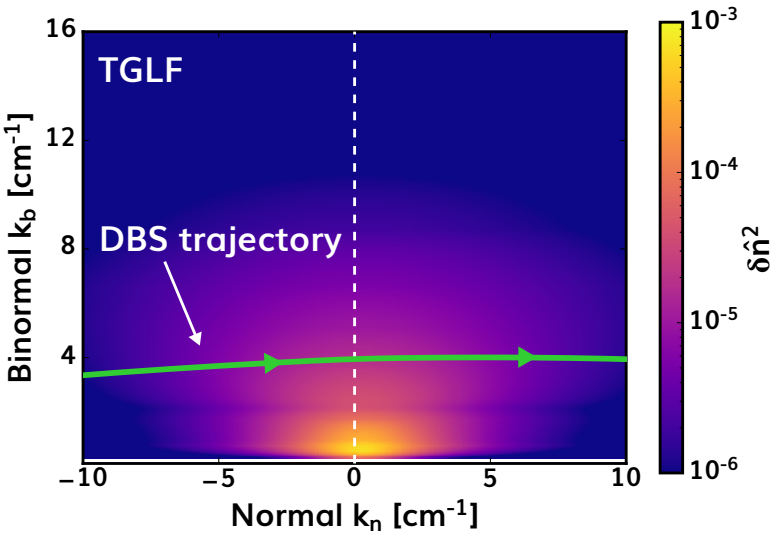

Figure 4.11: TGLF $\delta\hat{n}^2(k_n, k_b)$ spectrum at $\rho = 0.67$ and $\theta = 0$. The green line is a projection of a DBS trajectory from the wavenumber scan. The arrows indicate the direction DBS traverses through the *measured* ($k_{n,\text{meas.}}$, $k_{b,\text{meas.}}$) phase-space along the path of the beam through the plasma.

The underlying data in Figure 4.11 is the same as Figure 4.10(d) except k_x, k_y have been converted to k_n, k_b using Equation C.16. As the DBS beam propagates from the edge, to the cutoff, then back outwards, the beam probes different wavenumbers. The line superimposed on the image in Figure 4.11 is a projection of a single DBS k-space trajectory. If we were to superimpose a different DBS trajectory with different launch angles, the line in Figure 4.11 would translate (approximately) vertically. Thus, varying the DBS launch angles allows us to sample roughly horizontal (approximately fixed k_b) slices of the $\delta\hat{n}$ spectrum. The location where the DBS trajectory intersects the $k_n = 0$ axis sets the measured binormal wavenumber at cutoff, $k_{\text{meas.}}$.

To forward-model the DBS measurements, we also require the DBS weighting function discussed previously in Section 3.7. Figure 4.12 shows several components of the DBS weighting function calculated using the SCOTTY code (see Eq. 3.52). The case shown in Figure 4.12 corresponds to the k-space trajectory of the beam in Figure 4.11. In particular, we show the 'ray' (Figure 4.12a), 'polarization' (Figure 4.12b), and 'turbulence' (Figure 4.12c) terms

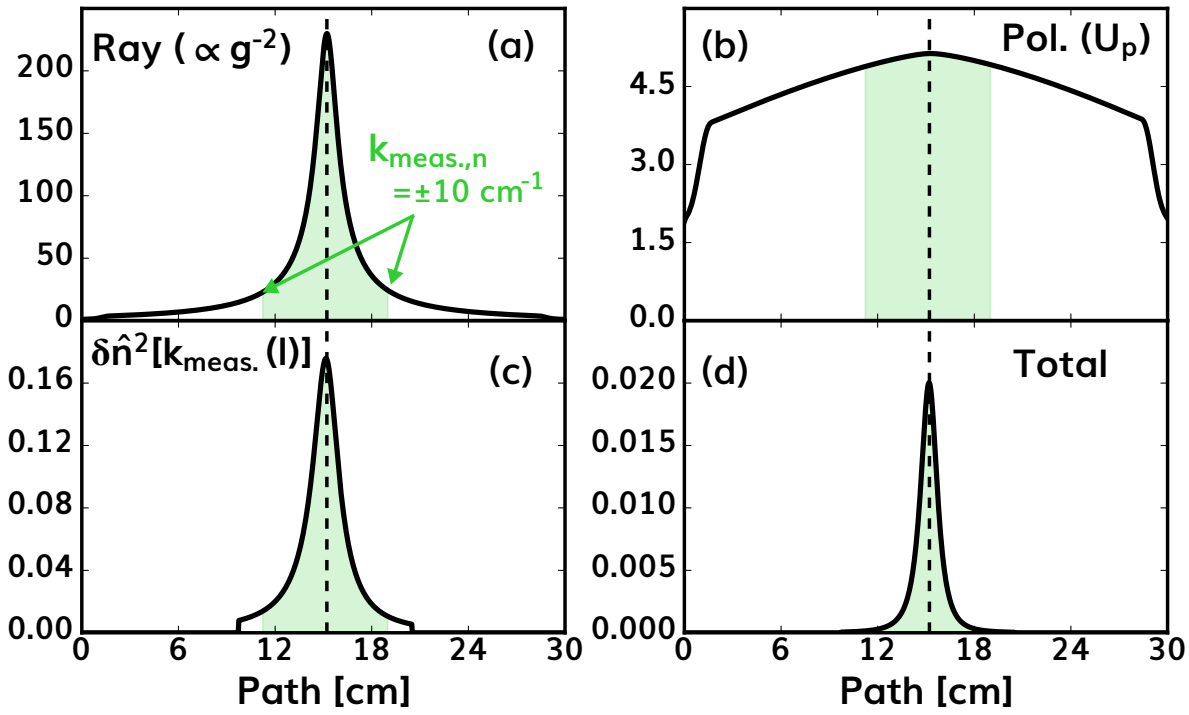

Figure 4.12: Components of the beam-DBS model computed by the SCOTTY code. 4.12(a,b) show the "Ray" and "Polarization" components of the weighting function. 4.12(c) shows the $\delta\hat{n}^2$ part of the integrand evaluated along the trajectory of the beam. 4.12(d) shows the total integrand (i.e. the product of the preceding terms). The "mismatch" is not shown as it's roughly a constant between 0.95 and 1.0 for this case. Finally, the shaded region connects this figure with the path shown in fig. 4.11.

of integrand in eq. 3.52. Recall that the ray component is $\sim k^{-2}$ (when $\theta_m \approx 0$; with k being the wavenumber of the central ray) and provides some localization for the signal. The annotation in Figure 4.12(a) is provided to connect Figures 4.12 and 4.11. The shaded region in Figure 4.12 corresponds to the horizontal bounds of Figure 4.11, i.e. where $k_{\text{meas.,n}} = \pm 10$ cm^{-1}. The localization provided by the 'turbulence' component of the weighting function – shown in Figure 4.12(c) – is due to the anisotropy of the $\delta\hat{n}^2$ spectrum in Figure 4.11. The $\delta\hat{n}^2$ spectrum generally exhibits low amplitude at higher radial wavenumbers. The absence of large-$|k_n|$ power in the $\delta\hat{n}^2(k_n, k_b)$ spectrum plays a significant role in localizing DBS measurements. The (k_n, k_b) anisotropy of the $\delta\hat{n}$ spectrum along with the DBS weighting function support the approximation that the majority of the scattered power originates from

a relatively narrow region near the cutoff.

Finally, to calculate a synthetic DBS back-scattered power wavenumber spectrum, $P_s^{\text{syn.}}(k_{\text{meas.}})$, from the results presented thus far, we make two additional assumptions:

1. Everywhere along each DBS trajectory, the $\delta\hat{n}(k_n, k_b)$ spectral power is concentrated near $k_n = 0$,

2. The $\delta\hat{n}$ spectrum does not vary significantly over the spread in DBS probed locations ($\rho \sim 0.67 \pm 0.07$).

The first assumption supports the approximation that the scattering is localized to the cutoff, where $k_{\text{meas.},n} = 0$. This allows us to use cutoff-localized gyrokinetics (CGYRO) and gyro-fluid (TGLF) results when evaluating the trajectory integral in Equation 3.52. The second assumption supports the approximation that the cutoff-localized $\delta\hat{n}^2$ results do not vary significantly across the DBS probed locations. This is further supported by the fact that turbulence drives (e.g. a/L_{T_e}) do not vary significantly over the range of probed locations (see figures 4.2 and 4.5). Both of these approximations will be relaxed in a later section. For now they are required to compare the P_s^{TGLF} and P_s^{CGYRO} spectra given that we only have one local ($\rho = 0.67$), large nonlinear CGYRO simulation.

Figure 4.13 provides a comparison of the synthetic, local ($\rho = 0.67$) P_s^{TGLF} and P_s^{CGYRO} spectra with DBS measurements. These $P_s^{\text{syn.}}(k_{\text{meas.}})$ spectra are calculated by first running a series of beam-tracing simulations (modeling the launch-angle scan). Separately, we use the TGLF and CGYRO $\delta\hat{n}(k_n, k_b)$ spectra at $\rho = 0.67$ and $\theta = 0$ shown in the previous section to calculate the integral in Eq. 3.52 over the path of each trajectory in the scan.

Normalization of synthetic diagnostic results

The results in Figure 4.13 are shown with arbitrary units [a.u.]. This is due to the fact that quantifying the absolute scattered power from DBS (e.g. in units of μW) is complicated and the subject of ongoing research. However, we have used consistent polarization, launch-frequency, and analysis to collect the DBS data shown throughout this chapter. Thus, the

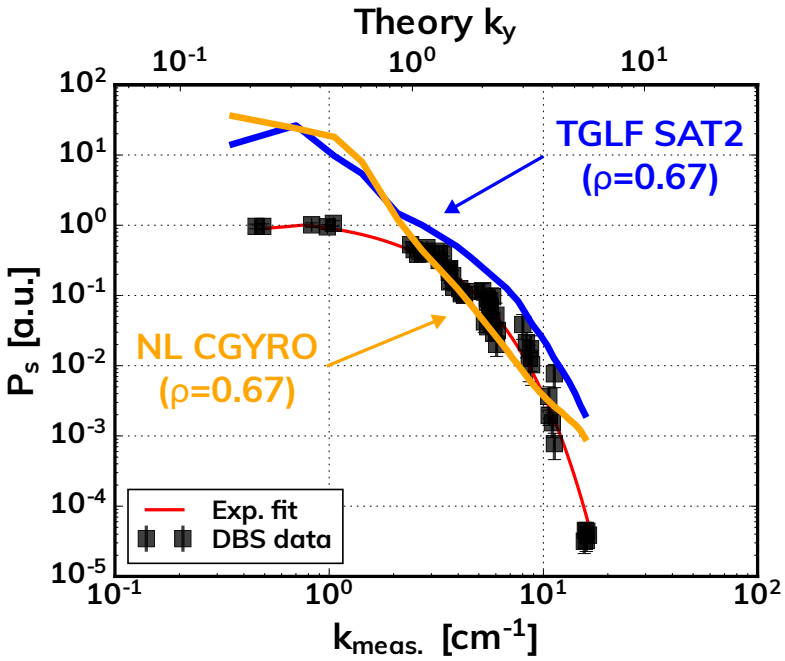

Figure 4.13: Comparison of synthetic $P_s(k)$ forward modeling results with DBS measurements. The upper x-axis is the theory k_y value (calculated using eq. C.16(b)) while the bottom x-axis is the measured wavenumber in cm^{-1}. The DBS data shown in Figure 4.13 is identical to the data shown in Figure 4.6. The discharge numbers and DBS system information has been suppressed for clarity.

relative magnitude of neighboring DBS data in Figure 4.13 is not arbitrary. Only one overall multiplicative scale factor has been applied to set $P_s = 1$ at $k_{\text{meas.}} = 1$ cm.

When comparing with synthetic diagnostic results, there is an additional free parameter: a multiplicative scale factor used to align the simulated results with data[7]. It is important to note that density fluctuations are treated consistently across the simulated launch-angle scan, i.e. we do not normalize each $P_s^{\text{syn.}}$ value separately. Instead, the entire synthetic wavenumber spectrum is scaled by one factor. Furthermore, the relative magnitude between TGLF and CGYRO is preserved i.e. both P_s^{TGLF} and P_s^{CGYRO} spectra are multiplied by the same normalizing scale-factor. This treatment allows us to *quantitatively* compare both the magnitude and shape of the predicted $P_s^{\text{TGLF}}(k_{\text{meas.}})$ and $P_s^{\text{CGYRO}}(k_{\text{meas.}})$ spectra with

[7]Because all P_s results are shown with a log-y scale, the multiplicative factor becomes a vertical shift up/down.

each other; but only the *shape* of the spectra can be compared quantitatively with DBS measurements. The scale factor applied to the synthetic wavenumber spectra was selected (arbitrarily) to align the nonlinear CGYRO wavenumber spectrum, $P_s^{\mathrm{CGYRO}}(k_{\mathrm{meas.}})$, with measurements at $k_y \approx 1$. It is important to note that the same normalization factor is used for all forward-modeled synthetic $P_s^{\mathrm{syn.}}$ spectra shown in this chapter.

4.4.3 Radial and poloidal variation in the $\delta\hat{n}$ spectrum

The results of the forward modeling, $P_s^{\mathrm{TGLF}}(k_{\mathrm{meas.}})$ and $P_s^{\mathrm{CGYRO}}(k_{\mathrm{meas.}})$ shown in Figure 4.13, are based on simulations performed at a single radial location ($\rho = 0.67$) and evaluated at $\theta = 0$. In this subsection we address efforts to extend these results to account for any possible poloidal and/or radial variation in the turbulence and its impact on predicting the DBS measurements. It should be noted that the CGYRO simulations presented here are flux-tube simulations performed at a single radial location. Therefore, while we can explore the possible θ-dependence of $\delta\hat{n}$ in CGYRO, we cannot use the CGYRO simulations here to investigate the radial dependence without performing additional (prohibitively expensive) global nonlinear simulations.

To extend the TGLF modeling from the previous subsection to account for radial/poloidal variation in the turbulence we use the following procedure: we identify the cutoff location and corresponding poloidal angle for each DBS beam-tracing trajectory (ρ_c and θ_c). Then, we run TGLF at each ρ_c, and use the full θ-dependent version of the TGLF model $\delta\phi$ spectrum (Equation 2.27) to calculate $\delta\hat{n}(k_x, k_y, \theta; \rho)$ (Equation 2.29). Finally, the general θ-dependant wavenumber mapping (Equation C.15) is used to transform k_x and k_y into the radial and binormal wavenumbers k_n, k_b. The back-scattered power is then calculated by performing the integral in Equation 3.52 for each (ρ_c, θ_c). This procedure accounts for variations in the local $\delta\hat{n}(k_n, k_b, \theta_c; \rho_c)$ spectra while maintaining the approximation that the scattering is localized to the cutoff location (ρ_c, θ_c). The result of this more advanced forward model is shown in Figure 4.14.

Figure 4.14 demonstrates that the TGLF-predicted θ-dependence of the $\delta\hat{n}(k_n, k_b, \theta; \rho)$

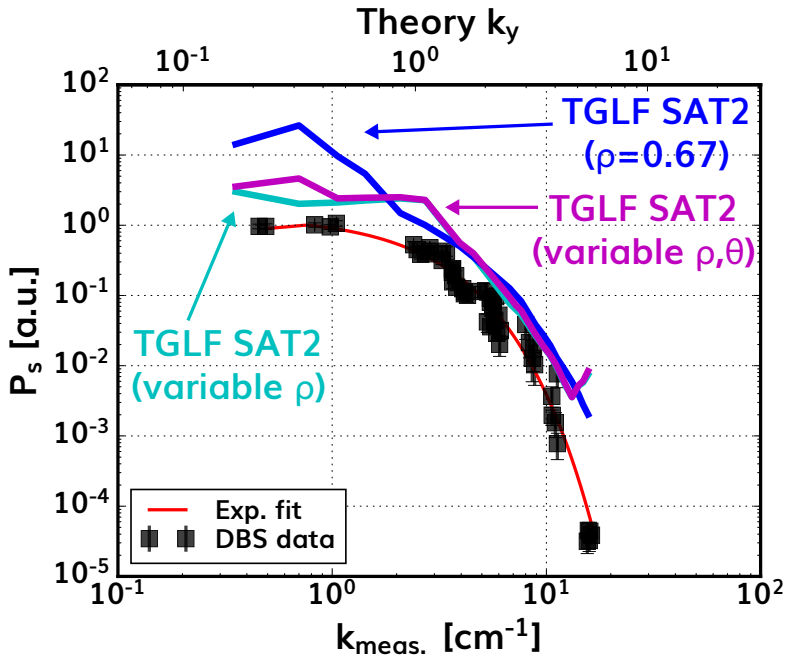

Figure 4.14: Comparison of synthetic $P_s^{\mathrm{TGLF}}(k)$ forward modeling results with DBS measurements. The upper x-axis is the theory k_y value (calculated using eq. C.16(b)) while the bottom x-axis is the measured wavenumber in cm^{-1}. The DBS data shown in Figure 4.14 is identical to the data shown in Figure 4.6. The discharge numbers and DBS system information has been suppressed for clarity.

spectrum is negligible compared to the TGLF-predicted variation with ρ. This is largely due to the fact that the the DBS measurements are close to the LFS midplane with $\theta_c \in [0, 20°]$. The θ-dependence predicted by TGLF will be verified against CGYRO later. The ρ-variation of the TGLF-predicted $\delta\hat{n}(k_n, k_b, \theta; \rho)$ spectrum is significant. The primary difference between the P_s^{TGLF} results in Figure 4.14 is the spectral decay over the $1 \leq k \leq 3$ cm^{-1} $(0.4 < k_y < 1.2)$ range. In fact, the P_s^{TGLF} result accounting for $\delta\hat{n}(\rho)$ appears to be in very good agreement with shape of the measured DBS spectrum at nearly every k. It appears that with a different choice in our normalizing scale-factor, the P_s^{TGLF} prediction can be vertically shifted lower (smaller normalizing constant) and made to pass roughly through all of the DBS data. More detailed analysis of this result will be discussed in discussed in Subsection 4.5.3.

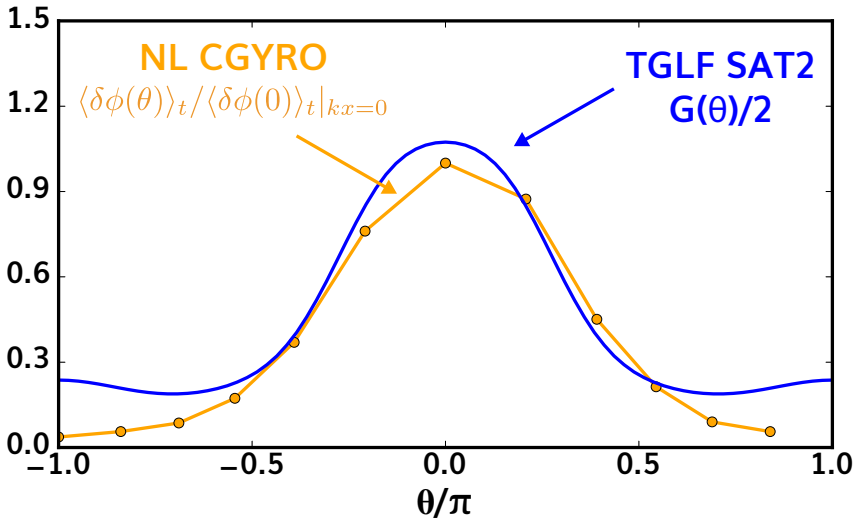

Figure 4.15: Comparison of the TGLF-SAT2 geometric factor $G(\theta)$ at $k_y \approx 1$ and the normalized amplitude of the fluctuating potential spectrum calculated from a nonlinear CGYRO simulation also evaluated at $k_y \approx 1$.

Testing the θ-dependence predicted by TGLF

The weak θ-dependence of the $\delta\hat{n}$ spectrum predicted by TGLF can be verified with nonlinear CGYRO simulations. For the TGLF model, the θ-dependence of $\delta\hat{n}$ is entirely contained with the $G(\theta)$ function built into the TGLF-SAT2 $\delta\hat{\phi}$ model (Equation 2.27). To verify $G(\theta)$ for this case, we performed an additional nonlinear ion-scale CGYRO-simulation with data output at many θ-locations (`THETA_PLOT=12`). The amplitude of the potential spectrum was time-averaged and evaluated at $k_x = 0$ and (arbitrarily) $k_y = 1.0$. Theoretically, $G_{k_y}(\theta) \approx \delta\hat{\phi}_{k_y}(\theta)/\delta\hat{\phi}_{k_y}(0)$ [33]. Figure 4.15 compares the normalized amplitude of the potential spectrum with the $G(\theta)$ model for this case. We find that the overall shape of $\delta\hat{\phi}(\theta)$ is captured by the TGLF model for $\theta \in [-\pi/2, \pi/2]$. Furthermore, the nonlinear CGYRO simulation predicts only a slight ($< 20\%$) reduction in the amplitude of the potential fluctuations over the DBS measurement region ($\theta/\pi \in [0, 0.1]$). This supports the approximation that any variation in the DBS cutoff poloidal location(s) does not impact the wavenumber spectrum measurement.

4.4.4 Inverse modeling DBS results

To solve the inverse problem outlined in Section 3.7, we use the experimental $P_s(k_{\text{meas.}})$ spectrum as the target of a nonlinear least-squares fitting procedure. We use the symbol $P_s^{\text{inv.}}(k_{\text{meas.}})$ to represent the synthetic back-scattered power spectrum resulting from a solution to the inverse problem. The parameters of an analytic $\delta\hat{n}$ model are optimized by comparing $P_s^{\text{inv.}}(k_{\text{meas.}})$ with the fit to DBS data, $P_s^{\text{fit}}(k)$ (Equation 4.1) at each $k = k_{\text{meas.}}$. The output of solving the inverse problem is both a set of optimized $\delta\hat{n}$ model parameters, and a $P_s^{\text{inv.}}(k_{\text{meas.}})$ spectrum that matches the DBS data (assuming a good fit). We use the following function presented in [8] as our model $\delta\hat{n}^2$ spectrum,

$$\langle|\delta\hat{n}|^2\rangle \propto \frac{1}{1+\left(\frac{|k_n|}{w_n}\right)^{\gamma}+\left(\frac{|k_b-k_b^*|}{w_b}\right)^{\beta}}. \tag{4.3}$$

This power-law model has five parameters: $\vec{\mu} = [w_n, \gamma, k_b^*, w_b, \beta]$. These parameters are not allowed to vary with radius as this would lead to 'over-fitting'. In other words, we make equivalent assumptions as those underlying the *local* ($\rho = 0.67$) forward modeling results shown in Subsection 4.4.2.

Importantly, DBS measurements cannot isolate the effects of the normal (radial) wavenumber spectrum on the scattered power. This is because scattering along the DBS trajectory essentially integrates over a wide range of k_n (see Figure 4.11). Therefore, the k_n parameters $[w_n, \gamma]$ are under-constrained by the DBS data. Inspired by the TGLF model, we fix $\gamma = 2$ to form a Lorentzian in k_n. Multiple fixed values of the spectral scale-length in the normal direction, w_n, were tested. We found the final $P_s^{\text{inv.}}$ to be somewhat insensitive to the precise value of w_n so long as the spectrum is not highly broadened in the k_n-direction, diminishing the cutoff k_b resolution. Therefore, we arbitrarily select a scale factor, $w_n = 2$ cm^{-1}. This simplifies the model, allowing us to iterate only the binormal parameters, $[k_b^*, w_b, \beta]$.

For each optimizer iteration, the $P_s^{\text{inv.}}(k_{\text{meas.}})$ spectrum is calculated using a fixed set of $\delta\hat{n}^2$ parameters: $\vec{\mu} = [k_b^*, w_b, \beta]$. Then, residuals are evaluated (in log-space) according to: Res. $= |\log P_s^{\text{inv.}}(k) - \log P_s^{\text{fit}}(k)|$. Based on these residuals, $\vec{\mu}$ is updated and the process is

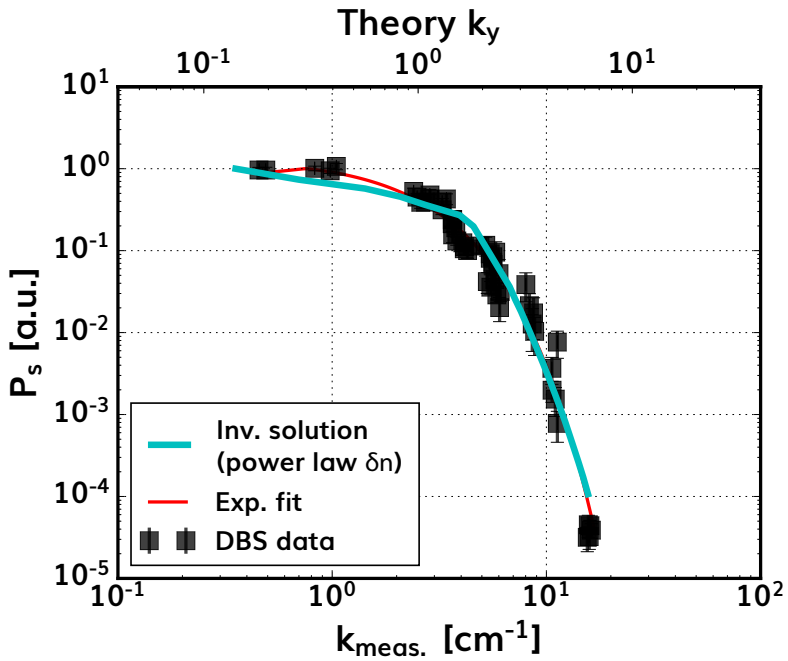

Figure 4.16: Comparison of synthetic $P_s(k)$ inverse modeling results with DBS measurements. The upper x-axis is the theory k_y value (calculated using eq. C.16(a)) while the bottom x-axis is the measured wavenumber in cm^{-1}. The DBS data shown in Figure 4.16 is identical to the data shown in Figure 4.6. The discharge numbers and DBS system information has been suppressed for clarity.

repeated until convergence. The inverse problem solution, $P_s^{\text{inv.}}(k_{\text{meas.}})$, is shown in Figure 4.16. The optimal binormal parameters for the model in eq. 4.3 are $k_b^* = 2.7$ cm^{-1}, $w_b = 2.4$ cm^{-1}, $\beta = 4.4$ (with $\gamma = 2$, $w_n = 2$ cm^{-1}). The binormal shift parameter, $k_b^* = 2.7$ cm^{-1}, corresponds to $k_y \approx 1$.

It should be emphasized that convergence is not unique using this approach, and that the functional form of Equation 4.3 injects bias. It was found that convergence is also possible with other models. For example, we also used an exponential-type spectrum of the form,

$$\langle |\delta\hat{n}|^2 \rangle \propto \exp\left(-\left(\frac{|k_n|}{w_n}\right)^{\gamma} - \left(\frac{|k_b - k_b^*|}{w_b}\right)^{\beta} \right). \tag{4.4}$$

Once again, we fix the parameters of the normal-direction such that $\gamma = 1$, and $w_n = 2$ cm^{-1}. The optimal binormal parameters in this case were: $k_b^* = 2.4$ cm^{-1}, $w_b = 2.5$ cm^{-1},

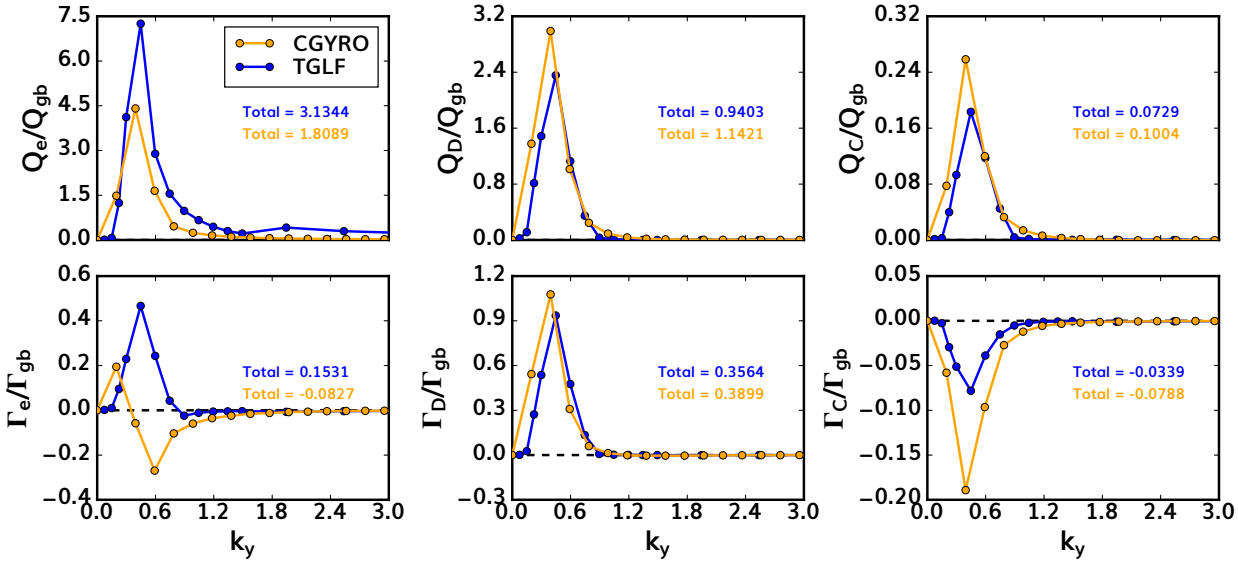

Figure 4.17: Comparison of gyro-Bohm normalized thermal and particle fluxes for each plasma species (e, D, C) calculated by TGLF-SAT2 and CGYRO.

$\beta = 1.1$. Once again, the binormal shift parameter, $k_b^* = 2.4$ cm^{-1}, corresponds to $k_y \approx 1$. The exponent, $\beta \approx 1.0$ indicates an almost purely exponential $\delta\hat{n}$ spectrum. Interestingly, the scale factor, w_b, from both the power-law fit and the exponential fit are approximately equal. This is likely driven by the fact that we have fixed w_n in both cases (to the same value). The ratio of w_n/w_b is indicative of the anisotropy in the $\delta\hat{n}$ spectrum. This will be discussed in more detail in Section 4.5.1.

4.4.5 Transport modeling

The results in Subsections 4.4.1 – 4.4.3 focus on the modeling efforts undertaken to predict and interpret DBS measurements of the back-scattered power wavenumber spectrum. While the DBS investigation is one of the primary results of this thesis - more general transport modeling is also important for interpreting the ECH H-mode plasma scenario. In this subsection we present results related to the transport modeling of the plasma selected for detailed analysis (DIII-D 189998, 3000 ms).

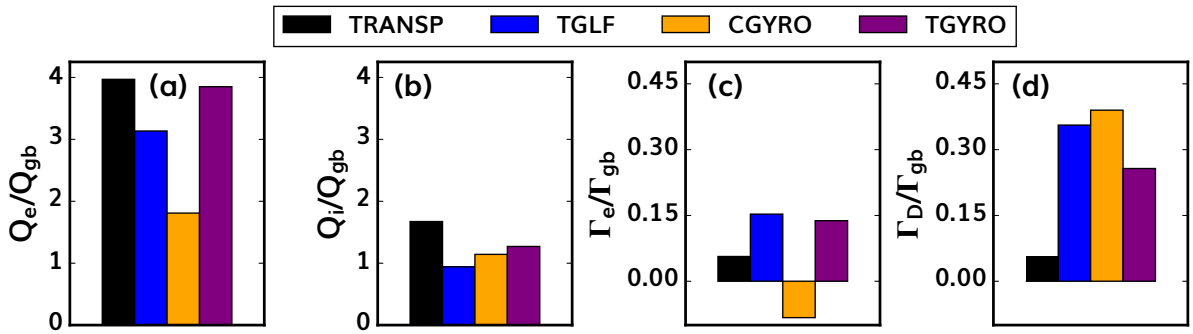

Figure 4.18: Comparison of gyro-Bohm normalized thermal and particle fluxes calculated by TGLF-SAT2, NL-CGYRO, and TRANSP at $\rho = 0.67$.

The gyro-Bohm normalized[8] thermal and particle flux k_y-spectra calculated by nonlinear CGYRO and TGLF at $\rho = 0.67$ are shown in Figure 4.17. In almost every transport channel the two codes agree as to the location and width of the peak flux in k_y. One exception is the electron particle flux, Γ_e, where CGYRO predicts an inward (negative) flux and null flux ($\Gamma_{e,k_y} \approx 0$) at the peak predicted by TGLF ($k_y \approx 0.4$). Another channel where the two codes disagree is the electron thermal flux, Q_e. TGLF predicts a small secondary peak in Q_e at $k_y \approx 2$ whereas CGYRO predicts a monotonically decreasing Q_e spectrum as k_y increases. Figure 4.18 compares the total fluxes predicted by TGLF and nonlinear CGYRO with the power balance fluxes inferred by the TRANSP calculation at $\rho = 0.67$. Both TGLF (blue) and CGYRO (orange) under-predict the total electron heat flux and the total ion heat flux. The particle fluxes also do not agree with the power balance values from TRANSP. However, it should be remarked that the particle source from wall recycling is difficult to model accurately (although, the lack of an accurate edge particle source model may be irrelevant given that the results shown in Figure 4.18 are from $\rho = 0.67$).

We use the code `TGYRO` [54] to self-consistently evolve the T_e and T_i profiles to attempt a match to the target thermal fluxes from TRANSP. Generally speaking, TGYRO solves an inverse problem: given plasma sources (inputs), what set of plasma profiles (outputs) are self-consistent? TGYRO is part of a class of 'transport solver' codes mentioned in Subsection 2.6.

[8]Recall, gyro-Bohm fluxes were defined in Section 2.2.

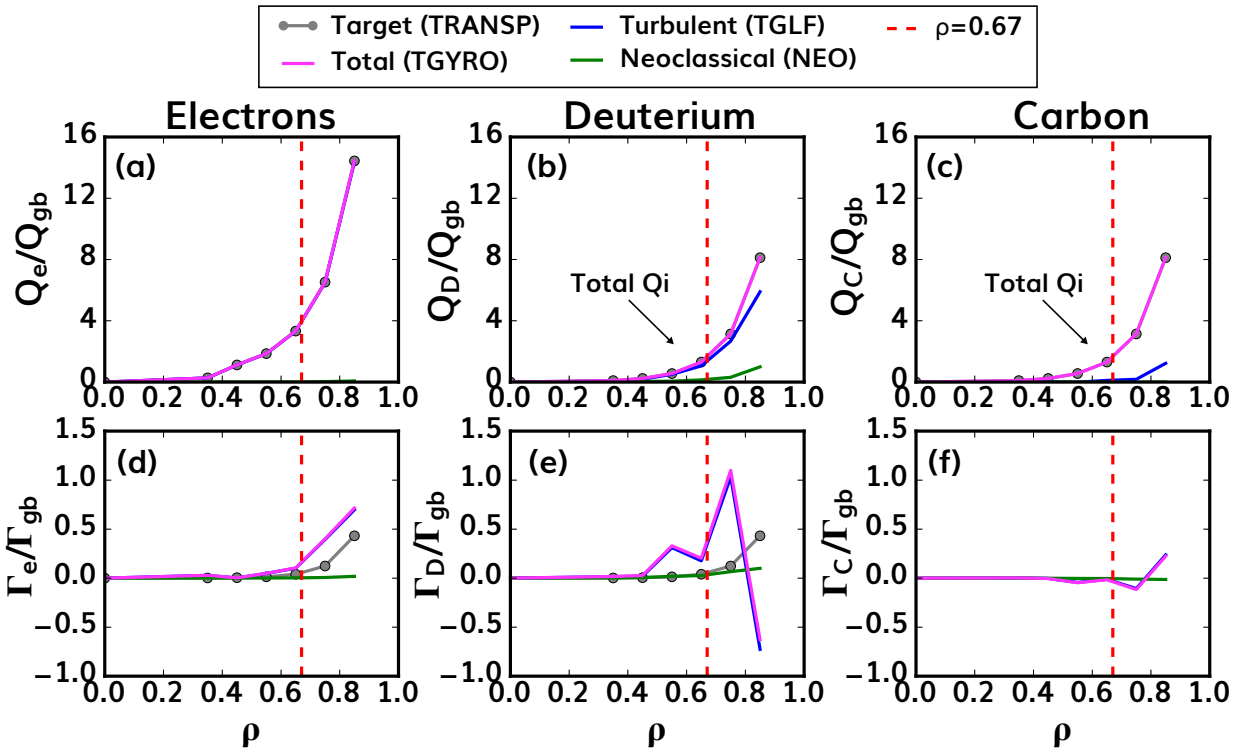

Figure 4.19: Comparison of gyro-Bohm normalized transport fluxes vs. radius (ρ) over the plasma core. The target (grey) is provided by the TRANSP code. The turbulent flux is calculated by TGLF at each radius (circles) along with the neoclassical flux calculated by NEO. The target and total thermal fluxes shown in the ion heat flux plots are the same (D + C). The nominal DBS location ($\rho = 0.67$) is shown with a vertical line.

In practice, TGYRO manages the 'flux-matching' procedure: given a set of profile (radial) control points, TGYRO will drive other codes (or use reduced models/analytic formulas) to compute turbulent and neoclassical transport fluxes along with other forms of energy exchange (e.g. radiation and collisions). Then, residuals are evaluated by comparing the calculated fluxes with the target fluxes from power-balance (TRANSP). Newton iteration (or another Jacobian-based minimization algorithm) is performed and the control points are adjusted, changing the profiles/gradients. Convergence is achieved when the simulated fluxes match the fluxes from power-balance. The code `NEO` [25] (discussed in Subsection 2.3.1) calculates the neoclassical fluxes and TGLF-SAT2 (discussed in Section 2.4) calculates the (quasilinear) turbulent fluxes.

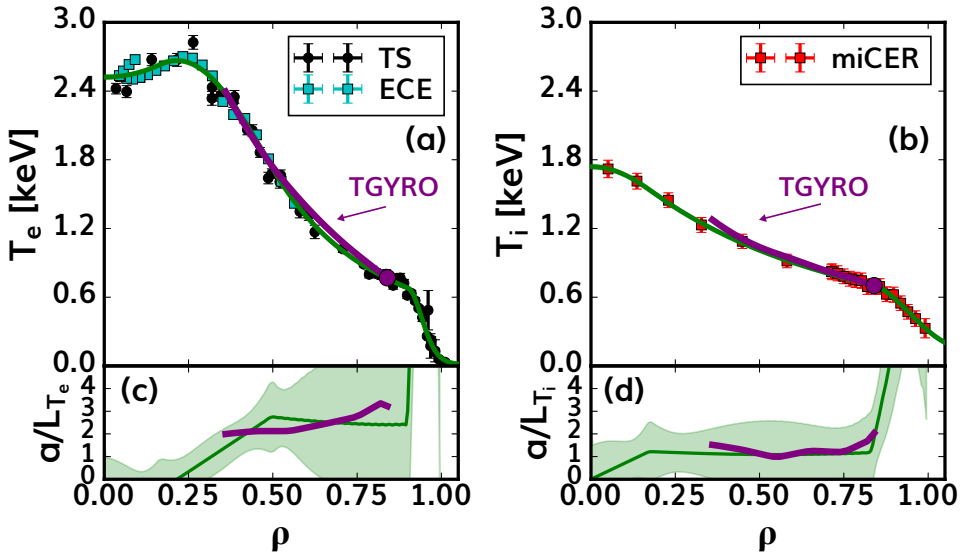

Figure 4.20: Comparison of the Q flux-matching T_e and T_D profiles from TGYRO with the experimental data and the fitted profile. The normalized inverse gradient scale-length of each profile is also shown beneath the profile.

The TGYRO transport-solver does find a thermal flux-matching solution for this set of profiles. With the TGYRO-adjusted profiles, flux-matching is greatly improved over a broad radial range in the core plasma. The TGYRO flux-matching result at multiple radii is shown in Figure 4.19. Figures 4.19(a) and 4.19(b) show that a good match to Q_e and Q_i was achieved. In fact, the total (pink) and target (grey) lines coincide in Figures 4.19(a,b). The neoclassical contributions to both Q_e and Q_i are negligible except for the outermost point in Q_i. The Carbon contribution to the total Q_i is also negligible except for a small turbulent contribution at the outer-most radius. The total fluxes at $\rho = 0.67$ from the TGYRO result are shown in Figure 4.18 in a purple color. Locally, at $\rho = 0.67$, the flux-matching appears only significantly improved in the Q_e channel relative to the fluxes calculated using the experiment profiles (blue, orange).

The TGYRO-modified T_e and T_D profiles are shown in Figure 4.20 over the radial range modified by TGYRO during the flux-matching procedure. The experimental data and fits are also repeated from Figure 4.2. The flux-matched profiles (purple) are approximately equal to the experimental profiles over the entire plasma core. The normalized gradient

scale-lengths are shown in figures 4.20(c,d). The TGYRO-modified scale lengths are well within the experimental uncertainty[9]. Furthermore, the TGYRO modification at the radial control points resulted in a very small change to a/L_{T_e} and a/L_{T_D} at $\rho \approx 0.67$.

The (thermal) flux-matching profiles can be evaluated using the forward-modeling synthetic DBS procedure, i.e. if we assume the flux-matched profiles are a more accurate representation of the plasma - how does that impact our prediction of the DBS measurements? Given that the n_e profile was not evolved by TGYRO, the ray-tracing calculations are not repeated and only the TGLF results are recalculated with the flux-matched T_e, T_D profiles. The resulting flux-matched DBS prediction (not shown) is nearly identical to the result using the experimental profiles (Figure 4.13). This is perhaps not surprising because the n_e profile was not evolved and therefore any changes to the $\delta\hat{n}$ spectrum (and thus the $P_s(k)$) would be the result of changes to T_e, T_D and their gradients. As shown previously in Figure 4.20, very little change occurred at $\rho \approx 0.67$ in support of flux-matching.

As noted previously, the TGYRO flux-matching used TGLF as the underlying model for the turbulent fluxes. It is not computationally feasible to run the TGYRO transport solver with nonlinear CGYRO as the turbulence model. Flux matching solutions with nonlinear gyrokinetics are especially infeasible for this case given that ideally the CGYRO simulations would capture the highest k_y values DBS is able to measure ($k_y \approx 6$). However, additional comparisons can be made by performing 1D parameter scans using TGLF. These can be compared with equivalent 1D scans using ion-scale nonlinear CGYRO simulations (discussed in Appendix C).

The result of independently scanning the electron and main-ion temperature scale lengths, a/L_{T_e} and a/L_{T_D} is shown in Figure 4.21. It is important to note that the scans plotted in Figure 4.21 do not vary parameters self-consistently, i.e. scanning a/L_{T_e} does not update the background T_e nor T_e-dependent parameters such as ν_{*e}. In Figure 4.21 the nominal

[9]The uncertainty on the inverse gradient scale length is calculated by propagating the uncertainty in the profile through the radial derivative operation.

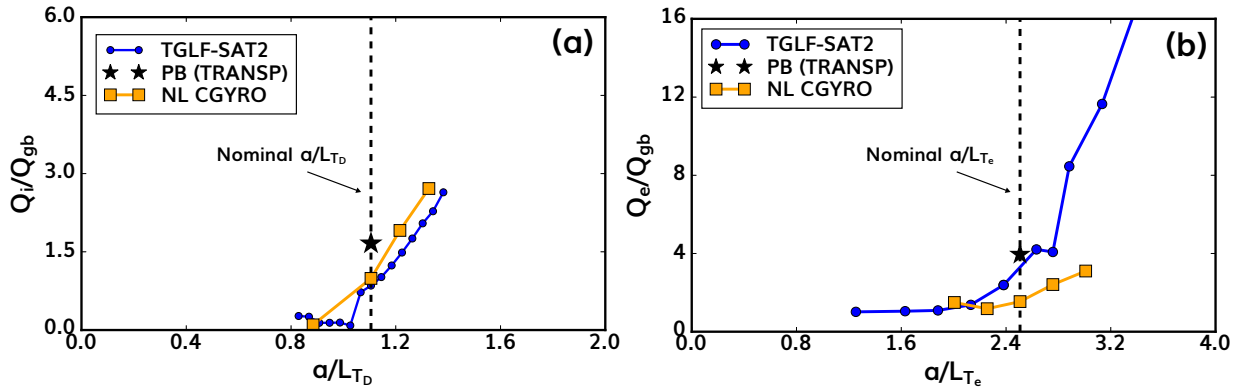

Figure 4.21: Comparison of independent a/L_{T_e} and a/L_{T_D} scans performed using TGLF-SAT2 and ion-scale nonlinear CGYRO simulations.

(experimental) a/L_T values are shown with vertical lines[10]. The TRANSP power-balance (PB) values are shown with stars.

The flux-gradient relationship, $(Q_i, a/L_{T_D})$ shown in Figure 4.21(a), predicted by TGLF and nonlinear CGYRO are in good agreement both in terms of the value and the transport stiffness, i.e. the slope of the trend. However, the electron $(Q_e, a/L_{T_e})$ relationships differ significantly between the two codes. Importantly, TGLF predicts a steep increase in Q_e just above the experimental a/L_{T_e} value. Further analysis of these TGLF results revealed that the increase in Q_e is caused by TEMs which – according to TGLF – become the dominant instability just above the experimental a/L_{T_e}. The TGLF-predicted TEM modes drive a peak in the Q_e flux at $k_y \approx 0.5$ and, in theory, should be captured by the ion-scale nonlinear CGYRO simulations (max $k_y = 1.2$) in Figure 4.21(b). This discrepancy between TGLF and nonlinear CGYRO will be discussed in more detail in Section 4.5.3.

[10]The flux-matching gradients are not shown in Figure 4.21 because they are very close in value to the experimental values at $\rho = 0.67$ (see Figure 4.20). Furthermore, the TGYRO flux-matching updated the entire T_e, T_D profiles and therefore other parameters were changing in the background independent of the gradients (e.g. ν_e). Thus, showing the flux-matching gradients might appear inconsistent with the scan in Figure 4.21, leading to confusion.

4.4.6 Summary of modeling results

The previous subsections presented a wide array of modeling results pertaining to the core of a representative ECH H-mode discharge. The key points are as follows:

1. At the average probed location ($\rho = 0.67$) TGLF-SAT2 reproduces linear (and some nonlinear) CGYRO results – garnering confidence in the TGLF model for this plasma. See Figures 4.7, 4.8, 4.9, 4.15, and 4.21(a). Notably, TGLF does not reproduce the nonlinear CGYRO density fluctuation spectrum, $\delta\hat{n}$, at intermediate/high-k_y scales (Figure 4.10).

2. The forward-modeled synthetic wavenumber spectra (P_s^{TGLF} and P_s^{CGYRO}) shown in Figure 4.13 have mixed agreement with the DBS measurements in terms of the rate of spectral decay. For CGYRO, the spectral decay agrees with DBS measurements at $k_y < 0.4$ and over the intermediate scale, $1.2 \leq k_y \leq 4.5$. However, over the range $0.4 < k_y < 1.2$ TGLF and CGYRO both predict a much steeper spectral decay compared to DBS measurements.

3. Radial and poloidal variation in the TGLF-$\delta\hat{n}$ spectrum was considered in forward modeling (Figure 4.14). Poloidal variation was found to have a negligible effect. Radial variation *appears* to be a significant factor in the shape of the measured spectrum (more on this in Section 4.5.3).

4. Inverse modeling of the DBS wavenumber spectrum (an example result is shown in Figure 4.16) found that multiple $\langle|\delta\hat{n}|^2\rangle$ analytic models are able to reproduce the DBS measurements.

5. Transport modeling with TGYRO found that TGLF-SAT2 can reproduce the TRANSP-inferred levels of heat flux with small changes to the T_e and T_D profiles (Figures 4.19, 4.20).

6. One dimensional scans of the a/L_{T_e} and a/L_{T_D} with TGLF and ion-scale nonlinear CGYRO revealed an important discrepancy between the codes. Namely, TGLF pre-

dicts that with a slight increase in the a/L_{T_e} TEMs become the dominant instabilities at $k_y < 1$ causing a substantial increase in Q_e (Figure 4.21). This behavior is not predicted by nonlinear CGYRO.

4.5 Analysis

4.5.1 The shape of the wavenumber spectrum

The measured DBS $P_s(k_{\text{meas.}})$ spectrum presented in Figure 4.6 exhibits variable spectral decay over the wavenumber range probed in the experiment, $0.5 \leq k \leq 16$ cm^{-1}. Table 4.1 provides a comparison with results from other fusion experiments. Previous studies generally report $\delta\hat{n}^2$ wavenumber spectra with variable decay, including a 'knee' feature near $k_{\text{meas.}}\rho_s = 1$. In previous studies, the 'knee' often bifurcates the wavenumber spectrum between a lower-k region with spectral decay index $\nu \approx 3$ and a higher-k region with $\nu > 3$ (here $\nu : \delta\hat{n}^2 \sim k^{-\nu}$). Our results are similar to what has been previously reported. We observe a spectral 'knee' at $k_{\text{meas.}} \approx 3.5$ cm^{-1} ($k_y \approx 1.4$) followed by a region ($3.5 \leq k_{\text{meas.}} \leq 8.5$ cm^{-1}) with $\nu \approx 2.6$. The high-k knee in our spectrum is less pronounced, located at $k \approx 8.5$ cm^{-1} ($k_y \approx 3.2$); separating the regime with $\nu = 2.6$ from a steeper region with $\nu = 9.4$. At low-k, preceding the knee at $k_y \approx 1.4$, we observe a relatively flat spectrum with $\nu \approx 0.6$. However, it should be noted that we do not have DBS measurements over the region $1 < k < 3$ cm^{-1}.

Many theoretical studies have sought to predict the form of spectral decay and the spectral energy transfer mechanism(s) in tokamak plasmas [123, 124]. Rather than compare with analytic models, we employ our synthetic DBS diagnostic to compare with nonlinear gyrokinetic simulations of the plasma under investigation. However, it is worth making general remarks about tokamak plasma wavenumber spectra. Variable spectral decay (in log-log space) distinguishes plasma fluctuations from fluid turbulence where a single spectral index may be applicable from driving at a large scale (low k) to dissipation at a small scale (high k). Plasmas naturally exhibit driving at multiple scales due to an array of unstable modes

Table 4.1: Published wavenumber spectrum results from other fusion experiments. To assemble this table we have equated P_s, $\delta\hat{n}^2$, and $(\delta\hat{n}/n)^2$. We have multiplied the spectral-index by two in any cases where authors have published a spectrum $\propto \delta\hat{n}$. Data shown in the table comes from a variety of confinement regimes, this may have an effect on the range of measured wavenumbers and the decay index, ν. The abbreviation 'Coll. TS' refers to collective Thomson scattering.

k-range cm^{-1} $(a,b) : a \leq k \leq b$	Decay (ν) $\delta\hat{n}^2 \sim k^{-\nu}$	Method	Radial Loc.	Device/Regime	Reference
(1, 3.5)	0.6	DBS	Core	DIII-D/H-mode	This thesis
(3.5, 8.5)	2.6				
(8.5, 16)	9.4				
(15, 25)	4.7	DBS	Core	MAST/L-mode	[125]
(4, 7)	2.2	DBS	Mid-r/a	AUG/L-mode	[78]
(7, 11)	7.2				
(2, 5)	0.5-2	DBS	$0.65 \leq \rho \leq 0.85$	TJ-II/L-mode	[126]
(9, 11)	5-10				
(3.5, 8.5)	2.7	DBS	$0.6 < \rho < 0.8$	TJ-II/L-mode	[127]
(8.5, 15)	9.2				
(3.5, 9)	1.8	DBS	Edge	TJ-II/L-mode	[128]
(9, 13)	10.2				
(3.5, 7.5)	2.6	DBS	Edge	TJ-II/H-mode	[128]
(7.5, 10)	11				
(6, 14)	3.5	Coll. TS	$0.7 < r/a < 1$	Tore Supra/L-mode	[129, 130]
(14, 26)	6.5				
(3, 11)	3.0	DBS	Mid-r/a	Tore Supra/L-mode	[95]
(3, 6)	< 3	Coll. TS	Line-averaged	Tore Supra/L-mode	[131]
(6, 15)	3				

(e.g. ITG/TEM/ETG in tokamaks). The observed variation in the decay index, ν, could be a symptom of different turbulence regimes, where the final ν value is a nonlinear balance of driving, dissipation mechanisms, and cascade phenomena (such as three wave coupling).

Nonlinear multi-scale gyrokinetic simulations by Howard *et al.* in [132] found that the relative importance of ITG/ETG impacted anisotropy in the density spectrum and the spectral energy transfer mechanism. Their cases with strong ETG activity (as we might expect in these ECH H-modes) exhibited a 'shoulder' in the simulated $\delta\hat{n}^2$ spectrum at $k_y \approx 3.5$ and a non-local inverse energy cascade from ETG wavenumbers ($k_y \sim [2-7.5]$) extending to ITG wavenumbers ($k_y \sim 0.4$). For the case presented here, DBS measurements do observe a change in spectral index at the high-k knee ($k_y \approx 3.2$). This appears similar to what is reported by Howard *et al.* [132]. However, despite strong electron heating, this knee is not present in the underlying $\delta\hat{n}^2$ spectra (Figure 4.10) and could be caused by instrumental effects discussed later in Subsection 4.5.2. It should be noted that the simulation presented here has $k_{y,max} = 6.2$ whereas the simulation presented in [132] has $k_{y,max} = 48$. Other explanations for the rapid spectral decay at high-k are discussed next.

Spectral decay at high-k

The measured $P_s(k)$ spectrum shown in Figure 4.6 exhibits rapid decay ($\sim k^{-9.4}$) at higher-k. Previous studies have also reported spectral decay indices, $\nu > 7$ including several examples from the TJ-II stellarator [127, 128]. While a value of $\nu \approx 9$ (or $\zeta \approx 4$ in the exponential $k\rho_s$ case) is seemingly large, these are well within the range of previously reported decay indices (exponential spectra are discussed later in this subsection).

DBS mismatch attenuation was also considered when analyzing the seemingly-rapid spectral decay at high $k_{\text{meas.}}$. During the experiment, toroidal steering with the DBS240 system was employed to maintain mismatch-angle $\theta_m < 1^\circ$ (at cutoff) for the entire DBS240 dataset. Additionally, the effects of mismatch are included in the SCOTTY calculation of the DBS weighting function. Therefore, any deviations from $\theta_m = 0$ are accounted for in the synthetic diagnostic.

The poloidal dependence of turbulence amplitude was also considered in investigating the seemingly-rapid spectral decay at high $k_{\text{meas.}}$. Returning to Figure 4.5(a), it is clear that high-k trajectories tend to probe further away from $\theta = 0$ (θ being the poloidal angle around the flux surface). The highest-k measurements probe closer to $\theta \approx 20°$. However, the modeling results presented in Section 4.4.3 suggest that the high-k_y decay is not a consequence of the poloidal variation.

Exponential spectral decay

In Section 4.2 we made the observation that the measured $P_s(k)$ spectrum appears to decay exponentially rather than according to a simple power-law. Hennequin *et al.* [129] reported collective Thomson scattering measurements on Tore Supra with an exponentially decaying spectrum, $|\delta\hat{n}|^2 \sim e^{-\zeta(k_\theta \rho_i)}$ with a value of $\zeta \approx 4$ over $0.5 \leq k_\theta \rho_i \leq 2.5$ for a variety of plasma conditions. Similarly, Schmitz *et al.* [133] reported DBS measurements on DIII-D exhibiting exponential spectral decay, $|\delta\hat{n}|^2 \sim e^{-\zeta(k_\theta \rho_s)}$, with $\zeta \approx 3$ in L-mode and $\zeta \approx 4$ in H-mode for $k_\theta \rho_s < 6$.

The measured DBS spectrum reported earlier in this chapter (Figure 4.6(b)) shows two values of the exponential decay factor, ζ. For values of $k_{\text{meas.}}\rho_s < 3.2$ the P_s spectrum has $\zeta \approx 1.7$. However, for $k_{\text{meas.}}\rho_s > 3.2$ the spectrum decays with $\zeta \approx 3.9$. This larger value agrees remarkably well with previous studies [129, 133]. Exponential wavenumber spectra with two decay factors were also reported by Vermare *et al.* [134] using DBS on Tore Supra. Vermare reported $|\delta\hat{n}|^2 \sim e^{-\zeta(k_\theta \rho_s)}$ for two values of collisionality ($\nu_* \approx 0.4$ and $\nu_* \approx 1.2$). For lower ν_* they found $\zeta = 3.9$ ($0.4 < k_\theta \rho_s < 0.7$) and $\zeta = 5.8$ ($0.7 < k_\theta \rho_s < 1.4$). Meanwhile, at high ν_* they reported $\zeta = 1.7$ ($0.4 < k_\theta \rho_s < 0.7$) and $\zeta = 5.2$ ($0.7 < k_\theta \rho_s < 1.4$). Interestingly, the value $\zeta \approx 4$ appears in the measurements reported here as well as measurements reported by Vermare, Hennequin, and Schmitz (albeit at different ranges of $k_\perp \rho_s$). Furthermore, we observe the same $\zeta \approx 1.7$ value as Vermare at low-$k\rho_s$ despite their measurements coming from higher ν_*. The similarity of these normalized exponential decay factors (ζ) suggests there may be a universal mechanism underlying the spatial structure of δn fluctuations.

Physically, the value of ζ can be interpreted if we assume $P_s(k)$ is proportional to the Fourier transform of the spatial δn autocorrelation function (cf. Equation 3.23). Then, an exponential spectrum in k-space corresponds to Lorentzian structure in real-space. If we define the correlation length of δn fluctuations in the binormal direction, L_b, as the half-width at half-maximum of the Lorentzian autocorrelation function, then $L_b = \zeta\rho_s$. Thus, in this simplified picture, ζ is the L_b correlation length in units of ρ_s. This interpretation implies a binormal correlation length on the order of 1–5ρ_s. This can be compared with reported measurements of *radial* correlation lengths, L_r, which have been reported on the order of 5–10ρ_s [135]. The fact that $L_b/L_r \neq 1$ is indicative of the anisotropic nature of turbulence in tokamaks. Although we might expect $L_b > L_r$, the algebraic decay of a Lorentzian real-space autocorrelation function leaves room for longer-range effects in the binormal direction.

Finally, it is worth returning to the discussion of exponential models for the DBS *frequency* spectrum presented in Subsection 3.1.6. Previously, we referred to work by Maggs *et al.* [96] where it was found that, in some cases, the DBS frequency spectrum exhibited exponential decay. In related work, Maggs *et al.* relate the exponential spectrum to chaotic dynamics arising from the interaction between unstable modes [98,99]. Thus, the measured exponential wavenumber spectrum reported in this chapter can be interpreted as suggesting spatially chaotic structure.

Interpretation of inverse-modeling results

Results of inverse-modeling the $P_s(k)$ wavenumber spectrum were presented in Subsection 4.4.4 (Figure 4.16). We found that multiple analytic models of $\langle|\delta\hat{n}(k_n, k_b)|^2\rangle$ were able to fit the measured DBS $P_s(k)$ after being integrated with the beam-DBS weighting function. We tested a power-law model (Equation 3.53) as well as an exponential model (Equation 3.54).

The power law model was inspired by work from Ruiz Ruiz *et al.* [8], where it was used to fit 2D $\langle|\delta\hat{n}(k_n, k_b)|^2\rangle$ spectra from nonlinear gyrokinetic simulations. In their case, a strongly ETG-driven case had spectral decay indices $\gamma = 2.9$ and $\beta = 3.1$ corresponding to the normal and binormal directions respectively. The ETG case in [8] also had $w_n/w_b \sim L_b/L_n = 0.75$

where L_b and L_n are the correlation lengths in the binormal and normal directions. The ratio L_b/L_n is theoretically related to the turbulent eddy aspect ratio. Meanwhile, the ITG dominant case in [8] had $\gamma = 3.9$ and $\beta = 3.2$ with $w_n/w_b \sim L_b/L_n = 0.6$. In our case, the fit to the DBS data found $\beta = 4.4$ with γ fixed at $\gamma = 2$ and $w_n/w_b \sim L_b/L_n = 0.83$ with w_n fixed to $w_n = 2$ cm^{-1}. Similar to our interpretation of the exponential decay factor (ζ), the ratio $L_b/L_n < 1$ suggests $L_b < L_n$.

The exponential $\langle|\delta\hat{n}(k_n, k_b)|^2\rangle$ model also resulted in an inverse-modeling fit to the DBS $P_s(k)$ measurements. In the exponential case the fit returned a binormal exponent of $\beta \approx 1$, indicating that an almost purely exponential $\langle|\delta\hat{n}(k_n, k_b)|^2\rangle$ spectrum can account for the DBS observations. With w_n fixed to the same value of $w_n = 2$ cm^{-1}, the fit finds $w_b = 2.5$ cm^{-1} such that $w_n/w_b \sim L_b/L_n = 0.8$, similar to the value from the power-law model.

4.5.2 Investigating DBS instrumental effects

Results presented in Subsection 4.4.2 included outputs of our novel synthetic DBS diagnostic. The synthetic diagnostic allows us to relate the measured $P_s(k_{\text{meas.}})$ to models of the underlying density fluctuation spectrum $\delta\hat{n}^2(k_n, k_b)$. By examining the relationship between $P_s^{\text{syn.}}$ and $\delta\hat{n}^2$, we can approximately separate diagnostic effects from measurements of $\delta\hat{n}^2$. Recall that under the beam-DBS theoretical framework, the DBS back-scattered power, P_s, is an integral of $\delta\hat{n}^2$ along the trajectory of the beam (Equation 3.52). Thus, it is important to consider the impact of the turbulence spectrum on signal localization (mentioned previously in Subsection 4.4.2), and the impact the weighting function, $\hat{U}$, may have on scattered power. In this subsection we discuss the impact $\hat{U}$ has on the relationship between $P_s^{\text{syn.}}$ and $\delta\hat{n}$ in more detail.

Figure 4.12 shows a situation where diagnostic effects are somewhat minimal. The total integrand (Figure 4.12(d)) has roughly the same shape as the probed $\langle|\delta\hat{n}|^2\rangle$ along the trajectory (Figure 4.12(c)). Therefore, when $P_s^{\text{syn.}}$ is calculated by integration, the result is essentially a constant multiplied by the spectrum, i.e. $P_s \propto \langle|\delta\hat{n}|^2\rangle$. If this proportionality holds true for every probed wavenumber, then it would be a reasonable approximation to

say DBS measures $\langle|\delta\hat{n}|^2\rangle$ (with some overall normalization).

The analysis presented in this chapter does not assume $P_s \propto \langle|\delta\hat{n}|^2\rangle$ *a priori*. The synthetic DBS diagnostic accounts for back-scattering along the ray trajectory and variations in the weighting function across the wavenumber scan. To investigate DBS instrumental effects we return to the local ($\rho = 0.67$, $\theta = 0$) forward-modeling $P_s^{\mathrm{TGLF}}(k)$ result shown in Figure 4.13. The $P_s^{\mathrm{TGLF}}(k)$ result can then be compared directly with the ($\rho = 0.67$, $\theta = 0$) $\delta\hat{n}^2(k_n, k_b)$ spectrum. For this comparison the $\delta\hat{n}^2$ spectrum must reduced to a one dimensional function of k_b. Two options for contracting the k_n dimension are compared: (1) taking a slice of $\delta\hat{n}^2(k_n, k_b)$ at $k_n = 0$ and (2) integrating over the k_n dimension at each k_b.

Figure 4.22 illustrates analysis comparing $P_s^{\mathrm{TGLF}}(k)$ and $\delta\hat{n}^2$. Figure 4.22(a) shows the $P_s^{\mathrm{TGLF}}(k)$ result along with the fit to the DBS measurements (both are repeated from Figure 4.13). Figure 4.22(a) also shows both the $k_n = 0$ slice of the TGLF $\delta\hat{n}^2$ spectrum and the integral over k_n. Figure 4.22(b) shows the ratio of P_s^{TGLF} with each contraction of the 2D $\langle|\delta\hat{n}|^2\rangle$ spectrum. If the approximation $P_s \propto \langle|\delta\hat{n}|^2\rangle$ were true, the line in Figure 4.22(b) would be horizontal, indicating the constant of proportionality. Interestingly, close inspection of Figure 4.22(b) shows that over the intermediate-k regime ($1 < k_b < 7$ cm^{-1}) the ratio $P_s^{\mathrm{TGLF}}/\langle|\delta\hat{n}|^2\rangle|_{k_n=0}$ (solid black line) does appear roughly horizontal. This supports the approximation of treating $P_s \propto \langle|\delta\hat{n}|^2\rangle$ in some cases (the curves in Figure 4.22(b) are not thought to be general results). Interestingly, the ratio of $P_s^{\mathrm{TGLF}}/\int dk_n\langle|\delta\hat{n}|^2\rangle$ (solid grey line) is clearly not horizontal at any scale. This suggests P_s^{TGLF} is not proportional to the k_n-integral of $\langle|\delta\hat{n}|^2\rangle$. The difference between the two ratios in Figure 4.22(b) suggests that, for a given k_b, the DBS P_s is more closely related to the $\langle|\delta\hat{n}|^2\rangle$ value at $k_n = 0$ than its k_n-integrated value. This is perhaps evidence that the 'ray' $\sim k^{-2}$ term (discussed in Subsection 3.1.4) in the DBS weighting function acts as a filter to concentrate the scattering signal to the cutoff (where the matching $k_n = 0$).

Outside of the intermediate-k regime, the $P_s^{\mathrm{TGLF}}/\langle|\delta\hat{n}|^2\rangle|_{k_n=0}$ curve in Figure 4.22(b) deviates from horizontal. This implies that the simple $P_s \propto \langle|\delta\hat{n}|^2\rangle$ relationship does not hold across the entire wavenumber scan. Diagnostic effects captured by the DBS weighting

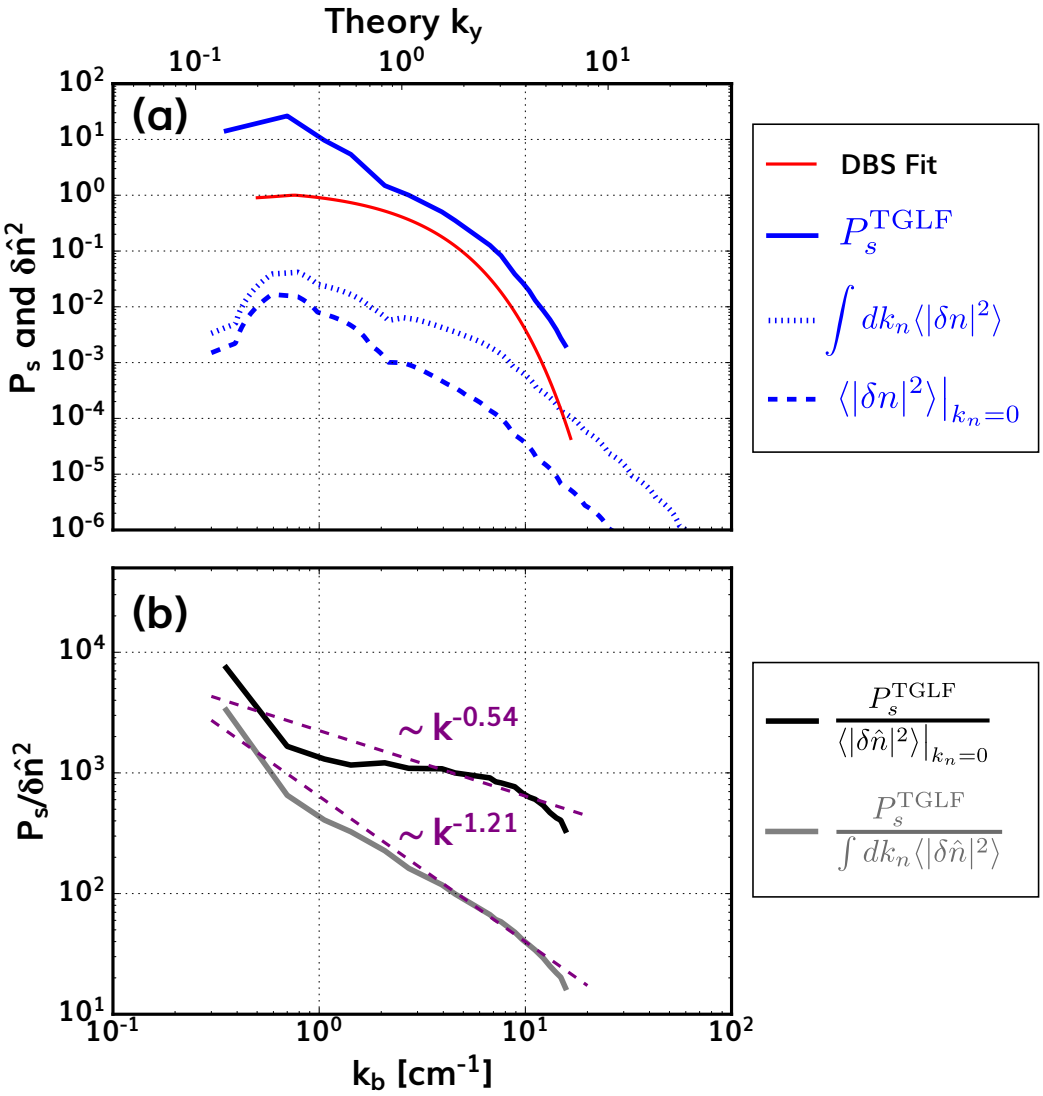

Figure 4.22: Illustration of the relationship between P_s and $\delta\hat{n}$. 4.22(a) shows the synthetic $P_s^{\mathrm{TGLF}}(k)$ (solid line) along with the $k_n = 0$ slice of the underlying $\delta\hat{n}^2$ spectrum (dashed line), the k_n integral of the underlying $\delta\hat{n}^2$ spectrum (dotted line), and the fit to the DBS measurements (red line). The $P_s^{\mathrm{TGLF}}(k)$ line is identical to the one shown in Figure 4.13. The results shown in (a) use a single radial location ($\rho = 0.67$). 4.22(b) shows two ratios of $P_s^{\mathrm{TGLF}}(k)/\delta\hat{n}^2$ on a log-log scale along with linear (power-law) fits.

function, $\hat{U}$, produce an overall relationship $P_s^{\mathrm{TGLF}} \propto k^{-0.5}\langle|\delta\hat{n}|^2\rangle$ (as indicated by the linear fit in Figure 4.22(b)). Thus, the predicted P_s^{TGLF} is steeper than the underlying $\langle|\delta\hat{n}|^2\rangle|_{k_n=0}$ spectrum. This effect is more pronounced when comparing P_s^{TGLF} with the k_n-integrated spectrum where the overall relationship is $P_s^{\mathrm{TGLF}} \propto k^{-1.2}\langle|\delta\hat{n}|^2\rangle$.

The differences between the $\langle|\delta\hat{n}|^2\rangle$ and P_s^{TGLF} in Figure 4.22(a) highlight the importance of treating DBS measurements with a synthetic diagnostic framework. It should be stressed that the precise ratios in Figure 4.22(b) are not a general result. The specifics of the DBS $\hat{U}$ vary with the background plasma and the choice of frequency, polarization, and launch angles.

4.5.3 Revisiting radial variation of $\delta\hat{n}$ predicted by TGLF

In Subsection 4.4.3 we discussed the radial variation in the $\delta\hat{n}^2$ predicted by TGLF. Figure 4.14, showed that the forward-modeled $P_s^{\mathrm{TGLF}}(k)$ spectrum becomes flat over $k < 3$ cm^{-1} ($k_y < 1.2$) when the (TGLF-predicted) radial variation in the $\delta\hat{n}^2$ spectrum is taken into account. The underlying reason for this is directly related to TGLF's prediction of dominant TEM turbulence at slightly increased a/L_{T_e} (see Figure 4.21(b)). The lowest-k points in the measured DBS spectrum come from slightly smaller ρ locations where the experimental a/L_{T_e} is slightly larger. At these inner radii, with larger a/L_{T_e}, TGLF predicts dominant TEM turbulence. This is the same effect causing the nonlinear increase in Q_e shown in Figure 4.21(b). Increased fluctuations at $k_y \approx 1$ and decreased fluctuations at $k_y \approx 0.3$ produce a flat $P_s^{\mathrm{TGLF}}(k)$, reproducing the shape of the measured $P_s(k)$ spectrum.

To show this effect more explicitly, we return to the forward modeled $P_s^{\mathrm{TGLF}}(k)$ at $\rho = 0.67$ (blue line in Figure 4.13). Figure 4.23 shows an additional synthetic $P_s^{\mathrm{TGLF}}(k)$ spectrum where the underlying TGLF simulation was modified to have 5% larger a/L_{T_e}. Figure 4.23 shows that the predicted spectrum becomes largely flat over the ion-scale ($k_y \leq 1$) with a mere +5% increment in a/L_{T_e}. Because this modification more closely resembles the shape of the measured DBS spectrum, it would seem the +5% a/L_{T_e} TGLF simulation is more realistic than the experimental profiles. However, given the a/L_{T_e} scans performed with nonlinear CGYRO (Figure 4.21(b)), we have reason to believe that this TGLF prediction is not in accordance with the higher-fidelity CGYRO. Therefore, although the dominant TEM regime at +5% a/L_{T_e} improves agreement between DBS measurements and the $P_s^{\mathrm{TGLF}}(k)$, there is some doubt as to whether TEM instabilities are the root cause of the flat spectrum

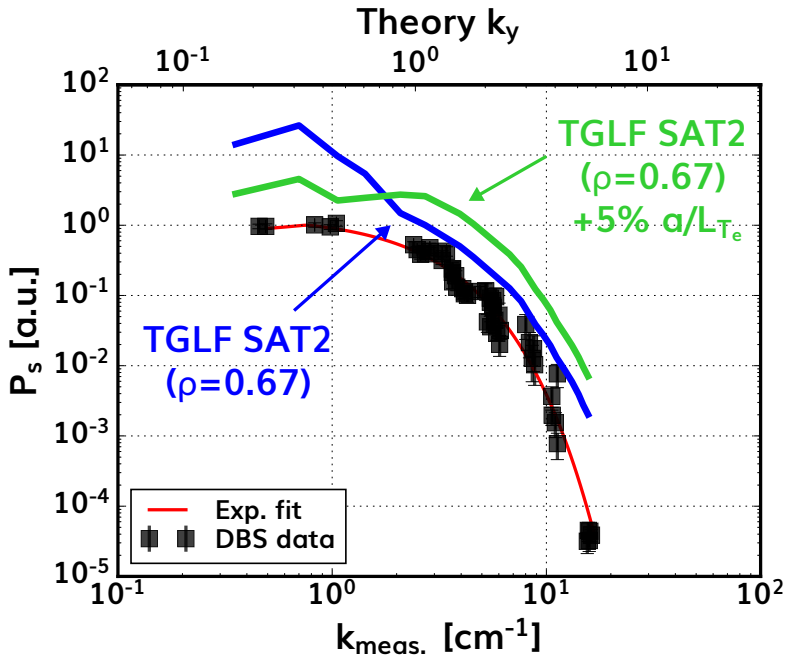

Figure 4.23: Comparison of synthetic $P_s^{\mathrm{TGLF}}(k)$ forward modeling results with DBS measurements. The upper x-axis is the theory k_y value (calculated using eq. **??**(a)) while the bottom x-axis is the measured wavenumber in cm^{-1}. The DBS data shown in Figure 4.14 is identical to the data shown in Figure 4.6. The discharge numbers and DBS system information has been suppressed for clarity. The green $P_s^{\mathrm{TGLF}}(k)$ result corresponds to a TGLF simulation where the a/L_{T_e} value is increased by 5%.

at low-k. Furthermore, the flux-matching solution found with TGYRO-TGLF in Subsection 4.4.5 actually *decreased* the experimental a/L_{T_e} at $\rho \leq 0.67$ to match the thermal fluxes.

It is also important to note that for $k_y \geq 1$ the forward-modeled $P_s^{\mathrm{TGLF}}(k)$ spectra shown in Figure 4.14 are roughly in agreement regardless of whether we include the ρ variation. This suggests that the higher-k portion of the density fluctuation spectrum appears insensitive to the precise radial location – validating the use of the $\rho = 0.67$ TGLF-$\delta\hat{n}$ at various radii.

4.5.4 Additional synthetic diagnostic modeling

Both the forward-modeled TGLF and CGYRO $P_s(k)$ spectra shown in Figure 4.13 exhibit a steeper spectral index at low-k relative to the DBS measurements. Specifically, the pre-

dicted spectral decay is steeper than measurements[11] over the range $0.4 < k_y < 1.2$. The are two possible explanations for the discrepancy: (1) Both nonlinear CGYRO and TGLF are inaccurately simulating[12] the fluctuations over this range of k_y or (2) The beam-DBS model (providing the DBS weighting function) is not accurately modeling the DBS diagnostic response over this range of k_y. Pursuing explanation (1) would require computationally intensive turbulence simulations exceeding the state of the art and is therefore deemed beyond the scope of this thesis. In this subsection we investigate explanation (2) by comparing low incidence angle beam tracing simulations with full-wave calculations of the probing DBS E-field introduced in Section 3.6.

It should be remarked that the beam-DBS model can fail to capture the DBS diagnostic response if the fluctuation amplitude becomes large enough to enter the nonlinear response regime introduced in Section 3.8. For sufficiently large density fluctuation amplitude we expect the level of back-scattered power to saturate. This effect would result in a flat *measured* $P_s(k)$ spectrum but would not be present in the synthetic $P_s^{\text{syn.}}(k)$ calculations (the beam-DBS model assumes a linear diagnostic response). Scans of the $\delta n/n$ amplitude in 2D full-wave COMSOL simulations found the linear/nonlinear threshold to be approximately $\delta n/n \approx 1\%$ for this plasma (Figure 3.12(b)). Meanwhile, the nonlinear CGYRO and TGLF simulations predict the (time-averaged) amplitude of low-k_y $\delta\hat{n}$ fluctuations to peak at $\delta n/n \approx 0.5\%$. Therefore, we are not obviously impacted by nonlinear scattering phenomena but we are also not far from the linear/nonlinear threshold at low-k.

To further investigate the beam-DBS weighting function at low-k, we will focus on cases with low poloidal launch angles. The lower-k measurements shown in Figure 4.6 were performed with a poloidal launch-angle of approximately 2.5°. To investigate this situation further, we performed a 2D-FW COMSOL simulation with 2.5° poloidal launch angle. The

[11]It should be noted that we do not have DBS measurements over the range of k where the spectral decay disagrees with simulations. Thus, the 'measured' spectral decay over this range is technically an interpolation over measurements at lower and higher k.

[12]Of course TGLF intends to mimic the higher-fidelity gyrokinetics within CGYRO, and some parameters of the TGLF saturation rule are fit to nonlinear CGYRO simulations - thus the two are not strictly independent models.

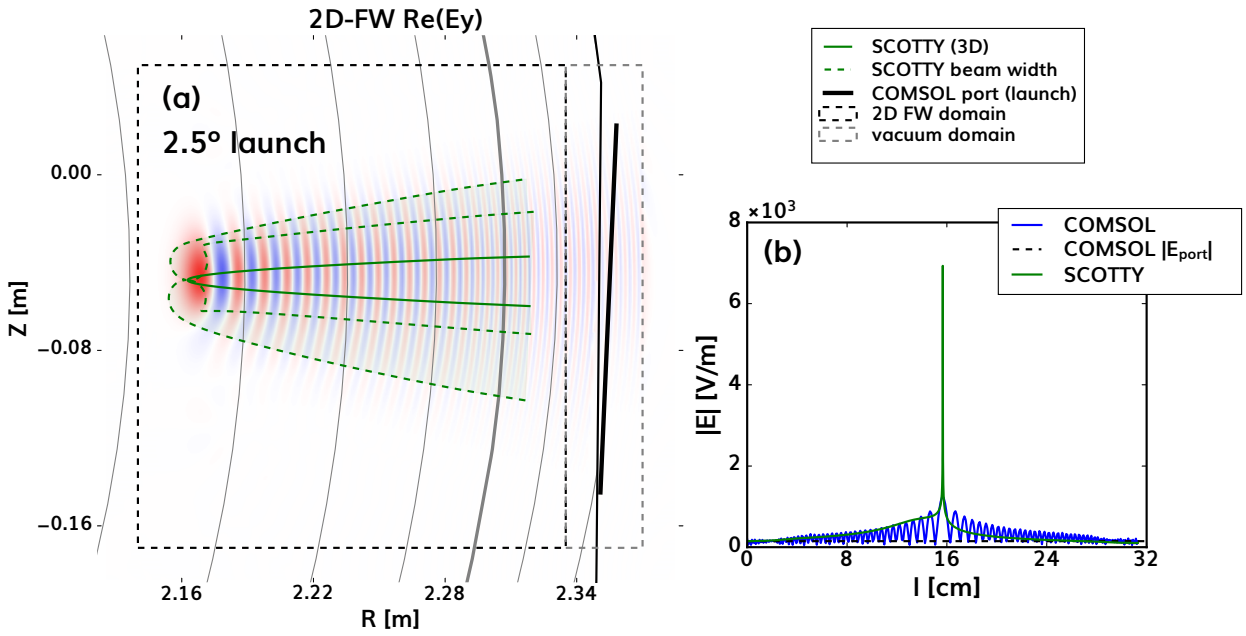

Figure 4.24: COMSOL results for low launch-angle DBS. Figure 4.24(a) shows the full-wave Re(E_y) field with the SCOTTY trajectory and beam envelope over-plotted. Figure 4.24(b) shows the magnitude of the wave electric field along the trajectory of the central ray. The case shown in Figure 4.24 corresponds to 72.5 GHz, X-mode polarization.

result of this simulation is shown in Figure 4.24. In Figure 4.24(a) we observe that the incident and reflected beams have folded onto one another with the outgoing reflected beam visible to the *right* of the COMSOL port before striking the PML. The SCOTTY beam tracing simulation in Figure 4.24(a) does appear to capture the overall envelop of the full wave result (dashed green lines) with the exception of excessive 'pinching' of the beam width at cutoff. Beam-pinching is the formation of a 'bottleneck' in the beam width calculated using beam tracing (see Section 3.5). This effect can be a sign of the failure of the beam-tracing method near fold-type caustics [136].

Figure 4.24(b) shows the electric field amplitude, $E = |\mathbf{E}|$, along the trajectory of the central ray as reported by SCOTTY and COMSOL[13]. The E-field comparison in Figure 4.24(b) shows that SCOTTY predicts a large, narrow peak at the cutoff location roughly

[13]Close inspection of Figure 4.24(a) suggests that the SCOTTY trajectory misses the peak of the field at cutoff. To extract the COMSOL field more accurately, we displace the SCOTTY trajectory by $\Delta R = +6$ mm and interpolate the COMSOL field onto the shifted trajectory.

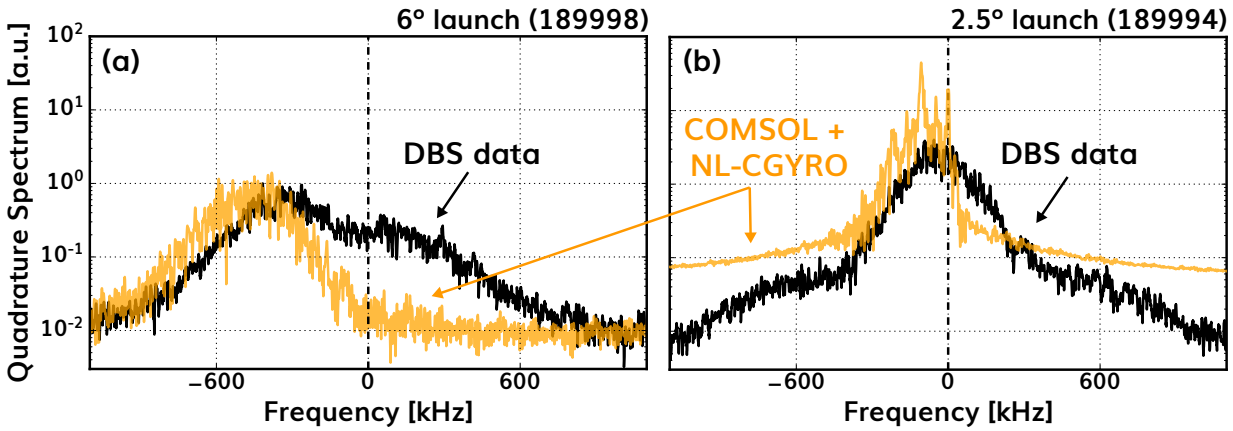

Figure 4.25: Synthetic DBS frequency spectra for the 72.5 GHz channel of the DBS60 system. The synthetic spectra are generated with the COMSOL 2D full-wave E-field and the $\delta\hat{n}$ from a nonlinear CGYRO simulation. Figure 4.25(a) shows the intermediate launch angle case while Figure 4.25(b) shows the low-incidence launch angle case.

6× the COMSOL value. This peak in the SCOTTY E enters the DBS weighting function as part of the 'ray' term. The end result of this type of peak will be to focus and enhance the DBS response at the cutoff. Thus, this effect may produce undue DBS sensitivity at low-k leading to a steeper predicted spectral decay. This effect may be responsible for the low-k portion of the $P_s^{\mathrm{TGLF}}/\langle|\delta\hat{n}|^2\rangle|_{k_n=0}$ ratio in Figure 4.22(b). Thus, the discrepancy in spectral decay between the DBS measurements and the synthetic $P_s^{\mathrm{syn.}}$ in Figure 4.13 may be partially due to a failure of the beam-DBS model at lower-$k_{\mathrm{meas.}}$.

The SCOTTY-COMSOL comparison shown in Figure 4.24 motivated an additional comparison between DBS measurements and simulations at low-$k_{\mathrm{meas.}}$. For this comparison we depart from the beam-DBS synthetic diagnostic discussed throughout this chapter. Instead, we combine 2D full-wave COMSOL results with a nonlinear CGYRO simulation to produce a synthetic *frequency* spectrum using methods outlined in Section 3.7. We compare the low incidence angle case (Figure 4.24) with an intermediate-k case using 6° poloidal launch-angle (similar to what was shown previously in Figure 3.10).

Figure 4.25 shows synthetic frequency spectra created by combining COMSOL and nonlinear CGYRO results (using Equation 3.56). The measured DBS (quadrature amplitude)

frequency spectrum was calculated using methods[14] discussed in Section 3.3 and is shown with arbitrary units [a.u.]. Both synthetic results shown in Figure 4.25 use the same overall multiplicative normalizing factor[15] to be consistent. Both measured DBS frequency spectra shown in Figure 4.25 come from the X-mode polarized, 72.5 GHz channel of the DBS60 system and can therefore be compared on the same scale.

The intermediate-k comparison in Figure 4.25(a) shows the COMSOL+CGYRO synthetic frequency spectrum agrees remarkably well with the measured, Doppler-shifted peak in the negative frequency half-plane[16]. The COMSOL+CGYRO model reproduces both the signal-to-noise level and width of the measured peak. However, the measured spectrum appears to contain multiple components including a broad feature in the positive frequency half-plane. This additional spectral component was not reproduced by the COMSOL+CGYRO model. Table 4.2 provides a comparison of the frequencies in Figure 4.25. In Figure 4.25(a), the Doppler shift of the synthetic spectrum is approximately 130 kHz larger (more negative) compared with the measured Doppler shift. Given $k_{\text{meas.}} \approx 5$ cm^{-1} for this case, $\Delta f_{\text{Dopp.}} = 130$ kHz implies a difference in velocity of $\Delta v \approx 1.7$ km/s.

Upon further investigation, the Doppler shift from the COMSOL+CGYRO model is almost entirely due to local $E \times B$ motion (synthetic $f_{\text{Dopp.}} - f_{E\times B} = 25$ kHz in Table 4.2). The local $E \times B$ rotation value enters the nonlinear CGYRO analysis through the value of $\omega_{E\times B} = E_r/RB_p$, the toroidal $E \times B$ rotation frequency (this will be discussed in more detail in Section 5.1.1). The local $\omega_{E\times B}$ value was input to CGYRO from charge exchange recombination (CER) rotation measurements with local ($\rho = 0.67$) uncertainty $\approx \pm 1$ km/s for this plasma. Therefore, the shift between the COMSOL+CGYRO model and the DBS data in Figure 4.25(a) may be due to an inaccurate local $\omega_{E\times B}$ value from CER. Alternatively, if we take the local $\omega_{E\times B}$ value from CER as ground-truth, the shift in Figure

[14]Specifically, for the spectra in Figure 4.25, we use NFFT=16,384, 50% overlap, 5 kHz smoothing, and 50-95% ELM filtering.

[15]In this case the normalizing factor was (arbitrarily) selected such that the synthetic peak in Figure 4.25(a) matches the measurements.

[16]In this case, increasingly negative frequency corresponds to lab-frame motion in the ion diamagnetic direction.

Table 4.2: Parameters related to the synthetic frequency spectra shown in Figure 4.25. All frequency values are given in kHz.

Quantity	intermediate-k – Figure 4.25(a)	low-k – Figure 4.25(b)
measured $f_{\text{Dopp.}}$	-325	-50
synthetic $f_{\text{Dopp.}}$	-458	-107
$\Delta f_{\text{Dopp.}} = \text{meas.} - \text{syn.}$	133	57
k	4.85 [cm^{-1}]	0.74 [cm^{-1}]
$\Delta v_{\text{Dopp.}} = 2\pi\Delta f_{\text{Dopp.}}/k$	1.7 [km/s]	4.8 [km/s]
$f_{E\times B}$ (CER)	-484	-74
measured $f_{\text{Dopp.}} - f_{E\times B}$	159 (elec. dir.)	24 (elec. dir.)
synthetic $f_{\text{Dopp.}} - f_{E\times B}$	25 (elec. dir.)	-33 (ion dir.)
measured $v_{\text{ph.}} = 2\pi(f_{\text{Dopp.}} - f_{E\times B})/k$	2.1 [km/s] (elec. dir.)	2.0 [km/s] (elec. dir.)
synthetic $v_{\text{ph.}} = 2\pi(f_{\text{Dopp.}} - f_{E\times B})/k$	0.3 [km/s] (elec. dir.)	-2.8 [km/s] (ion dir.)
Linear CGYRO $v_{\text{ph.}}$	0.75 [km/s] (elec. dir.)	-0.25 [km/s] (ion. dir.)

4.25(a) implies that DBS observes a turbulence phase velocity in the electron diamagnetic direction of $v_{\text{ph.}} \approx 2.1$ km/s which is not reproduced in the CGYRO simulation. The implied $v_{\text{ph.}} \approx 2.1$ km/s is larger than the linear estimate of the turbulence phase velocity, $v_{ph.} \approx 0.75$ km/s based on the CGYRO eigenvalue spectrum (Figure 4.7).

Unlike the intermediate-k case shown in Figure 4.25(a), the low-k synthetic frequency spectrum in Figure 4.25(b) is significantly different from the DBS measurements. The synthetic spectrum has a series of narrow ($\Delta f_s \approx 10$ kHz) spikes located at $f_{\text{Dopp.}} \pm nf_s$ with $f_s \approx 56$ kHz and $n \in [-2, -1, 0, 1, 2]$. The spacing of the spikes appears to be $f_s \approx$ syn. $f_{\text{Dopp.}}/2$. These spikes are not observed in the measured spectrum. Similar to the intermediate-k case, the synthetic spectrum is shifted to a more negative Doppler shift compared to the measured spectrum. In this case, the difference in Doppler shift between the synthetic spectrum and the measurements is $\Delta f_{\text{Dopp.}} = 57$ kHz. Given $k_{\text{meas.}} \approx 0.74$ cm^{-1} for this case, $\Delta f_{\text{Dopp.}} = 57$ kHz implies $\Delta v \approx 4.8$ km/s. This discrepancy in velocity is very large (on the same order as the local $v_{E\times B}$). Furthermore, in contrast with the intermediate-k case, the Doppler shift of the COMSOL+CGYRO spectrum (largest spike in Figure 4.25(b)) is shifted in the *ion* diamagnetic direction relative to the $f_{E\times B}$ value implied by CER measurements. The DBS measurements are shifted in the electron diamagnetic

direction relative to the CER $f_{E\times B}$, same as the intermediate-k case.

In summary, the synthetic frequency spectra shown in Figure 4.25 provide another means to compare DBS measurements with simulations. The synthetic frequency spectrum for the intermediate-k case shown in Figure 4.25(a) appears more similar to the measured spectrum than the low-k case shown in Figure 4.25(b). However, we still cannot distinguish whether any discrepancies are a consequence of an inaccurate DBS model (i.e. the COMSOL E-field and Equation 3.56) or a consequence of an inaccurate simulation of $\delta\hat{n}$ by nonlinear CGYRO. In reality it may be a mixture of effects. We also must be careful in interpreting discrepancies in the Doppler shifts visible in Figure 4.25 given that the CGYRO $\omega_{E\times B}$ value originates from another diagnostic (CER) with its own uncertainties.

4.6 Conclusions

In this chapter we reported results from an investigation of the (binormal) wavenumber spectrum of density fluctuations using the Doppler back-scattering diagnostic. Wavenumber spectrum measurements we made in ECH H-mode plasmas where microturbulence driven by electron pressure gradients (TEM, ETG modes) was expected to contribute significantly to transport. During the experiment, ECH H-modes were reliably obtained and provided a suitable background for fluctuation measurements. Plasmas obtained low core collisionality $\nu_{*e} \approx 0.1$ and high $\eta_e \approx 3$. Using two DBS systems, we performed an extensive scan of the DBS launch-angle(s) while leveraging the toroidal steering capability of the DBS240 system to make high-k measurements without losing signal to mismatch attenuation.

The measured back-scattered power wavenumber spectrum, $P_s(k)$, is the primary experimental result from this investigation. When analyzed in terms of power-laws, $k^{-\nu}$, the measured spectrum exhibited variable spectral decay: $\nu \approx 0.6$ ($k < 3.5$ cm^{-1}), $\nu \approx 2.6$ ($3.5 < k < 8.5$ cm^{-1}), and $\nu \approx 9.4$ ($k > 8.5$ cm^{-1}). When analyzed in log-linear space the measured spectrum was found to exhibit approximately exponential decay overall. Exponential decay was analyzed in normalized $k_\perp\rho_s$-space and two exponential decay factors, ζ for

$e^{-\zeta(k_\perp \rho_s)}$, were found. Over the majority of the measurements $\zeta \approx 1.7$ was found to describe the exponential spectral decay. For the highest-$k_\perp \rho_s$ measurements, the decay increased to $\zeta \approx 3.9$. Results from this investigation were compared with previous studies and the physical implications of variable spectral decay in $\delta\hat{n}^2$ were discussed.

Synthetic diagnostic modeling was used to test models of plasma turbulence given the measured $P_s(k)$ spectrum. Forward-modeling of DBS measurements was performed using the beam-DBS framework (3D beam-tracing with the code SCOTTY) and theory-based models of the $\delta\hat{n}$ spectrum (from CGYRO and TGLF). The resulting synthetic $P_s^{\text{syn.}}(k)$ spectrum was compared directly with measurements. The predicted spectral shape at $k_y \leq 0.3$ and $k_y \geq 1.2$, was in good agreement with the DBS measurements. Over the range $0.4 < k_y < 1.2$ the predicted spectrum decayed more rapidly than the measured spectrum. In Subsections 4.5.2 and 4.5.4 we presented some evidence that the beam-DBS model may become inaccurate near the cutoff at low incidence angles, leading to steeper $P_s^{\text{syn.}}$ predictions at low $k_{\text{meas.}}$. However, the precise cause of increased spectral decay for $0.4 < k_y < 1.2$ cannot be attributed completely to the DBS model, i.e. it may be a failure of the turbulence simulations. In Subsection 4.5.4 we departed from the beam-DBS model to performing an additional comparison using the DBS frequency spectrum. Measured frequency spectra were compared with synthetic frequency spectra calculated by combining 2D full-wave COMSOL and nonlinear CGYRO simulations. The frequency spectrum comparison reveled mixed agreement with significant differences between the intermediate vs. low-k cases. It remains unclear if discrepancies are due to the model for DBS or the simulations of δn fluctuations.

Beyond DBS modeling, transport modeling presented in Subsection 4.4.5 was performed to interpret the transport character of the ECH H-mode regime. Both TGLF and nonlinear CGYRO predict the transport in all channels to be dominated by ion-scale modes at $k_y < 1$. Both CGYRO and TGLF under-predict the experimentally-inferred thermal fluxes at $\rho = 0.67$ when simulations are performed with the experimental profiles. Flux-matching was performed with the TGYRO transport solver. Iteration with TGYRO-TGLF resulted in a close match of the thermal fluxes over the core of the plasma ($\rho \in [0.35, 0.85]$). One-

dimensional scans of the ion and electron temperature gradient scale-lengths (a/L_{T_e}, a/L_{T_D}) with TGLF and ion-scale nonlinear CGYRO simulations found that TGLF was able to reproduce the flux-gradient relationship in the ion thermal channel. However, in the electron thermal channel TGLF predicts the dominance of TEM instabilities at marginally larger a/L_{T_e} with an associated nonlinear increase in Q_e. This prediction from TGLF was not reproduced by nonlinear CGYRO. Therefore, while flux-matching with TGLF was possible – it is unclear if the underlying quasi-linear predictions of transport in the ECH H-mode regime are faithful to the higher-fidelity gyrokinetics.

CHAPTER 5

Cross-diagnostic comparison of rotation measurements

In this chapter we present cross-diagnostic comparisons of rotation measurements made by the DBS and Charge Exchange Recombination Spectroscopy (CER) diagnostics. The goal of this investigation was to rigorously quantify the tendency for the $E \times B$ rotation values inferred from DBS and CER to agree (or disagree) under a variety of NBI-applied torque conditions. DBS makes rotation measurements through the Doppler shift of scattered electromagnetic radiation (scattering is primarily due to electrons). CER makes rotation measurements through the Doppler shift of photons emitted while impurity ions (Carbon) interact with neutrals from NBI. Given that DBS and CER make measurements through different physical processes, their agreement can bolster confidence in each technique, suggesting mutual validation. Furthermore, since CER is an NBI-dependant diagnostic, it is challenging for CER measurements to capture the neutral beam's own fast timescale (< 10 ms) impact on the rotation profile. However, DBS measurements are available regardless of the neutral beam and can theoretically observe rapid changes in $E \times B$ rotation. The majority of the work presented in this chapter has been published by the author in [9].

The primary results of this study include rigorous analysis of the DBS velocity measurements including the propagation of uncertainties through ray tracing simulations and lineshape fitting in the frequency domain. We present radial profiles of the $E \times B$ rotation frequency for three background NBI-torque levels. Extended analysis includes: estimation of the turbulence phase velocity from TGLF simulations, statistical analysis of the DBS-CER agreement, the impact of prompt-torque on the rotation profile, and a comparison of the $E \times B$ shearing rate derived from each diagnostics' measurements.

5.1 Background

5.1.1 Rotation in tokamaks

Neoclassical theory for rotating tokamak plasmas was developed by Hinton and Wong in [137]. Hinton and Wong presented a small gyro-radius expansion of the Fokker-Planck equation, retaining velocities on the order of the ion thermal speed in a general axisymmetric tokamak magnetic field of the form,

$$\mathbf{B} = I(\psi)\nabla\phi + \nabla\phi + \nabla\psi. \tag{5.1}$$

In Equation 5.1, ψ is the poloidal magnetic flux, ϕ is the toroidal coordinate, and $I(\psi) = RB_\phi$ is a flux function. The general form of the velocity was shown to be,

$$\mathbf{u} = \omega(\psi)R\hat{\mathbf{e}}_\phi + F(\psi)\mathbf{B}, \tag{5.2}$$

where $\omega(\psi)$ is a toroidal angular rotation flux function, R is the major radius, $\hat{\mathbf{e}}_\phi = R\nabla\phi$ is the unit vector in the toroidal direction, and $F(\psi)$ is another scalar flux function. Helander and Sigmar [138] discuss that the velocity in Equation 5.2 is in fact the most general form for an incompressible flow tangential to flux surfaces in a tokamak. Any poloidal rotation within the flux surface would be included included in the quantity $F(\psi)$.

Hinton and Wong [137] find that, to lowest order in ρ_*, the toroidal angular speed in Equation 5.2 is $\omega(\psi) = -d\Phi/d\psi = E_r/RB_\theta \equiv \omega_{E\times B}(\psi)$. Where Φ is the electrostatic potential, E_r is the radial electric field, and B_θ is the poloidal magnetic field. Hinton and Wong also show that, at this order in ρ_*, the scalar function $F(\psi) = 0$. Thus, the only bulk plasma rotation theoretically allowed is rigid toroidal rotation due to a background radial electric field. Helander and Sigmar [138] explain this rotation is such that the local E_r vanishes in the rotating frame. Note that while the $E \times B$ velocity itself is manifestly in the binormal direction (mutually perpendicular to both B and E_r), the quantity E_r/RB_θ is a *toroidal* angular frequency.

First order (in ρ_*) expressions for neoclassical flows can be found in work by Kim *et al.* [139]. At first order, terms involving the (species-dependant) diamagnetic flow appear in Equation 5.2. It can be shown that the bulk flow velocity takes the form,

$$\mathbf{u}_a = \omega_a(\psi) R \hat{\mathbf{e}}_\phi + u_{\theta,a}\mathbf{B}, \tag{5.3}$$

where a index the plasma species and we introduce the following quantities,

$$\omega_a(\psi) = V_{\psi,a}/I(\psi), \tag{5.4a}$$

$$u_{\theta,a} = -V_{\psi,a}/B^2 + u_{\parallel,a}/B, \tag{5.4b}$$

$$V_{\psi,a} = I(\psi)\left[\omega_{E\times B} - \frac{1}{q_a n_a}\frac{dp_a}{d\psi}\right]. \tag{5.4c}$$

In comparing Equation 5.2 and 5.3 we see that the flux function F is the poloidal rotation speed, $F(\psi) = u_{\theta,a}(\psi)$. The neoclassical poloidal velocity involves the diamagnetic drift term and $\omega_{E\times B}$. Additionally, Equation 5.4(b) shows that the poloidal and *parallel* flows are linked. Conservation of momentum can be used to derive an expression for the evolution of the poloidal flow. It can be shown that poloidal flows are strongly damped on the ion-ion collision timescale [140]. Thus, while neoclassical rotation includes toroidal and poloidal components, poloidal rotation is expected to be smaller than $E \times B$ toroidal rotation and strongly damped toward the form in Equation 5.3.

Radial force balance

Equilibrium pressure-balance on flux surfaces requires that,

$$\mathbf{E} = \frac{\nabla p_a}{q_a n_a} - (\mathbf{u}_a \times \mathbf{B}). \tag{5.5}$$

If we take the dot product of the above equation with $\hat{\mathbf{e}}_r = \hat{\mathbf{e}}_\psi = \nabla\psi/|\nabla\psi|$ we find,

$$\omega_{E\times B} = \frac{1}{q_a n_a}\frac{dp_a}{d\psi} - \left(\frac{B_\phi}{B_\theta}\right)\frac{u_{\theta,a}}{R} + \frac{u_{\phi,a}}{R}, \tag{5.6}$$

where we have used $|\nabla\psi| = RB_\theta$. Equation 5.6 is more commonly written as an equation for E_r,

$$E_r = \frac{\nabla p_a}{q_a n_a} - u_{\theta,a} B_\phi + u_{\phi,a} B_\theta. \tag{5.7}$$

This is often called the radial force balance equation and is used in the analysis of charge exchange data discussed in the next subsection.

5.1.2 The CER diagnostic

The Charge-Exchange Recombination Spectroscopy (CER) diagnostic measures the Doppler shift in radiation from ions in the plasma undergoing a charge-exchange reaction with neutral atoms from Neutral Beam Injection (NBI). In this case, the ions are Carbon impurities from the DIII-D graphite wall and the injected neutral atoms are deuterium. When participating in charge-exchange, impurity ions transiently enter an excited atomic state and then – after the lifetime of the state – emit a photon and relax to a ground state. The emitted photons are collected by CER spectrometers positioned around the tokamak. Multiple quantities are derived from the received photons: the intensity of the radiation is related to the impurity density, the Doppler shift of the atomic line gives a velocity, and the broadening of the atomic line is used to calculate the impurity temperature. The direction of the velocity inferred from the CER Doppler shift depends on the line-of-sight of the spectrometer. Vertical, radial, and tangential lines-of-sight are used to determine different components of the impurity velocity [141].

Multiple corrections must be applied to CER measurements to accurately derive the impurity density, temperature, and velocity. Notably, one must correct for the energy-dependence of the cross section for charge-exchange [142, 143]. Measurements of poloidal rotation require vertical lines-of-sight and must be corrected for gyro-motion coupled with atomic physics effects. Corrections to the poloidal velocity are often a significant fraction of the measurement. For a more complete description of the CER methodology for extracting poloidal rotation quantities see [141]. It is worth noting that the C^{6+} ion density profile calculated by the brightness of CER lines also depends on simulated neutral beam deposition

profiles which themselves depend on the electron density and temperature. Thus, CER analysis includes outputs from other diagnostics to calculate the final observables.

For the rotation comparison at hand, we use CER measurements to derive the radial electric field, E_r, using the radial force balance equation (Eq. 5.7 above) [144]. For use with CER measurements, u_a, n_a, and q_a are the velocity, density, and charge of the measured species (a) respectively. Theoretically, the E_r appearing in Equation 5.7 is the self-consistent field produced by the motion of all plasma species. Therefore, the E_r provided by CER should be independent of the observed species. As discussed in Section 3.1.5, the $E \times B$ angular frequency, $\omega_{E\times B}$ is the preferred quantity for making $E \times B$ rotation comparisons because it is theoretically a flux-function. Thus, the $\omega_{E\times B}$ value from CER is simply Equation 5.6, where kinetic quantities are evaluated for the Carbon impurity species (given that CER measures Carbon in this case).

There is no general ordering for the three terms in Equation 5.6 since each terms' magnitude varies strongly with radius (e.g. the $dp_s/d\psi$ term can be small in the core plasma but large in an H-mode pedestal). Furthermore, depending on the magnitude of external sources of momentum, the rotation terms can be virtually any magnitude. However, as discussed previously, background poloidal rotation is $\mathcal{O}(\rho_*)$ smaller than toroidal $E \times B$ rotation according to neoclassical theory, so we generally expect $u_\phi > u_\theta$. In the L-mode plasmas presented here, given weak pressure gradients and unbalanced external NBI torque, we expect the toroidal rotation velocity term to dominate, but it is important to note that each term is accounted for in the analysis.

5.2 Experiment

The plasma used for this investigation is an L-mode DIII-D discharge (180882). This discharge was designed to test upgrades to the DIII-D NBI system to allow for off-axis heating and current-drive using the 210° beam-line [145]. Importantly, this discharge contains a feed-forward scan of the NBI-applied torque. Figure 2.3 provides a plan-view of the DIII-D

tokamak illustrating the orientation of the various neutral beams for this discharge. It is important to note that the neutral beam located at the 210° port is oriented counter-I_p (as shown in Figure 2.3).

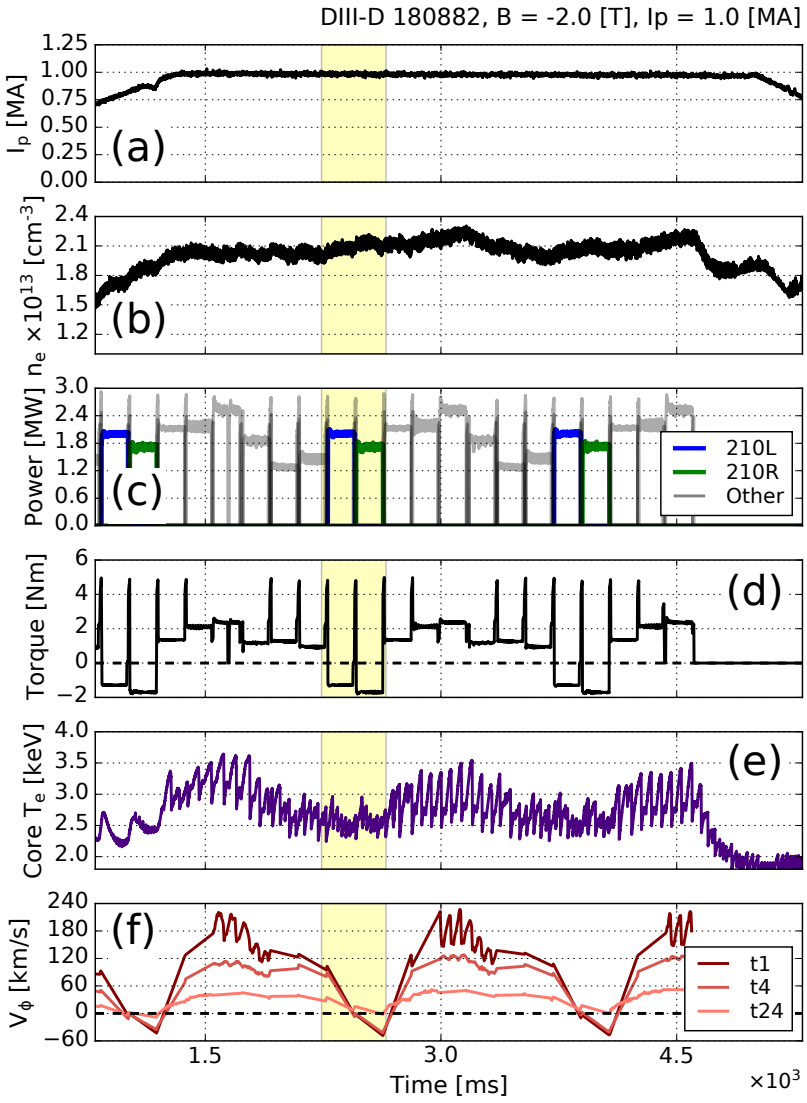

Figure 5.1: Overview of DIII-D discharge 180882 used for this study. 5.1(a) shows the plasma current, 5.1(b) shows the line-averaged density, 5.1(c) shows the injected power from NBI, 5.1(d) shows the torque applied by NBI, 5.1(e) shows the electron temperature from electron-cyclotron emission in the core region, and 5.1(f) shows the toroidal rotation in the deep core (t1, $R = 1.8$ m), mid region (t4, $R = 2.0$ m) and edge (t24, $R = 2.2$ m). The colored lines in 5.1(c) indicate counter-I_p NBI. The yellow shaded portion of the figure indicates where we perform our analysis.

Figure 5.1 shows the evolution of plasma discharge. The yellow shaded region indicates our time span of interest. The plasma current is constant at $I_p = 1.0$ MA, the toroidal magnetic field is $B_\phi = -2.0$ T (opposing I_p), and the line-averaged plasma density is approximately 2×10^{13} cm^{-3}. To avoid an L-H transition the plasma shape was placed in an upper single null configuration with edge safety factor $q_{95} \approx 5.0$ and normalized plasma beta $\beta_n \approx 0.6$. High q_{95} and low β_n produce a relatively MHD-quiescent plasma. The core electron temperature, seen in Figure 5.1(e), exhibits sawteeth oscillations when strong co-injection occurs. Sawteeth oscillations are core MHD instabilities associated with the collapse and rearrangement of flux surfaces with safety factor $q < 1$ [19]. The sawteeth oscillations appear subdued when the applied torque is negative. Lastly, the toroidal rotation measured by CER at various radial positions is visible in Figure 5.1(f). As expected, the toroidal rotation decreases dramatically when the 210 beam is injected.

Figure 5.1(c) shows the power delivered by NBI. The power from the 210L/R beams is indicated by colored lines to highlight the counter injection. An estimation of the applied torque from the NBI is shown in Figure 5.1(d). This estimation is based on the beam orientations and accelerating voltages. We focus our analysis on the large change in applied torque when the 210 neutral beam is injected ($2280 < t < 2630$ ms). The two 210 sources (L, R) fire sequentially starting at 2280 ms. Both sources apply a 170 ms pulse with a 10 ms gap in between. In order to perform a meaningful cross-diagnostic comparison, we must identify locations and times where both diagnostics have data. Details of the time resolution and analysis specifics for both DBS and CER are given in the next section.

5.3 CER, DBS measurements and data analysis

The CER diagnostic system uses 10 ms duration diagnostic 'blips' from the 330L/R and 30L neutral beams to make measurements (see Figure 2.3). As discussed in Subsection 5.1.2, CER makes measurements along specific lines-of-sight. These lines-of-sight intersect the paths of different NBI sources at different radial locations. Thus, more than one NBI source is required to measure a complete radial profile. Given the sequence of blips used in this

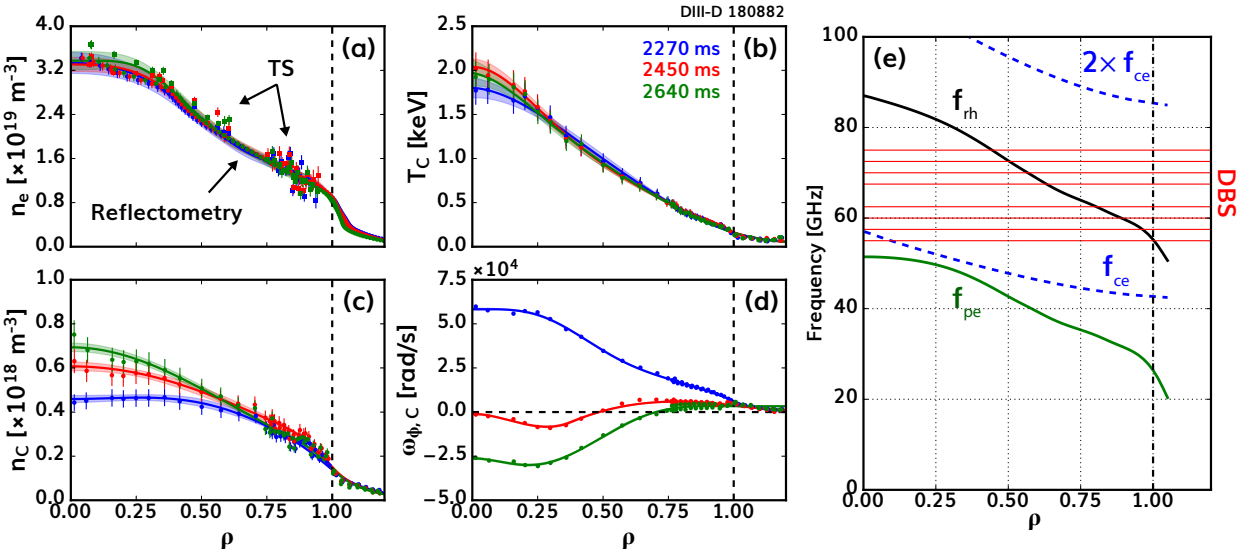

Figure 5.2: Kinetic profiles for discharge 180882 at the nominal times for DBS-CER comparison along with a profile of the cutoffs relevant to DBS at 2270 ms. Each figure (a-d) shows spline fits along with 20 ms time-averaged data. 5.2(a) shows the electron density with Thomson scattering (TS) and profile reflectometry measurements. 5.2(b,c,d) show the CER-measured Carbon impurity temperature, density, and toroidal rotation velocity respectively. 5.2(e) shows fundamental frequencies evaluated along the low-field-side midplane. The DBS frequencies are shown with red horizontal lines.

plasma, the complete radial profile of CER measurements comes from a 20 ms time span. Thus, ±10 ms is the fundamental time resolution of the CER profiles for the present analysis. Higher time-resolution diagnostics are ultimately mapped to this time-basis. Three separate sets of NBI blips are visible as large spikes in the highlighted portion of Figures 5.1(c,d). The midpoint of each 20 ms blip span is used as a nominal time for comparison with DBS. These times are: 2270, 2450, and 2640 ms.

Figure 5.2 shows kinetic profiles for this plasma discharge at the three nominal times. We find all profiles remain relatively unchanged except for the core impurity density and the carbon toroidal rotation frequency (due to the changing NBI torque). Figure 5.2(e) shows radial profiles of relevant DBS frequencies evaluated along the low field side midplane. Because the density profile in Figure 5.2(a) is largely unchanged over our time span of interest, we expect the probed DBS locations to remain approximately unchanged over the

torque scan. However, to observe any prompt changes in the rotation caused by the NBI blips, we will leverage the high time resolution of DBS and the similarly high time resolution of the profile reflectometry diagnostic [117]. The reflectometry profiles of n_e are averaged over 2 ms intervals for DBS ray tracing simulations. The reflectometry profiles shown in Figure 5.2(a) are averaged over a 20 ms interval for comparison with Thomson scattering, the 2 ms time resolution n_e profiles (not shown) are similar but with higher statistical variance.

The DBS data used in this investigation comes from the eight-channel DBS60 system. X-mode polarization is used with a relatively low poloidal launch angle of 3°. DBS data were digitized at 5 MHz and processed using spectral methods presented in Section 3.3. The quadrature spectrogram of the 72.5 GHz channel at $\rho \approx 0.5$ is shown in Figure 5.3(a) along with the neutral beam torque in Figure 5.3(b). Three time slices of the spectrogram in Figure 5.3(a) are shown in 5.3(c) with fits (dashed lines). When performing fits, spectra are subject to a ±40 kHz notch-filter about $f = 0$. This is to avoid fitting the narrow "spike" with no Doppler shift which is possibly due to spurious reflections or high-k_r scattering mentioned in Section 3.3.

In this investigation it was noted that the shape of the spectrum changed considerably over the time window of interest. The shape near the Doppler-shifted peak appears to change between Gaussian and exponential (parabolic and linear in semilog-y space). Based on this observation we use the four-parameter Generalized Gaussian (GG) lineshape to fit the DBS spectra. This lineshape has the form,

$$\hat{S}_{GG}(f; A, f_{\text{Dopp.}}, \sigma, \beta) = \frac{A\beta}{2\sqrt{2}\sigma\Gamma(1/\beta)} \exp\left(-\frac{|f - f_{\text{Dopp.}}|}{\sqrt{2}\sigma}\right)^{\beta}, \tag{5.8}$$

(repeated from Appendix B). For the spectrum shown in Figure 5.3(a), the GG function resulted in an average reduced chi-squared 17% closer to 1.0 versus standard three-parameter Gaussian fits. Fits to the DBS spectra are performed at every time-slice of the DBS spectrograms to systematically identify the Doppler shift. Evolution in the spectral full-width-half-max (FWHM) is also captured by the GG fitting function, FWHM $= 2\sqrt{2}\sigma[\ln(2)]^{1/\beta}$ for $\beta > 0$. The evolution of the FWHM from this dataset was shown earlier in Figure 3.3. The

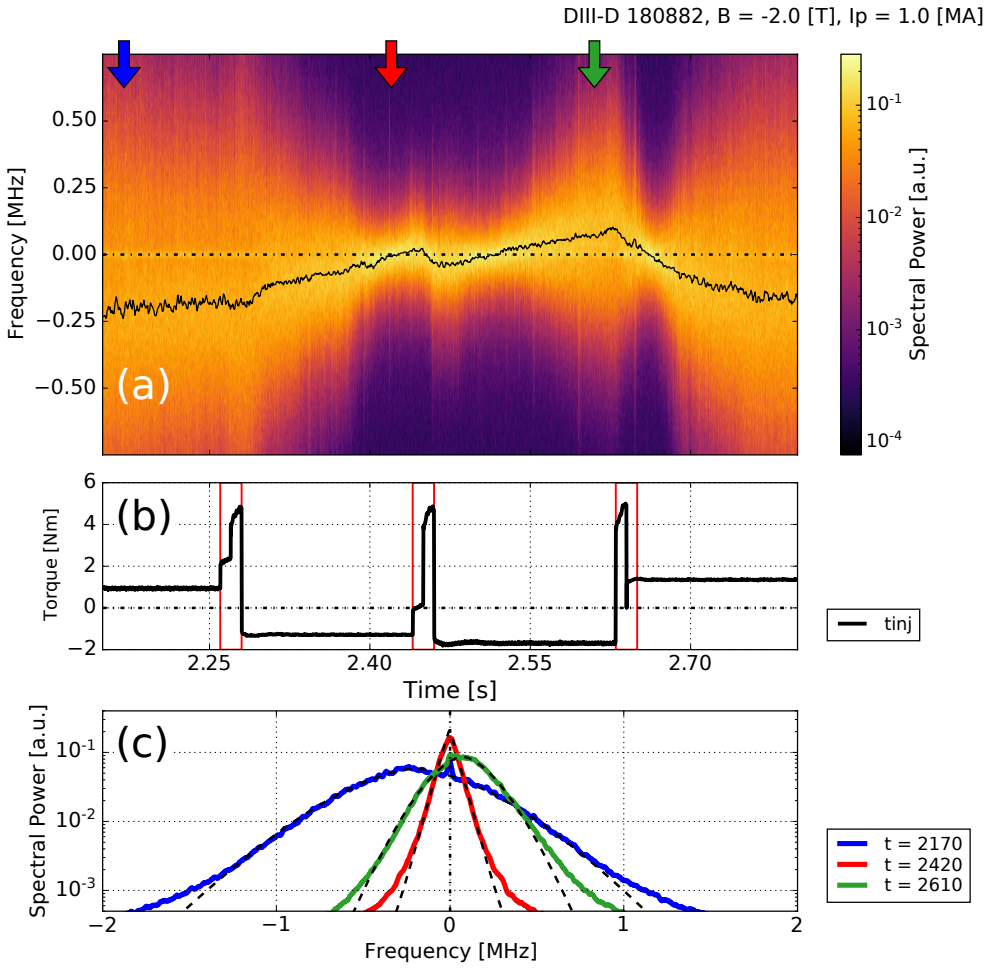

Figure 5.3: DBS quadrature spectrogram displaying the effects of variable NBI torque. 5.3(a) shows the spectrogram of the 72.5 GHz DBS along with the Doppler shift (solid black curve) from GG fits. The red vertical lines in (b) indicate the 20 ms spans where DBS-CER comparisons are possible. 5.3(c) shows particular slices of the spectrogram in (a) along with GG fits (dashed lines) to the peaks of the spectra demonstrating the determination of the Doppler shift. The arrows at the top of 5.3(a) indicate the time-slices for the curves in 5.3(c)

Doppler shift from these fits is superimposed on the spectrogram in Figure 5.3(a). Finally, fit parameters are combined over 2 ms windows to obtain statistical uncertainties. Therefore, over the 20 ms span of CER data, DBS has 10 Doppler shift measurements for each channel. This sets the time-scale of the DBS measurements to ± 1 ms.

Ray tracing simulations using the `GENRAY` code were performed to determine the measured wavenumber and location for every 2 ms DBS interval. Each ray tracing simulation is

provided with the high time-resolution n_e profile from reflectometry and an `EFIT` equilibrium reconstruction synchronized to the Thomson scattering sampling rate (3 ms). Given the Doppler shift, measured wavenumber, and equilibrium parameters, Equation 3.37 is used to evaluate the DBS $\omega_{E\times B}$ on a 2 ms timescale. The time spans where the final DBS-CER comparisons are possible are indicated by red vertical lines in Figure 5.3(b).

5.3.1 Uncertainty quantification

There are two independent sources of potential error when performing DBS data analysis. First, the relatively simple uncertainty associated with fitting for the Doppler shift in the DBS spectrogram. This error is retained and propagated through to the final value of $\omega_{E\times B}$. However, fitting for the Doppler shift is subject to systematic errors associated with the particular spectral model selected. With the flexible Generalized Gaussian model (Equation 5.8) we ensure good fits are archived despite the variable shape of the DBS spectrum. The second type of potential error in DBS analysis arises when propagating uncertain inputs through ray tracing simulations. Uncertainty in both the magnetic equilibrium reconstruction (from EFIT) and the electron density profile (from reflectometry) were considered. Ultimately, uncertainty in the magnetic equilibrium was not included to be consistent with the CER method of uncertainty quantification – which does not consider magnetic equilibrium uncertainty. Furthermore, varying the magnetic equilibrium appeared to have no *independent* effect on ray tracing results when compared to varying the density profile.

Uncertainty in the electron density profile was found to cause significant variation in the GENRAY-reported value of the wavenumber at the scattering location. To address this, we performed a Monte Carlo-style variation of the density profile within its 1σ error bars. Varying the density profile changes all outputs of the GENRAY simulation including the wavenumber and the scattering location. Given the highly-correlated nature of adjacent reflectometry measurements, our method of randomly shifting and scaling the density profile may result in over-estimation of this form of error. The error bars in the report DBS $\omega_{E\times B}$ profiles account for both sources of DBS uncertainty: fit-errors for the Doppler shift, and

the uncertainty in other variables in Equation 3.37 associated with propagating uncertain density profiles through GENRAY.

The error-band on the CER $\omega_{E\times B}$ profile accounts for uncertainty in both the ∇P and $(\mathbf{u}\times\mathbf{B})$ terms in the radial force-balance equation (Equation 5.7). However, given the disparity in magnitude between these two components of E_r and the weak pressure gradient in this L-mode plasma, the uncertainty in the $(\mathbf{u}\times\mathbf{B})$ term dominates over the ∇P uncertainty. Uncertainties in the velocity measured by CER are handled by a similar Monte Carlo approach of randomizing inputs to the CER-E_r analysis.

5.4 Results

The effect of the counter-injected neutral beam is captured in the DBS spectrogram shown in Figure 5.3(a). The Doppler shift changes from approximately -250 kHz to 0 kHz over the first 170 ms counter-I_p NB pulse. When the second pulse begins 10 ms later, the Doppler shift changes sign and increases from 0 to approximately 90 kHz. After the second pulse is complete, the Doppler shift restores its steady-state value of approximately -250 kHz over a 100 ms period.

Comparison between DBS and CER is possible during the time spans indicated by vertical lines in Figure 5.3(b). The midpoints of each span are the nominal times: 2270, 2450, and 2640 (all $\pm$10) ms. Figure 5.4 provides the DBS-CER $\omega_{E\times B}$ comparisons. Figures 5.4(a,c,e) show the DBS values with $\pm$1 ms resolution and Figures 5.4(b,d,f) show an average of the DBS results with the same $\pm$10 ms time resolution as the CER profile. The average DBS profile is computed by an inverse variance weighted average of the $\pm$1 ms DBS data. It is also worthwhile to calculate absolute residuals between the measurements. We use absolute residuals, $|d| = |\omega_{E\times B,\mathrm{CER}} - \omega_{E\times B,\mathrm{DBS}}|$ due to the fact that the rotation is nearly zero in some cases, and thus division to produce scaled residuals is not appropriate. The residuals are calculated at radial locations where DBS measurements are made and then averaged over the profile. We use the symbol $\overline{|d|}$ to indicate the radially averaged absolute residuals.

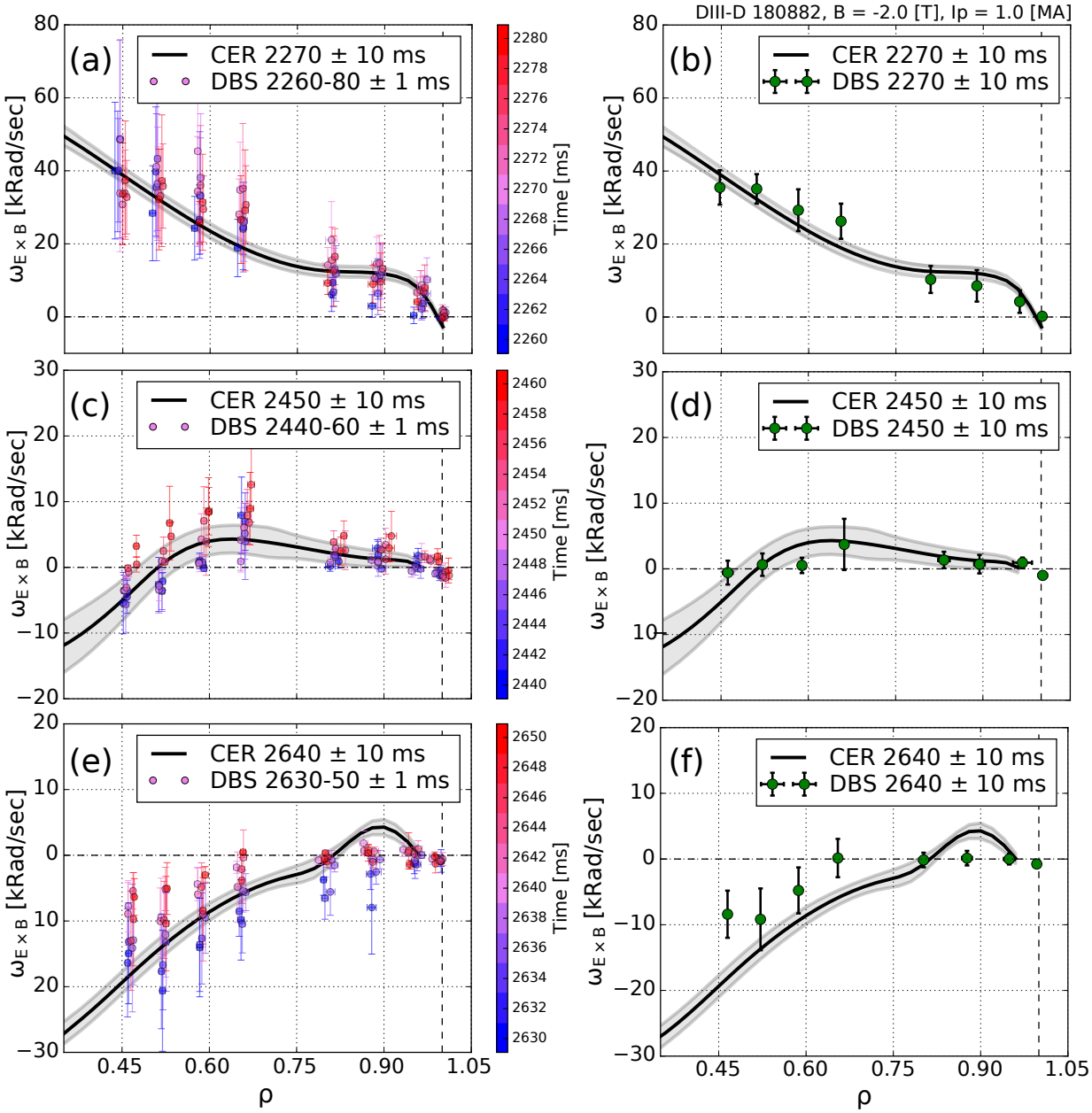

Figure 5.4: Profiles of $\omega_{E\times B}$ from DBS and CER. 5.4(a,c,e) show the ±1 ms DBS data, 5.4(b,d,f) show the averaged DBS profile. Note that the y-axis limits change across the three sets of profiles.

The first comparison of $\omega_{E\times B}$ is shown in Figures 5.4(a,b). At 2270 ms the counter-injected beam has not yet been applied. The DBS and CER computed values of $\omega_{E\times B}$ generally agree well across the entire co-I_p directed profile. The CER profile passes through all DBS error-bars except the fifth channel where both 1σ bounds (barely) intersect each

other. The radial average of the absolute residuals for this profile is $\overline{|d|} = 4.0$ kRad/s. The second comparison is made in Figures 5.4(c,d). At 2450 ms the first 170 ms counter-injected NBI pulse has been applied. The result of the negative applied torque is evident as the rotation profile is decreased to near zero. Both DBS and CER measure a flat and low-magnitude rotation profile. The radial average of the absolute residuals for this profile is $\overline{|d|} = 1.3$ kRad/s. The third comparison is made in Figures 5.4(e,f). At this time the second counter-injected beam pulse has concluded and the rotation has decreased further to the point where rotation is reversed toward the core. There is a notable difference between the inner four averaged DBS channels and the CER result. Due to this discrepancy, the radial average of the absolute residuals for this profile is largest with a value of $\overline{|d|} = 4.2$ kRad/s. In the latter two comparisons, Figures 5.4(c-f), the CER profile was truncated at $\rho = 0.96$. This choice was made because the CER analysis used in this case is optimized for the core and not appropriate as you approach the LCFS. When a different edge-optimized CER analysis is used, the resulting edge $E_r \approx 0$, in agreement with DBS.

5.5 Analysis

5.5.1 Estimation of the turbulence phase velocity

Our ability to approximate the DBS-measured velocity as $v_{\text{meas.}} \approx v_{E\times B}$ (and by extension calculate E_r and $\omega_{E\times B}$) depends on the magnitude of the turbulence phase velocity discussed in Section 3.1.5. To estimate the magnitude of $v_{\text{ph.}}$, we use the code TGLF to calculate the linear eigenvalue spectrum over the plasma minor radius given profiles shown in Figure 5.2. We use Equation C.16 to convert the dimensionless TGLF k_y to k_b [rad/cm] and we convert the dimensionless real frequency, ω_{k_y} using the local c_s/a. The phase velocity is then calculated by evaluating $v_{\text{ph.}} = \omega_{k_b}/k_b$ at the DBS $k_b = k_{\text{meas.}}$.

Figure 5.5 shows radial profiles of the measured DBS velocity, $v_{\text{meas.}} = \omega_{\text{Dopp.}}/k_{\text{meas.}}$, and estimates of the phase velocity using TGLF. In Figure 5.5(a) we show profiles of $v_{\text{meas.}}$ and the TGLF $v_{\text{ph.}}$ at each nominal time. Figure 5.5(b) contains the same values as (a)

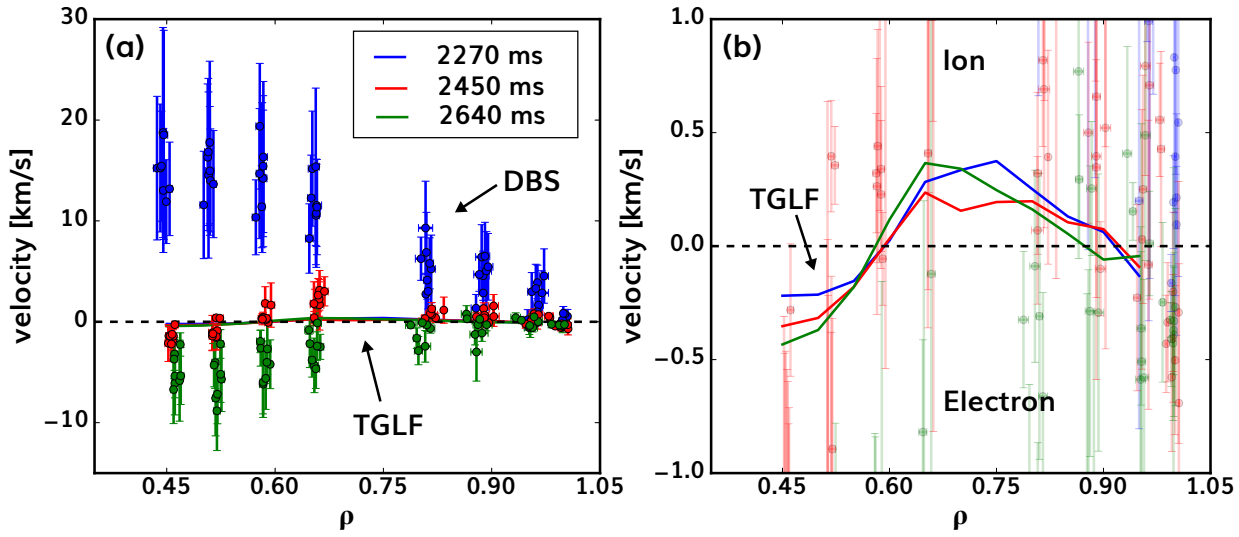

Figure 5.5: DBS velocity measurements compared with the phase velocity predicting using TGLF.

but is zoomed to ±1 km/s to show the TGLF estimate. Figure 5.5(b) also indicates the ion/electron diamagnetic directions. Based on this estimate, the $|v_{\text{ph.}}| < 0.5$ [km/s] over all radii and times. This estimate of $v_{\text{ph.}}$ is less than the radially averaged uncertainty on $v_{\text{meas.}}$ for each time: $\bar{\sigma}_v \approx 3.9, 0.9, 1.4$ [km/s]. Therefore, it is reasonable to neglect $v_{\text{ph.}}$ and approximate $v_{\text{meas.}} \approx v_{E\times B}$.

5.5.2 Statistical cross-diagnostic analysis

The uncertainty of the CER/DBS diagnostics can be assessed further by collecting all averaged DBS values from Figures 5.4(b,d,f) along with all CER values at matching radial positions. The average 1σ errorbar across all DBS values is $\bar{\sigma}_{\text{DBS}} = 2.6$ kRad/sec and the average 1σ from CER is $\bar{\sigma}_{\text{CER}} = 1.5$ kRad/sec. The sum of the average 1σ values, $\bar{\sigma}_{\text{DBS}} + \bar{\sigma}_{\text{CER}} = 4.1$, is similar in magnitude to the radial average of the absolute residuals, $\overline{|d|} = 4, 1.3, 4.2$ kRad/s, suggesting a tendency to agree within their respective uncertainties.

Figure 5.6 shows the collection of all (averaged) DBS and corresponding CER values from Figures 5.4(b,d,f) plotted against each other. The Pearson correlation coefficient is $r = 0.96$ suggesting strong positive correlation. The errorbars on points in Figure 5.6 are not used to

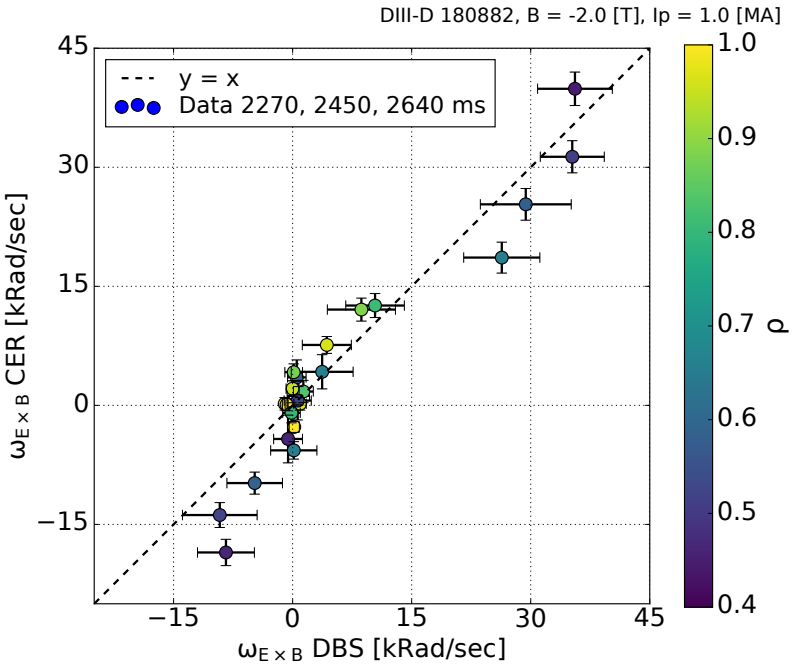

Figure 5.6: Scatter plot of DBS and CER $\omega_{E\times B}$ values from Figures 5.4(b,d,f). The CER values and their error are taken from radial positions matching DBS. The color of the points indicates their radial (ρ) positions. The dashed line $y = x$ signifies perfect agreement and is only to guide the eye.

weight the calculation of Pearson r.

To assess DBS-CER agreement more rigorously we use the mean-difference plot[1] shown in Figure 5.7 [146]. The y-value indicates the difference between DBS and CER values at the same radial position, $d = \omega_{E\times B,\mathrm{DBS}} - \omega_{E\times B,\mathrm{CER}}$. The x-value is the two-point weighted-average of $\omega_{E\times B,\mathrm{DBS}}$ and $\omega_{E\times B,\mathrm{CER}}$ at each position. Statistics are calculated for the differences, d, weighted by their uncertainty. We find an average difference, $\bar{d} = -0.1$ kRad/sec and standard deviation of differences, $\sigma_d = 2.5$ kRad/s. It is common to compute the 'limits of agreement', $\bar{d} \pm 2\sigma_d = -0.1 \pm 5$ kRad/sec, indicated by red horizontal lines in Figure 5.7. Points outside of this agreement-region are discussed in the next section. Assuming the differences are normally distributed, the agreement-region between the red horizontal lines in Figure 5.7 is the 95% confidence region for discrepancies between DBS and CER.

[1]Sometimes called a Bland-Altman plot

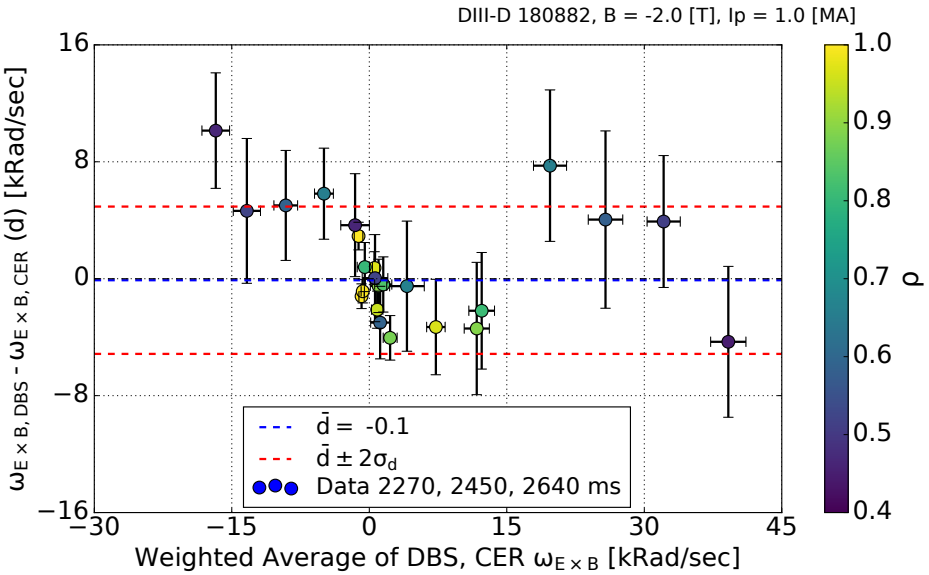

Figure 5.7: Mean-difference plot of DBS and CER values of $\omega_{E\times B}$. The CER values and their error are taken from radial positions matching DBS. The color of the points indicates their radial (ρ) positions. The blue horizontal line is the weighted average of the difference $\bar{d} = -0.1$ kRad/sec. The red horizontal lines provide the 'limits of agreement', $\bar{d} \pm 2\sigma_d = -0.1 \pm 5$ kRad/sec.

5.5.3 Effects of prompt torque

During neutral beam injection, high energy neutral particles are ionized and born onto orbits in the plasma. The motion of fast ions born onto trapped orbits produces a fast radial current. This fast radial current, $\mathbf{j}_f$, is canceled by a radial current established in the bulk plasma by ambipolarity. The result is a fast 'prompt torque' caused by $\mathbf{j}_f \times \mathbf{B}$ and a slower transfer of momentum from collisional forces on the fast ions [147]. The prompt $\mathbf{j}_f \times \mathbf{B}$ torque occurs almost instantly as the beam ions are ionized. Analysis by J. deGrassie in [148] found that 90% of the torque impulse is imparted to the plasma within 10 ms. By contrast, the collisional transfer of beam momentum occurs on a much slower timescale characterized by the beam slowing-down time which can be approximated following Wesson [19] using,

$$\tau \text{ [ms]} \approx 78 \frac{T_e^{3/2}}{n_e} \ln\left(1 + \left(\frac{\mathcal{E}_b}{19 T_e}\right)^{3/2}\right), \tag{5.9}$$

with n_e in units of $\times 10^{19}$ m^{-3} and $\mathcal{E}_b$, T_e in units of keV. For the plasma considered here, this estimate gives $\tau \approx 100$ ms. This value is in rough agreement with the slower evolutionary periods of the DBS Doppler shift in Figure 5.3(a).

We attribute some discrepancies in the final DBS-CER $\omega_{E\times B}$ profiles (Figure 5.4) to the effects of prompt torque imparted by the beam blips used for CER measurement. The estimated magnitude of the applied torque is shown in Figure 5.3(b). For the first nominal time (2270 ms), the estimated applied torque increases sequentially from 0.9 to 2.3 to 4.5 Nm. The high time-resolution DBS $\omega_{E\times B}$ values shown in Figure 5.4(a) do not appear to vary systematically with time in the core. However, there is a trend visible in the edge DBS points, suggesting a prompt increase in edge $\omega_{E\times B}$ during blip. For the second nominal time (2450 ms), the estimated applied torque increases from -1.3 to 0.0 to 4.5 Nm. The high time resolution DBS measurements in Figure 5.4(c) show a clear trend with time in almost every DBS channel. Finally, for the third comparison-time (2640 ms) the estimated torque varies from -1.7 to 4.5 to 1.3 Nm. The DBS measurements in Figure 5.4(e) are clearly non-stationary in time with the innermost channels increasing by more than $\Delta\omega_{E\times B} \approx 10$ kRad/s over the time of the blip.

The high time-resolution DBS $\omega_{E\times B}$ values in Figures 5.4(c,e) indicate a systematic increase of $\omega_{E\times B}$ in time, particularly in the inner four channels. This spread of points is most pronounced in Figure 5.4(e) when the most abrupt change in the estimated torque occurs, $\Delta T_{inj} = 6.2$ Nm. This causes the final time-averaged DBS values in Figure 5.4(f) to be offset from the CER values. We attribute this to the prompt-torque creating a non-stationary E_r in the plasma over the duration of the blips. The measurements most affected by prompt torque - inner four channels in Figure 5.4(f) - are also the lowest four points in Figure 5.6 and the outlying four points in the upper-left of Figure 5.7.

To estimate the prompt torque density from DBS measurements we begin with the conservation of momentum for plasma species a and follow arguments made in [147, 148],

$$m_a n_a \frac{\partial \mathbf{u}_a}{\partial t} = -\nabla p_a - \nabla \cdot \boldsymbol{\pi}_a + q_a n_a (\mathbf{E} + \mathbf{u}_a \times \mathbf{B}) + \mathbf{F} \tag{5.10}$$

where $\mathbf{F}$ represents a source of momentum and $\boldsymbol{\pi}_a$ is the trace-less momentum stress tensor [138]. Then, we take a dot product of Equation 5.10 with $\hat{\mathbf{e}}_\phi = R\nabla\phi$ and compute a flux-surface average $\langle \dots \rangle_\theta$ to find,

$$m_a n_a \frac{\partial}{\partial t}\langle R u_{\phi,a}\rangle_\theta = -\langle R\nabla\phi \cdot (\nabla\cdot\boldsymbol{\pi}_a)\rangle_\theta + \langle \mathbf{j}_a \cdot \nabla\psi\rangle_\theta + \langle R\nabla\phi\cdot\mathbf{F}\rangle_\theta. \tag{5.11}$$

The first term on the right hand side describes transport of toroidal momentum across flux surfaces, this occurs on a slow timescale. In fact, in many cases the momentum transport time is similar to the energy confinement time $\tau_\phi \approx \tau_E$ [149]. The term involving $\mathbf{F}$ describes the collisional transfer of momentum which also happens on a slow timescale (the slowing-down time discussed previously). Finally, we use Equation 5.3 and retain only terms to lowest order in ρ_*. The resulting equation describes fast-timescale evolution of toroidal angular momentum,

$$m_a n_a \frac{\partial}{\partial t}\langle R^2\omega_a\rangle_\theta \approx \langle \mathbf{j}_a\cdot\nabla\psi\rangle_\theta. \tag{5.12}$$

Recall that, to lowest order in ρ_*, $\omega_a = \omega_{E\times B}(\psi)$ is a flux-function. Then, we sum over plasma species and use arguments made in [148] to replace the total current on the RHS with $-\mathbf{j_f}$. The result is,

$$\sum_a m_a n_a \langle R^2\rangle_\theta \frac{\partial \omega_{E\times B}}{\partial t} \approx -\langle \mathbf{j}_f\cdot\nabla\psi\rangle_\theta. \tag{5.13}$$

The LHS of Equation 5.13 is the time derivative of the total flux surface averaged angular moment density, $\partial\langle\ell_\phi\rangle_\theta/\partial t$. The RHS of Equation 5.13 is the flux-surface averaged toroidal prompt torque density, $\langle\eta_\phi\rangle_\theta = -\langle \mathbf{j}_f\cdot\nabla\psi\rangle_\theta$. The total torque on the plasma contained within a flux-surface ρ is calculated by volume-integration of the torque density,

$$\tau_\phi = \int_0^\rho d\rho V'\langle\eta_\phi\rangle_\theta, \tag{5.14}$$

where V' accounts for the change in plasma volume with ρ.

To make a crude estimate of the prompt torque using DBS measurements, we focus on the

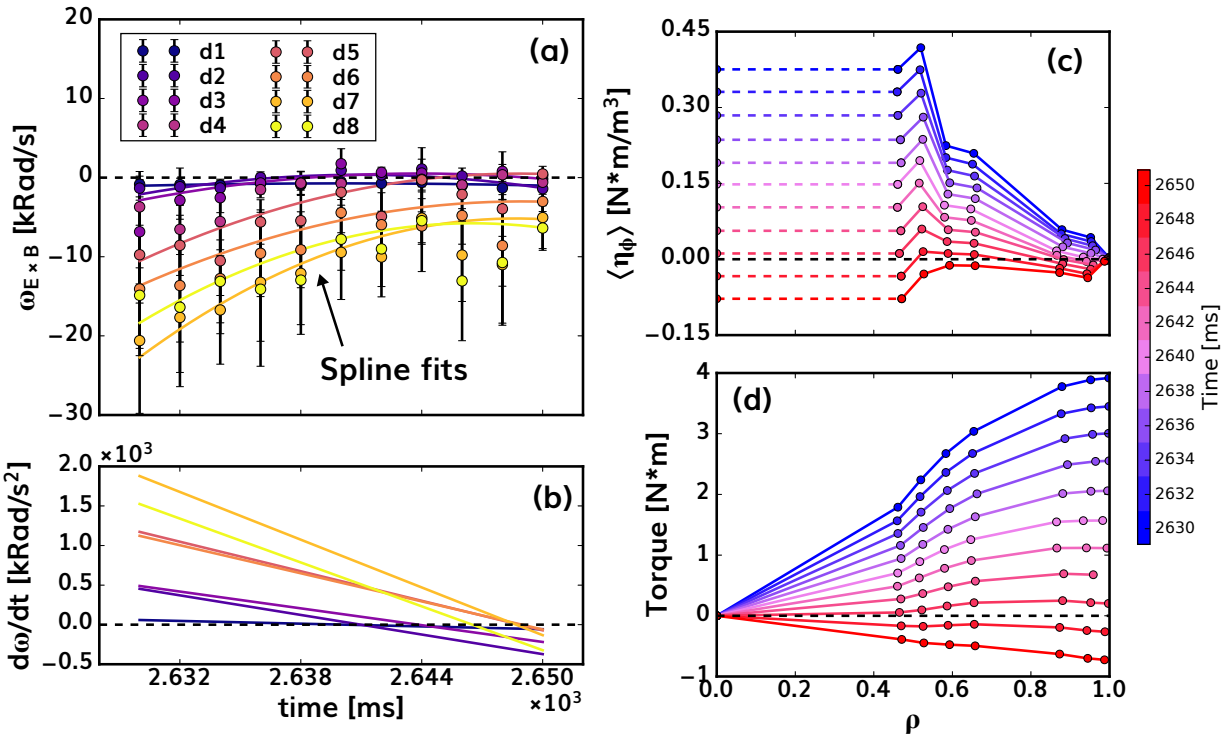

Figure 5.8: Estimation of prompt torque using DBS measurements. 5.8(a) shows the DBS $\omega_{E\times B}$ data from Figure 5.4(e) vs. time along with the inverse-variance weighted spline fits for each channel. 5.8(b) shows the spline derivatives, providing the rate of change of rotation with time. 5.8(c) shows the result of Equation 5.13 with the dashed lines indicating crude extrapolation to the core. 5.8(d) shows the result of Equation 5.14.

fast time evolution of $\omega_{E\times B}$ from 2630 - 2650 ms. We use inverse variance weighted splines to fit the time evolution of $\omega_{E\times B}$ in each DBS channel. The spline fit provides the derivative in time, i.e. $\partial\omega_{E\times B}/\partial t$. Then, Equation 5.13 is used to calculate the evolving $\langle\eta_\phi\rangle_\theta$. To calculate the total toroidal prompt torque we must (crudely) extrapolate the torque density from the eight DBS measurements to the core ($\rho = 0$) before applying Equation 5.14. Figure 5.8 illustrates the technique of using high time resolution DBS measurements to approximate the beam-blip prompt torque. The estimated toroidal torque on the plasma is ≈ 4 Nm at the earliest time. This value decreases toward zero as the plasma E_r evolves to establish a new steady-state value ($\partial\omega_{E\times B}/\partial t \to 0$) visible as the derivative decreasing in Figure 5.8(b). This is not to say that the beam applied torque goes to zero, rather the transient *prompt* torque effect on E_r approaches zero. The estimated value of 4 Nm agrees remarkably well with the

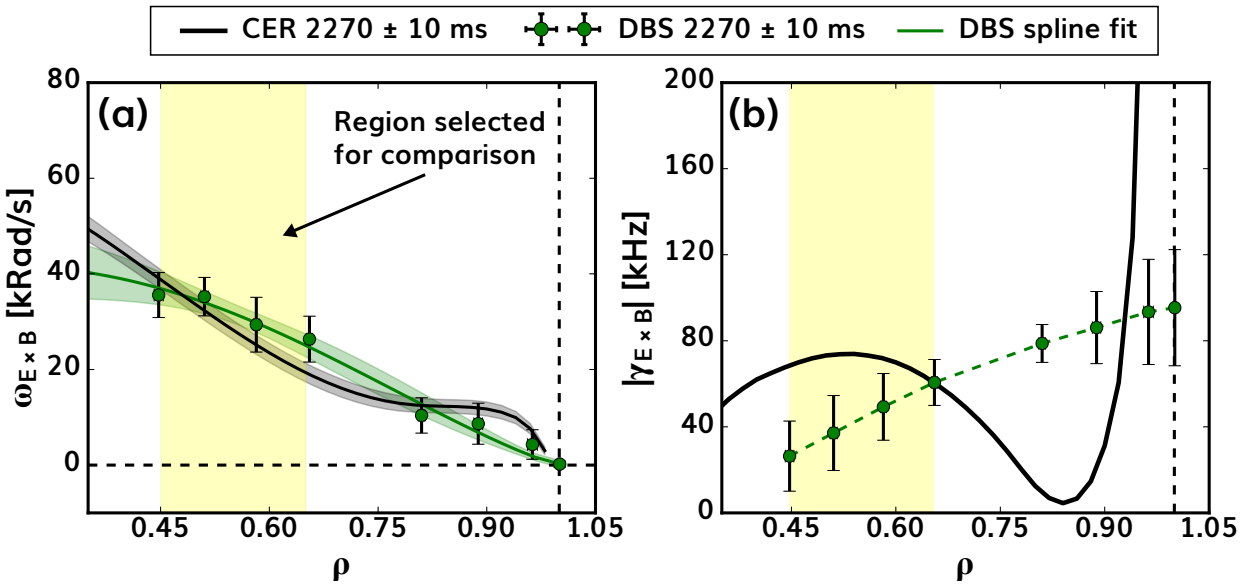

Figure 5.9: Calculation of $\gamma_{E\times B}$ using DBS measurements. 5.9(a) shows the DBS $\omega_{E\times B}$ data from Figure 5.4(b) with the inverse-variance weighted spline fit. 5.9(b) shows the result of Equation 5.15.

estimated torque value based the NBI parameters (voltages, tangency, etc.) $T_{inj} \approx 4.5$ Nm (see Figure 5.3(b)).

5.5.4 Comparison of the $E \times B$ shearing rate

The normalized radial (ψ) derivative of $\omega_{E\times B}$ is the $E \times B$ shearing-rate,

$$\gamma_{E\times B} = \frac{(RB_\theta)^2}{B}\frac{\partial}{\partial\psi}\omega_{E\times B}. \tag{5.15}$$

The magnitude of $\gamma_{E\times B}$ plays an important role in the theory of turbulence suppression in magnetic confinement devices [150]. To compare CER and DBS values of $\gamma_{E\times B}$ we focus on the core ($\rho < 0.7$) at the first nominal time (2270 ms). This location and time appears minimally affected by prompt torque (see Figure 5.4(a,b)). To create a radial profile from the DBS measurements we use an ensemble of inverse variance weighted spline fits to the eight $\omega_{E\times B}$ points and their corresponding values of ψ. Derivatives of the splines (with respect to ψ) are averaged together and used to calculate $\gamma_{E\times B}$.

Figure 5.9 shows the cross-diagnostic $\gamma_{E\times B}$ profile comparison. Figure 5.9(a) shows the DBS data and CER profile from Figure 5.4(b) with the additional spline fit to the DBS data[2]. Figure 5.9(b) shows the calculated profiles of $|\gamma_{E\times b}|$ using the profiles in 5.9(a). Over the shaded vertical region in Figure 5.9, the DBS and CER values of $|\gamma_{E\times B}|$ range from total agreement to disagreement by a factor of ≈ 2. Meanwhile, the $|\gamma_{E\times B}|$ values calculated using the *edge* DBS channels disagrees with CER by a larger margin. However, these channels appear to be somewhat affected by prompt torque (see Figure 5.4(a)) hence our focus on the core region for comparison.

Although the $\gamma_{E\times B}$ comparison shown in Figure 5.9(b) is specific to this plasma, time, and radial location; this analysis is meant to illustrate the potential level of uncertainty in a derived quantity such as $\gamma_{E\times B}$. This factor of $\times$1–2 agreement between CER and DBS can inform scans of $\gamma_{E\times B}$ when performing transport modeling and simulations involving $E \times B$-shear suppression.

5.6 Conclusions

In this chapter we presented DBS measurements of the $E \times B$ rotation in an L-mode DIII-D discharge with varying external torque. Rigorous cross-diagnostic comparisons we made between DBS and charge exchange recombination spectroscopy (CER). During DBS data analysis, we propagated uncertainties in the density profile through ray tracing simulations and used nonlinear least-squares fits to the frequency spectrum to derive the measured velocity and its uncertainty. We found that $\omega_{E\times B}$ values derived from DBS and CER generally agree with an average difference near zero, $\bar{d} = -0.1$ kRad/s. The 2σ confidence region for their disagreement was found to be ± 5 kRad/s, including points known to be affected by prompt torque. Statistically speaking, this implies that in 95% of cases the DBS and CER values of $\omega_{E\times B}$ will agree within 5 kRad/s of each other.

[2]We use the `MonteCarloSpline` routine within OMFIT to perform the fit. We also constrain the gradient of $\omega_{E\times B}$ to be zero on axis ($\rho = 0$) similar to CER.

The high time resolution (± 1 ms) DBS measurements were able to observe prompt (< 10 ms) modifications to the E_r profile from diagnostic neutral beam blips. The perturbation from NBI-blips was proportional to the change in the approximate torque imparted by the blip. The largest change in torque, $\Delta T_{inj} \approx 6.2$ Nm, caused the most significant modification of E_r. Additional analysis of the DBS data estimated the NBI torque density from the time rate-of-change of $E \times B$ rotation. Despite crude extrapolation to the plasma core, we found the total torque to be roughly in agreement with the estimate based on the NBI parameters. We also used DBS and CER profiles of $\omega_{E\times B}$ to calculate the $E \times B$ shearing rate, $\gamma_{E\times B}$. In the core, where DBS measurements appear to be less impacted by prompt-torque, we found the DBS/CER derived $\gamma_{E\times B}$ values to be within a factor of two from one another.

CHAPTER 6

Conclusions and future work

6.1 DBS modeling

Chapter 3 presented a comprehensive overview of the Doppler back-scattering diagnostic including a novel synthetic diagnostic model and 2D full-wave simulations. The synthetic DBS methods introduced in Chapter 3 and applied in Chapter 4 provide a new means of predicting and interpreting DBS measurements in a theory-based manner. The ultimate goal of a synthetic DBS model is to account for – or remove – instrumental effects which may impact fluctuation measurements. Furthermore, a diagnostic model with sufficient physics can also aid in understanding the instrument itself, leading to innovations and optimization of measurement techniques.

We demonstrated two models for DBS: one based on beam-tracing (a reduced model for electromagnetic wave propagation), and a second based on higher-fidelity full-wave simulations. Both DBS models are flexible, and can use either analytic expressions for, or simulations of density fluctuations to model scattering. To facilitate comparisons with theory, we developed a novel method for post-processing the outputs of the quasilinear code TGLF. There are two primary benefits to using reduced models (beam-tracing and TGLF): (1) the ability to quickly make predictions and perform parameter scans with lower simulation overhead and (2) the modular nature of the physics within the diagnostic model. Faster modeling time has the potential to greatly benefit the DBS community. For example, through predict-first experimental planning, one can identify theoretically-important wavenumbers to inform aiming the DBS probe beam during an experiment. Furthermore, scans of plasma parameters with fixed DBS aiming can answer questions such as: given a

change in x, would we theoretically observe a change in measured DBS power? The modular nature of the beam-DBS diagnostic model makes it easier to separate diagnostic effects (e.g. mismatch attenuation, 'ray' cutoff enhancement, etc.) when interpreting results.

The new full-wave DBS model uses the commercial software COMSOL. This new DBS model allows us to benchmark beam-tracing results and study full-wave effects using realistic plasma parameters. For example, the full-wave model was used to evaluate nonlinear scattering effects in Chapter 3. In Chapter 4 the full-wave electric field was combined with nonlinear CGYRO simulations to produce a synthetic DBS frequency spectrum. Both applications present exciting opportunities for future work. Full-wave modeling can be used to study cross-polarization scattering (CPS), wave tunneling, cross-beam DBS, etc.. Given the success of the 2D full-wave model, 3D modeling should be pursued to understand the the behavior of the DBS beam near critical layers and verify beam-tracing results (e.g. test beam-pinching discussed in Subsection 4.5.4).

Future work pertaining to DBS includes further development of theory-based models for the DBS frequency spectrum. For example, in the context of the Taylor model, a database study of DBS spectra could uncover trends in the model parameters (the Kubo number, K, and the auto-correlation time, τ_{ac}) with respect to the probed wavenumber. Similarly, in terms of the exponential frequency model discussed in Subsection 3.1.6 one could perform a similar database study of the exponential decay time-constant to uncover trends in the implied chaotic dynamics. One could also derive new models for the frequency spectrum by analyzing databases of nonlinear gyrokinetic simulations – similar to the development strategy for quasi-linear transport models. One could imagine a quasi-linear model for the DBS frequency spectrum based on linear mode frequencies and a combination of k-space resolution and turbulent frequency-broadening effects. Lastly, more development is needed in both the ray and beam models for DBS at lower incidence angles. Presently, both ray tracing and beam tracing methods struggle in this limit. It would benefit the analysis of DBS (and other research areas) to have more robust models for wave propagation near caustics in magnetized plasmas.

6.2 Wavenumber spectrum investigation

Chapter 4 describes an investigation of the wavenumber spectrum of density fluctuations in ECH H-mode tokamak discharges. We were able to sustain H-mode plasmas with very low collisionality (core $\nu_{*e} \approx 0.1$) and pure auxiliary electron-heating. Core ECH yielded $T_e/T_i > 1$ over the entire plasma core and large values of the dimensionless quantity $\eta_e \approx 3$. Scans of the DBS launch-angles during the experiment provided unique measurements of the back-scattered power wavenumber spectrum, $P_s(k)$, in the core plasma. The measured wavenumber spectrum appears to decay exponentially with spectral indices ($k^{-\nu}$) and exponential decay factors ($e^{-\zeta(k\rho_s)}$) largely in agreement with what has been reported previously. Future work should address the physics controlling the spectral decay of density fluctuations in magnetically confined plasmas including extending measurements to lower and higher k and performing cross-diagnostic δn comparisons.

Significant modeling efforts were directed toward developing a theory-based prediction of the DBS wavenumber spectrum. As part of this DBS-oriented modeling, we performed calculations with the quasi-linear code TGLF as well as linear and nonlinear gyrokinetics simulations with the code CGYRO. The linear eigenvalue spectra from both TGLF and CGYRO show curvature-driven ITG modes are dominant at normalized wavenumbers $k_y \leq 0.7$. TGLF also reports marginally subdominant TEM modes over this wavenumber range[1]. The transport spectra (Q_{k_y}, Γ_{k_y}) from both codes suggest fluxes are driven by ion-scale modes despite our expectation that electron modes would be active in this plasma regime. Notably, TGLF and nonlinear CGYRO disagree as to the direction of the electron particle flux and the magnitude of total Q_e, Γ_e fluxes. The TGLF-CGYRO disagreement can be directly attributed to the quasi-linear weights (phase shifts) given that the eigenvalue spectrum and the saturated potential model (SAT-rule) were verified for this case. The CGYRO and TGLF synthetic wavenumber spectra (Figure 4.13) do match the shape of the measured wavenumber spectrum for $k_y \leq 0.3$ and $k_y \geq 1.2$. However, the spectral decay predicted by the synthetic

[1]In Figure 4.7 one of the marginally subdominant TEMs becomes the dominant mode at $k_y \approx 0.3$.

diagnostic does not match the measurements over $0.4 < k_y < 1.2$. Additional modeling efforts were directed at the low-k portion of the wavenumber spectrum. Full-wave modeling at low-k combined with nonlinear CGYRO simulations does suggest that some component of the modeling begins less accurate at low-k (see Subsection 4.5.4). We are unable to definitively attribute measurement/theory $P_s(k)$ discrepancies solely to the turbulence simulations nor the instrument function model. Future work on this front includes further investigation into the physics of DBS measurements at the lowest and highest wavenumbers. Additionally, it would be beneficial to develop a synthetic frequency spectrum model based on reduced models of turbulence – as the frequency spectrum is readily calculated from DBS data (as opposed to the wavenumber spectrum which requires dedicated scans).

Transport modeling with the code TGYRO found that TGLF is capable of matching the experimental thermal fluxes at multiple radii with small adjustments to the observed T_e and T_i profiles. However, TGLF appears to exhibit undue sensitivity to the normalized electron temperature gradient scale length, a/L_{T_e}, which was not reproduced by nonlinear CGYRO. The sharp increase in Q_e with a/L_{T_e} was found to be caused by a transition to a completely TEM-dominated regime – again, this was not observed in nonlinear CGYRO (see Figure 4.21). The TGLF sensitivity to a/L_{T_e} also impacted our interpretation of the synthetic DBS wavenumber spectrum. It was found that the synthetic $P_s^{\mathrm{TGLF}}(k)$ in the completely TEM-dominated case (nominal $+5\%$ a/L_{T_e}) appears to completely reproduce the shape of the measured DBS spectrum (Figure 4.23). However, given the fact that nonlinear CGYRO does not reproduce the TGLF behavior – there are doubts as to whether ITG/TEM dominance is the root cause of the discrepancy in the $P_s(k)$ spectral decay for $0.4 < k_y < 1.2$ between the nominal synthetic and measured wavenumber spectra[2] (see Figure 4.13). This conclusion suggests that the TGLF model may not properly capture the TEM instability boundary, despite being able to match thermal fluxes. Another lesson-learned from this modeling is: in cases where TGLF predicts stiff, nonlinear flux-gradient behavior one should verify the

[2]Recall that the saturation rule of TGLF attempts to mimic the underlying higher-fidelity gyrokinetics of CGYRO. Thus, one tends to trust the CGYRO results more than TGLF results. It is possible that TGLF is – by chance – modeling reality more closely than CGYRO. However the underlying physics in the TGLF model is a fundamentally a reduction of CGYRO.

behavior is reproduced by higher-fidelity gyrokinetics. Future work addressing this issue is non-trivial, and may involve changes to the TGLF model to reduce stiffness. Another interesting avenue for future work would be to extend transport-solvers such as TGYRO to include synthetic diagnostics such that the quality of a flux-matching solution can be put in context with fluctuation measurements.

6.3 Cross-diagnostic rotation comparisons

Chapter 5 presented an investigation of $E \times B$ rotation using DBS. We presented rigorous cross-diagnostic comparisons with the charge-exchange recombination spectroscopy (CER) diagnostic under varying external NBI torque conditions. We propagated two sources of uncertainty in DBS analysis: (1) fit uncertainty for the DBS Doppler shift and (2) uncertainty in the electron density profile. The latter was propagated through ray tracing simulations, leading to an ensemble of probed locations and wavenumbers. The final cross-diagnostic comparison was made through the toroidal $E \times B$ angular velocity, $\omega_{E\times B}$, which is theoretically a flux-function. The magnitude of the turbulence phase velocity was estimated using linear TGLF eigenvalue spectrum calculations. The estimated phase velocity was found to negligible compared to the $E \times B$ velocity – supporting the approximation the measured Doppler shift is due to $E \times B$ motion for this plasma.

Statistical analysis of the CER and DBS profiles of $\omega_{E\times B}$ found that the two diagnostics tend to agree within their respective uncertainties. Across the entire dataset of $\omega_{E\times B}$ values the average difference between DBS and CER is $\bar{d} = -0.1$ kRad/s. The 95% confidence interval for the differences was found to be ± 5 kRad/s. Further analysis of the high time-resolution (± 1 ms) DBS measurements revealed rapid modification to the derived $\omega_{E\times B}$ value caused by the NBI 'blips' used for CER measurement. The rate of change in $\omega_{E\times B}$ with time was used to deduce the NBI prompt torque density. The volume-integrated prompt torque based on DBS measurements appears to be in rough agreement with the routine estimates of the total NBI torque. Finally, the $E \times B$ shearing rate, $\gamma_{E\times B}$, was calculated from both CER and DBS data revealing variable agreement across the plasma radius. At radii which

appear minimally affected by prompt-torque, the DBS-$\gamma_{E\times B}$ value was a factor of $\approx 2\times$ smaller than the CER values. This provides some insight into the range of uncertainty in the $\gamma_{E\times B}$ values used in turbulence simulations when data from only one diagnostic is used.

Future work related to this investigation should focus on standardizing the practice of propagating uncertainties through ray tracing simulations and using DBS measurements to supplement CER rotation profiles. In principle, profiles of E_r can be routinely calculated from DBS data as long as an estimate of the phase velocity magnitude is available. For the case presented in Chapter 5, we are confident in neglecting the turbulence phase velocity not only because its linear estimate is small, but because of the small average CER-DBS difference value ($\bar{d}$). Conversely, the statistical analysis presented here suggests that, for any singular DBS-CER comparison, the difference should exceed $\omega_{E\times B}$ values of 5 kRad/s ($v \approx 2$ [km/s]) to be statistically significant. However, for an ensemble of DBS-CER differences, d, an offset may be statistically significant if it exceeds the average $\bar{d} = -0.1$ kRad/s reported here. This can inform future studies where the direction of the turbulence phase velocity is inferred from DBS-CER differences. Furthermore, future work can include a more detailed investigation of non-stationary E_r on fast timescales including using DBS to estimate the magnitude of *intrinsic* torque when NBI is not used (and thus CER measurements are not available).

APPENDIX A

The OMFIT DBS module

This appendix provides details regarding the OMFIT DBS module developed by the author as part of this doctoral research. As mentioned in Section 3.3, OMFIT is open-source software tool used throughout the tokamak research community to facilitate the analysis of experimental data, manage and post-process simulations, and build modeling workflows for more customized analysis. Broadly speaking, OMFIT has two components: the OMFIT framework, and the physics modules. The framework of OMFIT provides underlying methods for importing, running, and coupling the physics modules together. Other aspects of the OMFIT framework are beyond the scope of this appendix. There are dozens of physics modules within OMFIT; almost all physics modules are collections of python programs[1]. More information regarding OMFIT and the physics modules can be found on the OMFIT website (`omfit.io`) and in [102].

The OMFIT DBS module supports a variety of workflows specific to DBS modeling and analysis. In the spirit of OMFIT, the DBS module comes with a comprehensive graphical user interface (GUI) to facilitate and guide analysis. The DBS module also interfaces with other physics modules and OMFIT framework classes to accelerate development time and reduce code-duplication. The DBS module also supports modeling and analysis on tokamaks besides DIII-D, for example MAST-U [10]. Finally, OMFIT and the DBS module are available and version-controlled through a GitHub repository[2]. In this appendix we describe several workflows supported by the DBS module.

[1]Some physics modules 'wrap' other programs written in IDL or FORTRAN

[2]`OMFIT-source` (access to the repository may be limited – see the OMFIT website).

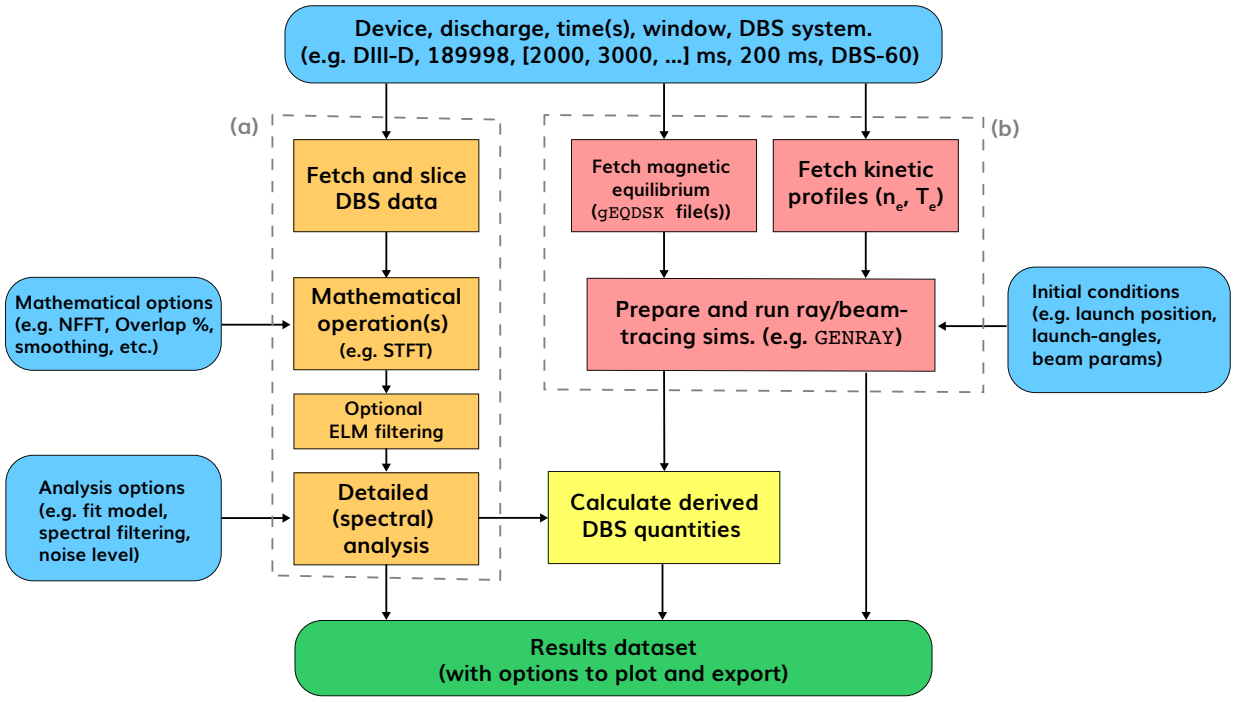

Figure A.1: Block diagram of the detailed data analysis workflow in the OMFIT DBS module. Inputs and outputs are shown as rounded boxes. Each rectangular block represents one or more programs. The portion of the diagram labeled (a) pertains to analysis of the DBS data itself. The portion of the diagram labeled (b) pertains to ray/beam-tracing simulations used to interpret DBS data.

A.1 Detailed analysis of experimental DBS data

The DBS module was originally designed for detailed analysis and interpretation of experimental DBS data from a single discharge and device[3]. Figure A.1 illustrates a typical DBS analysis workflow. In Figure A.1, inputs are shown as blue boxes on the periphery of the diagram. At the beginning of analysis, the user specifies: the device, one discharge number, a list of times (hereafter referred to as the nominal times), a (time) window, and the DBS system(s) under consideration. At the end of the analysis, the user obtains one results-dataset for each requested DBS system. Each results-dataset contains for example, the Doppler shift, the wavenumber $k_{\text{meas.}}$, the probed location, etc.. Each component of the results-dataset is

[3]In OMFIT a 'device' refers to a tokamak, e.g. DIII-D.

an array with two dimensions: channels, and nominal times.

In Figure A.1, the portion of the diagram labeled (a) contains the analysis of DBS data itself. The DBS data (digitized quadrature outputs: I and Q) are fetched and sliced (in time) according to user inputs. The user selects the desired mathematical operations to be performed on the raw DBS data. The default mathematical operation is the windowed, short-time-Fourier-transform (STFT) of the demodulated scattering signal, $S(t) = I(t) + iQ(t)$, resulting in the quadrature spectrum (discussed in Section 3.3). However, the module can also perform spectral coherence calculations and compute windowed-STFT spectra of the amplitude, $A(t) = \sqrt{I^2(t) + Q^2(t)}$, and phase, $\phi(t) = \arctan\left(Q(t)/I(t)\right)$, of the scattering signal. Other mathematical operations are also supported, for example the phase-derivative approach to determining the DBS Doppler shift. However for this description we will focus on the quadrature spectrum. The DBS module is flexible and other mathematical operations can be added in the future.

The output of the previous 'mathematical operation' stage of the DBS module is a three dimensional array with dimensions: X, time, and nominal-time. The time dimension is local to each nominal time, its size is set by the user-provided time window at the beginning of analysis (and other calculation parameters e.g. overlap and NFFT). The X dimension depends on the mathematical operation; for standard spectral analysis X is frequency. The user is then directed to a secondary 'spectral analysis' GUI for detailed data analysis of each three-dimensional array. For standard quadrature spectral analysis this consists of determining the Doppler shift and spectral power using methods outlined in Section 3.3 and Appendix B. Once the detailed data analysis is complete, the outputs (Doppler shift, spectral power, spectral full-width-half-max, etc.) are stored in the results dataset object.

In Figure A.1, the portion of the diagram labeled (b) contains the setup and execution of ray/beam-tracing simulations (discussed in Sections 3.4, 3.5). These simulations generally require the magnetic equilibrium and the plasma density as inputs. The DBS module oversees fetching of experimental magnetic equilibria (in the form of `gEQDSK` files) and electron density profiles for each nominal time. The DBS module automatically calculates the fun-

damental frequencies shown in Figure 3.2 and presents them in an interactive figure. The DBS module allows the user to load other OMFIT physics modules to oversee the ray/beam tracing. Currently, `GENRAY`, `SCOTTY`, and `TORBEAM` are all supported via their respective OMFIT modules. Finally, the ray/beam-tracing simulations are executed in parallel, generally through an HPC workload manager (e.g. `SLURM`). Lastly, 'derived' DBS quantities are calculated by combining the ray/beam-tracing outputs with outputs of the spectral analysis, e.g. $v_{\text{meas.}} = 2\pi f_{\text{Dopp.}}/k_{\text{meas.}}$. The ray/beam-tracing outputs and any derived outputs are stored in the results-dataset. The DBS module offers a variety of plotting options and allows the user to export the results-dataset to a file for use outside of OMFIT.

A.2 DBS modeling and experimental planning

In addition to the data analysis and interpretation described in the previous section, the OMFIT-DBS module can be used for experiment-planning and other predictive modeling. In an experiment-planning workflow the user specifies the device, a target discharge, one or more times, and DBS system(s). Then, the user fetches magnetic equilibria and kinetic profiles – skipping the DBS data analysis portion of Figure A.1. The DBS module includes methods for modifying an experimental magnetic equilibrium. Namely, methods to scale the magnetic field and/or plasma current without changing the flux surface geometry. The user can also scale the density and/or temperature profiles or provide a new set of hypothetical profiles. Then, the fundamental frequencies (e.g. Figure 3.2) are calculated, allowing the user to inspect DBS access in the hypothetical plasma.

For more detailed planning, the (potentially modified) magnetic equilibrium and kinetic profiles can be input to ray/beam-tracing simulations. Scans of the poloidal and/or toroidal launch-angles can also be performed. Launch-angle scans allows the user to predict the range of probed locations and wavenumbers. The OMFIT-DBS module includes methods for orchestrating launch-angle scans using the supported ray/beam tracing codes. Figure A.2 provides an example launch-angle scan using the GENRAY code. The launch-angle scan is performed by varying the poloidal launch-angle (β) over the range, $5° \leq \beta \leq 9°$, with fixed

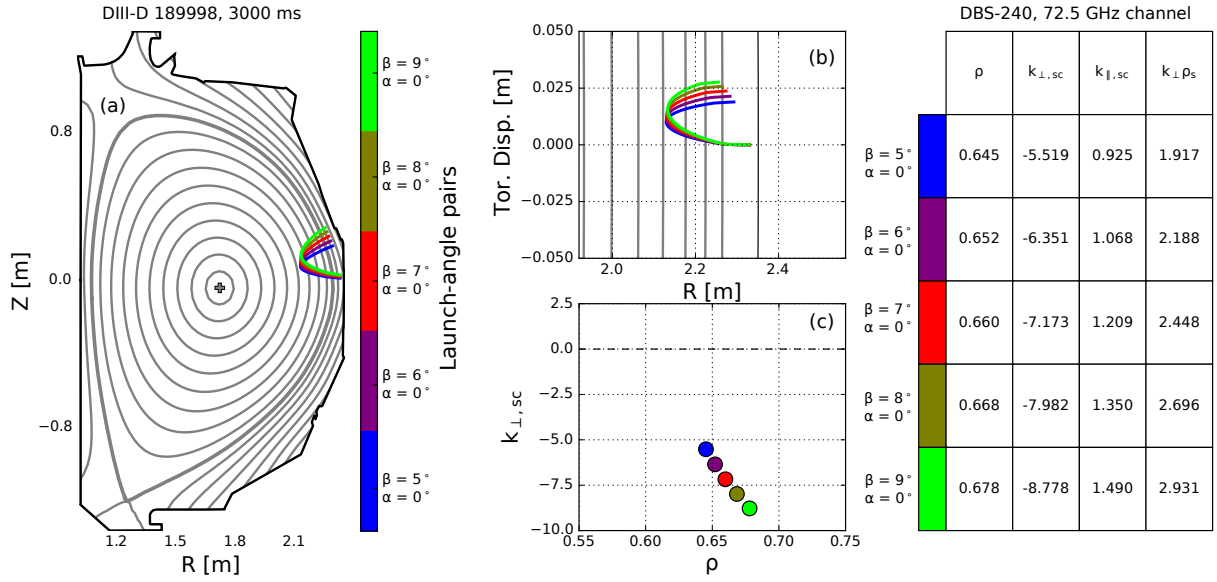

Figure A.2: Example OMFIT DBS module output illustrating a scan of the poloidal launch angle (β). Figure A.2(a) shows a poloidal projection of the plasma with rays from the launch-angle scan superimposed. Figure A.2(b) shows the toroidal displacement of rays shown in (a). Figure A.2(c) shows the probed-locations (ρ) and scattering wavenumbers ($k_{\perp,sc}$). The background plasma used in the angle scan was discussed in Chapter 4.

toroidal launch-angle $\alpha = 0°$. In Figure A.2(a) we show a poloidal projection of a magnetic equilibrium with rays from the scan. In Figure A.2(b) we show the toroidal displacement of the rays when viewed from above. In Figure A.2(c) we show the resulting probed locations (ρ) and $k_{\text{meas.}} = k_{\perp,sc} = -2k_{\perp,i}$. The subscript 'sc' refers to the *scattering* wavenumber, an alternative notation to $k_{\text{meas.}}$. Figure A.2 also shows a tabulation of results (automatically generated by the DBS module for launch-angle scans).

The angle-scan methods built into the OMFIT DBS module can also be used for wavenumber-targeting. The k-targeting routine determines the poloidal and toroidal launch-angles necessary to achieve a particular $\mathbf{k}_{\text{meas.}}$. Wavenumber-targeting is commonly used to minimize mismatch-attenuation (discussed in Section 3.1) by iteratively seeking the poloidal and toroidal launch-angles such that both $k_{\parallel,i} = 0$ and $k_{\perp,i} = -\frac{1}{2}k_{\text{meas.}}$ at cutoff. Figure A.3 illustrates a k-targeting output for the case shown previously in Figure A.2. For the example in Figure A.3, we target $k_{\parallel,sc} = 0$ and $k_{\perp,sc} = 8$ cm^{-1}. The resulting set of launch-angles:

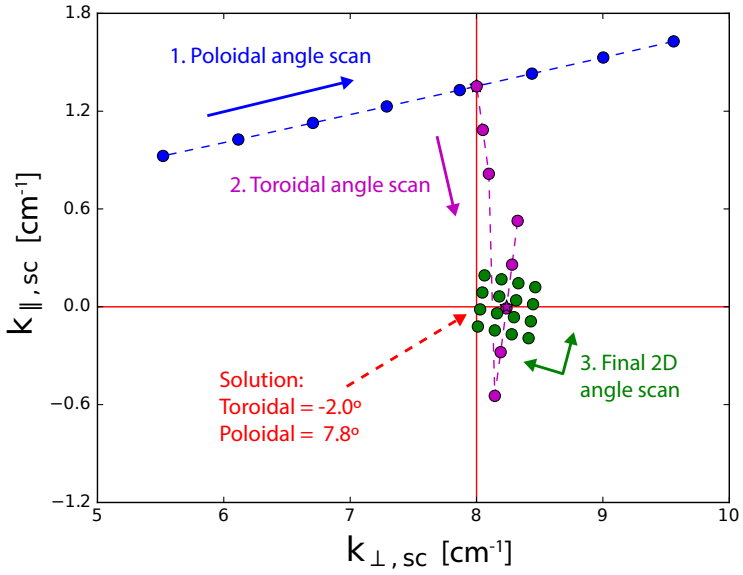

Figure A.3: Example OMFIT DBS module output for the wavenumber-targeting workflow. The background plasma and DBS channel used in this k-targeting example are shown in Figure A.2. The sequence of the k-targeting algorithm is shown with annotations.

$\beta = 7.8°$ and $\alpha = -2.0°$ correspond to the point in Figure A.3 closest to the the target. In this situation $\alpha < 0°$ corresponds to the out-of-plane direction in Figure A.2(a) and negative toroidal displacement in Figure A.2(b). Intuitively, aiming $\alpha < 0°$ servers to negate the positive toroidal displacement in Figure A.2(b), ideally resulting in $k_{\parallel,sc} = 0$ at cutoff.

Finally, the OMFIT DBS module supports other theory-based predictive DBS modeling. The synthetic beam-DBS diagnostic discussed in Section 3.7 has been incorporated into the OMFIT-DBS module for predictions of the DBS scattered power and estimates of the turbulent phase velocity. Figure A.4 illustrates two synthetic-DBS workflows. In each case the user begins with a set of profiles and a magnetic equilibrium file. The workflow on the left side of Figure A.4 (labeled (a)) corresponds to calculating a synthetic DBS wavenumber spectrum (e.g. one of the primary results in Chapter 4). The user performs a series of beam-tracing simulations corresponding to a launch-angle ($k_{\text{meas.}}$) scan. Then, at least one turbulence simulation at a nominal probed-location is performed. To account for radial variation in the turbulence simulations, the user has the option to perform additional turbulence simulations if the probed locations are significantly different. The output of the

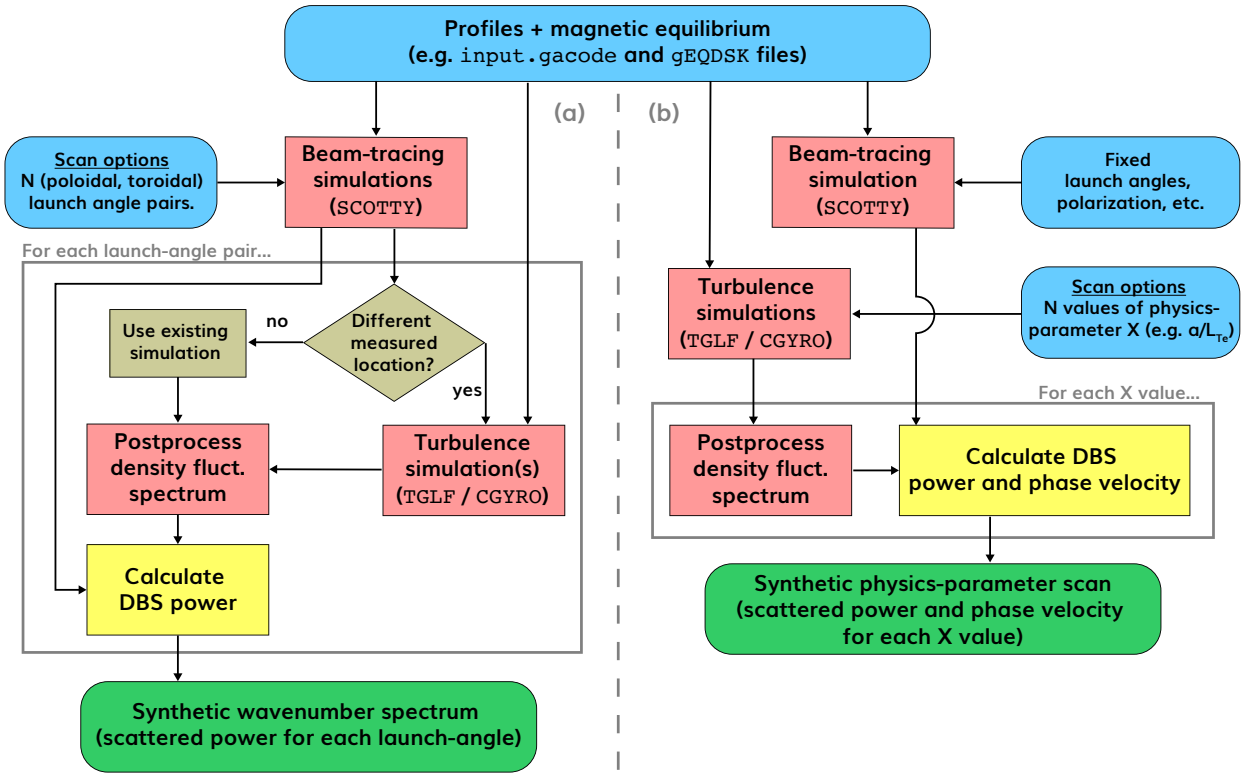

Figure A.4: Block diagram illustrating synthetic DBS workflows within the OMFIT-DBS module. The portion of the diagram labeled (a) pertains to calculation of a synthetic DBS scattered-power wavenumber spectrum. The portion of the diagram labeled (b) pertains to predictions of the DBS scattered power and turbulence phase velocity as a function of an arbitrary turbulence parameter (e.g. a/L_{T_e}).

turbulence simulations are post-processed to calculate the density fluctuation wavenumber spectrum, $\delta\hat{n}(k_n, k_b; \rho, \theta)$. Finally, the DBS scattered power is calculated and stored for each loop iteration. The result is a synthetic DBS wavenumber spectrum, $P_s^{\text{syn.}}(k_{\text{meas.}})$.

An alternative synthetic DBS workflow is illustrated on the right side of Figure A.4 (labeled (b)). In this workflow, one beam-tracing simulation is performed providing a single probed location and $k_{\text{meas.}}$. Separately, the user performs a scan over a physics parameter input to turbulence simulations (e.g. a/L_{T_e}, ν_{*e}, T_e/T_i, etc.). Then, for each turbulence simulation output, the synthetic DBS scattered power, $P_s^{\text{syn.}}$, is calculated. Similarly, if TGLF or linear CGYRO is used, an estimate of the turbulence phase velocity can be calculated from the real ω evaluated at $k_{\text{meas.}}$ (discussed in Subsection 5.5.1). The output of this workflow

is a prediction of the DBS $P_s^{\text{syn.}}$ (and/or $v_{\text{ph.}}$) vs. X (the physics parameter). These results can be used to answer the question: Given a particular DBS launch-angle and background plasma – how would a change in X affect the DBS scattered power or Doppler shift (through $v_{\text{ph.}}$)?

APPENDIX B

Models for the DBS frequency spectrum

The shape of the DBS frequency spectrum was discussed in Sections 3.1.6 and 3.3. In this Appendix we present the theory-based Taylor model for the frequency spectrum as well as other ad-hoc models for the frequency spectrum used in the analysis of DBS data.

B.1 Taylor model

The Taylor model for the frequency spectrum is owes its name to work by G. I. Taylor [151] where an expression for the ensemble averaged squared displacement of particles in a turbulent fluid was derived using classical Lagrangian fluid mechanics. The result from Taylor was later combined with a statistical interpretation of frequency spectra from collective scattering measurements by D. Gresillon *et al.* [152]. The resulting 'Taylor model' was applied for collective scattering and DBS data analysis in [94,95]. In their doctoral thesis, A. Casati [69] referenced the connection between the Taylor model and the method of cumulant expansion. The cumulant expansion method for describing stochastic broadening of frequency spectra was developed by R. Kubo in [153, 154] and discussed in the context of plasma physics in [155].

Starting with Equation 3.21 (repeated here),

$$A_{\mathbf{k}}(t) = \int_V d^3r \delta n(\mathbf{r}, t) U(\mathbf{r}) e^{-i\mathbf{k}\cdot\mathbf{r}}, \tag{B.1}$$

the instantaneous received signal amplitude for a fixed wavenumber ($\mathbf{k} = \mathbf{k}_{\text{meas.}}$) is $A_{\mathbf{k}}(t)$.

The goal is to calculate the (temporal) auto-correlation function,

$$\langle A_{\mathbf{k}}(t)A^*_{\mathbf{k}}(t')\rangle = \left\langle \int_V \int_{V'} d^3r d^3r' \delta n(\mathbf{r},t)\delta n(\mathbf{r}',t')U(\mathbf{r})U(\mathbf{r}')e^{-i\mathbf{k}\cdot(\mathbf{r}-\mathbf{r}')} \right\rangle. \tag{B.2}$$

Following D. Gresillon *et al.* [152], we wish to separate the spatial and temporal statistics of the turbulence by making the coordinate transformation, $\mathbf{r}'' = \mathbf{r}' - \mathbf{\Delta}(\mathbf{r}'', \tau)$ with $\tau = t' - t$. The microscopic displacements $\mathbf{\Delta}$ are such that $\delta n(\mathbf{r}', t+\tau) = \delta n(\mathbf{r}'', t)$. The differential integral volume is assumed to be approximately unchanged as particle number is conserved and the DBS weighting function, $U(\mathbf{r})$, varies on a disparate scale relative to $\mathbf{\Delta}$. The signal amplitude auto-correlation becomes,

$$\langle A_{\mathbf{k}}(t)A^*_{\mathbf{k}}(t+\tau)\rangle = \left\langle \int_V \int_{V''} d^3r d^3r'' \delta n(\mathbf{r},t)\delta n(\mathbf{r}'',t)U(\mathbf{r})U(\mathbf{r}'')e^{-i\mathbf{k}\cdot(\mathbf{r}-\mathbf{r}'')}e^{i\mathbf{k}\cdot\mathbf{\Delta}(\mathbf{r}'',\tau)} \right\rangle. \tag{B.3}$$

To make further simplifications we use the independence approximation to separate the τ-dependant exponential from the ensemble average. This approximation is valid when the *spatial* δn statistics become independent from the time-evolution statistics governing the stochastic displacements $\mathbf{\Delta}$. The resulting equation is,

$$\langle A_{\mathbf{k}}(t)A^*_{\mathbf{k}}(t+\tau)\rangle = \left\langle \int_V \int_{V''} d^3r d^3r'' \delta n(\mathbf{r},t)\delta n(\mathbf{r}'',t)U(\mathbf{r})U(\mathbf{r}'')e^{-i\mathbf{k}\cdot(\mathbf{r}-\mathbf{r}'')} \right\rangle \left\langle e^{i\mathbf{k}\cdot\mathbf{\Delta}(\tau)} \right\rangle. \tag{B.4}$$

This approximation makes the first bracketed term independent of the time τ. This first term encodes the wavenumber-response of the signal amplitude, we will define it as $F(\mathbf{k})$. We will also assume the dynamics are (temporally) stationary such that the signal amplitude is independent of the instantaneous time t. The resulting auto-correlation function is,

$$R_{\mathbf{k}}(\tau) = \langle A_{\mathbf{k}}(0)A^*_{\mathbf{k}}(\tau)\rangle = F(\mathbf{k}) \left\langle e^{i\mathbf{k}\cdot\mathbf{\Delta}(\tau)} \right\rangle. \tag{B.5}$$

The approximations leading to Equation B.5 imply that the time-dynamics (and therefore the frequency spectrum) of the received signal amplitude are completely determined by the

stochastic displacements of the plasma density,

$$\mathbf{\Delta}(\tau) = \overline{\mathbf{v}}\tau + \int_0^\tau \delta\mathbf{v}(t)dt, \tag{B.6}$$

where $\overline{\mathbf{v}}$ is an average velocity and $\delta\mathbf{v}(t)$ are the stochastic velocity fluctuations. The remaining ensemble-average term in Equation B.5 can be handled rigorously using the cumulant expansion methods from R. Kubo [154]. The exponential is expanded as,

$$\left\langle e^{i\mathbf{k}\cdot\mathbf{\Delta}(\tau)} \right\rangle = e^{i\mathbf{k}\cdot\overline{\mathbf{v}}\tau} \exp\left(\sum_{n=1}^{\infty} (ik)^n \int_0^\tau dt_1 \int_0^{t_1} dt_2 \cdots \int_0^{t_{n-1}} dt_n \langle\langle \delta v(t_1) \dots \delta v(t_n) \rangle\rangle \right), \tag{B.7}$$

where $\langle\langle \dots \rangle\rangle$ represents the cumulant. If we assume the stochastic velocity fluctuations are normally distributed, $\delta v \sim \mathcal{N}(0, \sigma_v^2)$, the sum in Equation B.7 is exact to second order[1]. Thus, Equation B.7 reduces to,

$$\left\langle e^{i\mathbf{k}\cdot\mathbf{\Delta}(\tau)} \right\rangle = e^{ik\overline{v}\tau} \exp\left(-k^2 \int_0^\tau dt_1 \int_0^{t_1} dt_2 \langle \delta v(t_1) \delta v(t_2) \rangle \right). \tag{B.8}$$

At this point we must prescribe a functional form for the auto-correlation of velocity fluctuations. Assuming Gaussian/Markovian statistics, the auto-correlation function has simple exponential decay,

$$\langle \delta v(t) \delta v(t') \rangle = u^2 e^{-|t-t'|/\tau_{ac}}, \tag{B.9}$$

where $u^2 \equiv \langle |\delta v|^2 \rangle$ is the mean-squared velocity fluctuation amplitude and τ_{ac} is the auto-correlation time of velocity fluctuations. Substituting Equation B.9 into Equation B.8 and performing the integrals results in,

$$\left\langle e^{i\mathbf{k}\cdot\mathbf{\Delta}(\tau)} \right\rangle = e^{ik\overline{v}\tau} \exp\left(-k^2 u^2 \tau_{ac}^2 (\tau/\tau_{ac} - 1 + e^{-\tau/\tau_{ac}}) \right). \tag{B.10}$$

Physically, the dimensionless factor $ku\tau_{ac}$ plays an equivalent role as the Kubo number, K,

[1]The first two cumulants of a Gaussian process are equal to the first two moments, all other cumulants are exactly zero.

in the stochastic frequency modulation theory developed in [154]. The triple-product $ku\tau_{ac}$ encodes the strength of the random frequency modulation (ku) over one δv auto-correlation time (τ_{ac}).

Finally, the normalized spectral density function can be calculated by calculating the Fourier transform of the auto-correlation function in Equation B.5[2]. The normalization removes the **k**-dependence,

$$S(\omega) = \frac{1}{\pi} \operatorname{Re} \int_0^\infty d\tau \frac{R_{\mathbf{k}}(\tau)}{R_{\mathbf{k}}(0)} e^{-i\omega\tau}. \tag{B.11}$$

The resulting $\exp(\ldots \exp(\ldots))$ integral can be evaluated using tabulated results in [156],

$$S(\omega) = \frac{\tau_{ac}}{\pi} e^{\beta} \operatorname{Re}[\beta^{-\mu}\gamma(\mu, \beta)] \tag{B.12}$$

wherein $\beta = k^2u^2\tau_{ac}^2$ and $\mu = \beta + i\tau_{ac}(\omega - k\overline{v})$ such that $\mu \in \mathbb{C}$ with $\operatorname{Re}(\mu) = \beta > 0$. In Equation B.12(b), $\gamma(a, b)$ is the lower incomplete gamma function defined as,

$$\gamma(a, b) \equiv \int_0^b dz z^{a-1} e^{-z}. \tag{B.13}$$

The numerical implementation of the lower incomplete gamma function available within standard numerical libraries (e.g. `scipy.special.gammainc`) does not support complex-valued inputs to $\gamma(\mu, \beta)$. We have developed a numerical implementation based on the

[2]This is the Wiener–Khinchin theorem which relies on the stationary statistics assumption.

following continued fraction representation of $\gamma(\mu,\beta)$[3],

$$\gamma(\mu,\beta) = \cfrac{\beta^{\mu}e^{-\beta}}{\mu - \cfrac{\mu\beta}{\mu+1+\cfrac{\beta}{\mu+2-\cfrac{(\mu+1)\beta}{\mu+3+\cfrac{2\beta}{\mu+4-\cfrac{(\mu+2)\beta}{\mu+5+\cfrac{3\beta}{\mu+6-\ddots}}}}}}}. \tag{B.14}$$

It's important to note that the top-level numerator of B.14 cancels exactly with the $e^{\beta}\beta^{-\mu}$ terms in Equation B.12. Leveraging this cancellation in the numerical implementation improves the stability of the continued fraction representation of $S(\omega)$. Figure B.1 shows multiple $S(\omega)$ curves for three values of the Kubo number, $K = ku\tau_{ac}$, evaluated using Equation B.12(b).

The limiting cases of the Taylor model can be easily understood in the time domain by inspecting Equation B.10. In the small K limit, i.e. when the velocity fluctuations are weak and have short auto-correlation time such that $\tau_{ac} \ll \tau$, the $R(\tau)$ is exponential, yielding a Lorentzian $S(\omega)$ upon taking the Fourier transform. In the opposing limit where velocity fluctuations are strong and have long auto-correlation time, $\tau_{ac} \gg \tau$, the inner exponential is expanded to second order and the resulting $R(\tau)$ is Gaussian, yielding a Gaussian $S(\omega)$ upon taking the Fourier transform.

[3] `Wikipedia`: Incomplete gamma function

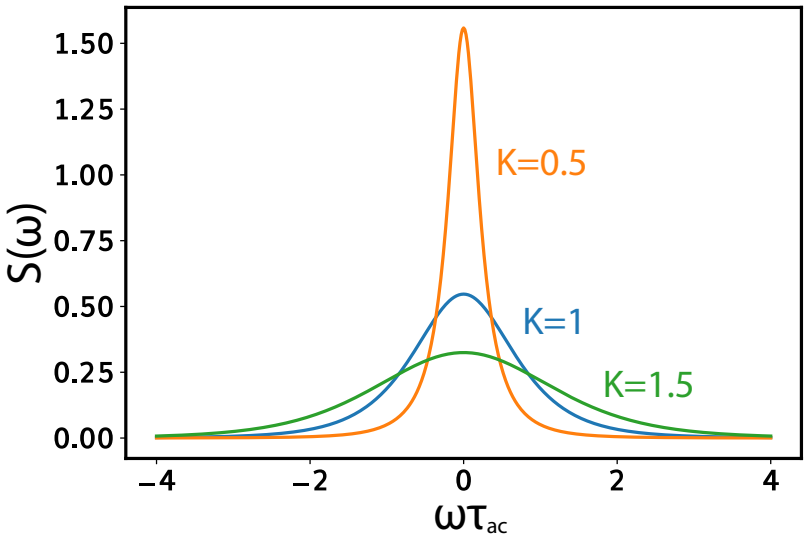

Figure B.1: Evaluation of the Taylor model $S(\omega)$ using B.12(b) for three values of the Kubo number, $K = ku\tau_{ac}$.

B.2 Three-parameter models

The three-parameter class of ad-hoc DBS models includes lineshapes with an amplitude (A), center frequency ($f_{\text{Dopp.}}$), and width (σ). Some examples of three parameter models are given below along with their square-integral ($= P_s$) and full-width at half-max (FWHM).

The Gaussian model,

$$\hat{S}_G(f; A, f_{\text{Dopp.}}, \sigma) = \frac{A}{\sqrt{2\pi}\sigma} \exp\left(-\frac{(f - f_{\text{Dopp.}})^2}{2\sigma^2}\right) \tag{B.15a}$$

$$\int_{-\infty}^{\infty} |\hat{S}_G|^2 df = \frac{A^2}{2\sqrt{\pi}\sigma} \tag{B.15b}$$

$$\text{FWHM}_G = 2\sqrt{2\ln 2}\sigma \tag{B.15c}$$

The Lorentzian model,

$$\hat{S}_L(f; A, f_{\text{Dopp.}}, \sigma) = \frac{A}{\pi\sigma}\left[1 + \left(\frac{f - f_{\text{Dopp.}}}{\sigma}\right)^2\right]^{-1} \tag{B.16a}$$

$$\int_{-\infty}^{\infty} |\hat{S}_L|^2 df = \frac{A^2}{2\pi\sigma} \tag{B.16b}$$

$$\text{FWHM}_L = 2\sigma \tag{B.16c}$$

The exponential (Laplace) model,

$$\hat{S}_e(f; A, f_{\text{Dopp.}}, \sigma) = \frac{A}{2\sigma}\exp\left(-\frac{|f - f_{\text{Dopp.}}|}{\sigma}\right). \tag{B.17a}$$

$$\int_{-\infty}^{\infty} |\hat{S}_e|^2 df = \frac{A^2}{4\sigma} \tag{B.17b}$$

$$\text{FWHM}_e = 2\ln(2)\sigma \tag{B.17c}$$

The logistic (sech-squared) model,

$$\hat{S}_{lg}(f; A, f_{\text{Dopp.}}, \sigma) = \frac{A}{4\sigma}\text{sech}^2\left(\frac{f - f_{\text{Dopp.}}}{2\sigma}\right). \tag{B.18a}$$

$$\int_{-\infty}^{\infty} |\hat{S}_{lg}|^2 df = \frac{A^2}{6\sigma} \tag{B.18b}$$

$$\text{FWHM}_{lg} = 4\sigma \cdot \text{acosh}(\sqrt{2}) \tag{B.18c}$$

B.3 Four-parameter models

The four-parameter class of ad-hoc DBS models includes lineshapes with an amplitude (A), center frequency ($f_{\text{Dopp.}}$), and two width/shape parameters. Some examples of four parameter models are given below along with their square-integral ($= P_s$) and full-width at half-max (FWHM). The added flexibility in these models often improves fits to DBS spectra. It was noted in Subsection 3.1.6 that the shape of the DBS spectra often lie between a Lorentzian and a Gaussian (or more generally between two of the three-parameter models listed above).

This motivates lineshapes that connect two distributions from the previous section.

For example, the Voigt model,

$$\hat{S}_V(f; A, f_{\text{Dopp.}}, \sigma_G, \sigma_L) = A\frac{\text{Re}\{w(z)\}}{\sigma_G\sqrt{2\pi}} \tag{B.19}$$

where $w(z)$ is the Faddeeva function with argument $z = (f - f_{\text{Dopp.}} + i\sigma_L)/\sigma_G\sqrt{2}$. For $\sigma_G \to 0$, $\hat{S}_V \to \hat{S}_L$ and for $\sigma_L \to 0$, $\hat{S}_V \to \hat{S}_G$. The square integral and FWHM of the Voigt lineshape are calculated numerically.

The (generalized) Student's T distribution,

$$\hat{S}_T(f; A, f_{\text{Dopp.}}, \sigma, \nu) = A\frac{\Gamma(\frac{\nu+1}{2})}{\Gamma(\frac{\nu}{2})\sqrt{\pi\nu\sigma^2}}\left[1 + \frac{1}{\nu}\left(\frac{f - f_{\text{Dopp.}}}{\sigma}\right)^2\right]^{-\frac{\nu+1}{2}} \tag{B.20a}$$

$$\int_{-\infty}^{\infty} |\hat{S}_T|^2 df = A^2\left[\frac{\Gamma(\frac{\nu+1}{2})}{\Gamma(\frac{\nu}{2})}\right]^2 \frac{\Gamma(\nu+\frac{1}{2})}{\Gamma(\nu+1)}\frac{1}{\sqrt{\pi\nu\sigma^2}} \tag{B.20b}$$

$$\text{FWHM}_T = 2\sigma\sqrt{\nu(2^{2/(\nu+1)} - 1)} \tag{B.20c}$$

connects the Lorentzian and Gaussian distributions through the parameter ν such that $\hat{S}_T(\nu = 1) = \hat{S}_L$ and $\hat{S}_T(\nu \to \infty) = \hat{S}_G$.

The Generalized Gaussian model,

$$\hat{S}_{GG}(f; A, f_{\text{Dopp.}}, \sigma, \beta) = \frac{A\beta}{2\sqrt{2}\sigma\Gamma(1/\beta)}\exp\left(-\frac{|f - f_{\text{Dopp.}}|}{\sqrt{2}\sigma}\right)^{\beta} \tag{B.21a}$$

$$\int_{-\infty}^{\infty} |\hat{S}_{GG}|^2 df = \frac{A^2\beta\Gamma(\frac{1}{2\beta})}{4\sigma\Gamma^2(\frac{1}{\beta})} \tag{B.21b}$$

$$\text{FWHM}_{GG} = 2\sqrt{2}\sigma[\ln(2)]^{1/\beta} \tag{B.21c}$$

connects the exponential and Gaussian distributions such that $\hat{S}_{GG}(\beta = 2) = \hat{S}_G$ and $\hat{S}_{GG}(\beta = 1) = \hat{S}_e$. The FWHM_{GG} formula is applicable for $\beta > 0$.

B.4 Mixture models

In the previous section we presented a collection of three and four parameter ad-hoc lineshape models for the DBS frequency spectrum. For frequency spectra with a single peak-like component these lineshape models can be fit to data using least-squares fitting algorithms. In this thesis we have made used of methods in the `lmfit` python module [157]. However, in situations with non-trivial frequency spectra where the peak-of-interest cannot be isolated through notch filtering, fitting a single lineshape model may produce inaccurate results. The most straightforward extension of the lineshape models is to create 'composite models' by taking a linear combination of individual lineshapes. However, least-squares fitting algorithms can become computationally slow for a large number of free parameters.

This issue motivated the adaptation of 'Mixture Models' (often used for clustering in Machine Learning (ML) applications) to the problem of quickly isolating multiple peaks in frequency spectra. Traditionally, mixture models are used to identify possible sub-populations and perform a probability density estimation given a collection of samples. To apply these methods to frequency spectra we treat the Fourier transform of the DBS signal as a PDF over frequencies. Frequency samples are then drawn according to the magnitude of $\hat{S}(f)$ and mixture models are applied to determine possible underlying populations in $\hat{S}$(f). The Expectation-Maximization (EM) algorithm is used to determine the maximum-likelihood parameters for the underlying distributions.

The Gaussian Mixture Model (GMM) from the `scikit-learn` [100] python package has been incorporated in the OMFIT-DBS module along with a Students-T Mixture Model (TMM) based on work by Peel [101]. Figure B.2 illustrates a three component GMM applied to DBS data. The discharge shown in Figure B.2 is not featured elsewhere in this dissertation. Figure B.2(b) shows that with three components the algorithm is able to capture the overall lineshape. The implementation of these MM methods in the OMFIT-DBS module allows one to select which mode (1,2,...) to isolate for further analysis.

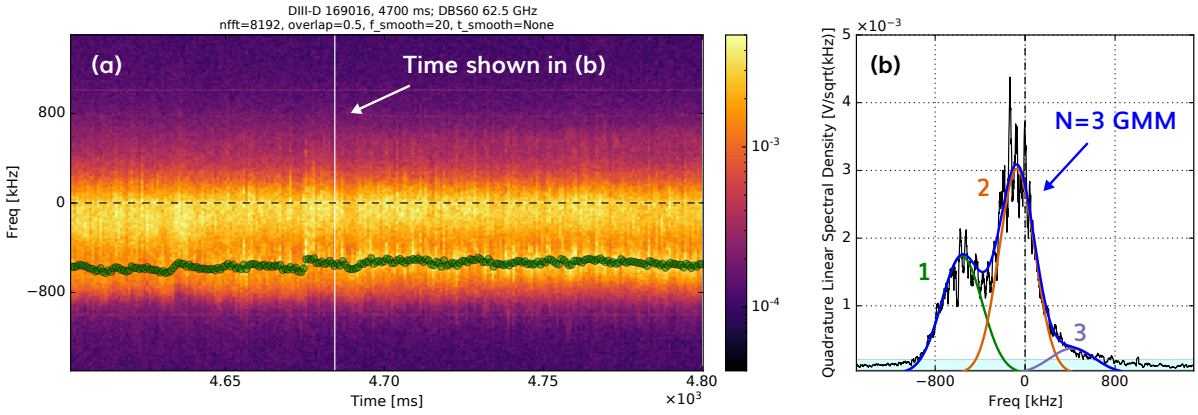

Figure B.2: Example of the Gaussian Mixture Method applied to DBS data. (a) shows a spectrogram featuring at least two modes. (b) shows a time-slice from (a) fit with a three component GMM.

APPENDIX C

The CGYRO code and simulation parameters

Gyrokinetic calculations presented in this dissertation make use of the code CGYRO [16]. This appendix discusses salient code conventions and provides a tabulation of simulation inputs. In particular, we discuss how wavenumbers perpendicular to the background magnetic field are defined in CGYRO. The binormal wavenumber (k_y) used in CGYRO is also used in the gyro-fluid code TGLF. The wavenumbers used in the codes must be converted to physical inverse-lengths for proper comparison with measurements. The issue of converting wavenumbers between simulation and experiment was addressed in work by J. Ruiz Ruiz [8].

CGYRO, like its predecessor GYRO [158], is an Eulerian gyrokinetic code. Both GYRO and CGYRO can be used to solve the linearized GK equation in addition to the nonlinear GKE discussed in subsection 2.3.2 of this thesis. One of the primary difference between the two codes is that CGYRO is fully spectral in the perpendicular direction, i.e. CGYRO solves the nonlinear GK equation in wavenumber-space. Thus, moments of the fluctuating, gyro-averaged distribution function over a grid of radial (k_x) and binormal (k_y) wavenumbers are readily available – motivating the use of wavenumber-space synthetic diagnostics. However, differences in the normalized theory-units, code variable-names, and lab coordinates can confuse validation exercises. The following subsection addresses wavenumber metrics in detail.

C.1 Wavenumber conventions

In Subsection 2.3.2 of this dissertation we discussed the gyrokinetic equation in the context of modeling turbulent transport in magnetized plasmas. We outlined a derivation of the

GKE including a WKB-type expansion of fluctuating quantities. Equation 2.18 (repeated here),

$$\delta X(\mathbf{x}, \varepsilon, \mu, \vartheta, t) = \sum_{\mathbf{k}_\perp} \delta X_{\mathbf{k}_\perp}(\mathbf{x}, \varepsilon, \mu, \vartheta, t) \exp[iS(\mathbf{x}, t)], \tag{C.1}$$

shows the decomposition of an arbitrary quantity (X) into an amplitude, $\delta X_{\mathbf{k}_\perp}$, and an eikonal phase, $S(\mathbf{x})$. In equation C.1, $\mathbf{x}$ refers to spatial coordinates while $(\varepsilon, \mu, \vartheta)$ are velocity-space coordinates. Perpendicular wavenumbers are defined in terms of the spatial gradient of the eikonal phase, $\mathbf{k}_\perp \equiv \nabla_{\mathbf{x}} S$. Generally speaking, $\mathbf{k}_\perp$ has normal (k_n) and binormal (k_b) components relative to the background magnetic field, $\mathbf{B}$. Thus, before we can write an explicit formula for the perpendicular wavenumbers we must specify the CGYRO field-aligned coordinates.

The following subsections provide theoretical background for the CGYRO wavenumber definitions including a discussion of the local (flux-tube) limit of gyrokinetics. We clarify the relationship between the binormal angular coordinate α and the binormal spatial coordinate y. Equation C.12 defines k_x and k_y used internally by CGYRO (and TGLF). Equation C.15 shows the relationship between the internal code definitions and the physical wavenumbers corresponding to real inverse-lengths. Finally we present a simplified formula for converting between k_x, k_y and k_n, k_b. The material for this Appendix is thanks to a thorough presentation of local gyrokinetics by H. Dudding in their Ph.D. thesis [35], work by J. Ruiz Ruiz [8], and work by J. Candy [16].

Theoretical background and CGYRO definitions

In CGYRO, the magnetic field is written in Clebsch form as $\mathbf{B} = \nabla\alpha \times \nabla\psi$, where ψ is the poloidal magnetic flux (divided by 2π) and the angular coordinate, $\alpha \equiv \phi + \nu(\psi, \theta)$, is the sum of a toroidal angle, ϕ, and another coordinate, $\nu(\psi, \theta)$, which is a function of the poloidal angle, θ, and encodes the helicity of the magnetic field[1]. In writing the magnetic field in this way, it is clear that both ψ and α are orthogonal to $\mathbf{B}$ (see Figure 2.2(c)). Thus,

[1]For a circular equilibrium $\nu \sim -q\theta$.

α and ψ are natural choices for the binormal and radial coordinates respectively. We are also free to use the minor radius, r, as the radial coordinate. Doing so allows the magnetic field to be written,

$$\mathbf{B} = \frac{d\psi}{dr}\nabla\alpha \times \nabla r. \tag{C.2}$$

To identify the perpendicular wavenumbers we perform a Fourier series expansion of an arbitrary function, $f(r, \alpha, \theta)$, to identify the eikonal $S(r, \alpha, \theta)$. Given that α is a periodic angular coordinate, its Fourier series expansion is simply,

$$f(r, \alpha, \theta) = \sum_n \hat{f}_n(r, \theta) e^{-in\alpha}, \tag{C.3}$$

where $n \in \mathbb{Z}$ is the toroidal mode number. However, poloidal periodicity requires that the toroidal mode amplitudes satisfy,

$$\hat{f}_n(r, \theta) = \hat{f}_n(r, \theta + 2\pi M) e^{in2\pi M q(r)}, \tag{C.4}$$

where $M \in \mathbb{Z}$. It is clear from the previous expression that the mode amplitudes are not periodic in the radial dimension and cannot generally be expanded in a Fourier series. To circumvent this, we transform to a local 'flux tube' of width L at a radial location $r = r_0$. Taking the local limit allows us to expand $q(r)$ in the neighborhood $r \approx r_0$ and impose periodic boundary conditions in the radial direction. While radial periodicity is not physical; so long as L is more than several turbulence correlation lengths, the periodicity at the boundaries is irrelevant [159]. Over the flux tube we can define a new radial variable $x = r - r_0$ and perform another Fourier series expansion,

$$f(x, \alpha, \theta) = \sum_n \sum_p \hat{f}_{n,p}(\theta) e^{-in\alpha} e^{i2\pi px/L}. \tag{C.5}$$

Rather than use the angular binormal coordinate α, it is conventional to define a binormal coordinate y with units of length. In CGYRO the re-definition of the binormal coordinate

is,

$$y = \frac{r_0}{q(r_0)}\alpha. \tag{C.6}$$

Thus, the 2D Fourier series expansion becomes,

$$f(x, y, \theta) = \sum_n \sum_p \hat{f}_{n,p}(\theta) e^{-inq(r_0)y/r_0} e^{i2\pi px/L}, \tag{C.7}$$

and the local magnetic field can be written in a very simple form,

$$\mathbf{B} = B_{\text{unit}} \nabla y \times \nabla x, \tag{C.8}$$

where the reference, normalizing magnetic field is defined as,

$$B_{\text{unit}} \equiv \frac{q(r)}{r}\frac{d\psi}{dr}. \tag{C.9}$$

The B_{unit} magnetic field is used to define other quantities such as the effective ion-sound gyro-radius,

$$\rho_{s,\text{unit}} \equiv \frac{c_s}{\Omega_{D,\text{unit}}}, \tag{C.10}$$

where $c_s \equiv \sqrt{T_e/m_D}$ is the (Deuterium) ion-sound speed, and $\Omega_{D,\text{unit}}$ is the Deuterium cyclotron frequency evaluated with $B = B_{\text{unit}}$. The $\rho_{s,\text{unit}}$ quantity is used to normalize spatial quantities throughout CGYRO. When we normalize $y' = y/\rho_{s,\text{unit}}$ and $x' = x/\rho_{s,\text{unit}}$, the 2D Fourier series expansion can be written,

$$f(x, y, \theta) = \sum_n \sum_p \hat{f}_{n,p}(\theta) e^{ik_y y'} e^{ik_x x'}, \tag{C.11}$$

with local, dimensionless wavenumbers defined as,

$$k_x \equiv \frac{2\pi p}{L}\rho_{s,\text{unit}} \tag{C.12a}$$

$$k_y \equiv -\frac{nq(r_0)}{r_0}\rho_{s,\text{unit}}. \tag{C.12b}$$

These dimensionless wavenumbers are used within the code CGYRO[2] but they do not correspond to physical inverse-lengths in the radial and binormal directions.

Physical wavenumbers

To derive the physical, flux-tube perpendicular wavenumbers we return to the Fourier series expansion in equation C.5. We re-define the periodic radial variable to $x \equiv 2\pi(r - r_0)/L_x \in [0, 2\pi)$ such that the 2D Fourier series expansion is simply,

$$f(x, \alpha, \theta) = \sum_n \sum_p \hat{f}_{n,p}(\theta) e^{i(px - n\alpha)}. \tag{C.13}$$

In comparing equations C.13 and C.1 (we have omitted the velocity-space coordinates), we identify the eikonal phase as $S = px - n\alpha$.

The explicit form of S allows us to calculate $\mathbf{k}_\perp \equiv \nabla_{\mathbf{x}} S$ using unit vectors in the normal and binormal directions: $\hat{\mathbf{e}}_n \equiv \nabla r/|\nabla r|$ and $\hat{\mathbf{e}}_b \equiv \hat{\mathbf{b}} \times \hat{\mathbf{e}}_n$. The physical flux tube perpendicular wavenumbers are,

$$k_n = \hat{\mathbf{e}}_n \cdot \mathbf{k}_\perp = \frac{2\pi p}{L}|\nabla r| - n\frac{\nabla r \cdot \nabla \alpha}{|\nabla r|} \tag{C.14a}$$

$$k_b = \hat{\mathbf{e}}_b \cdot \mathbf{k}_\perp = -n\left(\hat{\mathbf{b}} \times \frac{\nabla r}{|\nabla r|}\right) \cdot \nabla \alpha. \tag{C.14b}$$

The relationship between the physical wavenumbers and the wavenumbers used in the code can be found by substituting equation C.12 into equation C.14,

$$k_n = \frac{k_x}{\rho_{s,\mathrm{unit}}}|\nabla r| - \frac{r k_y}{q\rho_{s,\mathrm{unit}}}\frac{\nabla r \cdot \nabla \alpha}{|\nabla r|} \tag{C.15a}$$

$$k_b = \frac{r k_y}{q\rho_{s,\mathrm{unit}}}\left(\hat{\mathbf{b}} \times \frac{\nabla r}{|\nabla r|}\right) \cdot \nabla \alpha. \tag{C.15b}$$

Equation C.15 provides the general mapping between the (k_x, k_y) used by the codes and

[2]This definition of k_y is also used by TGLF (up to a factor of -1).

(k_n, k_b).

Limiting cases

The wavenumber relationships in equation C.15 can be simplified in the limit of up/down symmetric (UDS) flux surfaces evaluated at the LFS midplane ($\theta = 0$). This limit is relevant because flux surfaces in the core tend to be up/down symmetric and the majority of fluctuation measurements are performed in the vicinity of $\theta = 0$. The UDS, $\theta \approx 0$ limit is,

$$k_n = \frac{k_x}{\rho_{s,\text{unit}}} |\nabla r| \tag{C.16a}$$

$$k_b = \frac{k_y}{\rho_{s,\text{unit}}} \frac{r}{q} \left[\frac{1}{R^2} + \left(\frac{\partial \alpha}{\partial \theta} \right)^2 / (\kappa r)^2 \right]^{1/2}, \tag{C.16b}$$

where R is the major radius of the flux surface and κ is the flux surface elongation. All quantities in equation C.16 are evaluated at $\theta = 0$.

Physically, the factor $|\nabla r|$ in equation C.16(a) scales the k_x CGYRO wavenumber to account for the expansion ($|\nabla r| < 1$) or compression ($|\nabla r| > 1$) of flux surfaces. On the LFS midplane the typical situation is compression due to Shafranov shift wherein the physical k_n becomes larger than k_x indicating that turbulent structures become radially smaller. In the binormal direction, equation C.16(b) shows that as flux surface elongation (κ) is increased, the scale factor on k_y decreases. This is representative of turbulent structures becoming larger in the binormal direction as flux surfaces become more elongated [8, 62].

Relevance to synthetic DBS diagnostics

In the synthetic diagnostic work presented in this thesis, we make use of Equation C.16 to convert simulated $\delta n(k_x, k_y)$ wavenumber spectra to physical wavenumber space, $\delta n(k_n, k_b)$. As discussed in Subsection 4.4.3, the DBS measurements come from a span of $\theta/\pi \in [0, 0.1]$. Work in Subsection 4.4.3 (Figure 4.15) showed that time-averaged potential fluctuations do not vary significantly over this range of θ. Similarly, we find the $\theta = 0$, UDS wavenumbers

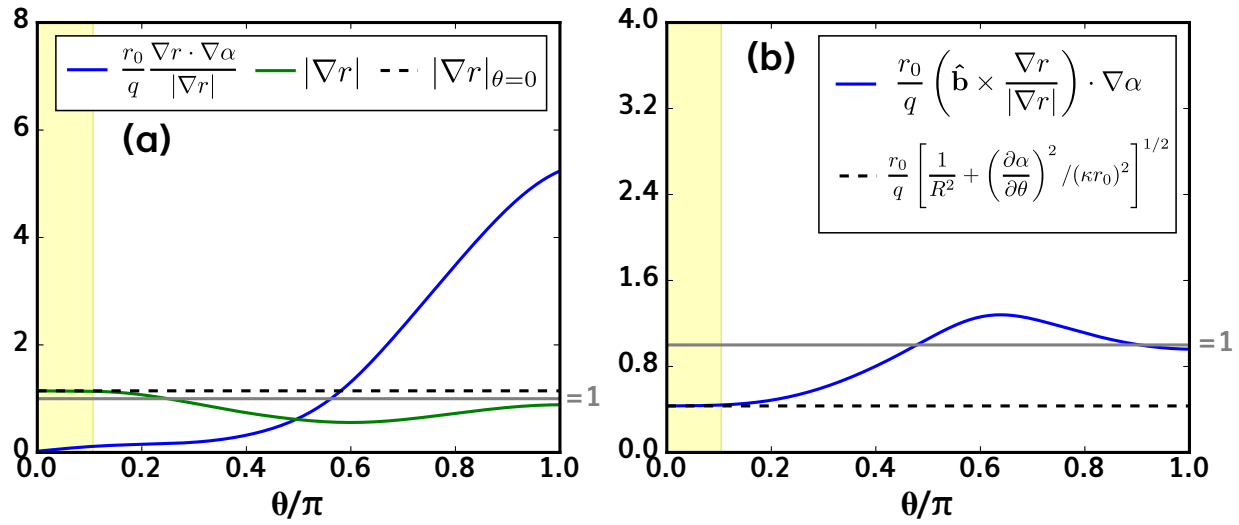

Figure C.1: Comparison of terms in equations C.15 and C.16 for the case presented in Chapter 4. In each case we take $k_y = 1$. (a) compares terms in the $k_n(k_x)$ formula while (b) compares terms in the $k_b(k_y)$ formula. The shaded region in each subplot is $\theta/\pi \leq 0.1$ where all DBS measurements are made.

(Equation C.16) are a good approximation to the general formula (Equation C.15) over this range of θ.

Figure C.1 provides a plot of terms in the wavenumber equations over the range $0 \leq \theta \leq \pi$ for the case discussed in Chapter 4 of this thesis. In both subplots (a,b) the UDS, $\theta = 0$ limits are shown with dashed horizontal lines. It is clear that UDS, $\theta = 0$ (Equation C.16) approximation is very good for $\theta/\pi \leq 0.1$. Horizontal lines at unity are provided to show $|\nabla r|_{\theta=0} > 1$ indicating flux surface compression. For the binormal wavenumber (Figure C.1(b)), the $\theta = 0$ value is far from unity – suggesting binormal distortion is significant and an approximation $k_y \approx k_b \rho_s$ would be significantly inaccurate.

C.2 Simulation parameters

This section documents the input parameters for nonlinear CGYRO simulations presented in Chapter 4. Parameters are based on experimental profile fits and a corresponding kinetic equilibrium reconstruction (kinetic-EFIT). Nonlinear CGYRO simulations were performed

at the average DBS location of $\rho = 0.67$ for DIII-D discharge 189998 at 3005 ms. Table C.1 provides local input parameters for the nonlinear flux-tube simulations. In all simulations we use the MXH flux surface parameterization [15], the Sugama collision model [16], gyrokinetic electrons, and $E \times B$-shear. Simulations were performed using GPUs on the National Energy Research Scientific Computing Center (NERSC) Perlmutter computer, a Department of Energy Office of Science User Facility using NERSC award ERCAP0029284.

Two categories of simulations were performed during the wavenumber spectrum investigation: ion-scale simulations and one more expensive simulation (we will refer the more expensive simulation as the 'large' simulation). The large simulation was designed to include wavenumbers up to the highest measured DBS wavenumber ($k_y \approx 6$) while maintaining sufficient k_y-resolution to resolve ion-scale modes. The ion-scale simulations were designed to capture the transport fluxes (which are peaked at $k_y \approx 0.4$; cf. Figure 4.17). Unless otherwise noted, simulations used $N_\theta = 24$ poloidal angles, $N_\xi = 16$, $N_\varepsilon = 8$, and 3 gyrokinetic species (Deuterium, Carbon, electrons).

Ion-scale simulations at were performed with $N_{k_y} = 32$ toroidal modes and `KY` $= 0.05$ implying a span of $0 \leq k_y \leq 1.55$. These simulations used $N_{k_x} = 540$ radial modes and `BOX_SIZE` $= 12$ resulting in a $128 \times 126\rho_{s,\text{unit}}$ numerical grid in the radial and binormal directions respectively. Some lower-resolution ion-scale simulations (particularly for parameter scans) were performed with $N_{k_y} = 16$ toroidal modes, $N_{k_x} = 540$ radial modes, `BOX_SIZE` $= 30$ and `KY` $= 0.16$ implying a span of $0 \leq k_y \leq 2.4$ and a $96 \times 40\rho_{s,\text{unit}}$ grid. These low-resolution ion-scale simulations were found to sufficiently resolve the transport fluxes with respect to the $N_{k_y} = 32$ simulations but were not used for detailed synthetic DBS investigations. Finally, the large simulation used $N_{k_y} = 32$ toroidal modes, $N_{k_x} = 1536$ radial modes, `BOX_SIZE` $= 48$ and `KY` $= 0.197$ implying a span of $0 \leq k_y \leq 6.11$ and a $125 \times 32\rho_{s,\text{unit}}$ grid.

Table C.1: Input parameters for nonlinear CGYRO simulations presented in Chapter 4.

Quantity	Value
a/L_{n_e}	0.96
a/L_{T_e}	2.51
a/L_{n_D}	1.13
a/L_{T_D}	1.11
a/L_{n_C}	0.28
n_D/n_e	0.795
n_C/n_e	0.034
$Z_{\text{eff.}}$	2.02
T_D/T_e	0.76
$\nu_{ei}[a/c_s]$	0.126
a/c_s [μs]	2.7
β_e	7.1×10^{-3}
$\rho^* = \rho_{s,\text{unit}}/a$	2.65×10^{-3}
q	2.74
$\hat{s} = rd(\ln q)/dr$	1.96
κ (elongation)	1.35
δ (triangularity)	0.16
ζ (squareness)	-0.01

REFERENCES

[1] Wurzel S E and Hsu S C 2022 *Physics of Plasmas* 29

[2] Hawryluk R, Batha S, Blanchard W, Beer M, Bell M, Bell R, Berk H, Bernabei S, Bitter M, Breizman B *et al.* 1998 *Physics of Plasmas* 5 1577–1589

[3] Rhodes T, Lantsov R, Wang G, Ellis R and Peebles W 2018 *Review of Scientific Instruments* 89

[4] Hall-Chen V H, Parra F I and Hillesheim J C 2022 *Plasma Physics and Controlled Fusion* 64 095002

[5] Damba J, Pratt Q, Hall-Chen V, Hong R, Lantsov R, Ellis R and Rhodes T 2022 *Review of Scientific Instruments* 93

[6] Hall-Chen V H, Damba J, Parra F I, Pratt Q T, Michael C A, Peng S, Rhodes T L, Crocker N A, Hillesheim J C, Hong R *et al.* 2022 *Review of Scientific Instruments* 93

[7] Pratt Q, Hall-Chen V, Neiser T, Hong R, Damba J, Rhodes T, Thome K, Yang J, Haskey S, Cote T *et al.* 2023 *Nuclear Fusion* 64 016001

[8] Ruiz J R, Parra F, Hall-Chen V, Christen N, Barnes M, Candy J, Garcia J, Giroud C, Guttenfelder W, Hillesheim J *et al.* 2022 *Plasma Physics and Controlled Fusion* 64 055019

[9] Pratt Q, Rhodes T, Chrystal C and Carter T 2022 *Plasma Physics and Controlled Fusion* 64 095017

[10] Rhodes T, Michael C, Shi P, Scannell R, Storment S, Pratt Q, Lantsov R, Fitzgerald I, Hall-Chen V, Crocker N *et al.* 2022 *Review of Scientific Instruments* 93

[11] Storment S, Scannell R, Shi P, Michael C, Pratt Q, Carter T and Rhodes T 2021 A new combined doppler backscattering and cross-polarization scattering system for measurement of density and magnetic turbulence in the mast-u spherical tokamak *APS Division of Plasma Physics Meeting Abstracts* vol 2021 pp BP11–020

[12] Li S, Jiang H, Ren Z, Xu C *et al.* 2014 Optimal tracking for a divergent-type parabolic pde system in current profile control *Abstract and Applied Analysis* vol 2014 (Hindawi)

[13] D'haeseleer W D, Hitchon W N G, Callen J D and Shohet J L 1991 *Flux coordinates and magnetic field structure: a guide to a fundamental tool of plasma theory* (Springer Berlin Heidelberg)

[14] Miller R, Chu M S, Greene J, Lin-Liu Y and Waltz R 1998 *Physics of Plasmas* 5 973–978

[15] Arbon R, Candy J and Belli E A 2020 *Plasma Physics and Controlled Fusion* 63 012001

[16] Candy J, Belli E A and Bravenec R 2016 *Journal of Computational Physics* 324 73–93

[17] Luxon J L 2002 *Nuclear Fusion* 42 614

[18] Lao L, John H S, Stambaugh R, Kellman A and Pfeiffer W 1985 *Nuclear fusion* 25 1611

[19] Wesson J and Campbell D J 2011 *Tokamaks* vol 149 (Oxford university press)

[20] Petty C, Luce T, Burrell K, Chiu S, Degrassie J, Forest C, Gohil P, Greenfield C, Groebner R, Harvey R *et al.* 1995 *Physics of Plasmas* 2 2342–2348

[21] ITER E *et al.* 1999 *Nuclear Fusion* 39 2175–2249

[22] Sugama H and Horton W 1997 *Physics of Plasmas* 4 405–418

[23] Hazeltine R 1973 *Plasma Physics* 15 77

[24] Sugama H, Okamoto M, Horton W and Wakatani M 1996 *Physics of Plasmas* 3 2379–2394

[25] Belli E and Candy J 2008 *Plasma Physics and Controlled Fusion* 50 095010

[26] Sugama H and Horton W 1998 *Physics of Plasmas* 5 2560–2573

[27] Horton W 1999 *Reviews of Modern Physics* 71 735

[28] Staebler G, Kinsey J and Waltz R 2007 *Physics of Plasmas* 14

[29] Staebler G, Kinsey J and Waltz R 2005 *Physics of Plasmas* 12

[30] Kinsey J, Staebler G and Waltz R 2008 *Physics of Plasmas* 15

[31] Staebler G, Candy J, Waltz R, Kinsey J and Solomon W 2013 *Nuclear Fusion* 53 113017

[32] Staebler G M, Candy J, Howard N T and Holland C 2016 *Physics of Plasmas* 23

[33] Staebler G M, Candy J, Belli E A, Kinsey J E, Bonanomi N and Patel B 2020 *Plasma Physics and Controlled Fusion* 63 015013

[34] Staebler G M, Belli E, Candy J, Kinsey J, Dudding H and Patel B 2021 *Nuclear Fusion* 61 116007

[35] Dudding H, Casson F, Dickinson D, Patel B, Roach C, Belli E and Staebler G 2022 *Nuclear Fusion* 62 096005

[36] Staebler G M, Belli E and Candy J 2023 *Physics of Plasmas* 30

[37] Guzdar P, Chen L, Tang W and Rutherford P 1980 Ion-temperature-gradient instability in toroidal plasmas Tech. rep. Princeton Plasma Physics Lab.(PPPL), Princeton, NJ (United States)

[38] Guo S and Romanelli F 1993 *Physics of Fluids B: Plasma Physics* 5 520–533

[39] Belli E and Candy J 2010 *Physics of Plasmas* 17

[40] Merz F and Jenko F 2010 *Nuclear Fusion* 50 054005

[41] Nordman H, Weiland J and Jarmén A 1990 *Nuclear Fusion* 30 983

[42] Dannert T and Jenko F 2005 *Physics of Plasmas* 12

[43] Casati A, Bourdelle C, Garbet X and Imbeaux F 2008 *Physics of Plasmas* 15

[44] Jenko F, Dorland W, Kotschenreuther M and Rogers B 2000 *Physics of plasmas* 7 1904–1910

[45] Waltz R, Candy J and Fahey M 2007 *Physics of plasmas* 14

[46] Jenko F, Dorland W and Hammett G 2001 *Physics of Plasmas* 8 4096–4104

[47] Mantica P, Angioni C, Bonanomi N, Citrin J, Grierson B, Koechl F, Mariani A, Staebler G, Eurofusion J, Eurofusion M *et al.* 2019 *Plasma Physics and Controlled Fusion* 62 014021

[48] Garbet X, Idomura Y, Villard L and Watanabe T 2010 *Nuclear Fusion* 50 043002

[49] Hakim A H, Mandell N R, Bernard T, Francisquez M, Hammett G and Shi E 2020 *Physics of Plasmas* 27

[50] Holland C, Luce T C, Grierson B A, Smith S P, Marinoni A, Burrell K H, Petty C and Bass E 2021 *Nuclear Fusion* 61 066033

[51] Smith S P, Petty C C, White A E, Holland C, Bravenec R, Austin M E, Zeng L and Meneghini O 2015 *Nuclear Fusion* 55 083011

[52] Lyons B, McClenaghan J, Slendebroek T, Meneghini O, Neiser T, Smith S, Weisberg D, Belli E, Candy J, Hanson J *et al.* 2023 *Physics of Plasmas* 30

[53] Romanelli M, Corrigan G, Parail V, Wiesen S, Ambrosino R, Belo P D S A, Garzotti L, Harting D, Koechl F, Koskela T *et al.* 2014 *Plasma and Fusion research* 9 3403023–3403023

[54] Candy J, Holland C, Waltz R, Fahey M R and Belli E 2009 *Physics of Plasmas* 16

[55] Meneghini O, Snyder P, Smith S, Candy J, Staebler G, Belli E, Lao L, Park J, Green D, Elwasif W *et al.* 2016 *Physics of Plasmas* 23

[56] Rodriguez-Fernandez P, Howard N, Saltzman A, Kantamneni S, Candy J, Holland C, Balandat M, Ament S and White A 2023 *arXiv preprint arXiv:2312.12610*

[57] White A E and Görler T 2017 *Plasma Phys. Controlled Fusion* 59 050101

[58] Rhodes T, Holland C, Smith S, White A, Burrell K, Candy J, DeBoo J, Doyle E, Hillesheim J, Kinsey J *et al.* 2011 *Nuclear Fusion* 51 063022

[59] White A, Peebles W, Rhodes T, Holland C, Wang G, Schmitz L, Carter T, Hillesheim J, Doyle E, Zeng L *et al.* 2010 *Physics of Plasmas* 17

[60] Freethy S, Görler T, Creely A, Conway G, Denk S, Happel T, Koenen C, Hennequin P, White A, Team A U *et al.* 2018 *Physics of Plasmas* 25

[61] Höfler K 2022

[62] Ruiz J R, Guttenfelder W, White A E, Howard N T, Candy J, Ren Y, Smith D, Loureiro N, Holland C and Domier C 2019 *Plasma Physics and Controlled Fusion* 61 115015

[63] Holland C, Kinsey J, DeBoo J, Burrell K, Luce T, Smith S, Petty C, White A, Rhodes T, Schmitz L *et al.* 2013 *Nuclear Fusion* 53 083027

[64] Nakata M, Honda M, Yoshida M, Urano H, Nunami M, Maeyama S, Watanabe T H and Sugama H 2016 *Nuclear Fusion* 56 086010

[65] Howard N, White A, Reinke M, Greenwald M, Holland C, Candy J and Walk J 2013 *Nuclear Fusion* 53 123011

[66] Howard N, Rodriguez-Fernandez P, Holland C, Odstrcil T, Grierson B, Sciortino F, McKee G, Yan Z, Wang G, Rhodes T *et al.* 2024 *Physics of Plasmas* 31

[67] Creely A, Howard N, Rodriguez-Fernandez P, Cao N, Hubbard A, Hughes J, Rice J, White A, Candy J, Staebler G *et al.* 2017 *Physics of Plasmas* 24

[68] Casati A, Gerbaud T, Hennequin P, Bourdelle C, Candy J, Clairet F, Garbet X, Grandgirard V, Gürcan Ö, Heuraux S *et al.* 2009 *Physical review letters* 102 165005

[69] Casati A 2012 *arXiv preprint arXiv:1204.3254*

[70] Holland C, DeBoo J, Rhodes T, Schmitz L, Hillesheim J, Wang G, White A, Austin M, Doyle E, Peebles W *et al.* 2012 *Nuclear Fusion* 52 063028

[71] Hillesheim J, Holland C, Schmitz L, Kubota S, Rhodes T and Carter T 2012 *Review of Scientific Instruments* 83

[72] Ernst D, Burrell K, Guttenfelder W, Rhodes T, Dimits A, Bravenec R, Grierson B, Holland C, Lohr J, Marinoni A *et al.* 2016 *Physics of Plasmas* 23

[73] Happel T, Navarro A B, Conway G, Angioni C, Bernert M, Dunne M, Fable E, Geiger B, Görler T, Jenko F *et al.* 2015 *Physics of Plasmas* 22

[74] Stroth U, Navarro A B, Conway G, Görler T, Happel T, Hennequin P, Lechte C, Manz P, Simon P, Biancalani A *et al.* 2015 *Nuclear Fusion* 55 083027

[75] Lechte C, Conway G, Görler T, Tröster C, Team A U *et al.* 2014 Doppler reflectometry simulations for asdex upgrade *41st EPS Conference on Plasma Physics*

[76] Lechte C, Conway G, Görler T, Tröster-Schmid C, Team A U *et al.* 2017 *Plasma Physics and Controlled Fusion* 59 075006

[77] Lechte C, Conway G, Görler T, Happel T, Team A U *et al.* 2020 *Plasma Science and Technology* 22 064006

[78] Happel T, Görler T, Hennequin P, Lechte C, Bernert M, Conway G, Freethy S, Honoré C, Pinzón J, Stroth U *et al.* 2017 *Plasma Physics and Controlled Fusion* 59 054009

[79] Peebles W, Rhodes T, Hillesheim J, Zeng L and Wannberg C 2010 *Review of Scientific Instruments* 81

[80] Conway G, Schirmer J, Klenge S, Suttrop W, Holzhauer E *et al.* 2004 *Plasma Physics and Controlled Fusion* 46 951

[81] Happel T, Estrada T, Blanco E, Tribaldos V, Cappa A and Bustos A 2009 *Review of Scientific Instruments* 80 073502

[82] Molina Cabrera P, Coda S, Porte L, Offeddu N, Lavanchy P, Silva M, Toussaint M and Team T 2018 *Review of Scientific Instruments* 89 083503

[83] Hu J, Zhou C, Liu A, Wang M, Doyle E, Peebles W, Wang G, Zhang X, Zhang J, Feng X *et al.* 2017 *Review of Scientific Instruments* 88 073504

[84] Conway G, Scott B, Schirmer J, Reich M, Kendl A, Team A U *et al.* 2005 *Plasma Physics and Controlled Fusion* 47 1165

[85] Schirmer J, Conway G, Holzhauer E, Suttrop W, Zohm H and Team A U 2007 *Plasma Physics and Controlled Fusion* 49 1019–1039

[86] Pinzón J, Estrada T, Happel T, Hennequin P, Blanco E, Stroth U, Teams T I *et al.* 2019 *Plasma Physics and Controlled Fusion* 61 105009

[87] Stix T H 1992 *Waves in plasmas* (Springer Science & Business Media)

[88] Bornatici M, Cano R, De Barbieri O and Engelmann F 1983 *Nuclear Fusion* 23 1153

[89] Sheffield J, Froula D, Glenzer S H and Luhmann Jr N C 2010 *Plasma scattering of electromagnetic radiation: theory and measurement techniques* (Academic press)

[90] Pinzón J, Happel T, Blanco E, Conway G, Estrada T and Stroth U 2017 *Plasma Physics and Controlled Fusion* 59 035005

[91] Gusakov E and Surkov A 2004 *Plasma physics and controlled fusion* 46 1143

[92] Piliya A and Popov A Y 2002 *Plasma physics and controlled fusion* 44 467

[93] Hirsch M and Holzhauer E 2004 *Plasma physics and controlled fusion* 46 593

[94] Hennequin P, Honoré C, Quéméneur A, Truc A, Gervais F, Fenzi C and Sabot R 1999 Analysis of density fluctuation frequency spectra in tore supra as a tool for studying plasma motion and transport properties *Proc. 26th EPS Conf. on Plasma Physics*

[95] Hennequin P, Honoré C, Truc A, Quéméneur A, Fenzi-Bonizec C, Bourdelle C, Garbet X, Hoang G *et al.* 2006 *Nuclear fusion* 46 S771

[96] Maggs J, Rhodes T L and Morales G 2015 *Plasma Physics and Controlled Fusion* 57 045004

[97] Sigeti D E 1995 *Physica D: Nonlinear Phenomena* 82 136–153

[98] Maggs J and Morales G 2012 *Physical Review E* 86 015401

[99] Maggs J and Morales G 2012 *Plasma Physics and Controlled Fusion* 54 124041

[100] Pedregosa F, Varoquaux G, Gramfort A, Michel V, Thirion B, Grisel O, Blondel M, Prettenhofer P, Weiss R, Dubourg V, Vanderplas J, Passos A, Cournapeau D, Brucher M, Perrot M and Duchesnay E 2011 *Journal of Machine Learning Research* 12 2825–2830

[101] Peel D and McLachlan G J 2000 *Statistics and computing* 10 339–348

[102] Meneghini O, Smith S, Lao L, Izacard O, Ren Q, Park J, Candy J, Wang Z, Luna C, Izzo V, Grierson B, Snyder P, Holland C, Penna J, Lu G, Raum P, McCubbin A, Orlov D, Belli E, Ferraro N, Prater R, Osborne T, Turnbull A and Staebler G 2015 *Nuclear Fusion* 55 083008 URL `http://iopscience.iop.org/article/10.1088/0029-5515/55/8/083008/meta`

[103] Smirnov A and Harvey R 2001 *CompX Report No. CompX-2000-01*

[104] Poli E, Bock A, Lochbrunner M, Maj O, Reich M, Snicker A, Stegmeir A, Volpe F, Bertelli N, Bilato R *et al.* 2018 *Computer Physics Communications* 225 36–46

[105] Goldsmith P F *et al.* 1998 *Quasioptical systems* (Chapman & Hall New York)

[106] Mazzucato E 1992 *Physics of Fluids B: Plasma Physics* 4 3460–3461

[107] Gusakov E, Surkov A and Popov A Y 2005 *Plasma physics and controlled fusion* 47 959

[108] Lopez N and Dodin I 2022 *Physics of Plasmas* 29

[109] Maj O, Pereverzev G V and Poli E 2009 *Physics of Plasmas* 16

[110] Chrystal C, Grierson B, Staebler G, Petty C, Solomon W, DeGrassie J, Burrell K, Tala T and Salmi A 2017 *Physics of Plasmas* 24 056113

[111] Shi Y, Ko W, Kwon J, Diamond P, Lee S, Ko S, Wang L, Yi S, Ida K, Terzolo L *et al.* 2013 *Nuclear Fusion* 53 113031

[112] Angioni C, Peeters A, Pereverzev G, Ryter F, Tardini G, Team A U *et al.* 2003 *Physical review letters* 90 205003

[113] Peeters A, Angioni C, Apostoliceanu M, Jenko F, Ryter F *et al.* 2005 *Physics of Plasmas* 12

[114] Holcomb C, Makowski M, Allen S, Meyer W and Van Zeeland M 2008 *Review of Scientific Instruments* 79

[115] Chrystal C, Burrell K, Grierson B A, Haskey S R, Groebner R, Kaplan D and Briesemeister A 2016 *Review of Scientific Instruments* 87 11E512

[116] Wang X, Mordijck S, Doyle E J, Rhodes T L, Zeng L, McKee G R, Austin M E, Meneghini O, Staebler G M and Smith S P 2017 *Nuclear Fusion* 57 116046

[117] Zeng L, Peebles W A, Doyle E J, Rhodes T L, Crocker N, Nguyen X, Wannberg C W and Wang G 2014 *Review of Scientific Instruments* 85 11D843

[118] Austin M and Lohr J 2003 *Review of scientific instruments* 74 1457–1459

[119] Logan N, Grierson B A, Haskey S, Smith S, Meneghini O and Eldon D 2018 *Fusion Science and Technology* 74 125–134

[120] Schilham A, Hogeweij G and Cardozo N L 2001 *Plasma physics and controlled fusion* 43 1699

[121] De Baar M, Beurskens M, Hogeweij G and Lopes Cardozo N 1999 *Physics of plasmas* 6 4645–4657

[122] Kullberg A, Morales G and Maggs J 2014 *Physics of Plasmas* 21

[123] Barnes M, Parra F and Schekochihin A 2011 *Physical Review Letters* 107 115003

[124] Gürcan Ö D, Garbet X, Hennequin P, Diamond P, Casati A and Falchetto G 2009 *Physical review letters* 102 255002

[125] Hillesheim J, Crocker N, Peebles W, Meyer H, Meakins A, Field A, Dunai D, Carr M, Hawkes N, Team M *et al.* 2015 *Nuclear Fusion* 55 073024

[126] Estrada T, Sánchez E, García-Regaña J, Alonso J, Ascasíbar E, Calvo I, Cappa A, Carralero D, Hidalgo C, Liniers M *et al.* 2019 *Nuclear Fusion* 59 076021

[127] Estrada T, Ascasíbar E, Blanco E, Cappa A, Diamond P, Happel T, Hidalgo C, Liniers M, van Milligen B P, Pastor I *et al.* 2012 *Plasma Physics and Controlled Fusion* 54 124024

[128] Happel T, Estrada T, Blanco E, Hidalgo C, Conway G, Stroth U and Team T I 2011 *Physics of Plasmas* 18

[129] Hennequin P, Sabot R, Honoré C, Hoang G, Garbet X, Truc A, Fenzi C and Quéméneur A 2004 *Plasma Physics and Controlled Fusion* 46 B121

[130] Hennequin P 2006 *Comptes Rendus Physique* 7 670–678

[131] Devynck P, Garbet X, Laviron C, Payan J, Saha S, Gervais F, Hennequin P, Quemeneur A and Truc A 1993 *Plasma physics and controlled fusion* 35 63

[132] Howard N, Holland C, White A, Greenwald M, Candy J and Creely A 2016 *Physics of Plasmas* 23 056109

[133] Schmitz L, Holland C, Rhodes T, Wang G, Zeng L, White A, Hillesheim J, Peebles W, Smith S, Prater R *et al.* 2012 *Nuclear Fusion* 52 023003

[134] Vermare L, Hennequin P, Gürcan Ö D, Bourdelle C, Clairet F, Garbet X, Sabot R, Team T S *et al.* 2011 *Physics of Plasmas* 18

[135] Rhodes T, Leboeuf J N, Sydora R, Doyle E, Moyer R, Rettig C, Burrell K, Thomas D, McKee G and Peebles W 2000 Turbulent radial correlation lengths in the diii-d tokamak Tech. rep. General Atomics, San Diego, CA (US)

[136] Maj O, Balakin A and Poli E 2010 *Plasma Physics and Controlled Fusion* 52 085006

[137] Hinton F and Wong S 1985 *The Physics of fluids* 28 3082–3098

[138] Helander P and Sigmar D J 2005 *Collisional transport in magnetized plasmas* vol 4 (Cambridge university press)

[139] Kim Y, Diamond P and Groebner R 1991 *Physics of Fluids B: Plasma Physics* 3 2050–2060

[140] Hinton F and Rosenbluth M 1999 *Plasma physics and controlled fusion* 41 A653

[141] Solomon W, Burrell K, Gohil P, Groebner R and Baylor L 2004 *Review of scientific instruments* 75 3481–3486

[142] Howell R, Fonck R, Knize R and Jaehnig K 1988 *Review of Scientific Instruments* 59 1521–1523

[143] Von Hellermann M, Mandl W, Summers H, Weisen H, Boileau A, Morgan P, Morsi H, Koenig R, Stamp M and Wolf R 1990 *Review of scientific instruments* 61 3479–3486

[144] Burrell K, Doyle E, Gohil P, Groebner R, Kim J, La Haye R, Lao L, Moyer R, Osborne T, Peebles W *et al.* 1994 *Physics of plasmas* 1 1536–1544

[145] Grierson B, Van Zeeland M, Scoville J, Crowley B, Bykov I, Park J, Heidbrink W, Nagy A, Haskey S and Liu D 2021 *Nuclear Fusion* 61 116049

[146] Giavarina D 2015 *Biochemia medica* 25 141–151

[147] Hinton F and Rosenbluth M 1999 *Physics Letters A* 259 267–275

[148] Degrassie J, Groebner R and Burrell K 2006 *Physics of plasmas* 13

[149] Tala T, Crombé K, De Vries P, Ferreira J, Mantica P, Peeters A, Andrew Y, Budny R, Corrigan G, Eriksson A *et al.* 2007 *Plasma Physics and Controlled Fusion* 49 B291

[150] Burrell K 1997 *Physics of Plasmas* 4 1499–1518

[151] Taylor G I 1922 *Proceedings of the london mathematical society* 2 196–212

[152] Grésillon D, Cabrit B, Villain J, Hanuise C, Truc A, Laviron C, Hennequin P, Gervais F, Quemeneur A, Garbet X *et al.* 1992 *Plasma Physics and Controlled Fusion* 34 1985

[153] Kubo R 1962 *Journal of the Physical Society of Japan* 17 1100–1120

[154] Kubo R 1969 *Advances in chemical physics* 15 101–127

[155] Hazeltine R D 2018 *The framework of plasma physics* (CRC Press)

[156] Zwillinger D and Jeffrey A 2007 *Table of integrals, series, and products* (Elsevier)

[157] Newville M, Stensitzki T, Allen D B, Rawlik M, Ingargiola A and Nelson A 2016 *Astrophysics Source Code Library* ascl–1606

[158] Candy J and Waltz R 2003 *Journal of Computational Physics* 186 545–581

[159] Beer M A, Cowley S and Hammett G 1995 *Physics of Plasmas* 2 2687–2700